Ph.D. Thesis

Molecularly imprinted polymers in chemical sensors electrochemically recognizing chosen toxins using a 'gate effect'

Patrycja Łach

IChF
Institute of Physical Chemistry PAS

Ph.D. Thesis

Molecularly imprinted polymers in chemical sensors electrochemically recognizing chosen toxins using a 'gate effect'

Patrycja Łach

Supervisor

Prof. Włodzimierz Kutner, Ph.D., D.Sc.
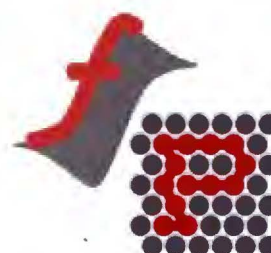
Auxiliary supervisor

Dr. Eng. Maciej Cieplak, Ph.D.

The thesis was prepared within the International Doctoral in Chemistry Studies
at the Institute of Physical Chemistry of the Polish Academy of Sciences in Warsaw
in the Molecular Films Research Group and the Functional Polymers Group

Molecular Films Research | **Kutner Group**

Functional Polymers

Warsaw, May 2023

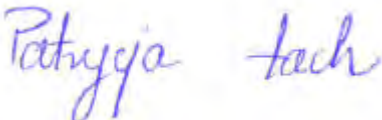*To my family*

Declaration of originality

I hereby declare that the research included in this thesis was carried out by myself or with support from others included in the acknowledgments.

I state that I have exercised care to ensure that the work is original and contains no previously published material or written by another person, except where citations have been made in the text. To the best of my knowledge, the content provided here does not violate any copyrights.

I accept that the Polish Academy of Sciences has the right to use plagiarism detection software to ensure the thesis's legitimacy.

I certify that no part of my thesis has been or will be submitted for obtaining a degree or diploma by the Institute of Physical Chemistry, Polish Academy of Science, or any other educational institution.

This thesis's copyright rests with the author; no information derived from it may be published without the author's consent.

Signature: *Patrycja Tach*

Date: 30.05.2023

Acknowledgments

First of all, I would like to emphasize that this work would not have been possible without many people's constant help and support.

Above all, I would like to express my deep gratitude to my supervisors, Professor Włodzimierz Kutner and Doctor Maciej Cieplak, for their guidance and mentorship throughout my research. Not only have they invested their precious time in providing me with constructive comments and suggestions, but their constant feedback and insights have greatly helped me refine my work. I do believe that their expertise and assistance have been crucial to the success of this project.

I would also like to acknowledge Professor Piyush Sidhu Sharma for always being there to lend a helping hand whenever I needed it. I cannot express enough how grateful I am for his unwavering encouragement, support, and essential contributions to my work.

I deeply thank Professor Sergey A. Piletsky, the head of Leicester Biotechnology Group, for the possibility of conducting research in his Group at the University of Leicester, UK. I am grateful for his guidance and willingness to share his experiences and insights. Moreover, I would like to acknowledge Doctor Francesco Canfarotta and Doctor Alvaro Garcia-Cruz for providing protocols for synthesizing MIP nanoparticles and sharing their knowledge about them. Our discussions have been instrumental in my professional growth, and I am truly thankful for their experience, help, and time teaching me MIP nanoparticles' preparation.

I would also like to thank all Molecular Films and Functional Polymers research groups' colleagues, especially Agnieszka (P.-L.), Agnieszka (W.-H.), Jakub, Karolina, Katarzyna, Marta, Paula, as well as other colleagues from the Institute of Physical Chemistry. I am grateful to have worked with a talented group of colleagues throughout my Ph.D. journey. I really appreciate their support and helpful discussions, which have been invaluable for me in completing this research project.

Finally, I would like to express my appreciation to all my family members, especially my parents and my sister, for their assistance, understanding, and patience throughout my life. Their support and belief in me have been my motivation to keep going.

Besides, I would like to acknowledge the following colleagues' help.

- Dr. Paweł Borowicz for performing PM-IRRAS experiments
- Prof. Francis D'Souza and Raghu Chitta for providing functional monomers FM 1, FM 2, and FcM
- M.Sc. Karolina Gołębiewska, Dr. Marta Majewska, and Dr. Krzysztof Noworyta for AFM imaging
- Dr. Alistair Groves for synthesizing squaramide-based monomer SQ6
- M.Sc. Jakub Kałęcki for performing SEM experiments, artwork, and fruitful collaboration
- Prof. Wojciech Lisowski and Dr. Kostiantyn Nikiforow for performing XPS experiments and discussion
- Dr. Piotr Pięta for helping with PM experiments at EQCM and fruitful collaboration
- Dr. Marta Sosnowska for discussion
- Mr. Jerzy Szaniawski for artwork

Funding

List of publications

1. **Lach, P.**; Sharma, P.S.; Golebiewska, K.; Cieplak, M.; D'Souza, F.; Kutner, W., *Chem. Eur. J.* **2017**, *23*, 1942–1949 (2022 Impact factor: 5.236, 19 citations), "Molecularly Imprinted Polymer Chemosensor for Selective Determination of an *N*-nitroso-L-proline Food Toxin." https://doi.org/10.1002/chem.201604799

2. Dabrowski, M.; **Lach, P.**; Cieplak, M.; Kutner, W., *Biosens. Bioelectron.* **2018**, *102*, 17–26, (2022 Impact factor: 12.545, 137 citations), "Nanostructured molecularly imprinted polymers for protein chemosensing." https://doi.org/10.1016/j.bios.2017.10.045

3. **Lach, P.**; Cieplak, M.; Majewska, M.; Noworyta, K. R.; Sharma, P.S.; Kutner, W., *Anal. Chem.* **2019**, *91*, 7546–7553, (2022 Impact factor: 8.008, 28 citations), "'Gate Effect' in *p*-Synephrine Electrochemical Sensing with a Molecularly Imprinted Polymer and Redox Probes." https://doi.org/10.1021/acs.analchem.8b05512

4. **Lach, P.**; Cieplak, M.; Noworyta, K. R.; Pieta, P.; Lisowski, W.; Kalecki, J.; Chitta, R.; D'Souza, F.; Kutner, W., Sharma, P. S., *Sens. Actuators B Chem.* **2021**, *344*, 130276 (2022 Impact factor: 9.221, 14 citations), "Self-reporting molecularly imprinted polymer with the covalently immobilized ferrocene redox probe for selective electrochemical sensing of *p*-synephrine." https://doi.org/10.1016/j.snb.2021.130276

5. Ayerdurai, V.; **Lach, P.**; Lis-Cieplak, A.; Cieplak, M.; Kutner, W.; Sharma, P. S., *Crit. Rev. Food Sci. Nutr.* **2022**, published online, (2022 Impact factor: 11.208), "An advantageous application of molecularly imprinted polymers in food processing and quality control." https://doi.org/10.1080/10408398.2022.2132208

6. **Lach, P.**; Garcia-Cruz, A.; Canfarotta, F.; Groves, A.; Kalecki, J.; Korol, D.; Borowicz, P.; Nikiforow, K.; Cieplak, M.; Kutner, W.; Piletsky, S. A.; Sharma, P.S, *Biosens. Bioelectron.* **2023**, accepted, (2022 Impact factor: 12.545), "Electroactive molecularly imprinted polymer nanoparticles for selective glyphosate determination."

Conference materials

1. **Lach, P.**; Cieplak, M.; Sharma, P. S.; Sosnowska, M.; D'Souza, F.; Kutner, W., *Proceedings on the 5th International Symposium on Sensor Science (I3S 2017)*, Barcelona, Spain 2017; Vol. 1, 772, Self-Reporting Molecularly Imprinted Polymer for Label-Free Selective Electrochemical Sensing of *p*-Synephrine.

Patents awarded

1. **Łach, P.**; Cieplak, M.; Sosnowska, M.; Kutner, W., Polish Patent No. Pat.233295, 17 June 2019, „Polimer wdrukowany molekularnie za pomocą *p*-synefryny, sposób jego otrzymywania oraz zastosowanie" (English translation of the patent title: "Molecularly imprinted polymer by means of *p*-synephrine and selective chemosensor for electrochemical marking of *p*-synephrine with a layer of the molecularly imprinted polymer as the recognizing unit"). https://ewyszukiwarka.pue.uprp.gov.pl/search/pwp-details/P.422854.

2. **Łach, P.**; Cieplak, M.; Sharma, P. S.; Iskierko, Z.; D'Souza, F.; Kutner, W., Polish Patent No. Pat.234732, 20 December 2019, „Chemosensor z molekularnie wdrukowanym polimerem tiofenowym do selektywnego oznaczania nitrozoaminowych toksyn, zwłaszcza *N*-nitrozo-L-proliny" (English translation of the patent title: "Chemosensor with molecularly imprinted polymer of thiophene for selective determination of nitrosamine toxins, preferably *N*-nitroso-L-proline"). https://ewyszukiwarka.pue.uprp.gov.pl/search/pwp-details/P.418332.

3. **Łach, P.**; Cieplak, M.; Sosnowska, M.; Sharma, P.S.; Chitta, R.; D'Souza, F.; Kutner, W., Polish Patent No. Pat.238793, 15 July 2021, „Polimer wydrukowany molekularnie z wbudowanym próbnikiem redoks i solą dostarczającą przeciwjony oraz selektywny czujnik chemiczny do elektrochemicznego oznaczania wybranych analitów z warstwą polimeru wydrukowanego molekularnie, jako jednostką rozpoznającą" (English translation of the patent title: "Molecularly imprinted polymer with inbuilt redox sampler and salt that provides counterions and the selective chemical sensor for electrochemical marking of selected analytes with a layer of the molecularly imprinted polymer as the recognizing unit"). https://ewyszukiwarka.pue.uprp.gov.pl/search/pwp-details/P.422855.

Presentations at scientific conferences

As a presenting author

Oral presentations

1. **Łach, P**.; Cieplak, M.; Kutner, W., „Wdrukowany molekularnie polimer z wbudowanym wewnątrz próbnikiem redoks zastosowany jako jednostka rozpoznająca i przetwornik sygnału w selektywnych czujnikach elektrochemicznych", 60. Zjazd Naukowy Polskiego Towarzystwa Chemicznego, Wrocław, Poland, 17–20 September 2017.

2. **Łach, P.**; Cieplak, M.; Majewska, M.; Noworyta, K.; Sharma, P. S.; Kutner, W., "Electrochemical chemosensor based on *p*-synephrine molecularly imprinted polymer using external or internal redox probe: ′gate effect′ in conductive molecularly imprinted polymers," 62. Zjazd Naukowy Polskiego Towarzystwa Chemicznego, Warszawa, Poland, 2–6 September 2019.

Poster presentations

1. **Łach, P.**; Sharma, P. S.; Cieplak, M.; D'Souza, F.; Kutner, W., "Molecularly imprinted polymer chemosensor for selective determination of *N*-nitroso-L-proline in food products of animal origin," 59. Zjazd Naukowy Polskiego Towarzystwa Chemicznego, Poznań, Poland, 19–23 September 2016.

2. **Lach, P.**; Sharma, P. S.; Golebiewska, K.; Cieplak, M.; D'Souza, F.; Kutner, W., "Molecularly imprinted polymer chemosensor for selective determination of *N*-nitroso-L-proline in food products of animal origin." Tenth German Biosensor Symposium (10th DBS)/First European Biosensor Symposium (1st EBS), Potsdam, Germany, 20–23 March 2017.

3. **Lach, P.**; Sharma, P. S.; Golebiewska, K.; Cieplak, M.; D'Souza, F.; Kutner, W., "Molecularly imprinted polymer chemosensor for selective determination of *N*-nitroso-L-proline in food products of animal origin," XIV Warszawskie Seminarium Doktorantów Chemików - ChemSession'17, Warszawa, Poland, 9 June 2017.

4. **Lach, P.**; Cieplak, M.; Sharma, P. S.; Sosnowska, M.; D'Souza, F.; Kutner, W., "Self-reporting Molecularly Imprinted Polymer for Label-free Selective Electrochemical Sensing of *p*-Synephrine," 8th International Workshop on Surface Modification for Chemical and Biochemical Sensing, Żelechów, Poland, 3–7 November 2017.

5. **Lach, P.**; Cieplak, M.; Sharma, P. S.; Sosnowska, M.; D'Souza, F.; Kutner, W., "Self-reporting Molecularly Imprinted Polymer for Label-free Selective Electrochemical Sensing of *p*-Synephrine," XV Warszawskie Seminarium Doktorantów Chemików - ChemSession'18, Warszawa, Poland, 8 June 2018.

6. **Lach, P.**; Cieplak, M.; Sharma, P. S.; Sosnowska, M.; D'Souza, F.; Kutner, W., "Self-reporting Molecularly Imprinted Polymer for Label-free Selective Electrochemical Sensing of p-Synephrine," The 10th International Conference on Molecular Imprinting, MIP 2018, Jerusalem, Israel, 24–28 June 2018.

7. **Łach, P.**; Cieplak, M.; Majewska, M.; Noworyta, K.; Sharma, P. S.; Kutner, W., "On the "gate effect" in electrochemical sensing with a molecularly imprinted polymer and redox probes," XVI Warszawskie Seminarium Doktorantów Chemików - ChemSession'19, Warszawa, Poland, 7 June 2019.

8. **Lach, P.**; Cieplak, M.; Majewska, M.; Noworyta, K.; Sharma, P. S.; D'Souza, F; Kutner, W., "Gate Effect" in Electrochemical Chemosensor Based on Conductive Molecularly Imprinted Polymer Using External or Internal Redox Probe," 9th International Workshop on Surface Modification for Chemical and Biochemical Sensing, Żelechów, Poland, 8–12 November 2019.

9. **Lach, P.**; Cieplak, M.; Garcia-Cruz, A.; Canfarotta, F.; Sharma, P.S.; Piletsky, S.A.; Kutner, W., "Chemosensor Based on Molecularly Imprinted Nanoparticles for Selective Determination of Glyphosate," 239th ECS Meeting with the 18th International Meeting on Chemical Sensors (IMCS), Digital Meeting, 30 May–3 June 2021.

Awards

1. Award of "Young Researchers of the Institute of Physical Chemistry of the Polish Academy of Sciences" ("Young Researchers IPC PAS") competition in 2019.

2. Award of "Young Researchers of the Institute of Physical Chemistry of the Polish Academy of Sciences" ("Young Researchers IPC PAS") competition in 2020.

3. Award of "Young Researchers of the Institute of Physical Chemistry of the Polish Academy of Sciences" ("Young Researchers IPC PAS") competition in 2021.

4. Best poster award at 8th International Workshop on Surface Modification for Chemical and Biochemical Sensing, Żelechów, Poland, 3–7 November 2017.

5. Best poster award at 9th International Workshop on Surface Modification for Chemical and Biochemical Sensing, Żelechów, Poland, 8–12 November 2019.

6. "Mobility of Young Researchers of the Institute of Physical Chemistry of the Polish Academy of Sciences" award covering costs of monthly research secondment in 2019.

7. The Institute of Physical Chemistry of the Polish Academy of Sciences distinction in the competition for the best work published in 2021.

List of abbreviations

1-NA – 1-naphthylamine

3D NPNi – 3D nanoporous nickel (skeleton)

4-VP – 4-vinylpyridine

AAm – allylamine

AAPS – *N*-(2-aminoethyl)-3-aminopropyltrimethoxysilane

AAT – acetic acid thiophene

ac – alternating current

ACN – acetonitrile

Ac-Pro – *N*-acetyl-L-proline

AFM – atomic force microscopy

AFP – alfa-fetoprotein

AgNP – silver nanoparticle

APTES – (3-aminopropyl)triethoxysilane

ATP – adenosine triphosphate

ATR – attenuated total reflection

AU – *N*-allylurea

AuNP – gold nanoparticle

BaP – benzo[a]pyrene

BAW – bulk acoustic wave

BHA – butylated hydroxyanisole

BHb – bovine hemoglobin

BiCoPc – phthalocyanine cobalt(II) sulphonate

BPA – bisphenol A

BTSE – 1,2-*bis*(triethoxysilyl)ethane

CAP – chloramphenicol

CBF – carbofuran

CD – cyclodextrin

CE – counter electrode

CEA – carcinoembryonic antigen

CHEM-FET – chemically sensitized field-effect transistor

CIL – cilostazol

CM 1 – 5,5',5"-methanetriyltris(2,2'-bithiophene)

CM 2 – 2,3'-bithiophene

CNT – carbon nanotube

CPE – carbon paste electrode

CS – chitosan

CV – cyclic voltammetry

dc – direct current

DFT – density functional theory

dhCIL – 3,4-dehydrocilostazol

DLS – dynamic light scattering

DMF – dimethylformamide

DNA – deoxyribonucleic acid

DPV – differential pulse voltammetry

DVB – divinylbenzene

DZN – diazinon

EBT – Eriochrome Black T

ECD – 1-(3-dimethylaminopropyl)-3-ethylcarbodiimide hydrochloride

EDOT – 3,4-ethylenedioxy-thiophene

EDX – energy dispersive X-ray (spectroscopy)

EGDMA – ethylene glycol dimethacrylate

EG-FET – extended-gate field-effect transistor

EGMP – ethylene glycol methacrylate phosphate

EIS – electrochemical impedance spectroscopy

ELISA – enzyme-linked immunosorbent assay

e-MIP – electrochemical MIP

EQCM – electrochemical quartz crystal microbalance

Ery – erythrocin

EVC – envision antibody complex

FB_1 – fumonisin B_1

Fc – ferrocene

Fc^+ – ferrocenium

FcM – *bis*-(2,2'-bithienyl)-4-ferrocenylphenyl methane

FET – field-effect transistor

FIA – flow-injection analysis

FM 1 – *p-bis*(2,2'-bithien-5-yl)-methylphenol

FM 2 – *p-bis*(2,2'-bithien-5-yl)methyl-o-catechol

FM 3 – 2,2'-bithiophene-5-carboxylic acid

FMAA – ferrocenylmethyl methacrylate

FMN – flavin mononucleotide

FTIR – Fourier-transform infrared (spectroscopy)

GCE – glassy carbon electrode

GDH – glucose dehydrogenase

GLY – glyphosate

GN – graphene

GNN – graphene nanosheet

GO – graphene oxide

GST-π – glutathione-s-transferase-π

HA – hyaluronic acid

HAP – hydroxyapatite

hCG – human chorionic gonadotropin

HEMA – 2-hydroxyethyl methacrylate

HPLC – high-performance liquid chromatography

HRP – horseradish peroxidase

HSA – human serum albumin

HTM – heat transfer method

IDP – imidacloprid

IF – imprinting factor

IIP – ion-imprinted polymer

IL – ionic liquid

IR – infrared (light)

IRRAS – infrared reflection-absorption spectroscopy

ISE – ion-selective electrode

ITA – itaconic acid

ITO – indium-tin oxide

IUPAC – International Union of Pure and Applied Chemistry

KE – kinetic energy

LOD – limit of detection

LSAW – leaky surface acoustic wave

LSV – linear sweep voltammetry

MAA – methacrylic acid

MB – magnetic bead

MICP – molecularly imprinted conducting polymer

MIP – molecularly imprinted polymer

MOF – metal-organic framework

MWCNT – multi-walled carbon nanotube

MIP NP – MIP nanoparticle

ncovNP – SARS-CoV-2 nucleocapsid protein

NHS – *N*-hydroxysuccinimide

NIP – non-imprinted polymer

NP – nanoparticle

OHP – outer Helmholtz plane

o-PD – *o*-phenylenediamine

PB – phosphate buffer

PrB – Prussian Blue

PBS – phosphate-buffered saline

PCM – polarizable continuum model

PDA – polydopamine

PDGF-BB – platelet-derived growth factor B-chain

PdI – polydispersity index

PEM – photoelastic modulator

PID – proportional-integral-derivative

PM – piezoelectric microgravimetry

PM-IRRAS – polarization-modulation infrared reflection-absorption spectroscopy

poly-A – polyadenine

PPD – poly(phenylenediamine)

PPY – polypyrrole

Pro-NO – *N*-nitroso-L-proline

PSA – prostate-specific antigen

PSP – propagating surface plasmon

PtNP – platinum nanoparticle

QCM – quartz crystal microbalance

QCR – quartz crystal resonator

QD – quantum dot

RCA – rolling circle amplification

RE – reference electrode

rGO – reduced graphene oxide

RNA – ribonucleic acid

RSD – relative standard deviation

SAM – self-assembled monolayer

SARS-CoV-2 – severe acute respiratory syndrome coronavirus 2

SAW – surface acoustic wave

$scCO_2$ – supercritical carbon dioxide

SDS – sodium dodecyl sulfate

SEM – scanning electron microscopy

SERS – surface-enhanced Raman spectroscopy

SG – sulfonated graphene

SIP – surface-imprinted polymer

SMX – sulfamethoxazole

SPCE – screen-printed carbon electrode

SPE – solid-phase extraction

SPEl – screen-printed electrode

SPPtE – screen-printed platinum electrode

SPR – surface plasmon resonance

SQ6 – squaramide-based monomer

St.dev. – standard deviation

SWV – square wave voltammetry

SYN – *p*-synephrine

$(TBA)ClO_4$ – tetra-n-butylammonium perchlorate

$(TBA)OH$ – tetra-n-butylammonium hydroxide

TDMACl – tridodecylmethylammonium chloride

$(TEA)ClO_4$ – tetra-n-ethylammonium perchlorate

TEM – transmission electron microscopy

TFEMA – 2,2,2-trifluoroethyl methacrylate

THC – tetrahydrocannabinol

TLC – thin-layer chromatography

TRIM – trimethylolpropane trimethacrylate

UHV – ultra-high vacuum

UV-vis – ultraviolet-visible (light)

VFc – vinylferrocene

VPBA – vinylphenylboronic acid

WE – working electrode

XPS – X-ray photoelectron spectroscopy

ZnP – zinc porphyrin

List of symbols

A – electrode surface area, cm^2

A' – acoustically active resonator area, cm^2

a_A – activity of the determined ion A

a_B – activity of the interfering ion B

Abs – absorbance

BE – electron binding energy, eV

C – capacitance, F

c – concentration, M or $g\ mL^{-1}$

C_{dl} – electrochemical double-layer capacitance, $F\ m^{-2}$

CPE – constant phase element

D – diffusion coefficient, $cm^2\ s^{-1}$

d – light path length of the cuvette, cm

$d(H)$ – hydrodynamic particle diameter

E – electrode potential, V

$E(t)$ – alternating voltage, V

E_0 – potential amplitude, mV

$E_{1/2}$ – half-wave potential, V

E_f^0 – formal potential of a reaction, V

E_i – initial potential, V

$E_{p/2}$ – half-peak potential, V

E_{pa} – potential of the anodic peak, V

E_{pc} – potential of the cathodic peak, V

E_v – vertex potential, V

ΔE – pulse amplitude, V

ΔE_p – difference of the anodic and cathodic peak potentials, V

ΔE_s – potential step height, mV

f – frequency, Hz

f_0 – fundamental resonance frequency of the resonator, here 10 MHz

Δf_{mass} – change in resonance frequency corresponding to the change in mass of a resonator, Hz

Δf_{vis} – change in resonance frequency corresponding to the change in viscosity and density of a liquid adjacent to the electrode surface of a resonator, Hz

F – Faraday's constant, 96485.3 C mol^{-1}

ΔG – Gibbs free energy change, kJ mol^{-1}

Int – intensity of transmitted light

Int_0 – intensity of incident light

$I(t)$ – alternating current, A

I_0 – current amplitude, A

I_{p} – peak current, A

I_{pa} – anodic peak current, A

I_{pc} – cathodic peak current, A

ΔI – relative change in the DPV peak current

$\Delta I_{\max}$ – maximal relative change in the DPV peak current

j – imaginary unit ($j^2 = -1$)

k – Boltzmann's constant

k' – free-space wavenumber

k^2 – electromechanical coupling factor of the resonator, 7.74×10^{-3} A^2 s^2 cm^{-2}

K – the concentration of the compound at equilibrium/equilibrium constant for heterogeneous solid, nM^{-1}

$K_{\mathrm{A,B}}^{\mathrm{pot}}$ – potentiometric selectivity coefficient

KE – kinetic energy of the emitted photoelectron, eV

K_{s} – stability constant

L – inductance

m – mass, g

n – number of electrons transferred in the elementary redox process

n' – homogeneity factor

n_{s} – refractive index of the dielectric

Q_{sat} – Langmuir-Freundlich maximum adsorption capacity

R – ideal gas constant, 8.3145 J mol^{-1} K^{-1}

$\overline{R}$ – dynamic resistance, Ω

R^2 – correlation coefficient

R_{ct} – charge transfer resistance, Ω

R_s – resistance of electrolyte solution, Ω

S/N – signal-to-noise ratio

t – time, s

t_m – sampling time after pulse application, ms

T – absolute temperature, K

T' – frequency-independent proportionality factor

$Trans$ – transmittance

ν – potential scan rate, mV s^{-1}

W – Warburg impedance, Ω

$W_{1/2}$ – DPV or SWV peak width at half height, mV

Z – impedance, Ω

z_A – charge of the determined ion A

z_B – charge of the interfering ion B

Z_{CPE} – impedance of a constant phase element, Ω

Z_{im} – imaginary component of impedance, Ω

Z_{real} – real component of impedance, Ω

$|Z|$ – magnitude of impedance

α – charge transfer coefficient

β – propagation constant of the propagating surface plasmon

Γ_o^* – maximum electrode coverage with the oxidized species

ε – molar absorptivity coefficient, M^{-1} cm^{-1} or mL cm^{-1} g^{-1}

ε_m – electric permittivity of the metal

η_L – dynamic viscosity, cP

μ_q – shear modulus of quartz, 2.947×10^{11} g s^{-2} cm^{-1}

ρ_L – liquid density, g cm^{-3}

ρ_q – quartz density, 2.648 g cm^{-3}

τ – staircase period, s

τ' – step width, s

φ – phase angle, °

Φ_{spec} – spectrometer work function

ω – angular frequency, rad s^{-1}

Abstract (in English)

Developing reliable, fast, simple, and cost-effective analytical procedures for determining toxins is still challenging. Molecularly imprinted polymers (MIPs), a great example of bio-mimicking recognition materials, can meet this challenge.

The present dissertation aimed to devise, fabricate and validate chemical sensors with MIPs as recognition units to selectively determine some toxins encountered in food and dietary supplements using the "gate effect." It describes several crucial issues.

The first part focuses on devising (MIP film)-based chemosensors selective to N-nitroso-L-proline (Pro-NO) food contaminant and p-synephrine (SYN) dietary supplement. Initially, Pro-NO and SYN were used as templates. First, the most appropriate functional monomers (FMs) were selected by calculating the stability of the pre-polymerization complexes of templates with selected thiophene-based FMs with the density functional theory (DFT). Then, with the chosen FMs, MIP films were deposited on the surface of conducting transducers by potentiodynamic electropolymerization. Next, the templates were extracted from MIPs. Complete removal of templates from polymers was confirmed by differential pulse voltammetry (DPV), electrochemical impedance spectroscopy (EIS), X-ray photoelectron spectroscopy (XPS), and polarization-modulation infrared reflection absorption spectroscopy (PM-IRRAS). The deposited MIPs morphology was determined by surface imaging with atomic force microscopy (AFM). The MIP chemosensors prepared that way were applied for Pro-NO and SYN determination using DPV, EIS, piezoelectric microgravimetry (PM), or surface plasmon resonance (SPR) spectroscopy. Moreover, analytical parameters of the chemosensors, including sensitivity, linear dynamic concentration range, selectivity, and the limit of detection (LOD), were determined.

To better understand the operation principle of MIP-based chemosensors, the second part of the research details an investigation of the so-called "gate effect" mechanism for the electrodes coated with conductive MIP films. Functionalized polythiophene polymer imprinted with SYN (SYN-MIP) film was used as a model polymer film. Different techniques, including cyclic voltammetry (CV), DPV, EIS, SPR, AFM, and UV-vis spectroscopy, were applied to unravel mechanisms accounting for changes in the electrochemical signal recorded at the electrode coated with the SYN-MIP film due to the binding of SYN analyte.

The above analysis enabled the devising of a self-reporting MIP electrochemical sensor with the covalently immobilized redox probe for label-free determination of the SYN model analyte. For that purpose, a new monomer, a ferrocene derivative (FcM), was synthesized and used for MIP film preparation. Its role was to provide an internal redox probe on the one hand and act as a cross-linking monomer on the other. Applying the system, the same as for the traditional ("gate effect")-operated SYN-MIP film chemosensor, allowed comparing the analytical performance of those two chemical sensors fabricated. Notably, the analytical parameters of the chemosensor with the covalently immobilized redox probe were superior compared to those determined for similar chemosensors lacking a self-reporting system.

The final part of the thesis describes devising and testing self-reporting chemosensors for glyphosate (GLY) herbicide determination. Electroactive molecularly imprinted nanoparticles (MIP NPs) with an internal redox probe were applied as recognition units in these sensors. The MIP NPs were synthesized using a solid-phase synthesis protocol, then characterized, and then covalently immobilized on the surface of electrodes. The electrochemical sensors prepared that way were successfully used for label-free sensing of GLY.

Abstract (in Polish)

Opracowanie niezawodnych, szybkich, prostych i tanich procedur analitycznych do oznaczania substancji toksycznych to wciąż ogromne wyzwanie. Przykładem materiałów rozpoznających, które mogą sprostać temu wyzwaniu są polimery wdrukowane molekularne (ang. molecularly imprinted polymers, MIPs).

Niniejsza rozprawa doktorska przedstawia badania przeprowadzone w celu opracowania, wykonania i sprawdzenia działania czujników elektrochemicznych, w których jako jednostki rozpoznające zastosowaliśmy MIP-y do selektywnego oznaczania wybranych substancji toksycznych występujących w żywności i suplementach diety z wykorzystaniem "efektu bramki". Rozprawa obejmuje kilka wzajemnie powiązanych zagadnień.

W pierwszej części przedstawiliśmy badania uwieńczone opracowaniem czujników elektrochemicznych z warstwami MIP-ów jako elementami rozpoznającymi, selektywnymi względem N-nitrozo-L-proliny (Pro-NO) i p-synefryny (SYN). Pro-NO i SYN zastosowaliśmy jako szablony wdrukowania molekularnego. Najpierw wybraliśmy najbardziej odpowiednie monomery funkcyjne (ang. functional monomers, FMs). W tym celu określiliśmy trwałość oddziaływań wybranych FM-ów, pochodnych tiofenu, z szablonami w kompleksie pre-polimeryzacyjnym spontanicznie tworzącym się w roztworze do polimeryzacji, za pomocą modelowania kwantowo-chemicznego z wykorzystaniem teorii funkcjonału gęstości (ang. density functional theory, DFT). Z kolei kompleksy te posłużyły do osadzenia MIP-ów na przewodzących przetwornikach za pomocą polimeryzacji potencjodynamicznej. Następnie wyekstrahowaliśmy szablony z warstw MIP-ów. Całkowite usunięcie szablonów z MIP-ów potwierdziliśmy za pomocą woltamperometrii pulsowej różnicowej (ang. differential pulse voltammetry, DPV), elektrochemicznej spektroskopii impedancyjnej (ang. electrochemical impedance spectroscopy, EIS) spektroskopii fotoelektronów w zakresie promieniowania X (ang. X-ray photoelectron spectroscopy, XPS) i spektroskopii odbiciowo-absorpcyjnej o modulowanej polaryzacji w podczerwieni (ang. polarization-modulation infrared reflection-absorption spectroscopy, PM-IRRAS). Morfologię osadzonych polimerów zobrazowaliśmy za pomocą mikroskopii sił atomowych (ang. atomic force microscopy, AFM). Tak przygotowanymi czujnikami oznaczyliśmy Pro-NO i SYN za pomocą DPV, EIS, mikrograwimetrii piezoelektrycznej

(ang. piezoelectric microgravimetry, PM) i spektroskopii rezonansu plazmonów powierzchniowych (ang. surface plasmon resonance. SPR). Ponadto na podstawie powyższych pomiarów wyznaczyliśmy parametry analityczne czujników w tym czułość, liniowy dynamiczny zakres stężeń, selektywność i granicę wykrywalności (ang. limit of detection, LOD).

Następna część rozprawy obejmuje szczegółową analizę mechanizmu tzw. "efektu bramki" przeprowadzoną dla elektrod pokrytych przewodzącymi warstwami MIP-ów na przykładzie warstwy MIP-u z wdrukowanym szablonem SYN (SYN-MIP). Za pomocą CV, DPV, EIS, SPR, AFM i spektroskopii UV-vis określiliśmy mechanizm zmiany sygnału elektrochemicznego elektrody pokrytej warstwą SYN-MIP w trakcie oznaczania SYN.

Analiza "efektu bramki" umożliwiła skonstruowanie samoraportującego elektrochemicznego czujnika typu MIP z kowalencyjnie wbudowanym próbnikiem redoks do oznaczania SYN w nieobecności próbnika redoks w roztworze badanym. Do przygotowania warstwy MIP-u zastosowaliśmy nowy monomer, tiofenową pochodną ferrocenu (FcM), który pełnił jednocześnie rolę wewnętrznego próbnika redoks i monomeru sieciującego. Zastosowanie tego samego układu co w przypadku konwencjonalnego czujnika SYN-MIP z próbnikiem redoks w roztworze i z wykorzystaniem "efekt bramki", pozwoliło na porównanie parametrów analitycznych tych dwóch czujników elektrochemicznych. Co istotne, parametry analityczne czujnika z kowalencyjnie wbudowanym próbnikiem redoks okazały się lepsze niż analogiczne parametry wyznaczone dla konwencjonalnego czujnika elektrochemicznego bez mechanizmu samoraportującego.

Ostatnia część rozprawy zawiera opis eksperymentów przeprowadzonych w celu opracowania samoraportujących czujników elektrochemicznych do selektywnego oznaczania herbicydu – glifosatu (GLY). Jako jednostkę rozpoznającą zastosowaliśmy tu elektrochemicznie aktywne nanodrobiny MIP-ów (MIP NPs) z kowalencyjnie wbudowanym ferrocenem. Zsyntetyzowane MIP NPs najpierw scharakteryzowaliśmy po czym unieruchomiliśmy je na powierzchni elektrod. Za pomocą tak przygotowanych czujników oznaczyliśmy GLY w nieobecności próbnika redoks w roztworze badanym.

Introduction and research goals

People are constantly exposed to toxic substances in their daily life. Toxicants may originate from different sources, including natural or human-made sources. Common origins of toxic compounds comprise industrial, agricultural, pharmaceutical, household, food, and natural sources where toxins are produced from living organisms. Consumers are continually subjected to numerous food contaminants in their diet, which is now a significant public concern. Toxins may cause different undesirable effects and pose a severe health threat to people. Continuous exposure to toxins may negatively affect the nervous, immune, or reproductive systems, leading to chronic diseases. Therefore, developing efficient, fast, robust, and inexpensive procedures for toxic substance determination is necessary.

The presented research aims to devise and fabricate chemical sensors with molecularly imprinted polymers (MIPs) as recognition units for the selective sensing of chosen toxic compounds, along with the relevant determination procedures. *N*-nitroso-L-proline (Pro-NO) - a representative of potentially carcinogenic *N*-nitrosamines, *p*-synephrine (SYN) - a dietary supplement that is suspected of causing serious cardiovascular diseases, and glyphosate (GLY) – a herbicide that may be responsible for numerous chronic diseases including cancers, asthma, diabetes, were chosen as target toxin analytes.

Notably, the crucial part of our research is a detailed investigation of the "gate effect" accounting for the operation of the studied conductive MIP film-based chemosensors. Electrochemical determination of electroinactive analytes with a traditional MIP chemosensor requires the addition of an external redox probe to the test solution. It is assumed that binding the target analyte molecules by MIP cavities leads to polymer swelling or shrinking, resulting in changes in MIP film permittivity for the redox probe and, thus, changes in faradaic currents corresponding to reduction or oxidation of the redox probe in electrochemical determinations. However, this mechanism does not explain all possible phenomena that may account for the change in the current of the redox probe due to analyte binding by the MIP. Therefore, the origin of changes in the current of the redox probe associated with the binding of SYN, selected as the model analyte, was herein explored thoroughly.

The "gate effect" mechanism study prompts fabricating self-reporting MIP chemical sensors with an immobilized ferrocene redox probe in the polymer matrix.

The applicability of our MIP chemosensor was examined by SYN determination in a (redox probe)-free solution. Moreover, the self-reporting sensor's performance was compared with the traditional sensor's performance operating based on the "gate effect" mechanism.

Table of Contents

Chapter 1

1. Literature review

In the last decades, people in developed countries are becoming increasingly conscious of factors influencing their health, including lifestyle, diet, and environmental effects. Many substances that can be found in food products can threaten health and even life. Therefore, finding reliable, fast, cost-effective methods for determining toxic food contaminants is crucial nowadays.

1.1 Introduction to chemical sensors

Chemical sensors (chemosensors) are analytical devices that meet the above requirements, as their primary role is the target analyte selective differentiation from its interferences. Since chemosensors are sensitive, rapid, and inexpensive, they may be promising tools for food safety monitoring. The International Union of Pure and Applied Chemistry (IUPAC) defines a chemosensor as "a device that transforms chemical information, ranging from the concentration of a specific sample component to total composition analysis, into an analytically useful signal."[1] The above chemical information may originate from a chemical reaction of the analyte or a physical property of the system investigated.[1] Usually, chemosensors consist of two functional units, i.e., a receptor and a transducer (Scheme 1.1-1). Moreover, some chemosensors may contain a separator, e.g., a membrane.
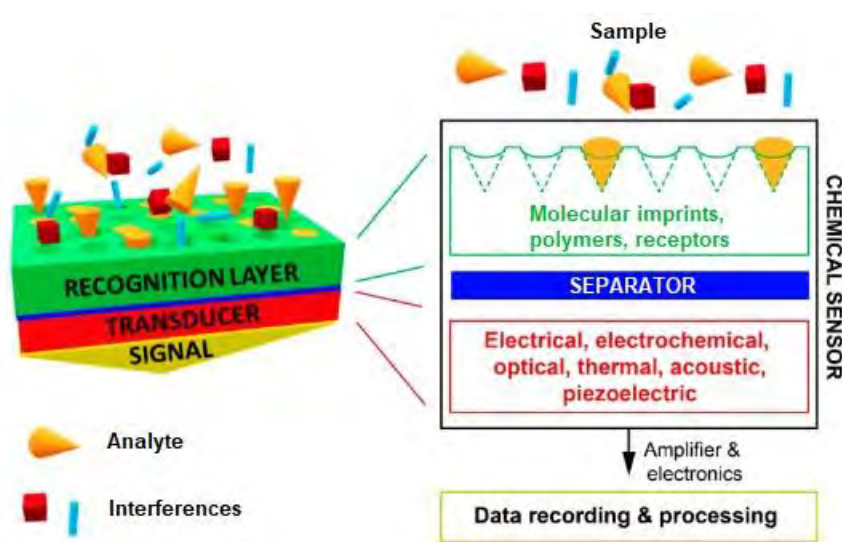
Scheme 1.1-1. The block diagram of a chemosensor containing a recognition layer, a separator, a transducer, and a signal detector.[2]

1

The chemosensor recognition unit transforms chemical information into energy that is measured by the transducer. The mechanism of this unit operation is related to a chemical reaction or a physical process that changes conductivity, absorbance, refractive index, mass, temperature, etc.

The IUPAC calls sensors the biosensors if an analytical signal originates from a biochemical reaction.[3] That is possible if recognition units are of biological origin. These include enzymes, antibodies, histones, nucleic acids, organelles, cells, and tissues. Then, the transducer changes the energy transmitting the chemical information received from the recognition unit into a proper analytical signal. The signal transduction may involve different phenomena, including optical or mass changes, heat effects, and electrochemical processes.

Similarly, the chemosensor recognition unit is responsible for distinguishing between the target analyte and its interferences. Therefore, finding such a recognition material is crucial for proper chemosensor operation. In chemosensors, the recognition unit is an artificial material.[4-18] Although biosensors are advantageous revealing, e.g., fast response, high sensitivity, and selectivity, they suffer drawbacks, including low stability and durability, especially under harsh conditions.[19-20] To overcome these deficiencies, several approaches have been developed, including modifying the sensor's surface with nature-inspired artificial recognition materials that can be nearly as sensitive as biological receptors but durable and stable simultaneously. One such approach is applying molecularly imprinted polymers (MIPs) as recognition units of chemosensors.

1.1.1 Preparation of molecularly imprinted polymers (MIPs)

MIPs, often called "plastic antibodies," are synthetic receptors that have gained increasing interest in recent decades as recognition units.[21] Several advantages of MIPs, including superior recognition properties, high affinity, selectivity to the target analyte, and chemical, mechanical and thermal stability higher than natural receptors, have led to their application as selective recognition units in chemosensors for the determination of various analytes.[22-28] Moreover, owing to MIPs' advantages of low-cost fabrication, rapid measurements, easy preparation, and operation, as well as the universal nature of molecular imprinting in polymer technology, MIPs have become attractive materials for commercial use and industry.[29-31] MIP-based chemosensors have been devised to determine many analytes, including those of low molecular weight and those complex such as proteins, viruses, or even whole bacteria.[8-18] Among them are herbicides, pesticides, drugs, sugars, chemical vapors, etc.[32-39] Moreover, various transductions were applied for analytes' sensing by MIP chemosensors, namely,

2

optical techniques such as absorbance, fluorescence, surface plasmon resonance (SPR) spectroscopy, and electrochemical techniques, including voltammetry, potentiometry, electric technique using chemically sensitized field-effect transistors (CHEM-FETs), electric measuring, e.g., electrolytic conductivity or electric permittivity as well as mass sensitive techniques, including piezoelectric microgravimetry (PM) at a quartz crystal microbalance exploiting either bulk (QCM) or surface acoustic wave (SAW) excitation.[2, 21, 40-41]

MIPs are prepared by selecting suitable functional monomers that may form stable pre-polymerization complexes with templates in solution. An analyte itself or its surrogate can be used as the template. Forming a stable template–monomer pre-polymerization complex capable of surviving subsequent polymerization is a crucial step of MIP preparation and may determine its recognition ability. Functional monomers can bear recognizing sites, including functional groups, π-conjugated systems, and heteroatoms that can interact with the template's binding sites via different interactions, including hydrogen and covalent bonds, π-π stacking, electrostatic attractions, hydrophobic and van der Walls interactions, etc. Next, the pre-polymerization complex is polymerized, typically in the cross-linking monomer presence, resulting in a sufficiently rigid polymer structure. Subsequently, the template is removed from the MIP, leaving empty molecularly imprinted cavities complementary to template molecules regarding their size, shape, and orientation of recognizing sites (Scheme 1.1-2). Such an MIP is ready to recognize the target analyte.
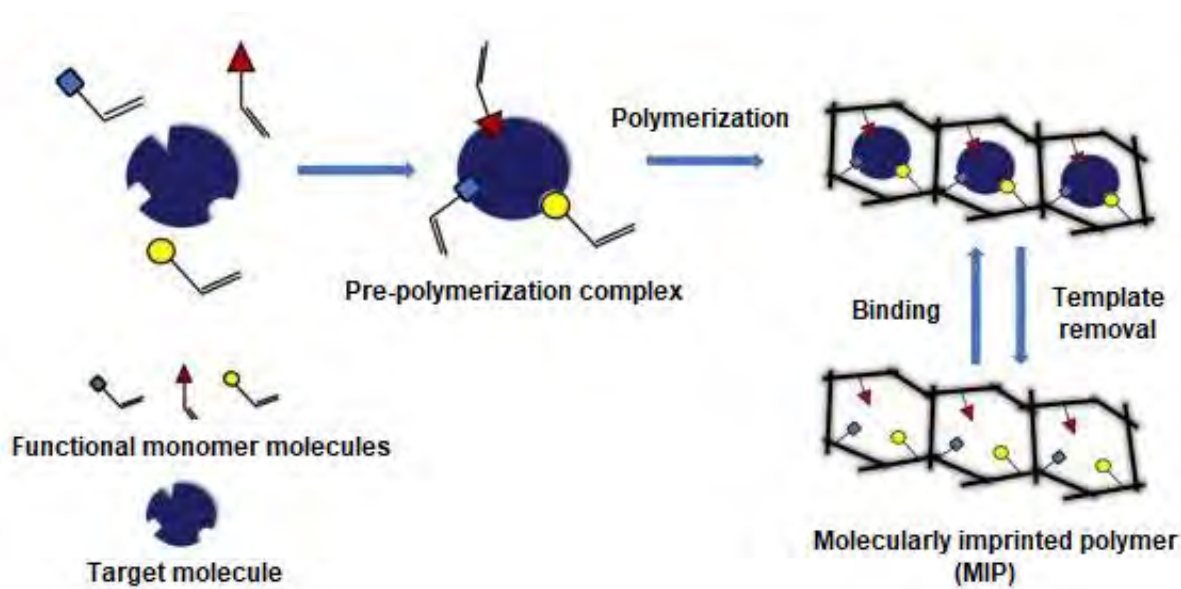
Scheme 1.1-2. The flowchart of MIP preparation.[42]

3

Depending on MIPs' potential applications, they can be prepared in various forms, namely bulk polymers, membranes, grains, micro-, and nanoparticles (NPs), or thin films deposited on the solid support surfaces. Furthermore, MIPs are frequently prepared via free radical polymerization, applying various preparation techniques, including bulk, precipitation, emulsion, and suspension methods, as well as surface and epitope imprinting, sol-gel transition, and electropolymerization (Scheme 1.1-3).

Bulk polymerization (Scheme 1.1-3a) is induced thermally or by ultraviolet irradiation in the presence of a soluble radical initiator and soluble functional and cross-linking monomers.[43-45] Bulk polymerization is easy to perform and cost-effective, but it requires a high amount of porogenic agent. Moreover, MIP particles are obtained by milling. Therefore, a resulting bulk polymer may be irregular in shape and size, and disadvantageously, recognizing sites may be destroyed in this procedure.

Precipitation polymerization (Scheme 1.1-3b) characterizes an initially homogeneous system in the continuous phase with soluble initiator as well as soluble functional and cross-linking monomers. Then, an insoluble polymer is formed upon initiation, and thus it precipitates out of the solution.[43-48] Precipitation polymerization is a simple and rapid method of MIP formation. However, it requires rigorous reaction control and is mainly applied to large-scale MIP production.

Emulsion polymerization (Scheme 1.1-3c) describes the polymerization whereby polymer spherical particles are formed from initially an inhomogeneous system of the dispersion medium, monomers, initiator, and possibly colloid stabilizer.[43, 49-53] The addition of a stabilizer or a surfactant is not necessary, but the presence of a hydrophobic monomer and a hydrophilic initiator is essential. Furthermore, surfactants and other polymerization agents may remain in the synthesized polymer. Then, they are difficult to remove. Generally, MIPs prepared by emulsion polymerization do not require any further processing.

During suspension polymerization (Scheme 1.1-3d), a polymer is formed from a dispersed monomer or monomer-solvent droplets suspended in the liquid phase.[54-58] This polymerization allows obtaining porous MIPs with regular shapes but requires employing hydrophobic monomers and initiators. Moreover, a stabilizer and surfactant must be applied.

Importantly, free radical polymerization methods often employ acrylic or vinylic monomers for non-conductive MIP preparation. These methods suffer from several drawbacks, including incomplete template removal from the polymer bulk during MIP preparation, which leads to constricted access of analyte molecules to MIP cavities during

4

analyte binding. The surface imprinting procedure (Scheme 1.1-3e) permits circumventing these disadvantages.

The surface imprinting consists of a pre-polymerization complex of functional monomers and template formation followed by polymerization, carried out on a solid substrate's surface in the presence of a cross-linking monomer and an initiator. An MIP is deposited as a nanometer-thick film. Then, a template is removed from the MIP, generating three-dimensional imprinting cavities located on the substrate surface.[59-61] Quantum dots (QDs), magnetic NPs, polystyrene microspheres, carbon nanomaterials, metal-organic frameworks (MOFs), and silica are frequently employed as solid-phase substrates in this method.[62] Surface imprinting enables preparing MIPs with high porosity and surface-to-volume ratio. Molecularly imprinted cavities formed are exposed on the surface, facilitating target analyte molecules binding to MIP cavities and thus achieving high selectivity, fast mass transfer, and high binding rate. On the other hand, this method suffers from unclear recognition mechanisms and poor templates' solubility in certain solvents.[59]

Moreover, an epitope imprinting method (Scheme 1.1-3f) was developed in response to the challenging imprinting of complex macromolecular compounds, such as proteins.[63-64] This method involves imprinting a short external part of a macromolecule template, called an epitope, instead of the whole macromolecule. This approach is cost-effective because not the whole costly macromolecular compound is necessary for imprinting. Moreover, the imprinting may be easily controlled and seems more resistant to harsh polymerization conditions. Due to the small size of the template, its removal is more facile than the removal of the whole imprinted macromolecule. Epitopes can be imprinted via bulk or surface imprinting.[64-65] The latter involves template immobilization on a solid support via various interactions, including physical adsorption, covalent bonding, boronate affinity, and metal ion chelation.[66-69]

Another popular method for MIPs preparation is a sol-gel transition (Scheme 1.1-3g). It involves a metal oxide precursor mixing with the template in the solution, followed by hydrolysis and polycondensation of the precursor to form a polymeric gel.[70-71] Sol-gel imprinting is a simple, one-step procedure that allows preparing a homogeneous, room-temperature stable polymer material using inorganic solvents, including water.[72] Moreover, the surface area and porosity of the polymer formed can easily be controlled.

Furthermore, MIPs may be prepared by electropolymerization (Scheme 1.1-3h). This method has gained a lot of interest because of the possibility of deposition of conducting and non-conducting polymers directly on the conducting or semiconducting transducer surface.

5

The method is fast and straightforward. Moreover, it enables precise control of polymer thickness and morphology.[73-74] Electropolymerization may be accomplished either anodically or cathodically. Most frequently, an MIP film is deposited by anodic oxidation of electroactive functional and cross-linking monomers controlled by the potential or current applied.[73, 75] The electro-oxidation results in simultaneous polymer doping with counter ions. The mechanism of anodic electropolymerization involves the oxidative formation of monomer radical cations. The excessive charge is applied for further electro-oxidation of the resulting oligomers. Either coupling between radical cations or a radical cation reaction with a neutral monomer results in the formation and growth of a polymer film on the electrode surface.[76]
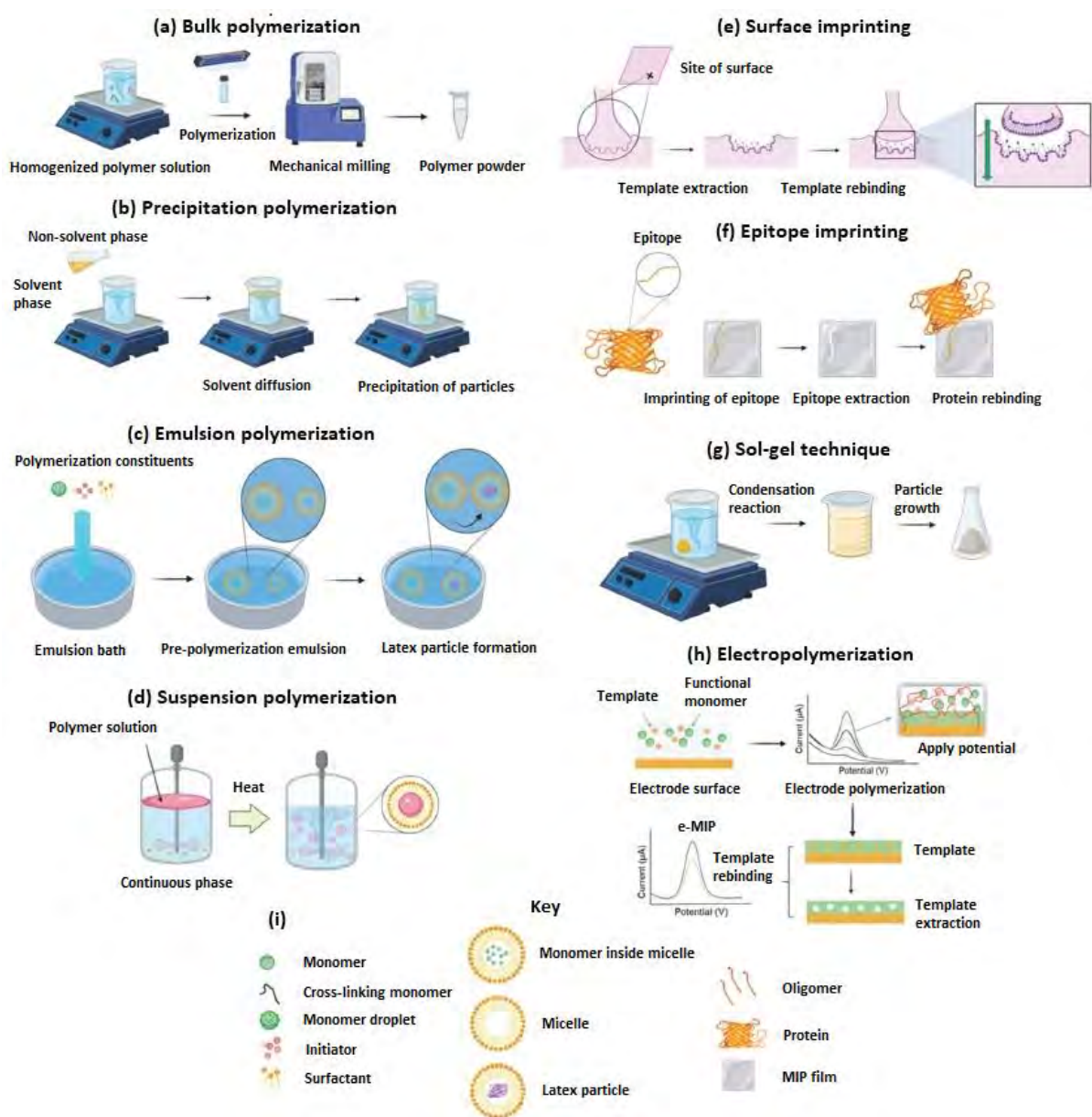
Scheme 1.1-3. Flowcharts of different methods of polymerization leading to the formation of a molecularly imprinted polymer (MIP).[77]

6

1.1.2 Applications of molecularly imprinted polymers (MIPs)

MIPs have already been applied in numerous science, technology, and industry fields due to their unique properties.[78] Different areas of MIP applications are depicted in Scheme 1.1-4.
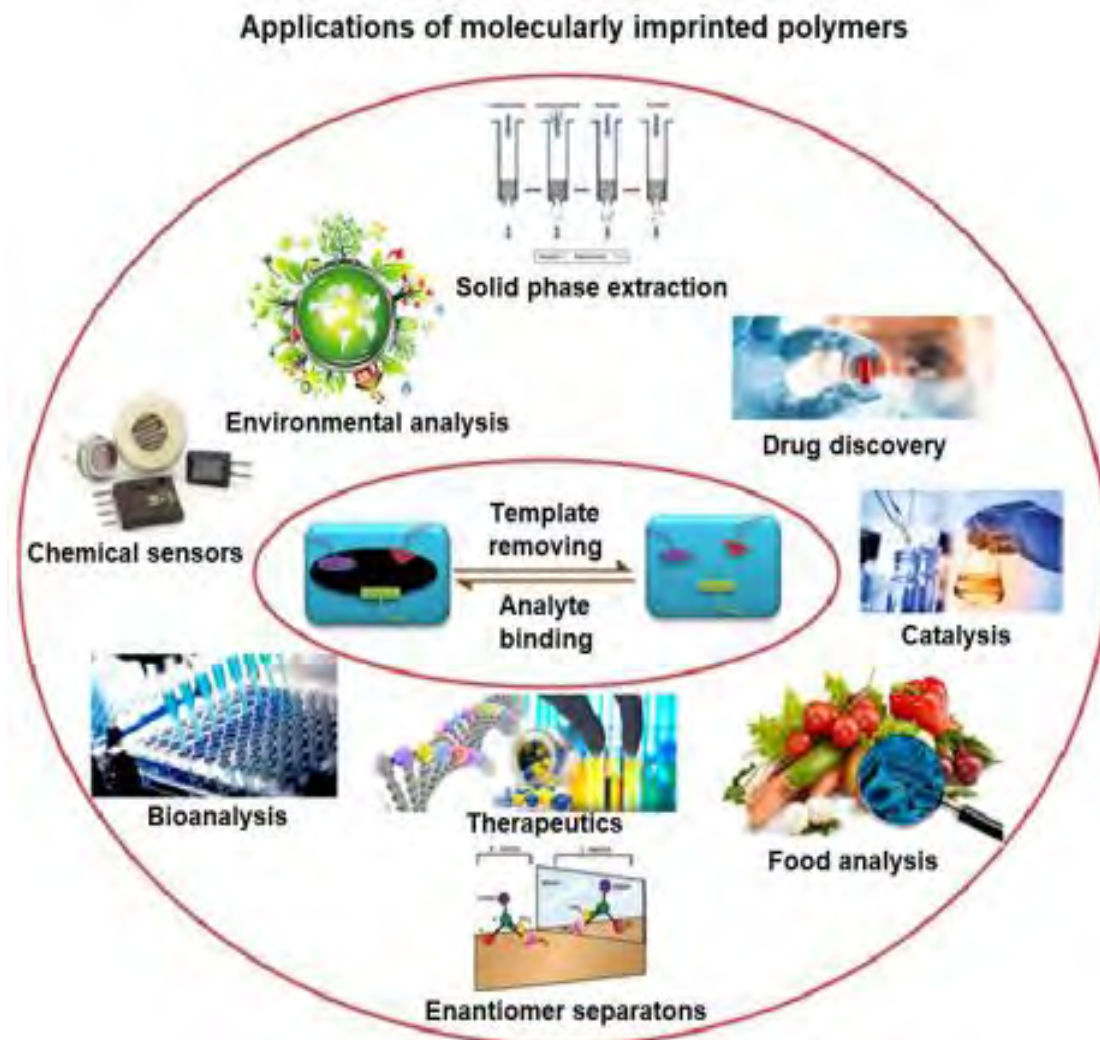
Scheme 1.1-4. Examples of application of MIPs.[78]

One of the most popular uses of molecular-imprinting-in-polymer technology involves chemical sensors' fabrication. The possibility of MIPs application as recognition units in chemical sensors is briefly described in Section 1.1.1 and discussed in detail in Section 1.2.

Another common application of MIPs involves sample preparation, mainly by extraction, such as solid-phase extraction (SPE).[79] MIPs can be applied as selective sorbents for separation in different fields, including chemical, pharmaceutical, and water purification industries or waste-material treatment.[80-83] MIPs prepared as membranes, micro- or NPs, or bulk materials are commonly used as packing materials and sorbents for SPE cartridges and

high-performance liquid chromatography (HPLC) columns. Moreover, molecular imprinting in polymer technology is used to synthesize and purify proteins, hormones, and enzymes. Furthermore, MIPs may be used as sorbents to remove toxins, environmental pollutants, heavy metals, or radionuclides from various matrices.[84-90] Additionally, this technology can be applied to enantiomeric separation, mainly in polymer chemistry and photochemistry, as well as drug synthesis, for separating certain enantiomers of chiral compounds from racemic mixtures.[83, 91-94]

Biotechnology, environment, and food safety are other fields where MIPs have found broad applications, e.g., as drug delivery systems,[95-96] or substitutes for antibodies in affinity chromatography and immunoassays.[97-98] Advantages of MIPs, including high stability, low cost, facile preparation, and low toxicity, allow them to become suitable carriers in drug delivery systems for many diseases treatments, including inflammation,[99] arrhythmia,[100] cancer,[101] and cardiovascular diseases.[102] Moreover, MIPs have been employed as catalytic materials.[103-104] These polymeric catalysts, acting like artificial enzyme analogs, reveal catalytic activity and stereoselectivity similar to enzymes. Furthermore, MIPs may exhibit higher accessibility and stability, as well as catalyze more different reactions than enzymes.[105] Catalytically active groups are usually introduced into polymers by copolymerization of monomers bearing catalytic functional groups resulting in polymers with a somewhat random arrangement of functionalities (Scheme 1.1-5a). Therefore, other approaches to forming polymeric catalysts include an attachment to the polymer of side chains containing linearly arranged functional groups (Scheme 1.1-5b) or polymerization or polycondensation of monomers bearing functional groups distributed linearly (Scheme 1.1-5c). Notably, in natural enzymes and antibodies, functionalities are located quite far from each other along the chain and are brought into a close spatial relationship as a result of specific chain folding, resulting in a complex, three-dimensional arrangement of functionalities called "discontinuate words" (Scheme 1.1-5d).[106]
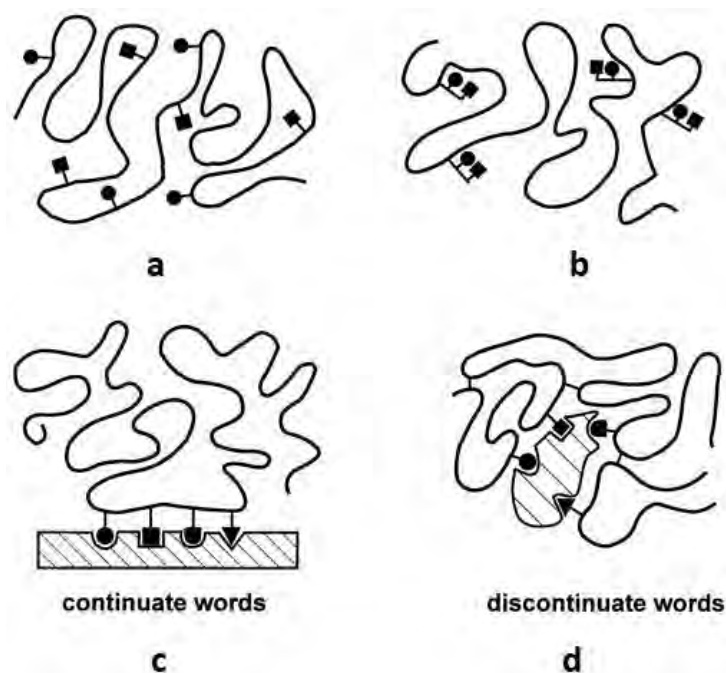
Scheme 1.1-5. Sketches of possible arrangements of functionalities in synthetic and natural polymers: (a) the functional groups randomly distributed along the polymer, (b) chains containing the desired arrangement of functionalities attached to the parent polymer, (c) the functional groups placed on the polymer chain one after the other interacting with corresponding groups on the receptor, (d) the functional groups located at different points on the polymer and brought into spatial proximity by the specific folding of the chain resulting in three-dimensional steric arrangements of the functionalities.[107]

1.2 Application of MIPs for food toxin sensing

One of the fields where MIPs have shown their potential is food science. In the past decades, industrialization and globalization have prompted the dissemination of toxins in the food chain, leading to risks to human health and even life. Contaminants such as allergens may occur naturally in food. Other toxins, including pesticides and veterinary drugs, can originate from the food production and processing stages. Additionally, some contamination may come from packaging and storing conditions.[108] Various analytical methods have been developed to determine contaminants in food products. However, food product control still remains challenging because of the complex food matrix and the presence of interferences.

The present section focuses on MIPs-using chemosensors' applications for determining toxins in food products.

1.2.1 Non-electrochemical methods for determination of chosen analytes in food using MIP-based chemosensors

MIPs might be integrated with different transducers to fabricate selective sensing systems determining various food toxins. Non-electrochemical transductions are frequently used for toxins sensing. Optical techniques are among the most popular due to their low cost, simplicity, and robustness. For instance, some reports describe colorimetric detections as transduction techniques integrated with MIP-based sensing systems.[109-113] Another common detection technique used for toxin sensing is fluorescence spectroscopy.[114] Scheme 1.2-1 shows the general mechanism of target analyte determination using a fluorescence sensor based on MIPs.[115] Analyte molecules binding to MIP cavities cause fluorescence signal changes originating from a fluorescent source attached to a chemosensor. Moreover, applying MIPs to the sensor fabrication improves their fluorescence signal transduction properties.
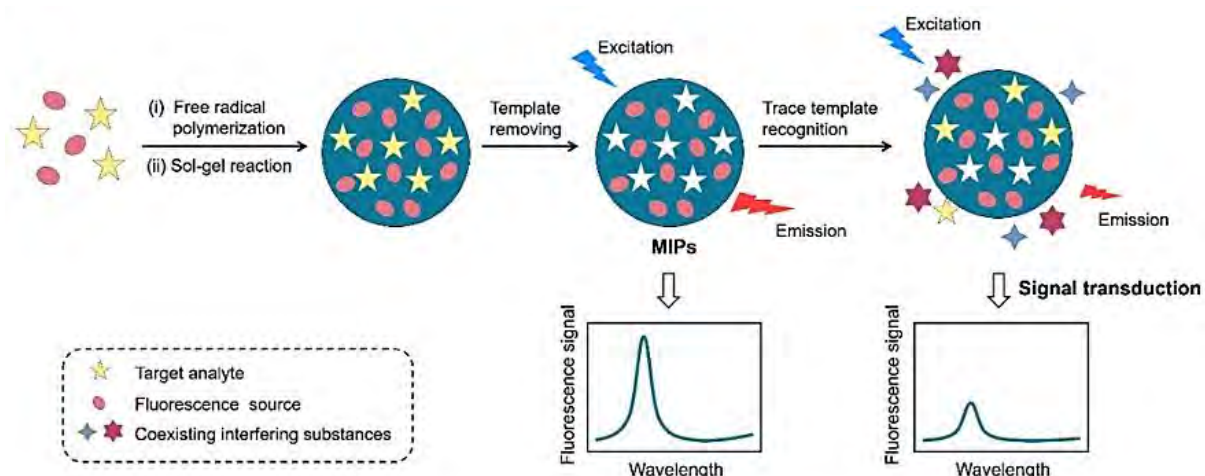
Scheme 1.2-1. The flowchart of the preparation and operation of a fluorescence chemosensor based on an MIP.[115]

Progress in imprinting technology and fluorescent nanomaterials preparation enhances the performance of detection of numerous food toxins. For instance, fluorescent determinations of various toxins were reported, including drug residues,[92, 116] hazardous food contaminants,[117-119] heavy metals,[120-121] and pesticides.[122-123] If analytes are fluorescent by themselves, direct detecting them with MIP-based chemosensors is possible. Fluorescence signals originating from the analyte binding involve, e.g., fluorescence intensity,[124] lifetime,[125] and polarization.[126] However, most analytes are not fluorescent. Therefore, they can only be detected indirectly. Indirect fluorescent detection involves either fluorescent functional monomers or other materials, including QDs, organic dyes, upconverting NPs, rare

10

earth materials, and metallic nanomaterials. The target analyte molecules binding to molecular cavities result in fluorescence enhancing or quenching. Accordingly, one study reported a competitive fluorescent MIP assay to detect histamine in fish samples.[119] MIP particles and histamine tagged with fluorescent derivative were added to the sample solution. Evaluation of the amount of fluorescence derivative left in the examined solution enabled indirect histamine determination. Moreover, fluorescent organic dyes characterized by high fluorescence quantum yield are frequently applied for indirect fluorescent determinations using MIP chemosensors.[127-129] Furthermore, QDs are often used for fluorescence sensing due to their high luminous efficiency, stable photochemical properties, and narrow-band emission spectra.[130-133] Fluorescent MIP chemosensors based on QDs of carbon,[134] C_3N_4,[135] and graphene[136] have been fabricated to devise less toxic and more eco-friendly units. Besides, upconverting NPs have gained much interest as fluorescent labels due to their low cytotoxicity and high photostability.[137-138] Noble metal nanoclusters are another example of a fluorescent material with great potential in preparing an MIP chemosensor with fluorescent detection.[139-141] Importantly, the toxicity of noble metal nanoclusters is lower than QDs' toxicity. Moreover, the noble metal nanoclusters' fluorescence is stronger than that of organic dyes. Rare earth metal materials are other fluorescent materials that have gained interest in optical sensors owing to their high stability, narrow-band emission, and low biological toxicity.[142] One approach involves the preparation of silica beads doped with an Eu(III) complex and coated with a copper-imprinted polymer nanoshell to determine Cu^{2+} cations.[143] Another report describes the synthesis of a fluorescence probe based on upconversion particles, such as YF_3:Yb^{3+} and Er^{3+}, coated with MIPs for sensing clenbuterol.[144] Further example provides the preparation of an MIP fluorescent probe by assembling MIP and Fe_3O_4 nanoparticles on $NaYF_4$:Yb^{3+}, Er^{3+} upconversion particles. This core-shell probe based on upconversion particles revealing molecular recognition, fluorescence, and magnetism features was used to determine chosen quinolones in fish samples.[145]

Also, SPR spectroscopy transduction is often combined with MIP sensing. SPR spectroscopy measurements are quite simple and fast, so it has become popular for determining many food contaminants.[146-149] This spectroscopy is an optical technique that measures the refractive index changes in the vicinity of thin metal layers, e.g., gold, silver, and copper, at the interface of media with different refractive indices, generating an analytical signal upon analyte binding. In SPR spectroscopy, coherent delocalized electron oscillations, called surface plasmons, are excited and detected via the Kretschmann configuration. In this configuration, polarized light incidences a prism coated with a metal film, generating surface

11

plasmons, and a subsequent reflection is detected (Scheme 1.2-2). After interfacing the MIP with the transducer, the binding of the target analyte causes changes in the refractive index of the MIP layer, resulting in a shift of an incidence light angle and wavelength at which resonance with surface plasmons is reached.[2, 150]
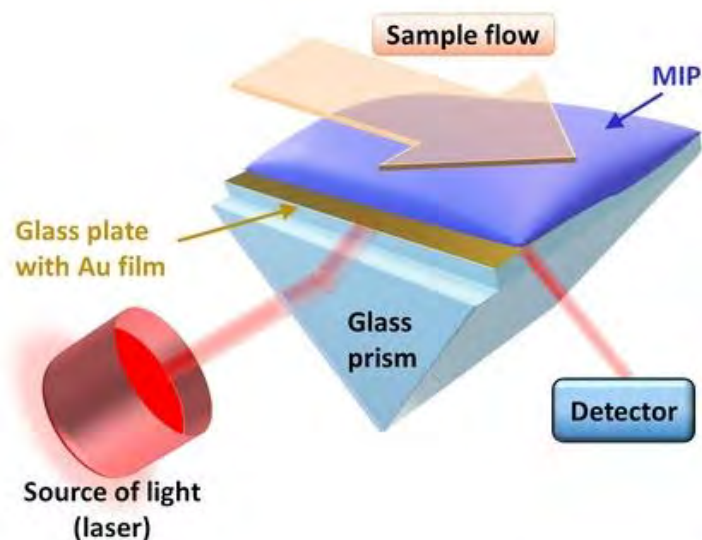
Scheme 1.2-2. The block diagram of an SPR spectroscopy chemosensor setup.[151]

Furthermore, metal NPs were introduced to MIP matrices to increase the sensitivity of SPR sensors.[152] One study reported an SPR sensor based on the (molecularly imprinted polymer)/(gold nanoparticles)/(reduced graphene oxide) (MIP/AuNPs/rGO) nano-hybrid film.[153] Combining the AuNPs/rGO composite with the MIP allowed for the construction of a chemosensor for the sensitive detection of ractopamine. Another approach involves using MIP NPs for SPR sensor fabrication.[154-156] For instance, a chemosensor with patulin-templated MIP NPs attached to the surface of SPR chips for patulin determination was devised.[157] Furthermore, an SPR sensor based on an MIP film deposited on the optical fiber surface by electropolymerization was prepared to determine melamine.[158] Moreover, the SPR platforms based on plastic optical fibers and MIPs were fabricated for furfural determination in wine[146] and perfluorinated compounds in water.[159]

Another technique coupled with MIP recognition is surface-enhanced Raman spectroscopy (SERS). SERS is highly sensitive, allowing food toxins determination even in the as low as the picomolar and femtomolar concentration range.[160-163] Usually, a traditional SERS sensor based on MIPs consists of a SERS substrate coated with an MIP film. The schematic sensor fabrication procedure, signal enhancement principle, and sensing mechanism are depicted in Scheme 1.2-3.

12
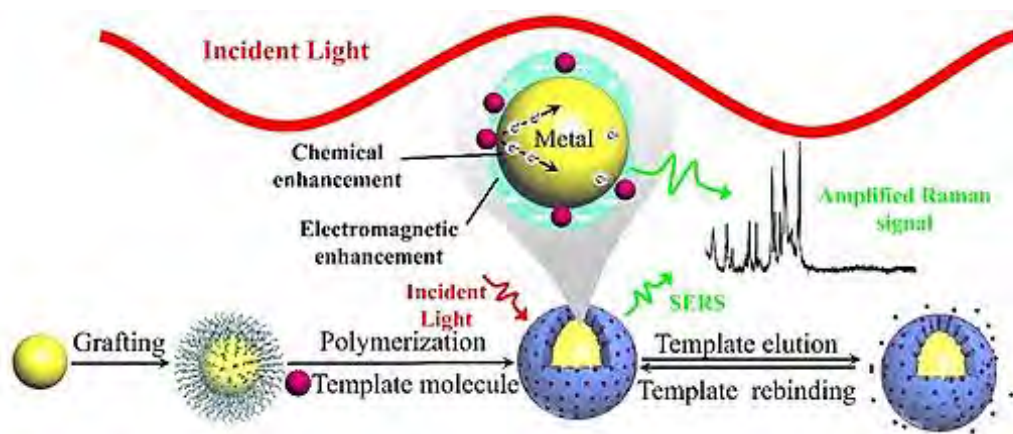
Scheme 1.2-3. The depiction of SERS chemosensor fabrication based on MIPs and the signal enhancement principle.[164]

Moreover, MIPs are frequently used for sample pre-treatment before SERS determination of target toxins.[110, 165-166] Furthermore, a chemosensor was fabricated using MIPs as the stationary phase of the thin-layer chromatography (TLC) plate. The SERS technique was applied to determine Sudan I. What is more, Au colloid was applied to enhance Raman signals.[167] Further example involves the fabrication of a sandwich-like sensor by integrating a porous MIP with an AuNP array for SERS detection of rhodamine 6G.[168] A sensor combining AgNPs with MIPs was also prepared for melamine determination.[169]

MIPs are also applied to enzyme-linked immunosorbent assay (ELISA) like assays. Commonly used ELISA tests are based on antibodies that bind to the target analyte and enzymes capable of triggering a visible color change upon adding a substrate. However, ELISA tests suffer from several deficiencies, including low stability and a complex, time-consuming procedure execution. Therefore, antibodies and enzymes are often replaced with more robust and stable MIPs.[170-171] An ELISA assay based on an MIP film to detect malachite green may serve as an example. Moreover, MIP NPs have been applied in diagnostic assays for food toxins sensing. For instance, the MIP NPs were fabricated to determine fumonisin B_1 (FB_1). In this case, an antibody used as a recognition unit in ELISA was replaced by MIP NPs with high affinity to FB_1.[172]

Another non-electrochemical technique combined with MIPs for food toxins determination is PM at a QCM using a bulk acoustic wave (BAW). For that, the surface of a QCR is coated with an MIP film (Scheme 1.2-4).
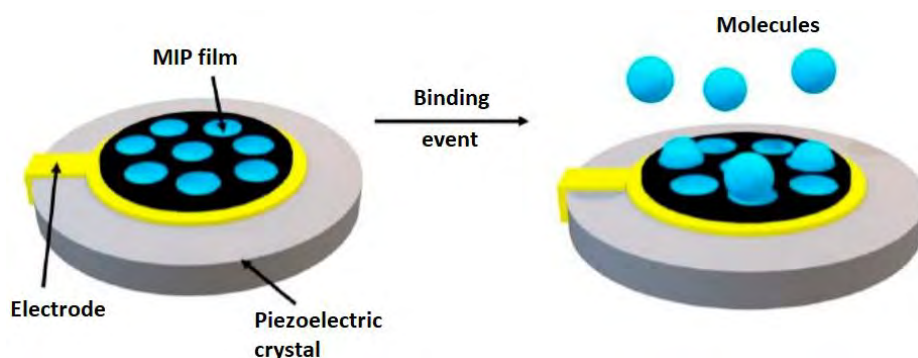
Scheme 1.2-4. The sketch of a quartz crystal resonator (QCR) coated with an MIP film.[2]

Analyte binding increases the MIP film mass, thus decreasing the QCR resonance frequency, which PM can measure using QCM. Hence, the amount of the analyte bound can readily be determined. Many reports describe the application of MIP chemosensing combined with PM for determining food toxins, including methimazole,[173] enrofloxacin,[174] melamine,[175] estrone,[176] methyl parathion,[177] metolcarb,[178] and many others.

Moreover, piezoelectric materials capable of propagating SAW along the sensor surface are used. In these materials, usually quartz, SAW is generated, and the resonance of a defined frequency occurs (Scheme 1.2-5). SAW sensors detect resonant frequency changes in the acoustic waves upon target analyte binding.[179] SAW PM can successfully be integrated with MIP sensing.[180] Accordingly, molecularly imprinted polypyrrole film was deposited on a SAW device for selective determination of GLY.[181] Moreover, an MIP-based SAW sensor was devised for selective label-free determination of sulfamethizole.[182]
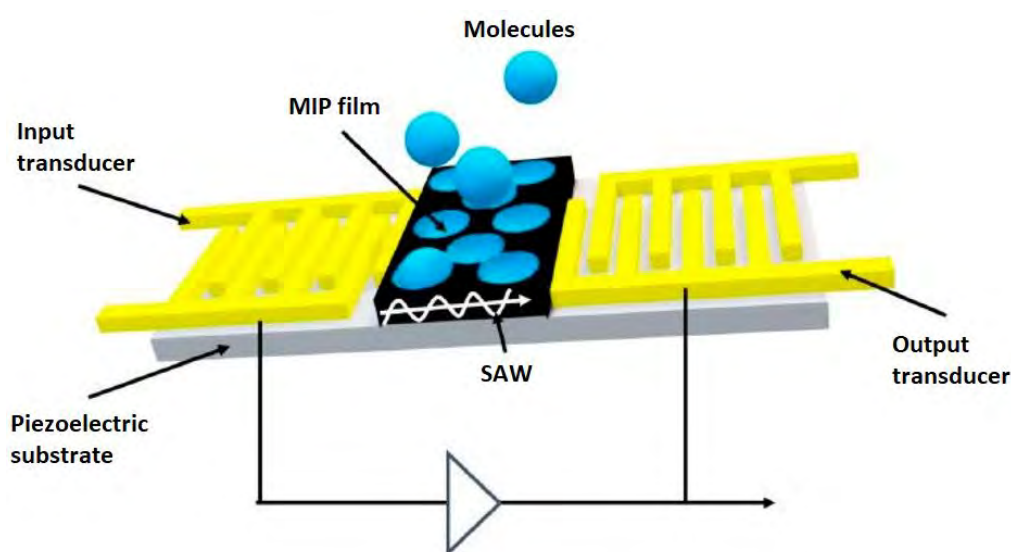
Scheme 1.2-5. The schematic view of a surface acoustic wave (SAW) chemosensor with an MIP film recognition unit.[2]

One of the main disadvantages of BAW and SAW sensors involves difficulties with miniaturizing them into hand-held devices. In contrast, devices exploiting field-effect transistors (FETs), particularly the extended-gate field-effect transistors (EG-FETs),[183] can easily be miniaturized and applied, e.g., for determining food allergen, gluten extract, in semolina flour.[184] Generally, a FET sensor comprises a semiconductor with an electron channel between two electrodes, i.e., the source and the drain. An additional metal-over-dielectric gate electrode is deposited on the semiconducting channel to apply a controlling source-drain voltage. The analyte binding by a recognizing film deposited on the gate changes the gate voltage, resulting in a difference in the current flowing from the source to the drain (Scheme 1.2.6).
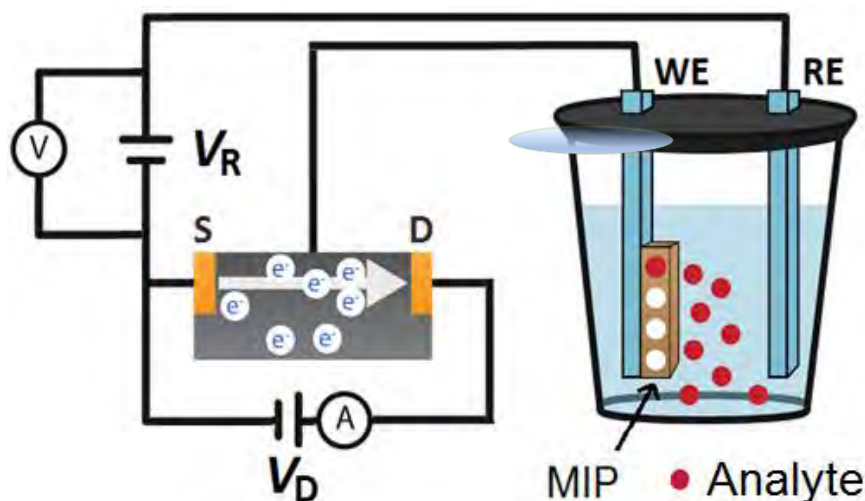
Scheme 1.2-6. The experimental setup based on the EG-FET design. An Au-layered glass slide coated with the MIP film serves as the extended gate (working electrode, WE) and a Pt plate as the reference electrode (RE). D and S symbols represent the drain and source components of the FET structure, respectively.[185]

Furthermore, a thermal readout was combined with MIP recognition to determine various analytes.[186-187] For instance, an MIP was applied in the thermistor for the label-free measurement of the nitrofurantoin analyte concentration.[188] Interestingly, a novel sensor based on surface-imprinted polymers with a modified heat-transfer method for detecting *Escherichia coli* bacteria was reported.[189] Bacteria binding to the receptor surface causes an increase in thermal resistance between the chip coated with a surface-imprinted polyurethane film and the liquid. Applying a printed meander structure as the heater and placing a sensing unit directly underneath the receptor layer allows bacteria to be determined in a broad concentration range of 10^2 to 10^6 CFU/mL. Another example of thermal detection of *E. coli*

15

involves screen-printed electrodes (SPEls) coated with surface-imprinted polymers (SIPs).[190] In this example, SIP-functionalization of SPEls was combined with the heat transfer method (HTM) to detect *E. coli* in milk samples. The thermal setup consisted of a copper chip holder serving as a heat provider (Scheme 1.2-7).
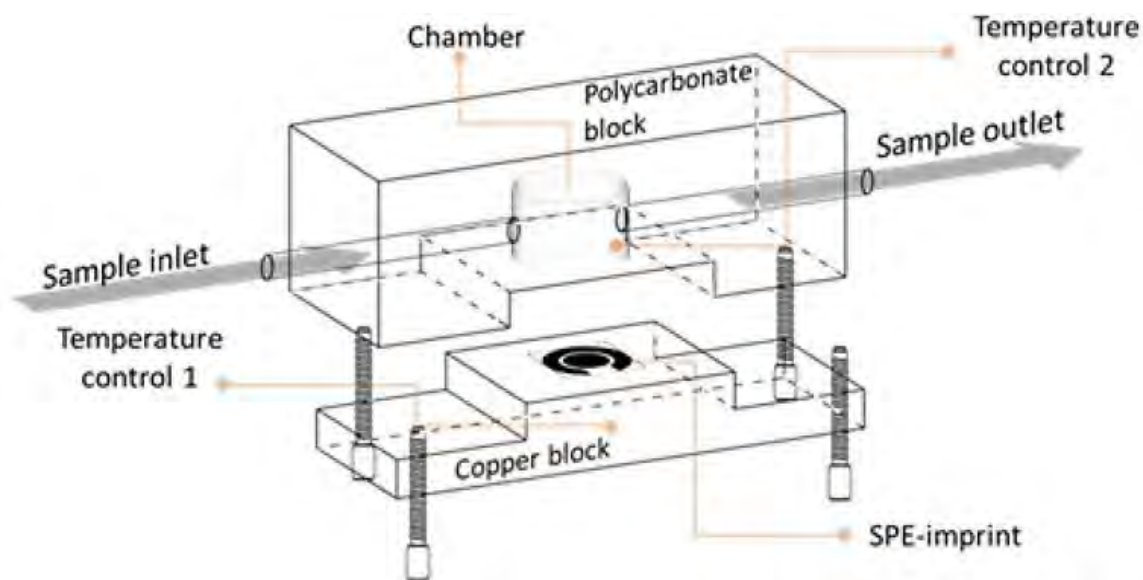
Scheme 1.2-7. Expanded view of a flow cell for thermal measurements at the screen-printed electrode (SPE) modified with a surface-imprinted polymer (SIP).[190]

A thermocouple, power heater, and a proportional-integral-derivative (PID) controller controlled the temperature underneath the sample. The heat was transported through the functionalized SPEl chips into the flow cell, allowing for sample monitoring. The temperature inside the cell was measured with the other thermocouple.

1.2.2 Electroanalytical techniques for sensing chosen toxins in food using MIP-based chemosensors

Electrochemical sensors using MIPs as recognition units have gained enormous attention because of combining fast, inexpensive, portable electrochemical transduction with robust, stable, and selective MIP recognition. The current subchapter focuses on applying electrochemical MIP chemosensors to determine food toxins.

Various analytical signals are recorded with electroanalytical techniques, including the potential in potentiometry, the current in voltammetry and amperometry, the conductance in conductometry, and the impedance and capacitance in impedimetry.[191]

In recent years, voltammetry has been the most frequently (82%) used electroanalytical technique coupled with MIP recognition for food toxins determination (Scheme 1.2-8).

16

Its main advantages include simplicity, high sensitivity, and rapid response. Less popular techniques are amperometry (8%) and impedimetry (7%).
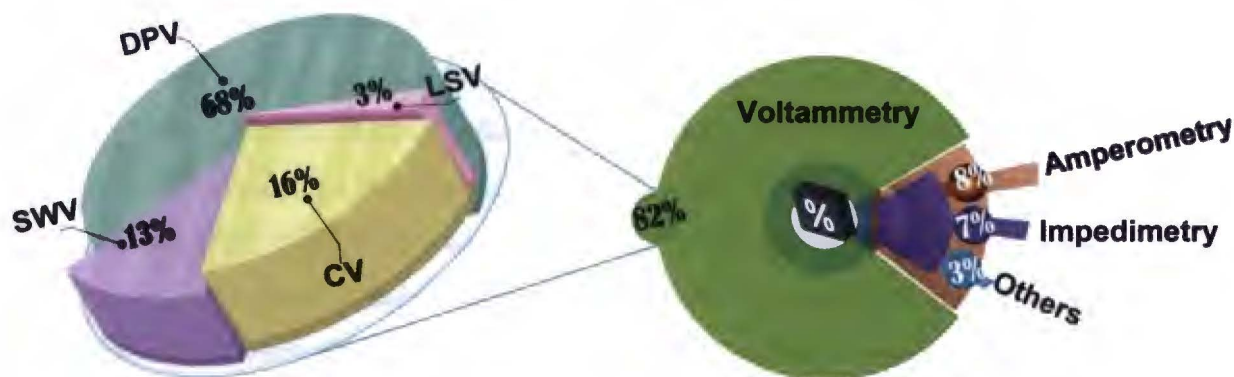
Scheme 1.2-8. The circular diagram of the application of electroanalytical techniques, including voltammetry, amperometry, impedance spectroscopy, and others, combined with MIPs, for food toxins determination between 2010 and 2021. Voltammetry techniques include differential pulse voltammetry (DPV), cyclic voltammetry (CV), square wave voltammetry (SWV), and linear sweep voltammetry (LSV), among others.[191]

As mentioned above, voltammetry is often combined with MIPs. It comprises several techniques, including CV, DPV, SWV, and linear sweep voltammetry (LSV). A typical setup for voltammetric measurements is depicted in Scheme 1.2-9. Usually, it involves a working electrode (WE) coated with an MIP film, a reference electrode (RE), and a counter electrode (CE) immersed in the solution filling a glass cell.
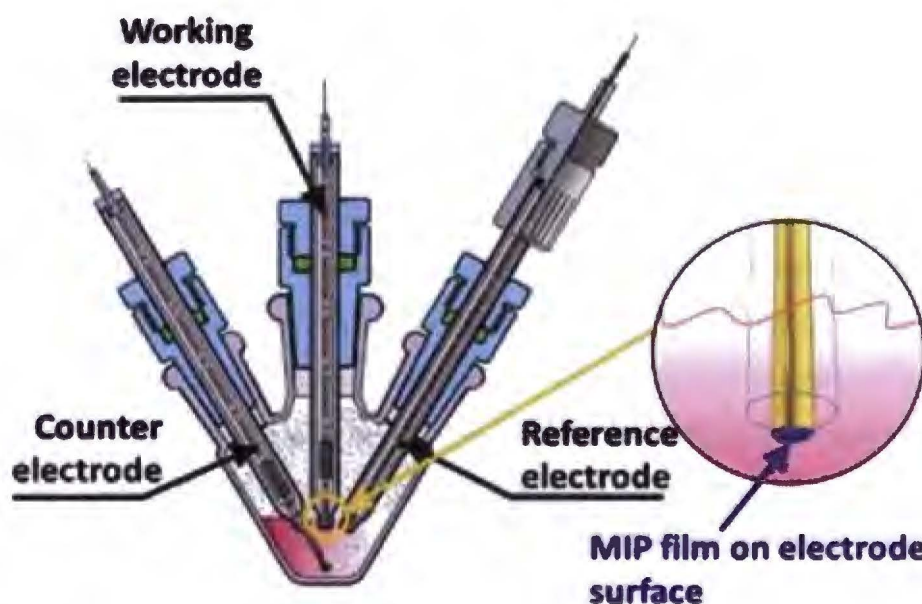
Scheme 1.2-9. The cross-sectional view of a three-electrode glass minicell for electrochemical measurements.[151]

17

CV is significantly less popular because its sensitivity is lower than, e.g., DPV. However, some articles report a combination of CV signal transducing with MIP chemosensing for food contaminants. For instance, a chemosensor based on a magnetic MIP was devised for the CV determination of scombrotoxin (histamine) in fish.[192] The histamine magnetic-MIP was synthesized using the core-shell method, then deposited onto magneto-actuated electrodes to directly assess histamine preconcentrated from fish samples. The histamine-MIP chemosensor may serve as another example of applying CV for histamine determination.[193] Histamine-imprinted polymer was synthesized by bulk polymerization. Then, after grinding, incorporated into a carbon paste electrode (CPE). The devised chemosensor featured two linear dynamic concentration ranges of $1 \times 10^{-10} - 7 \times 10^{-9}$ M and $7 \times 10^{-9} - 4 \times 10^{-7}$ M with the limit of detection (LOD) of 7.4×10^{-11} M. Interestingly, CV determination of metronidazole with a chemosensor based on the MIP-decorated 3D nanoporous nickel (3D NPNi) skeleton reached a very low LOD of 2×10^{-14} M.[194] Electrode surface modification with the 3D NPNi framework provided an enlarged conductive surface area and enhanced electron transfer.

Although CV is sometimes combined with the MIP for target analytes determination, it usually suffers from low sensitivity and poor signal-to-background characteristics. Therefore, it is more frequently used for sensor characterization than analyte sensing.[195-198]

Furthermore, LSV is often used for food contaminants determination. For instance, a chemosensor combining MIP with graphene (GN) was devised to determine an imidacloprid (IDP) pesticide with LSV.[199] A cathodic peak current of IDP, recorded using a glassy carbon electrode (GCE) modified with MIP/GN, linearly increased with the IDP concentration increase in the range of 0.5 to 15 μM with the LOD of 0.10 μM. Moreover, the chemosensor performance was evaluated for rice samples. Furthermore, a sensor based on molecularly imprinted poly(*p*-aminobenzenethiol-co-*p*-aminobenzoic acid) was devised for LSV determination of eugenol.[200] What is more, a graphene-(carbon nanotubes) ionic-liquid-functionalized composite (GN-CNTs-IL) was used to increase chemosensor selectivity. It led to a linear chemosensor response to eugenol in the concentration range of 5.0×10^{-7} to 2.0×10^{-5} M. More MIP-based chemosensors were reported using LSV determination of various toxins, including GLY in tap water samples,[201] tetracycline in honey,[202] and Sunset Yellow in soft drinks.[196]

SWV is another electroanalytical transduction technique frequently combined with MIP-based chemosensing because of its simplicity and high sensitivity.[197, 203-207] Modification of GCE with MIP and GO was proposed for sulfonamide sensing.[206] In another research,

18

quinoxaline-2-carboxylic acid was determined using a chemosensor comprising GCE coated with a polypyrrole-(graphene oxide)-[binuclear phthalocyanine cobalt(II) sulphonate] (PPY-GO-BiCoPc) functional composite decorated with an MIP.[207] Introducing of the PPY-GO-BiCoPc functional composite increased the sensitivity of the chemosensor, allowing to obtain broad two linear dynamic concentration ranges of 1.0×10^{-8} to 1.0×10^{-4} and 1.0×10^{-4} to 5.0×10^{-4} M with the LOD of 2.1 nM. An (MIP NPs)-based chemosensor was devised for diazinon (DZN) pesticide determination.[197] DZN-imprinted polymer NPs were prepared by suspension polymerization for chemosensor fabrication, then applied for CPE decoration.

As mentioned above, DPV is the most popular among voltammetric techniques due to its high sensitivity originating from capacity current minimizing. Numerous reports describe chemosensors based on MIPs with DPV determination of different food toxins, including antibiotics,[204, 208-214] mycotoxins,[215-218] flavorings,[219] pesticides,[220-221] antibacterial agents,[222] fungicides,[223] veterinary drugs,[224] hazardous food additives,[225-227] potential carcinogens, e.g., *N*-nitrosamines,[228-229] and contaminants from food packagings.[230] Recent articles have reported other strategies for DPV determination of food toxins using MIP chemosensors. For instance, a chemosensor based on MIP deposited on GCE coated with electrochemically reduced GO (rGO) was fabricated for bisphenol A sensing in bovine milk.[231] Furthermore, a sensing platform for erythrocin (Ery) antibiotic determination was fabricated.[198] For its preparation, GCE was modified with carbon nanohorns, followed by electropolymerization of dopamine and subsequent electropolymerization of 2-aminopyridine in the presence of Ery. DPV results demonstrated that this electrode modification enabled determining Ery selectively. Moreover, introducing carbon nanohorns and polydopamine (PDA) increased, respectively, sensitivity and stability.

Notably, voltammetric techniques may be used to determine either electroactive or electroinactive target analytes. The latter can be determined by applying the so-called "gate effect." For that, one way is to add an external redox probe to the test solution. Analyte binding causes changes in MIP film properties, changing the faradaic current of the redox probe.[232] The "gate effect" is described in detail in Subsection 1.3 below.

Significantly, electrochemically active toxins can be detected by amperometry. The oxidation or reduction current of the target analyte is recorded at a constant potential applied. This potential, if adequately adjusted, enables the redox process of the target analytes to proceed under the mass transport rate control. The current measured is directly proportional to the analyte concentration.[233] Generally, amperometric measurements are performed under stirred or flow solution conditions because electroactive compounds' mass transport is

19

effective if governed by convection. The amperometric current signal recorded at electrodes coated with MIPs depends on the mass transfer rate of electroactive target analytes to the MIP film.[234] The main amperometry limitation is that electroactive in the chosen potential range species other than the target analyte should be absent in the test solution. Nevertheless, many reports describe the application of amperometric MIP sensors for food contaminant determination. For instance, a molecularly imprinted PDA film-based chemosensor was proposed for the electrochemical determination of sulfamethoxazole (SMX) antibiotic.[235] The PDA-MIP film was deposited on the gold electrode surface by electropolymerization. The linear dynamic concentration range of the chemosensor prepared was 0.8 to 170 μM SMX with a LOD of 800 nM and high selectivity to different interferences. Another article reported amperometric flow-injection analysis (FIA) determination of carbofuran (CBF) using a CNT-paste electrode modified with gold-coated-magnetite coated with MIP (MIP-CNTs-Fe_3O_4@Au/CPE).[236] Application of the CNTs-Fe_3O_4@Au nanomaterial increased surface area as well as the number of binding sites, leading to an enhanced electron transfer. The fabricated chemosensor demonstrated a linear response to CBF concentration in the range of 0.1 to 100 μM and the LOD of 3.8 nM.

Moreover, procedures using chronoamperometric detection were proposed, including an MIP chemosensor based on an Au electrode modified with chitosan-platinum NPs (CS-PtNPs) and graphene-gold nanoparticle (GN-AuNP) nanocomposites for erythromycin antibiotic sensing,[237] Furthermore, an MIP chemosensor using a GCE coated with graphene-Prussian Blue (GN-PrB) composites for butylated hydroxyanisole (BHA) synthetic antioxidant determination,[238] and a sensor based on polypyrrole-(sulfonated graphene)/(hyaluronic acid)-(multi-walled carbon nanotubes) [(PPy-SG)/(HA-MWCNTs)] for tryptamine sensing were devised.[237] Furthermore, an Au electrode was modified with chitosan-silver nanoparticles (CS-AgNP) and graphene-(multiwalled carbon nanotubes) (GN-MWCNTs) composites, then coated with MIPs for neomycin antibiotic determination.[239] Electrode modification with CS-AgNP and GN-MWCNTs composites of high electrical conductivity enabled the preparation of very sensitive and selective chemosensors for neomycin determination. Under optimum conditions, a linear dynamic concentration range of 9×10^{-9} to 7×10^{-6} M was wide, and the LOD of 7.63×10^{-9} M was low.

Potentiometry is another electroanalytical technique applied for food toxins sensing. The potentiometric sensors field has rapidly grown in the last few years.[240] Generally, potentiometry measures the electrochemical potential of charged species. For that,

20

an electrode featuring a membrane loaded with an ionophore, i.e., an ion-selective electrode (ISE), is used as an indicator electrode along with a reference electrode of a stable potential (Scheme 1.2-10).
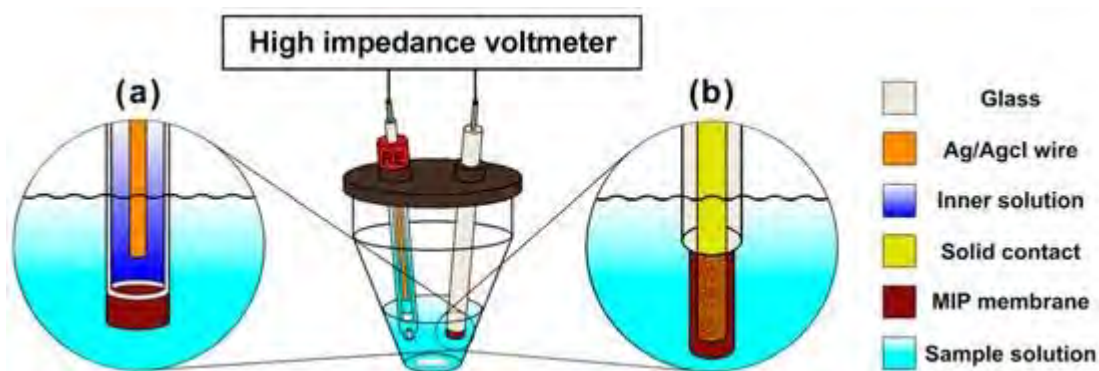
Scheme 1.2-10. The sketch of a typical cell set-up for potentiometric measurements featuring either (a) an internal-reference ion-selective electrode (ISE) or (b) a coated-wire ISE and an external reference electrode (RE).[2]

ISE converts the target ion activity into a potential and then quantifies the ion activity with the Nikolsky-Eisenman equation (Equation 1.1-1).

$$E_A = \text{Const.} + \frac{2.303RT}{z_A F} \log(a_A + K_{A,B}^{pot} a_B^{z_A/z_B}) \qquad \text{(Equation 1.1-1)}$$

where E is the electrode potential [V], R stands for the ideal gas constant ($8.3145 \text{ J mol}^{-1} \text{ K}^{-1}$), T is absolute temperature [K], a_A and a_B are the activity of the determined (A), and interfering (B) ion, respectively, and F is the Faraday's constant ($F = 96485.3 \text{ C mol}^{-1}$) and

$$K_{A,B}^{pot} = \frac{a_A}{a_B^{z_A/z_B}} \qquad \text{(Equation 1.1-2)}$$

is the potentiometric selectivity coefficient, where ion A and B charges, z_A and z_B, respectively, have the same sign, positive or negative.

MIPs have been applied as selective recognition units to devise ISE potentiometric sensors with an MIP film acting as the ionophore. The membrane of this sensor generally consists of two layers, i.e., the transduction layer for the ion indicated and the MIP recognition layer, deposited on the transduction layer, capable of sensing the target analyte. This membrane is connected to a voltmeter, enabling the measurement of the potential difference between the reference and indicator electrode. Usually, the mechanism of ISE

sensing involves membrane processes described by the Nikolsky-Eisenman equation.[241] MIP chemosensors are broadly applied for food toxins determination using Nikolsky-Eisenman equation-governed potentiometric methods.[242-251] For instance, a potentiometric MIP chemosensor was prepared for melamine determination in milk.[242] The chemosensor revealed a near-Nernstian response to protonated melamine in the 5.0×10^{-6} to 1.0×10^{-2} mol/L concentration range with high selectivity to inorganic cations. Another study reported the fabrication of a chemosensor based on a molecularly imprinted conducting polymer (MICP) film for potentiometric determination of taurine.[243] For the MICP film preparation, a film of 3,4-ethylenedioxy-thiophene/acetic acid thiophene (EDOT/AAT) copolymer doped with flavin mononucleotide (FMN) was prepared by electropolymerization. Results of potentiometric measurements showed a linear dynamic concentration range of 10^{-4} to 10^{-2} M protonated taurine. Notably, the devised chemosensor was largely insensitive to inorganic cation interferences, including potassium, sodium, calcium, and magnesium cations.

Noticeably, potentiometric chemosensors based on ion-imprinted polymers (IIPs) for determining inorganic ionic toxins, e.g., heavy metal ions, have become increasingly popular.[244] The sources of heavy metals exposure include not only the environment but also food products and drinking water.[252] Unfortunately, IIPs sensors often suffer from poor selectivity because of the small size of ions that cannot be imprinted effectively. Moreover, forming strong coordination interactions between commonly used functional monomers and heavy metal ions is difficult.[253] A CPE chemosensor based on nanomaterials such as graphene nanosheets and alumina NPs, an Hg^{2+}-ion imprinted polymer acting as a sensing unit, and an ionic liquid used as the binder was proposed to overcome these difficulties. Furthermore, 4-(2-thiazolylazo)resorcinol was applied as the ligand selective for Hg^{2+} during polymer preparation. A fabricated sensor was used for potentiometric determination of Hg^{2+}, showing a linear response to Hg^{2+} concentration in the range of 4.00×10^{-9} to 1.30×10^{-3} M.[245] Then, other sensors for heavy metal ions were reported. For instance, a Cd(II) ion selective electrode was fabricated and tested based on an IIP to determine Cd(II) ions.[245] Another study describes the application of potentiometric membrane sensors for the dinotefuran insecticide determination in cucumber and soil samples.[246] Besides, different MIP chemosensors were applied for potentiometric determination of pesticides in food matrices, including atrazine herbicide,[247-248] cyromazine pesticide,[249] and lindane (γ-hexachlorocyclohexane) pesticide.[250] Potentiometry is mainly applied to determine charged organic compounds and inorganic ions because a charge on the target analyte is required to generate a potentiometric response.[254] However, some procedures were proposed

22

to overcome this limitation. For instance, a polymeric membrane ISE was proposed based on a uniform-sized MIP as the recognition unit and a charged compound with a structure similar to that of the target analyte as an indicator ion for signal transduction. This system enables potentiometric determination of a chlorpyrifos pesticide neutral organic compound.[251] Traditional potentiometric measurements are performed under equilibrium conditions to obtain a classical Nernstian response. Recently, novel sensors based on non-equilibrium sensing were reported. A potentiometric sensing of anionic mercury species in Cl^--rich samples may serve as an example.[255] Importantly, sensors sensitive to Hg^{2+} can be used only in the absence of Cl^-, since Hg^{2+} may form coordination complexes with Cl^-. Thus, the sensor for $HgCl_3^-$ determining in Cl^--rich samples was proposed to overcome this limitation. The *tert*-butylcalix[4]arene-tetrakis(*N,N*-dimethylthioacetamide) neutral carrier (lead ionophore IV) as the chloro-mercury anion-selective ionophore and tridodecylmethylammonium chloride (TDMACl) as the anion exchanger were used for the sensor preparation. Since lead ionophore IV contains sulfur atoms, which effectively coordinate mercury atoms, it was selected as the ion carrier for the anionic chloro-mercury complex. Moreover, TDMACl was introduced to the sensing membrane to decrease cation interference and decrease membrane resistance. Furthermore, the configuration of asymmetric membrane rotating ISE based on the non-equilibrium steady-state diffusion of primary ions at the sample–membrane interface was applied to improve the sensor sensitivity, enabling lower the LOD to 4.5×10^{-10} M for $HgCl_3^-$ in 0.05 M NaCl. The non-equilibrium potential response was enhanced due to promoting the accumulation of primary ions in the boundary layer of the ISE membrane by applying the asymmetric membrane and rotating the membrane electrode.

Potentiometry is a frequently used technique for the determination of various toxins. However, by definition, the response of the potentiometric sensor is linear to the logarithm of the target analyte concentration. Therefore, it is not sensitive to small changes in the analyte concentration, although a dynamic concentration range is usually broad.

Another electrochemical technique, EIS, is also worth mentioning. This technique is often used for sensor characterization and a better understanding of mechanisms of the electrode processes.[209, 214, 216, 248, 256] However, it can also serve as a sensitive transduction tool for food contamination sensing.[217, 229, 257-265]

1.3 "Gate effect" mechanism in analytes' sensing with MIP chemosensors

1.3.1 Investigating the "gate effect"

The present subsection describes a detailed study of the so-called "gate effect" mechanism applied in signal transduction in MIP chemosensors. It discusses possible reasons for the redox probe current change resulting from analyte binding.

One of the first studies on the "gate effect" described the molecular imprinting-based biomimetic receptor system for detecting sialic acid.[266] This fluorescent MIP-based sensor was prepared from vinylphenylboronic acid (VPBA), allylamine (AAm), and ethylene glycol dimethacrylate (EGDMA) conventional monomers in the presence of a sialic acid template. The chemosensor allowed determining the target analyte in the concentration range of 0.5 to 10 μM. Importantly, fluorescence enhancement was due to the interaction of the sialic acid molecules with MIP cavities. Presumably, the analyte binding caused a change in the porous structure of the imprinted polymer, which led to a change in the MIP sensor signal (Scheme 1.3-1). This effect is called the "gate effect."

The origin of the sensor response was explained by the interactions between template molecules and MIP cavities, leading to a conformational reorganization of the MIP structure (Scheme 1.3-1). This reorganization affected the molecules' diffusion through the MIP. Moreover, MIP immersed in a buffer solution swelled because of surface ionization and osmotic pressure, increasing the polymer domain volume. Substances diffusion through MIP cavities was limited by the diameter of pores in the polymer. Supposedly, analyte binding caused a rearrangement resulting from interactions between analyte molecules and MIP cavities, thus expelling water molecules and ions already present in MIP cavities. Consequently, the MIP might shrink due to the binding of analyte molecules, increasing pore size, thus resulting in a more permeable structure.

As demonstrated above, the "gate effect" term could be applied to the non-electrochemical determination of target analytes by MIP chemosensors. However, the "gate effect" is mainly related to the electrochemical sensing of electroinactive analytes. For those cases, adding external redox probes to test solutions is necessary to generate an electrochemical response. Changes in the signal recorded at the MIP film-coated electrode allow for determining the target analyte. This transduction approach is based on the "gate effect" relevant to changes in MIP properties induced by analyte binding to the MIP. It was

postulated that the analyte molecules binding by cavities in an MIP film leads to MIP swelling. This swelling changes MIP permeability to the redox probe, resulting in changes in faradaic currents corresponding to the electro-oxidation or electroreduction of the probe.
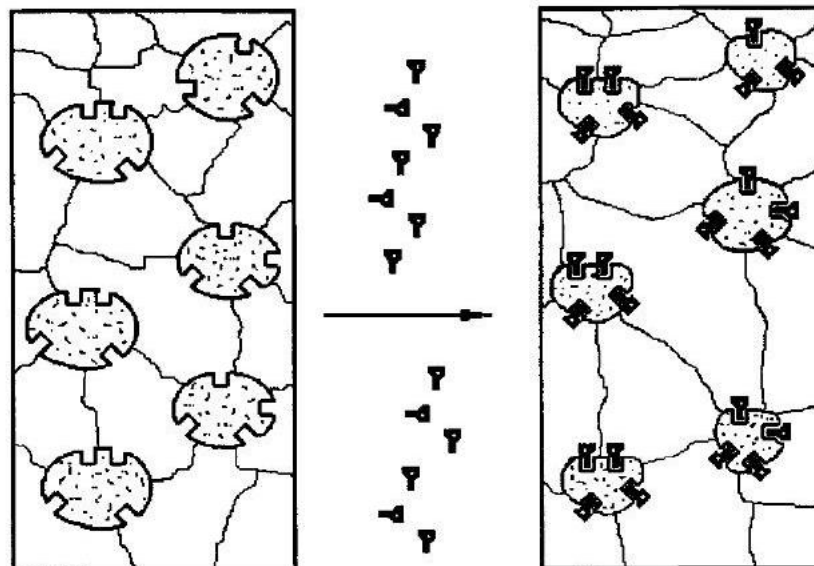
Scheme 1.3-1. The sketch of possible changes in the MIP structure caused by analyte binding.[266]

The "gate effect" in electrochemical sensing was first demonstrated in the study of the determination of theophylline.[267] In this study, Yoshimi et al. reported on a thin molecularly imprinted poly(methacrylic acid-*co*-ethyleneglycol dimethacrylate) film deposited on an indium-tin-oxide (ITO) electrode. This film exhibited increased ferrocyanide redox probe diffusive permeability due to theophylline binding. The CV results signified a faradaic current increase in the presence of the theophylline analyte caused by enhanced diffusion of ferrocyanide through the MIP film deposited on the electrode surface. Notably, this behavior was not observed for a non-imprinted polymer (NIP). CV results were confirmed by atomic force microscopy (AFM) imaging. AFM images showed an increase in MIP porosity in the theophylline presence.

Moreover, the "gate effect" mechanism explained changes in anodic current due to the MIP cavities binding of heparin template molecules.[268] Interactions between heparin and the MIP deposited on the ITO electrode caused a change in the accessibility of the MIP to the ferrocyanide redox probe. Remarkably, in CV experiments, current density was enhanced for heparin concentrations below $0.3 \, \mathrm{mg \, mL^{-1}}$ and dropped for concentrations above $0.3 \, \mathrm{mg \, mL^{-1}}$. These results showed that MIP porosity increased at low heparin

25

concentrations and decreased at high concentrations. The authors speculated that this behavior resulted from heparin's wide molecular weight distribution. In a low analyte concentration range, heparin molecules are bound to the MIP cavities imprinted with a high molecular weight heparin template. This binding attracts the functional monomer's cationic trimethyl ammonium group, which worsens the MIP pore. On the other hand, at high heparin concentrations, some adsorbed heparin molecules could block MIP cavities, decreasing redox probe accessibility to the cavities. Furthermore, another research involved the operation of a chemosensor based on MIP NPs. Those MIP NPs were prepared by solid-phase synthesis, then used as a recognition unit of a chemosensor for electrochemical determination of FB$_1$.[217] The chemosensor was fabricated by depositing the polypyrrole-(zinc porphyrin), PPy/ZnP, conducting composite underlayer on the Pt disk electrode. This underlayer formation allowed subsequent attaching of MIP NPs to this underlayer. DPV and EIS were applied as transduction techniques. The DPV signal recorded in the presence of the $[Fe(CN)_6]^{4-}/[Fe(CN)_6]^{3-}$ redox probe increased with an increase of the FB$_1$ concentration in the linear dynamic concentration range of 1 fM to 10 pM. Most likely, FB$_1$ binding changed the conformation of the polymer composite, increasing its porosity and, hence, enhancing redox probe diffusion through the composite to the electrode surface. Presumably, in the FB$_1$ analyte absence, a negatively charged ferrocyanide redox probe was repulsed from hydrophobic MIP NPs, hindering the charge transfer through the composite. FB$_1$ analyte binding changed MIP NPs conformation. Thus, the film became more permeable to the redox probe and the counter ion, which enhanced electron transfer through the polymer and increased the DPV signal. Moreover, the composite was electroactive at 0.35 V vs. Ag|AgCl. Thus, the EIS technique could monitor the faradaic process because the R_{ct} changed in the presence of FB$_1$. The composite R_{ct} increased with the analyte concentration increase. Presumably, FB$_1$ binding resulted in structural changes in the MIP, thus increasing the R_{ct}.

Notably, many reports demonstrated that the analyte binding might cause a decrease in the current. A simplified illustration of the indirect determination of analytes using the K$_4$[Fe(CN)$_6$] redox probe is presented in Scheme 1.3-2.

In one investigation, an MIP film-coated ITO electrode was applied to glucose determination in an aqueous solution.[269] This enzyme-free sensor for glucose was prepared by chemical copolymerizing 4-vinylphenylboronic acid, methylene bisacrylamide, and the glucose template. CV measurements revealed that the anodic current peak of the ferrocyanide redox probe decreased with an increase in the glucose concentration. Results suggested that the MIP polymer shrank because of the glucose binding and swelled during glucose

26

dissociating. Therefore, MIP matrix shrinking hindered the diffusion of the redox probe to the electrode resulting in a drop in current density.
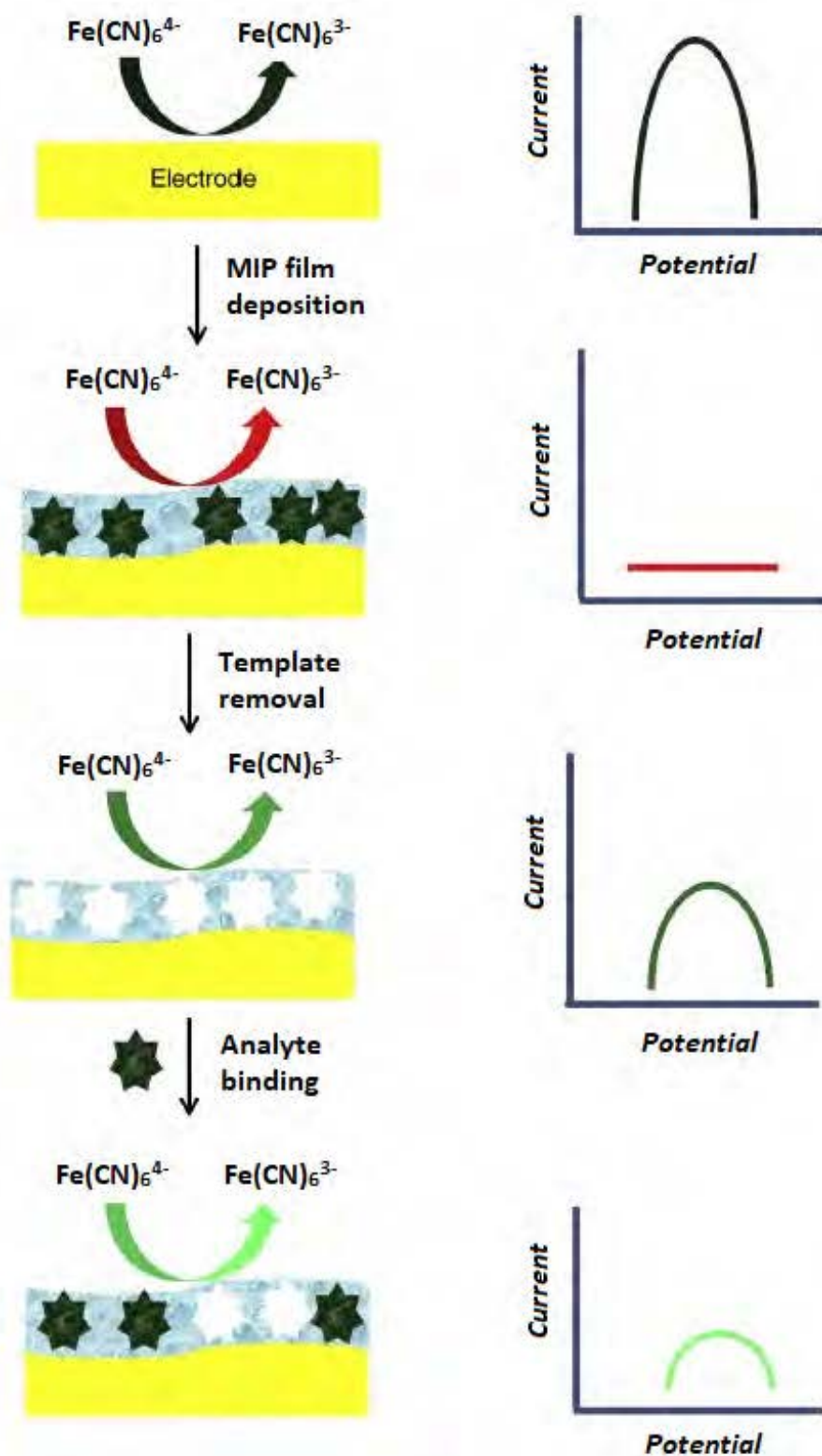
Scheme 1.3-2. The flowchart of the "gate effect" operation in the indirect electrochemical determination of an electroinactive analyte and the corresponding DPV signals recorded at the MIP film-coated electrode.

27

However, MIP film shrinking or swelling because of analyte binding is not the only plausible mechanism responsible for changes in electrochemical signal during the indirect determination of analytes. The "gate effect" may also originate from other phenomena.[232] Those could be divided into diffusion and (electrical effects)-related mechanisms. The former concerns the rate change in the redox probe diffusion through the polymer caused by a change in MIP permeability resulting from analyte binding. The latter involves the change in the electrochemical properties of the MIP film. The effect of shrinking or swelling of an MIP film mentioned above is classified as a phenomenon related to diffusion.

Remarkably, the number of studies describing indirect sensing of electroinactive analytes by MIP chemosensors using the "gate effect" has expanded rapidly in the last few years.[42, 270-273] For instance, a sensor sensitive to chloramphenicol (CAP) was fabricated.[274] It was prepared by electropolymerization of Eriochrome Black T (EBT) in the presence of CAP on laser-induced GN electrodes. The analytical performance of the devised sensor was examined by CV and EIS in the presence of the $K_3[Fe(CN)_6]/K_4[Fe(CN)_6]$ redox probe.

Semicircles in the Nyquist plots with diameters corresponding to the charge transfer resistance (R_{ct}) increased with the increase in the CAP concentration. EIS measurements indicated that the electrical resistance of the surface increased with the increase in the CAP concentration in the linear dynamic concentration range of 1 nM to 10 mM. Another study described a sensor based on MIP-decorated magnetite NPs to determine SMX.[275] EIS experiments showed that R_{ct} increased with the increase of the SMX concentration as MIP cavities bound increasing amounts of SMX analyte molecules from the test solution of the $K_3[Fe(CN)_6]/K_4[Fe(CN)_6]$ redox probe. The linear response of the sensor ranged from 0.1 nM to 10 mM. Another study reported the formation of protein-imprinted self-assembled monolayers (SAMs) from functional thiols and disulfide compounds for sensor fabrication. Due to imprinted cavities featuring multiple recognizing sites, SAMs allowed for highly selective binding of the target protein, bovine hemoglobin (BHb). DPV measurements indicated that the peak for the $K_3[Fe(CN)_6]/K_4[Fe(CN)_6]$ redox probe recorded at the gold electrode modified with Bhb-templated SAMs decreased with the increase of the analyte concentration as a consequence of the "gate effect." Similar behavior of a DPV signal originating from redox probe oxidation was observed at the screen-printed gold electrode coated with the MIP templated with the HER2-ECD protein breast cancer biomarker.[276] The DPV peak linearly decreased with the increase in the HER2-ECD concentration range of 10 to 70 ng/mL. Another research reported artemisinin determination using an electrochemical sensor based on MIP fabricated by electropolymerization of the *o*-phenylenediamine (*o*-PD)

28

functional monomer in the presence of the artemisinin template.[277] The chemosensor response was analyzed by CV and SWV using the $K_3[Fe(CN)_6]/K_4[Fe(CN)_6]$ redox probe. Results of CV and SWV measurements demonstrated that the redox probe current decreased with the increase in the artemisinin analyte concentration. Furthermore, a chemosensor using MIP NPs for DPV and EIS determination of cilostazol (CIL) and its primary active metabolite, 3,4-dehydrocilostazol (dhCIL), was reported.[278] CIL-templated MIP NPs were synthesized by precipitation polymerization, then the template was extracted from the NPs, and MIP NPs prepared that way were subsequently sedimented on the Au disk electrode, followed by tyramine electropolymerization. The electrodes coated with the polytyramine film with embedded MIP NPs were used for DPV and EIS determination of CIL and dhCIL in an acetonitrile solution of ferrocene redox probe by exploring the "gate effect." Importantly, the DPV peak recorded at the MIP NPs coated electrode immersed in the ferrocene redox probe solution decreased with the increase of CIL concentration in the linear concentration range of 134 nM to 2.58 μM CIL. Moreover, EIS spectra were recorded for the same solution composition. Notably, the chemosensor responded to the CIL metabolite, dhCI. Therefore, it was suitable for sensing CIL and dhCIL together.

Interestingly, an MIP chemosensor exploiting the "gate effect" mechanism was even used to detect severe acute respiratory syndrome coronavirus 2 (SARS-CoV-2) nucleocapsid protein (ncovNP).[279] The ncovNP-MIP sensor was fabricated by modifying a thin-film Au electrode with ncovNP-MIP as a recognition unit prepared from the poly(*m*-phenylenediamine) functional monomer. A DPV peak recorded at the electrode coated with ncovNP-MIP in the presence of $[Fe(CN)_6]^{4-}/[Fe(CN)_6]^{3-}$ redox probe decreased with the increase of the ncovNP analyte concentration, implying hindered charge transfer carried by redox probe through the film to the electrode.

Another example of the possible diffusion-related mechanism might be the physical blocking of MIP cavities by analyte molecules. However, this blocking is mainly encountered in thin films of nonconductive MIPs imprinted with macromolecules as templates, e.g., a prostate-specific antigen (PSA),[280] myoglobin,[281-283] cardiac troponin T,[284] glutathione-s-transferase-π (GST-π),[285] concanavalin A,[286] immunoglobulin G,[287] hexameric heme protein,[288] and human serum albumin (HSA).[289] These studies reported the R_{ct} increase manifested by the growth in diameters of Nyquist plot semicircles[282-283] as well as the decrease in the SWV peak[281-283] or CV peaks[284, 289] height due to analyte binding in the redox probe presence. Moreover, SPR,[285] BAW,[286] and SAW[287] measurements were used to evaluate the recognition ability of the MIP films. Thus, imprinting and subsequent

29

macromolecule removal resulted in MIP cavities with much larger diameters than redox probe molecules. Therefore, the analyte macromolecules binding to MIP cavities could hinder redox probe molecules' diffusion through these cavities. That could happen if an MIP were applied to determine charged analytes.

Another possible diffusion-related mechanism is charge accumulation in the MIP film. The charged analytes binding by MIPs of chemo−sensors could lead to charge accumulation in these MIPs. Therefore, analyte detection might be affected. Accordingly, positive charge accumulation could hinder the diffusion of the redox probe bearing the same charge. Unfortunately, no research reports have described using different redox probes in analyte sensing. The "gate effect" mechanism controlled by diffusion is schematically illustrated in Scheme 1.3-3.
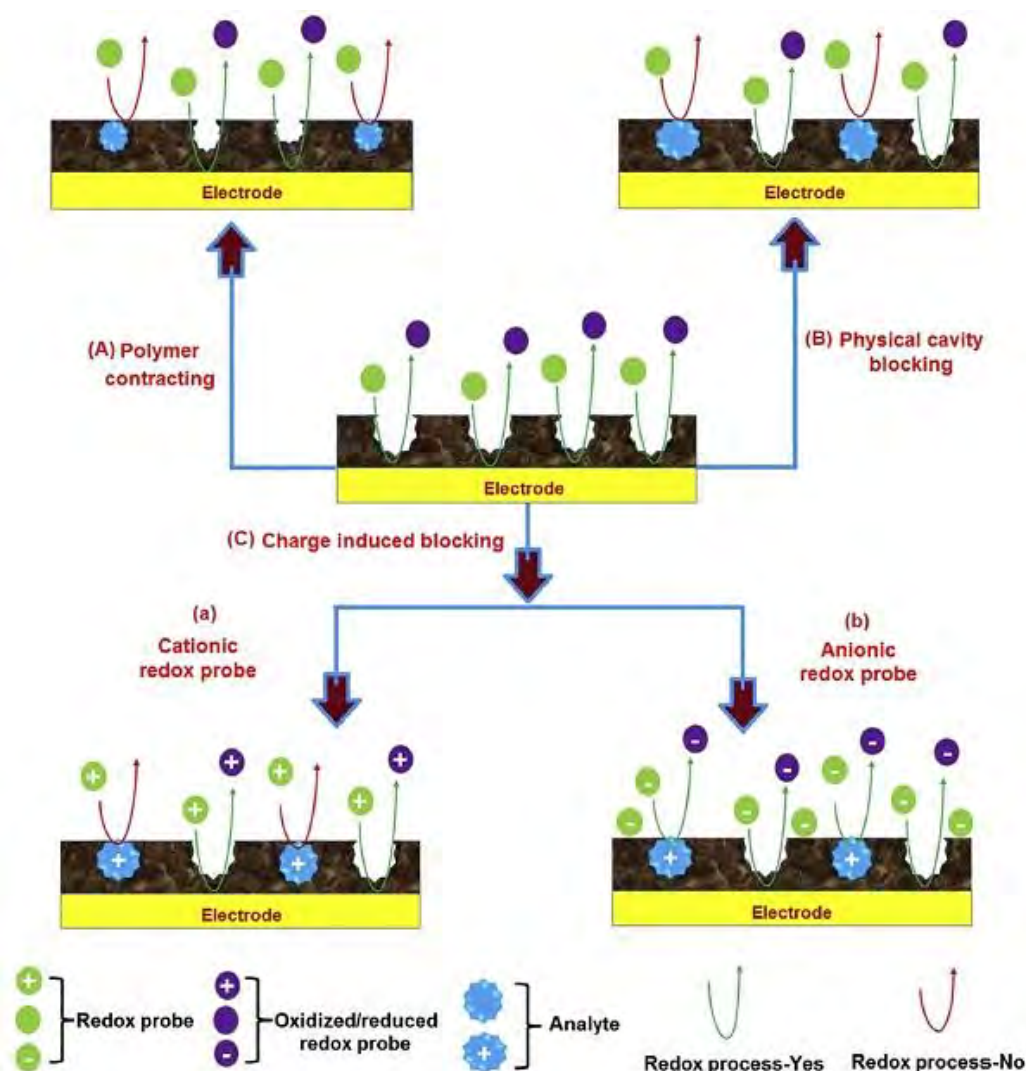
Scheme 1.3-3. The schematic illustration of the diffusion-related "gate effect." (A) MIP film expanding and shrinking, (B) physical blocking of MIP cavities by analyte molecules, and (C) positive accumulated charge-induced blocking in the MIP film (a) in the presence of redox probe charged (a) positively and (b) negatively.[232]

30

If discussing the MIP swelling and shrinking mechanism, it is worth mentioning that certain polymers, such as poly(phenylenediamine), and PPD, commonly applied to prepare electrochemical sensors,[290-294] could exhibit permeability properties.[295] The PPD film permeability was defined as an analyte's ability to permeate through this film. This permeability may strongly depend on polymerization conditions, including the pH of the solution for polymerization and potentiostatic or potentiodynamic deposition. Therefore, analyzing these polymers' permeability properties is recommended before determining the analyte.

Moreover, MIPs' properties are crucial regarding analyte determination. The examples mentioned above are mainly related to non-conductive polymers, while the conductivity of MIPs might play an essential role in analyte binding. Therefore, the "gate effect" may also relate to the electrical effects of the MIP film itself. Thus, analyte binding changes MIP film conductivity. This effect is considered doping-dedoping, leading to an increase or decrease in faradaic current originating from the redox probe. Since analyte molecules binding to MIP cavities could generate or quench polarons via, e.g., doping-dedoping, this binding should affect UV-vis or near-infrared spectra. The electric double layer formed at the electrode-electrolyte solution interface consists of compact and diffuse layers separated by the outer Helmholtz plane, OHP (Scheme 1.3-4a). Coating the electrode with an MIP film complicates the double-layer structure. Then, different processes may occur, including charge accumulation, diffusion, and analyte sorption in the film (Scheme 1.3-4b). EIS is often used to investigate those complex systems. This technique allows for determining different parameters, including solution resistance (R_s), charge transfer resistance (R_{ct}), the Warburg impedance (W), and the double-layer capacitance (C_{dl}) of the MIP film-coated electrode. Monitoring those parameters during analyte determination allows in-depth MIP film-coated electrode operation analysis.

For that, Randles-Ershler equivalent circuit is commonly used and fitted to the experimental Nyquist plot.[296-298] Importantly, analyte binding may affect R_{ct}, C_{dl}, and W. Thus, the charge transfer and the redox probe diffusion from the electrolyte solution to the electrode depend on the MIP film properties. The R_{ct} parameter characterizing a faradaic process[16, 260, 299-300] is related to the electron transfer between the conductive MIP film and the redox probe, as well as the counter ion transfer through the MIP-(electrolyte solution) interface for charge compensation. On the other hand, the C_{dl} is used to characterize a non-faradaic process.[263, 293, 301-303] Some articles describe changes in the C_{dl} of electrodes coated

with MIP films due to analyte binding using different than the Randles-Ershler models of the electrode-(electrolyte solution) interface.[301, 304-305]

Notably, conductive MIP films whose electrochemical properties depend on external factors may behave like insulators or semiconductors in their neutral form and turn to a conductive material after charging and doping with counter ions.[306] The positive charge of radical cation appearing in the polymer during electro-oxidation is compensated by anion ingress from the solution, often accompanied by polymer swelling. Reversible electro-oxidation and electroreduction of MIPs may lead to their conformational and structural changes, including expanding, shrinking, conformational compacting, and closing. Moreover, part of polarons and counter ions remain trapped in the conductive polymer, enhancing electronic conductivity.[307] Since the MIP film-coated electrode is quite a complex system, two extreme possibilities exist for a double-layer location. One assumes the double-layer formation inside the MIP near the electrode surface (Scheme 1.3-4b). Another possibility is the double-layer location far from the electrode surface, i.e., at the (MIP film)-(electrolyte solution) interface (Scheme 1.3-4c).
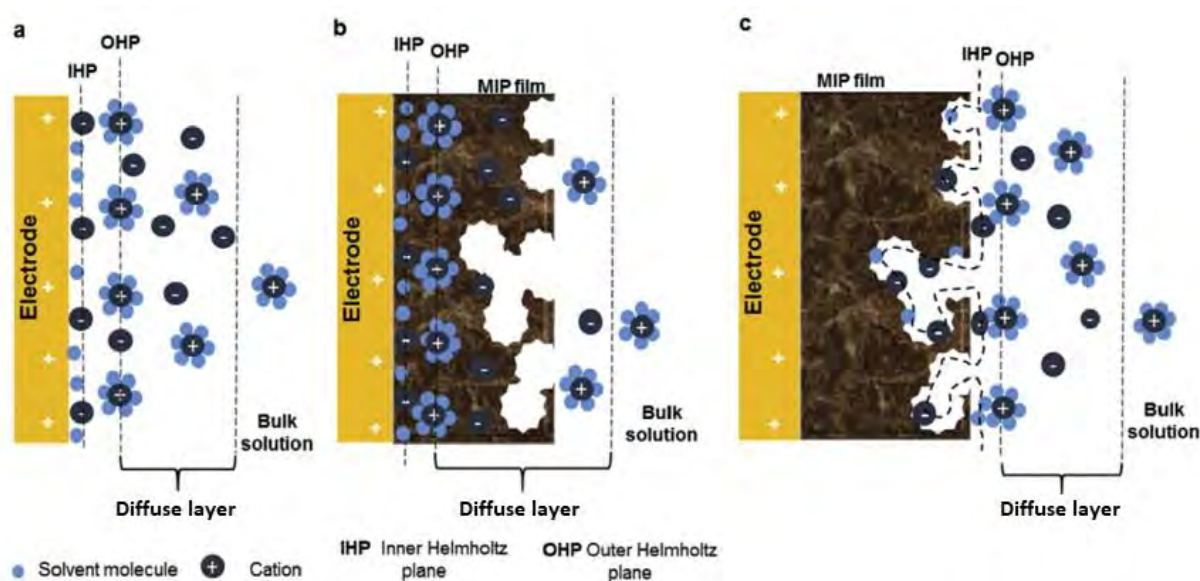
Scheme 1.3-4. The illustration of the electric double-layer structure in the case of specific ion adsorption (a) at the bare and (b, c) at the MIP film-coated electrodes; (b) close to the electrode surface, inside of the polymer, and (c) far from the electrode surface, at the polymer-solution interface.[232]

As mentioned above, indirect electrochemical determination of analytes by MIP chemosensors using the "gate effect" requires the external redox probe presence in the test solution. This determination enables generating of an electrochemical signal by the redox

probe, allowing for sensing electroinactive analytes. However, this determination suffers from several drawbacks. The necessity of using an external redox probe restricts sample preparation and precludes MIP chemosensors' application for in vivo analyte determination.

Moreover, this determination may strongly depend on experimental conditions, leading to structural changes in the MIP film itself, regardless of the target analyte presence.[308] Other factors involve nonspecific adsorption of real sample components and nonspecific pores formation after template extraction from the MIP.

1.3.2 Devising, fabricating, and testing self-reporting electrochemical sensors

Since the indirect determination of electroinactive analytes suffers from many deficiencies, self-reporting electrochemical sensors involving (redox probe in solution)-free determination of these analytes were devised, fabricated, and tested. Electrochemical immunosensors are one example. These immunosensors are biosensors using an electrode-confined antibody as the recognizing unit and monitoring the electrochemical signal originating from the binding of the target analyte to the antibody (Scheme 1.3-5).[309]
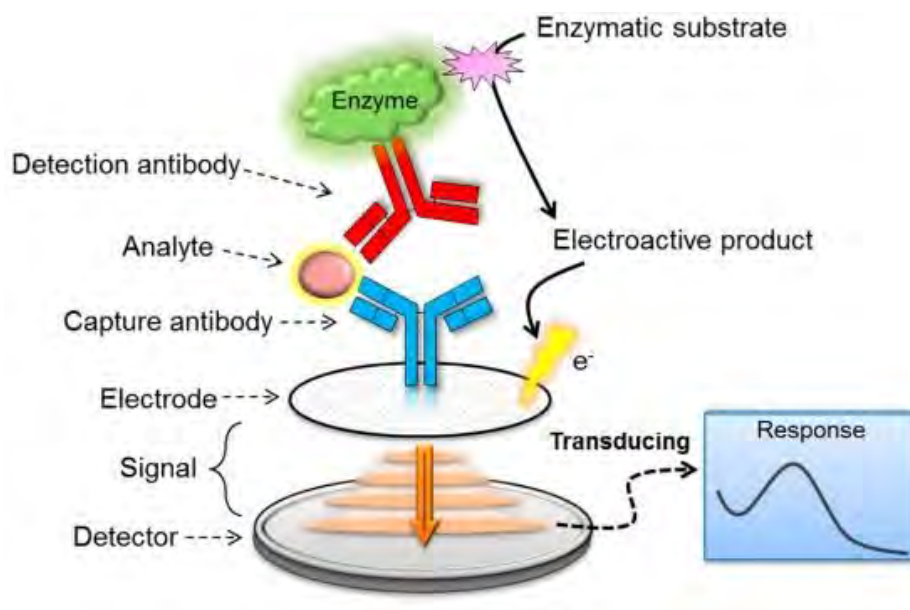
Scheme 1.3-5. The basic principle of operation of an electrochemical immunosensor.[309]

The immunosensors design is based on specific non-covalent affinity interactions between antibodies and antigens, providing a wide range of applications from biomedical monitoring and environmental analysis to food quality control. Since antibodies are electroinactive, they must be functionalized with redox probes or enzymes to produce an electrochemical signal. Moreover, the crucial step in immunosensor fabrication is

33

immobilizing antibodies on the surface, thus obtaining stable antibody-analyte complexes. Surface chemistry control is necessary for obtaining proper orientation and accessibility of antibodies and minimizing non-specific binding. Among different transduction techniques used for antibody-based sensing, electrochemical immunosensing has attracted attention because of its high sensitivity, rapid response, structure and operation simplicity, and sensors' low production cost.[310-311] Furthermore, different methods of antibody labeling with probes have been developed to detect and amplify analytical signals during electrochemical sensing (Scheme 1.3-6).[312] One such strategy involves the application of nanomaterials serving as carriers (Scheme 1.3-6a). Another utilizes metal and semiconductor NPs as electroactive labels (Scheme 1.3-6b). Moreover, nanopolymers functionalized with enzymes (Scheme 1.3-6c) are used as well as reducing agents that convert the oxidized state to the reduced state of species through redox cycling of enzyme reactions (Scheme 1.3-6d).
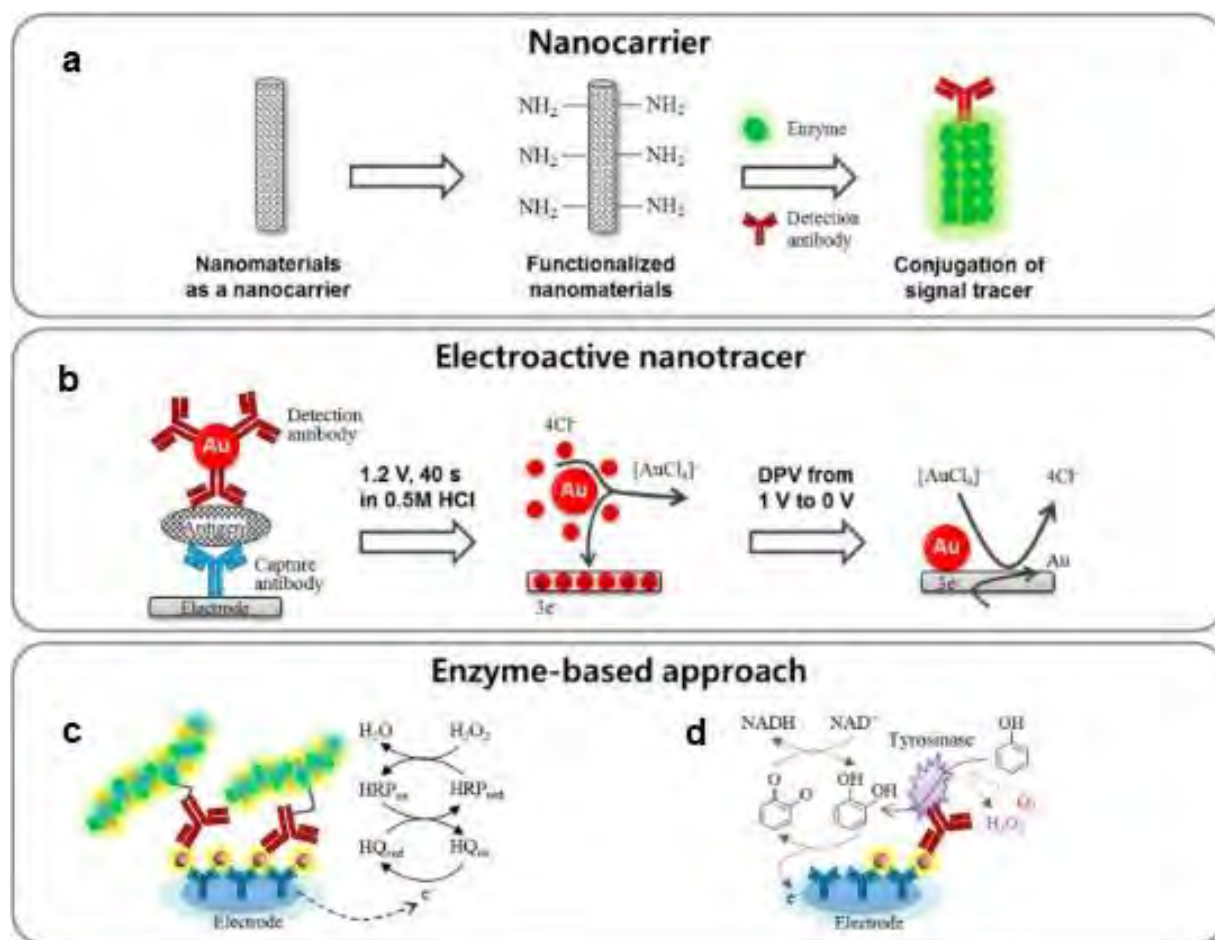
Scheme 1.3-6. The electrochemical signal enhancement for analyte detection by immunosensors via charge carriers labeling with (a) nanocarrier, (b) electroactive nanotracer, (c) nanopolymer functionalized with an enzyme, and (d) redox cycling of enzyme reactions.[309]

Many nanomaterials, including multi-walled carbon nanotubes (MWCNTs), magnetic beads (MBs), AuNPs, GO, dendrimers, and electroactive component-encapsulated NPs have been applied as nanocarriers in immunosensors with electrochemical detection. For instance, an AuNPs-supported anti-hIgG conjugated MB (anti-hIgG/AuNPs/MB) redox probe was prepared to fabricate an electrochemical hIgG immunosensor.[313] The AuNPs were introduced to increase the number of MB molecules in bioconjugate probes and thus amplify the detection signal. Furthermore, a ferrocene-tagged peptide nanowire was fabricated for immunosensing human IgG.[314] The peptide nanowires were used to load the ferrocene redox probe. Nanomaterials, especially metal NPs, can also be used as electroactive nanotracers. In that case, the NPs are usually coated with the antibody, generating an electrochemical signal based on the redox properties of the NPs. For instance, the immunosensor for human chorionic gonadotropin (hCG) utilizing AuNPs as the electrochemical probes and DPV transduction was proposed.[315] The AuNPs were pre-oxidized at a sufficiently high potential in an acidic solution, followed by the immediate reduction of $AuCl_4^-$ to Au^0. This immunosensor operation principle involved changes in the DPV peak current of Au ions electroreduction in an acidic solution.

Moreover, enzymes with high catalytic properties have frequently been used as tracers via antibody labeling together with electron mediators in typical electrochemical enzyme immunoassays. For example, an immunosensor for alfa-fetoprotein (AFP) determination, using horseradish peroxidase (HRP)-functionalized envision antibody complex (EVC) as the probe, was devised.[316] Importantly, an antibody-enzyme network structure was composed of a dextran-amine skeleton enabling the coupling of many HRP and secondary antibody molecules. This coupling allowed many enzyme molecules to participate in the binding, thus amplifying the signal. The detection principle involved inhibiting the electrochemical signal of hydroquinone in the phosphate-buffered saline (PBS) after forming the antigen-antibody complex. This signal was directly proportional to the AFP concentration. The enzyme-based signal can further be enhanced by modulating the redox cycling associated with electron mediators, e.g., ferrocene.[317] Moreover, a novel tyrosinase-responsive nonenzymatic redox cycling was proposed to amplify the electrochemical signal for carcinoembryonic antigen (CEA).[318]

Notably, aptamers may be an excellent alternative to antibodies for the (probe in solution)-free determination of target analytes. Accordingly, another example of self-reporting electrochemical biosensors may be aptamer-based sensors (aptasensors) tagged with redox probes. Aptamers are oligonucleotides of single-stranded deoxyribonucleic acid (DNA)

35

or ribonucleic acid (RNA) that can serve as biorecognition units binding different target analytes, including small-molecule compounds, sugars, peptides, proteins, and whole cells.[319-321] Advantages of aptamers include high affinity, thermal and chemical stability, and the possibility of modification by introducing various functionalities. Aptamers and antibodies have similar affinity to the analytes, but aptamers are more flexible and stable than antibodies. Moreover, their immobilization on a support surface is easier. Aptasensors use different signal transduction methods. However, electrochemical aptasensors have gained the most interest. Similarly to antibody immunosensors, aptamers are electroinactive. Therefore, they must be labeled with redox probes to generate an electrochemical signal. For that purpose, ferrocene and methylene blue are frequently used as tagging redox probes.[322] Interaction between the target analyte and the aptamer featuring a redox probe changes an electrochemical detection signal (Scheme 1.3-7). Significantly, different sensing methods have been developed for aptamers. For instance, analyte detection is based on signal OFF (Scheme 1.3-7a). In more detail, aptamer initially remains in the configuration stabilized by hydrogen bonds with its redox probe placed near the electrode surface. In this case, the target analyte (bacteria) binding to the aptamer changes aptamer conformation. Then, the redox probe moves away from the electrode, decreasing the electrochemical signal as the charge transfer rate decreases. In the signal ON detection strategy (Scheme 1.3-7b), the aptamer is in random conformation if the analyte is absent. Analyte binding changes aptamer conformation, moving the redox probe tag near the electrode. This probe relocation increases the signal as the charge transfer rate increases. Another possibility involves the preparation of a nucleic acid single strand complementary to the aptamer (Scheme 1.3-7c). Analyte interaction with the aptamer changes its conformation that displaces this single strand. The (redox probe)-labeled aptamer is then moved closer to the electrode surface, increasing the electrochemical signal.

Furthermore, sandwich configurations are introduced to electrochemical aptasensors to improve their selectivity and sensitivity. Usually, enzymes are used to amplify analyte sensing due to their catalytic properties. For instance, one study reported glucose dehydrogenase (GDH) serving as the biocatalytic probe for the enhanced amperometric detection of thrombin.[323] For further sensitivity improvement, aptamer-functionalized platinum NPs (PtNPs) were applied as catalytic probes instead of enzymes (Scheme 1.3-8a). The introduction of PtNPs catalyzing the electroreduction of H_2O_2 allowed for electrocatalytically amplified determination of thrombin.[324] Moreover, NPs may serve as charge carriers for protein determination by aptasensors (Scheme 1.3-8b). For example,

36

research was devoted to the amplified detection of thrombin.[325] AuNPs were functionalized with anti-thrombin aptamers containing polyadenine (poly-A). The analyte was captured by immobilized anti-thrombin antibody and detected by anti-thrombin aptamer-AuNPs bio bar codes. Due to the large surface area of NPs, they can carry many aptamers, enhancing the electrochemical signal for detecting thrombin analyte. Another sandwich-type sensing method involves aptamer-based rolling circle amplification (aptamer-RCA) for electrochemical detection of platelet-derived growth factor B-chain (PDGF-BB) serving as a model target.[326] The aptamer-primer sequence mediated an in-situ RCA reaction generating several copies of the circular DNA template, thus enhancing the detection sensitivity (Scheme 1.3-8c).
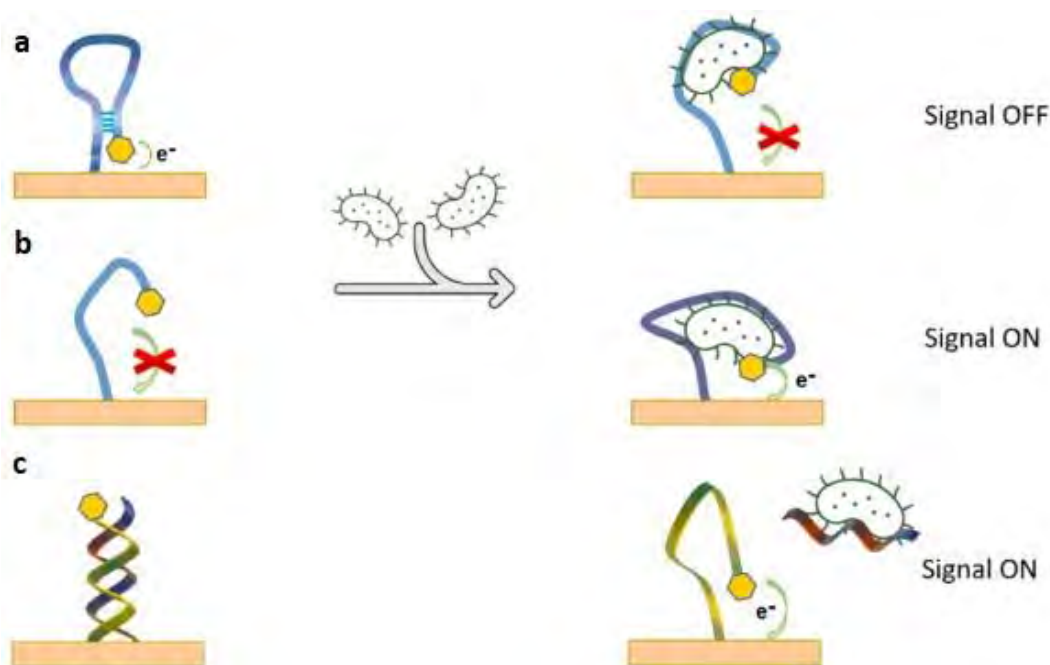
Scheme 1.3-7. The schematic depiction of the detection principle of aptasensors in (left-hand side) the absence of the bacteria analyte and (right-hand side) the presence of bacteria analyte showing (a) aptamer labeled with a redox probe resulting in signal OFF detection, (b) aptamer labeled with a redox probe resulting in signal ON detection, (c) duplex aptamer with single-strand removal by bacteria, resulting in signal ON detection.[322]

Moreover, for electrochemical signal transduction and amplification, not only NPs have been introduced for sandwich-type aptasensors preparation, but also MOFs[328] or hydroxyapatite (HAP) NPs.[329]

Various electrochemical aptasensors have recently been devised, including potentiometric,[330-333] impedimetric,[334-337] and voltamperometric[338-340] sensors.
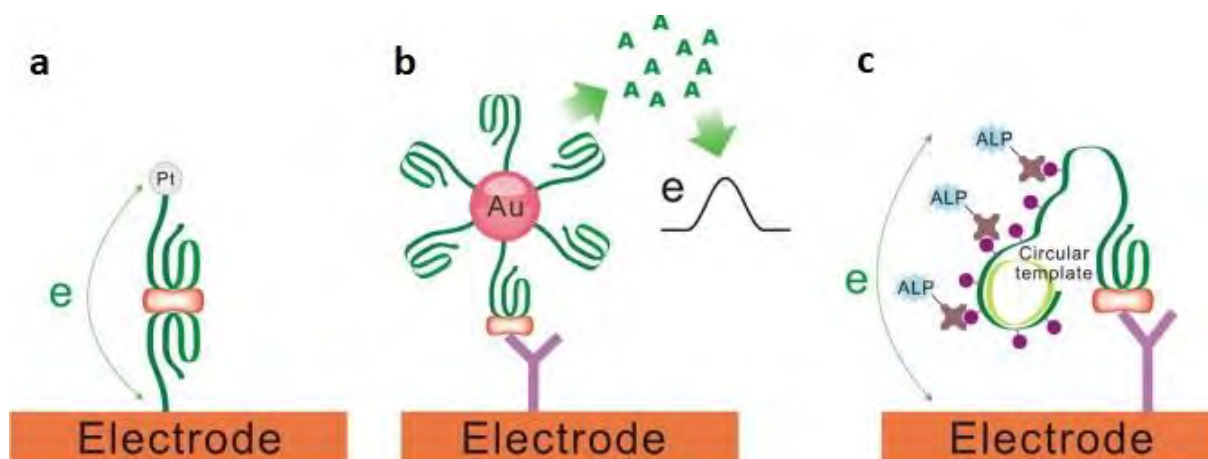
Scheme 1.3-8. Principles of operation of sandwich-type electrochemical aptasensors with signal amplification. (a) Aptamer functionalized with PtNPs serving as catalytic probes to catalyze the electroreduction of H_2O_2. (b) AuNPs functionalized with aptamers containing poly-A acting as reporting probes; the adenine nucleobases released were directly detected to generate enhanced signals. (c) The aptamer-primer mediated in-situ rolling circle amplification (RCA) reaction serving as the reporter.[327]

1.3.3 Devising, preparing, and testing MIP self-reporting electrochemical sensors

Remarkably, some attempts were made to immobilize the redox probe inside the MIP matrix to devise self-reporting MIP chemosensors. One of the first attempts proposed a chemosensor based on an electrochemical MIP (e-MIP) for determining a model analyte, benzo[a]pyrene (BaP).[341] For that, the ferrocene redox probe molecules were inserted in MIP cavities by copolymerizing the vinylferrocene (VFc) monomer with the EDMA cross-linking monomer in the presence of the BaP template. Then, the MIP was integrated with a CPE (Scheme 1.3-9).

As the ferrocene cyclopentadienyl rings might interact with BaP molecules via aromatic π-π stacking, the BaP analyte binding might change the properties of the ferrocene redox probe. Moreover, control electrochemical non-imprinted polymer (e-NIP) was prepared in the same manner as e-MIP but without BaP to validate the imprinting. DPV and SWV provided sensor responses. The measurements revealed that at the (e-MIP)-CPE, the peak decreased much more, due to analyte binding, than the peak at the control (e-NIP)-CPE. Unfortunately, the sensitivity and selectivity of the sensor were unsatisfactory. Therefore, the authors improved this e-MIP sensor performance by applying VFc along with 4-vinylpyridine (4-VP) as the aromatic co-monomer and divinylbenzene (DVB) or EDMA as the cross-linking monomer.[342] The 4-VP and DVB monomers might interact with BaP via π-π stacking due to the presence of aromatic rings in their structures. Thus, they might enhance π-π stacking

38

between the monomers and BaP. Indeed, VFc with 4-VP co-monomer integration with EDMA or DVB application increased sensor adsorption capability 6–8 times compared to the sensor based on the VFc-EDMA reference polymer. However, incorporating VFc and DVB into the polymer structure did not increase the imprinting factor (*IF*).
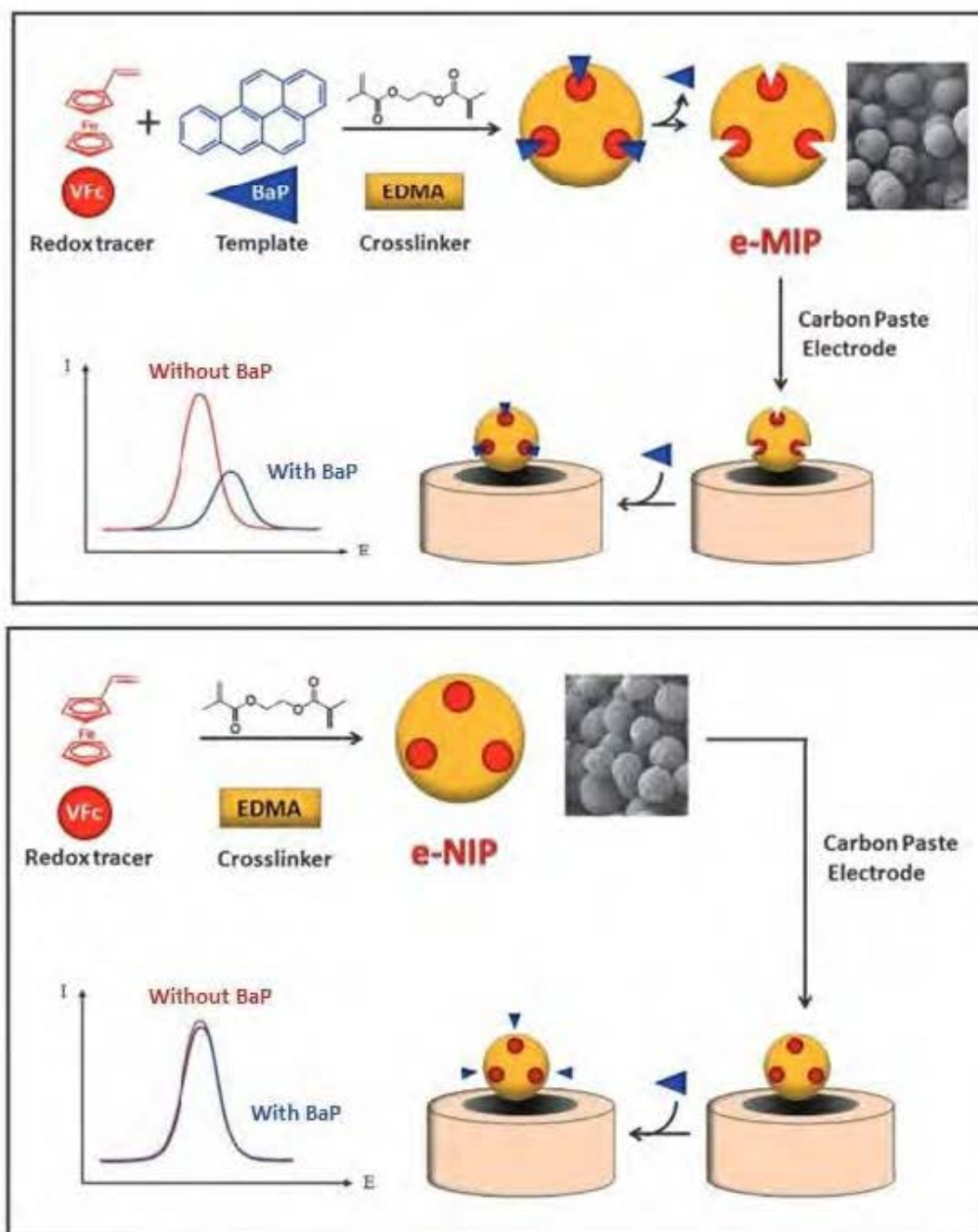
Scheme 1.3-9. Flowcharts of (top) e-MIPs and (bottom) e-NIPs preparation, and their subsequent introduction to the carbon paste electrode (CPE), followed by the electrochemical signal recording at the CPE modified with e-MIP or e-NIP in the presence and absence of the benzo[a]pyrene (BaP) analyte.[341]

39

Furthermore, e-MIPs based on ferrocenyl methacrylate were incorporated in screen-printed carbon electrodes (SPCEs) for electrochemical bisphenol A (BPA) determination.[343] For that, ferrocene methacrylate, used as the redox probe, was co-polymerized with the 4-VP and EDMA cross-linking monomers in the presence of the BPA template. Then, e-MIP and corresponding e-NIP microbeads were prepared by precipitation polymerization. Subsequently, these microbeads were introduced to a graphite-hydroxyethylcellulose composite paste for preparing an SPCE. Next, CV responses of SPECEs modified with e-MIPs and e-NIPs were measured. Cyclic voltammograms recorded at the (e-MIP)-SPCE and (e-NIP)-SPCE showed anodic and cathodic peaks corresponding to the redox process of the ferricenium/ferrocene couple. Significantly, the CV peak recorded at the (e-MIP)-SPCE was much higher than at the (e-NIP)-SPCE. This peak height difference might be related to more electroactive ferrocenyl groups present in the imprinted cavities formed after BPA extraction from e-MIP; thus, the peak increase. Importantly, the peak decreased with the BPA concentration increase. Possibly, analyte binding hid ferrocenyl groups attached to MIP cavities. This interaction between the BPA analyte and the redox probe immobilized in the MIP hindered the counter ions diffusion to the redox probe, thus decreasing the peak. Another research resulted in fabricating a sensor using electroactive MIP NPs selective to the vancomycin antibiotic.[344] The MIP NPs were prepared by solid-phase synthesis, introducing ferrocene derivative (VFc and ferrocenylmethyl methacrylate) monomers into the polymer structure. Then, thus synthesized MIP NPs were self-assembled on the Nafion film-coated GCE (Scheme 1.3-10). These MIP NPs were characterized by dynamic light scattering (DLS) and CV. Moreover, the number of ferrocene moieties was estimated using XPS. Sensor performance was analyzed by CV. CV peaks decreased with the increase of the analyte concentration in the linear dynamic concentration range of 83 to 410 µM. Presumably, the analyte binding changed the redox properties of ferrocene moieties, thus decreasing the peaks. This behavior was presumably induced by the change in impedance of the electron transfer between ferrocene groups embedded in the MIP and the electrode because of the interaction of electroinactive analyte molecules with MIP cavities. Notably, the electrochemical results confirmed the successful application of the chemosensor for selective vancomycin determination.
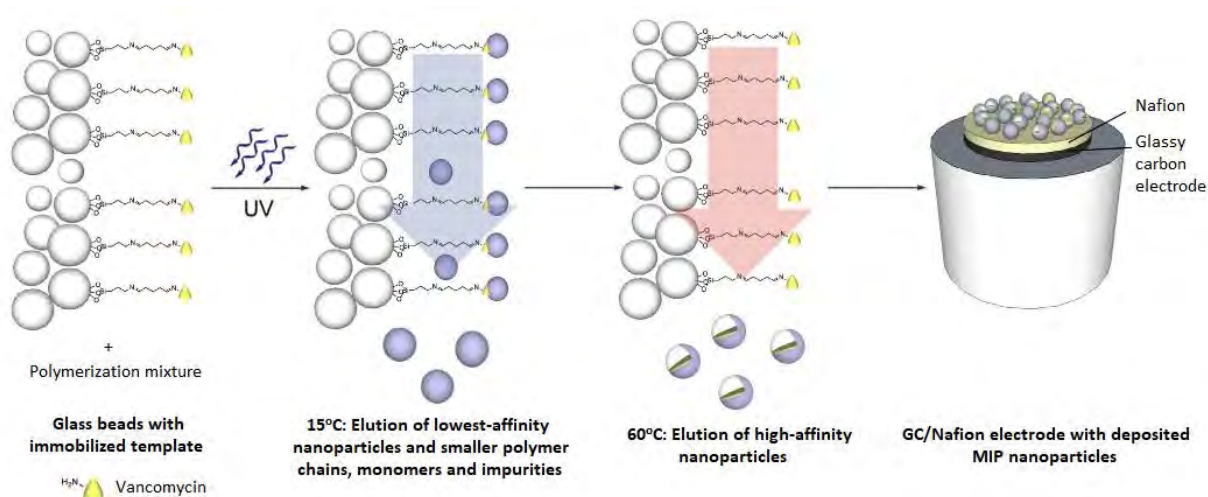
Scheme 1.3-10. The flowchart of MIP NPs preparation by solid-phase synthesis followed by their deposition on a Nafion film-coated glassy carbon electrode (GCE).[344]

In recent years, more studies reported the sensing application of MIP NPs integrated with redox probes. One example is a chemosensor based on MIP NPs tagged with the ferrocene redox probe for the electrochemical determination of different analytes, including paracetamol, glucose, trypsin, glucose, C4-homoserine lactone, and tetrahydrocannabinol (THC).[345] The MIP NPs were prepared by solid-phase synthesis,[346] and then used to modify the SPEl surface. Moreover, linking the redox probe with MIP NPs enabled the combining of both the sensor's recognizing and reporting functions. Recorded DPV peaks increased with the increase in analytes' concentrations. Most likely, analyte binding to MIP NPs changed polymer conformation and swelling, leading to ferrocene moieties exposure at the surface of NPs and consequently enhanced electron transfer to the electrode. Therefore, the current recorded at the (MIP NPs)-modified electrode was directly associated with the target analyte concentration (Scheme 1.3-11). Moreover, DLS measurements revealed that MIP NPs diameters were bigger in the presence of analytes.

Similarly, a sensor exploring electroactive MIP NPs for selective electrochemical determination of sitagliptin was reported.[347] The MIP NPs were integrated with a ferrocene redox probe, combining the sensing and reporting functions. Another research involved preparing and testing an electrochemical (MIP NPs)-based insulin-determining sensor.[348] The in-silico insulin epitope was mapped to design MIP NPs computationally. As in the studies described above, an electroactive ferrocene monomer acting as an internal redox probe was used for sensor preparation.

41
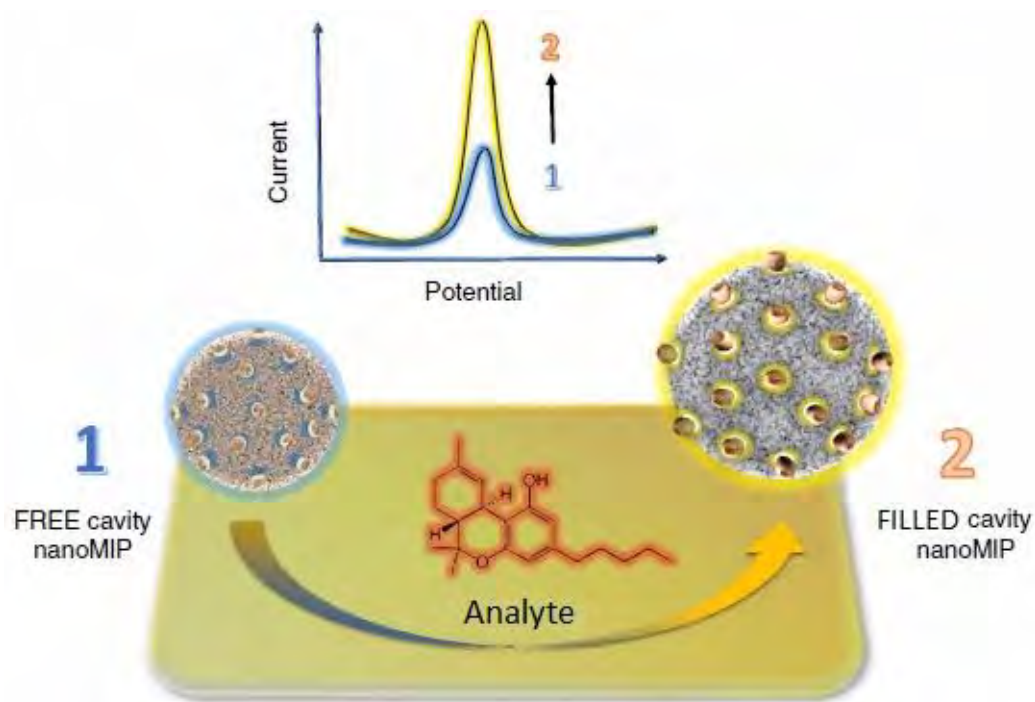
Scheme 1.3-11. The principle of operation of the electroactive (MIP NPs)-based sensor using tetrahydrocannabinol (THC) as a model analyte.[345]

Furthermore, a chemosensor was reported using electroactive MIP NPs for paracetamol determination.[349] MIP NPs were prepared by the solid-phase synthesis in all studies mentioned above. Different techniques, including DLS, transmission electron microscopy (TEM), scanning electron microscopy (SEM), as well as SPR and Fourier-transform infrared (FTIR) spectroscopy, characterized the MIP NPs. Moreover, the sensors' performance was optimized, followed by DPV analyte determinations. Notably, the DPV recorded peaks increased with the analyte concentration increase in all cases. A different strategy was adopted in a study describing a ferrocene-based monomer application for preparing an MIP chemosensor for determining electroactive 1-naphthylamine (1-NA).[350] This chemosensor exploited a composite of a cyclodextrin-functionalized graphene nanosheet and molecularly imprinted poly(vinylferrocene), GNN/CD-MIPVFc. The VFc functional monomer, acting as an electron mediator, improved the chemosensor's sensitivity. DPV was used to measure the chemosensor response. The composite enhanced the chemosensor's electrocatalytic activity leading to DPV peaks for 1-NA higher than those recorded at the chemosensor based on acrylic functional monomers. Furthermore, a ferrocenyl-based MIP chemosensor selective for electroactive BPA was devised.[351] Toward that, the ferrocenylmethyl methacrylate (FMMA) functional monomer was co-polymerized with the EGDMA cross-linking monomer in the presence of the BPA template and a porogenic solvent, supercritical carbon dioxide

42

($scCO_2$), then drop-cast on the surface of SPCE. The ferrocene-based functional monomer was applied to facilitate electron transfer for BPA determination. Therefore, the chemosensor response was assessed by DPV measurements. The irreversible oxidation peak of BPA recorded at the electrode modified with MIP linearly increased with the BPA concentration increase in the 4.7 to 8 nM range.

Chapter 2

2. Experimental part

This chapter provides information about all chemicals, procedures, instrumentation, and techniques applied to perform measurements presented in the thesis.

2.1 Chemicals

Templates/analytes, functional monomers, cross-linking monomers, and interferences used for the research are listed below.

Table 2.1-1. Templates/analytes.
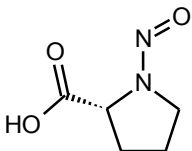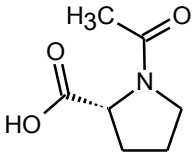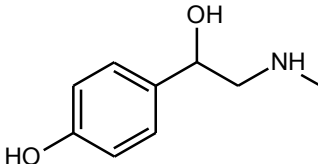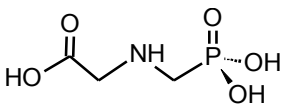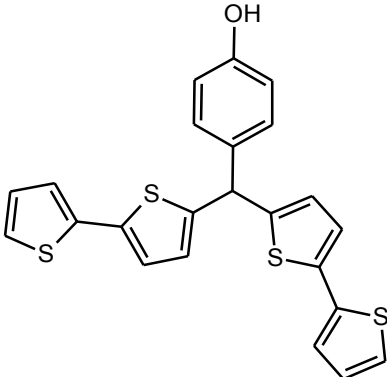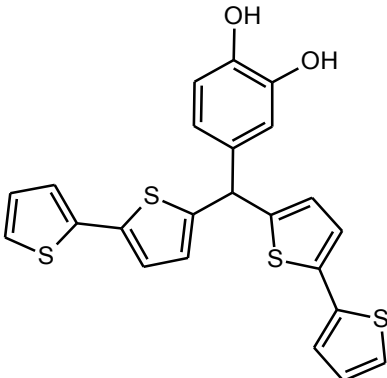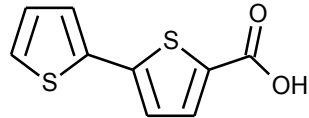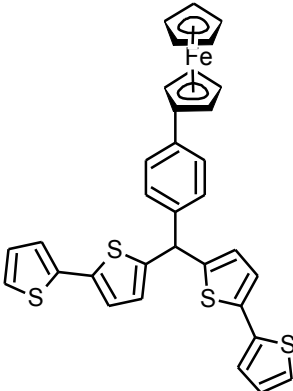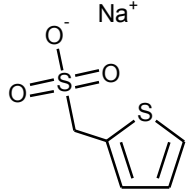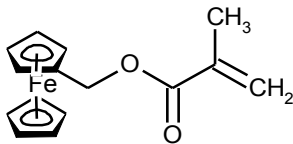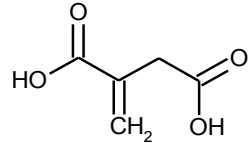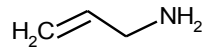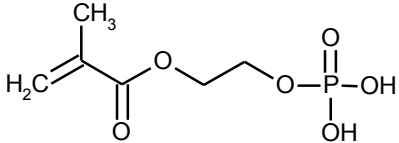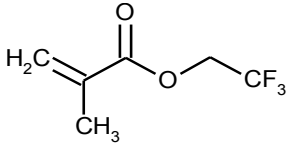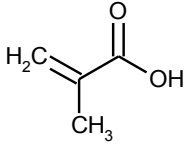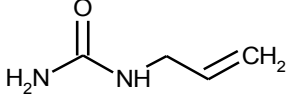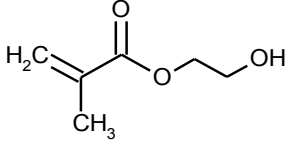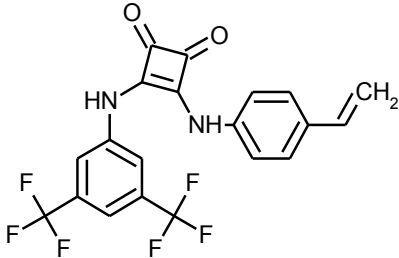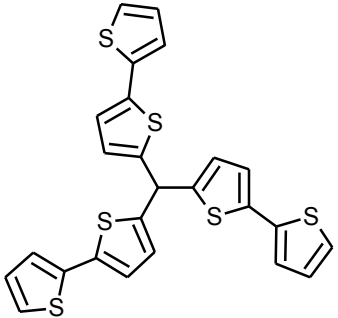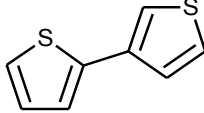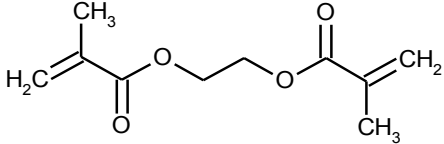
No.	Compound name	CAS number	Structural formula	Source
1	*N*-Nitroso-L-proline, Pro-NO	7519-36-0		Toronto Research Chemicals, Inc.
2	*N*-Acetyl-L-proline, Ac-Pro	68-95-1		Sigma Aldrich (now Merck KGaA)
3	*p*-Synephrine, SYN	94-07-5		Sigma Aldrich (now Merck KGaA)
4	Glyphosate, GLY	1071-83-6		Sigma Aldrich (now Merck KGaA)

44

Table 2.1-2. Functional monomers and cross-linking monomers.

No.	Compound name	Function	CAS number	Structural formula	Source
1	*p-bis*(2,2'-Bithien-5-yl)-methylphenol, FM 1	The functional monomer for the (Pro-NO)-MIP film chemosensor	-		Synthesized at the University of North Texas, Denton, TX, USA
2	*p-bis*(2,2'-Bithien-5-yl)methyl-o-catechol, FM 2	The functional monomer for the (Pro-NO)-MIP film chemosensor	-		Synthesized at the University of North Texas, Denton, TX, USA
3	2,2'-Bithiophene-5-carboxylic acid, FM 3	The functional monomer for the SYN-MIP film chemosensor	2060-55-1		Enamine Ltd.

45

4	*bis*-(2,2'-Bithienyl)-4-ferrocenylphenyl methane, FcM	Monomer providing an internal redox probe and playing the role of the cross-linking monomer for a self-reporting MIP film chemosensor	-		Synthesized at the University of North Texas, Denton, TX, USA
5	Sodium thiophen-2-ylmethanesulfonate	Monomer providing sulfonyl groups for a self-reporting MIP film chemosensor	61380-07-2		Enamine Ltd.
6	Ferrocenylmethyl methacrylate, FMAA	The functional monomer for the GLY-MIP NPs chemosensors	31566-61-7		Fluorochem Ltd.
7	Itaconic acid, ITA	The functional monomer for the GLY-MIP NPs-1 chemosensor	97-65-4		Sigma-Aldrich (now Merck KGaA)
8	Allylamine, AAm	The functional monomer for the GLY-MIP NPs-2	107-11-9		Sigma-Aldrich (now Merck KGaA)

46

			chemosensor and the GLY-MIP NPs-4 chemosensor		
9	Ethylene glycol methacrylate phosphate, EGMP	The functional monomer for the GLY-MIP NPs-2 chemosensor	24599-21-1		Sigma-Aldrich (now Merck KGaA)
10	2,2,2-Trifluoroethyl methacrylate, TFEMA	The functional monomer for the GLY-MIP NPs-3 chemosensor	352-87-4		Acros Organics
11	Methacrylic acid, MAA	The functional monomer for the GLY-MIP NPs-3 chemosensor	79-41-4		Acros Organics
12	N-Allylurea, AU	The functional monomer for the GLY-MIP NPs-3 chemosensor	557-11-9		Sigma-Aldrich (now Merck KGaA)
13	2-Hydroxyethyl methacrylate, HEMA	The functional monomer for the GLY-MIP NPs-4 chemosensor	868-77-9		Sigma-Aldrich (now Merck KGaA)

47

14	Squaramide-based monomer, SQ6	The functional monomer for the GLY-MIP NPs-4 chemosensor	-		Synthesized at the MIP Diagnostic according to the literature procedure[352]
15	5,5',5''-Methanetriyltris(2,2'-bithiophene), CM 1	The cross-linking monomer for the (Pro-NO)-MIP film chemosensor	-		Synthesized at the Institute of Physical Chemistry, Polish Academy of Sciences, Warsaw, Poland
16	2,3'-Bithiophene, CM 2	The cross-linking monomer for the SYN-MIP film chemosensor	2404-89-9		Sigma-Aldrich (now Merck KGaA)
17	Ethylene glycol dimethacrylate, EGDMA	The cross-linking monomer for the GLY-MIP NPs chemosensor	97-90-5		Sigma-Aldrich (now Merck KGaA)

48
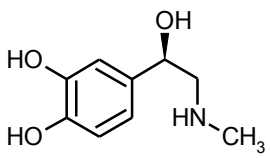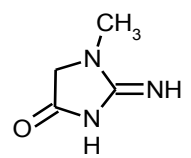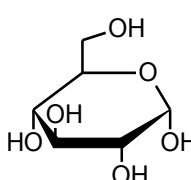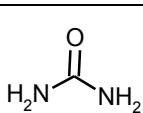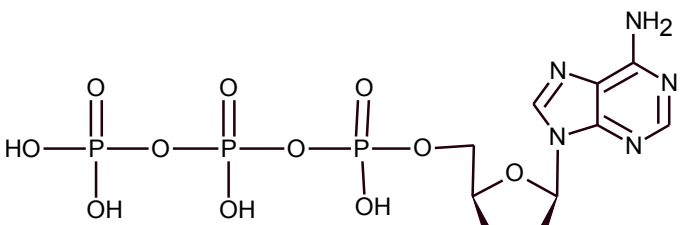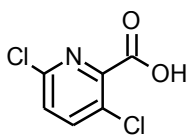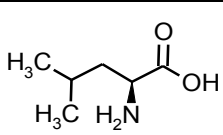
| 18 | Trimethylolpropane trimethacrylate, TRIM | The cross-linking monomer for the GLY-MIP NPs chemosensor | 3290-92-4 | | Sigma-Aldrich (now Merck KGaA) |
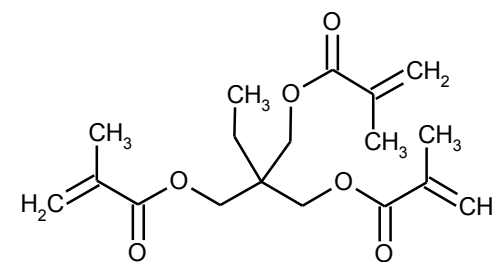
Table 2.1-3. Interferences

No.	Compound name	CAS number	Structural formula	Source
1	Adrenalin	51-43-4		Sigma Aldrich (now Merck KGaA)
2	Creatinine	60-27-5		Sigma Aldrich (now Merck KGaA)
3	D-(+)-Glucose	50-99-7		Sigma Aldrich (now Merck KGaA)
4	Urea	57-13-6		Sigma Aldrich (now Merck KGaA)
5	Adenosine triphosphate	56-65-5		Sigma Aldrich (now Merck KGaA)
6	Clopyralid	1702-17-6		Merck
7	L-Leucine	61-90-5		Sigma Aldrich (now Merck KGaA)

Other reagents and solvents employed are listed below. They were used as received.

- 1,3,5-Benzenetricarboxylic acid, trimesic acid, C_6H_3-1,3,5-$(COOH)_3$, CAS 554-95-0, Sigma-Aldrich (now Merck KGaA)

- 1,2-Benzenedicarboxylic acid ($\geq$99.5%), Phthalic acid, C_6H_4-1,2-$(CO_2H)_2$, CAS 88-99-3, Sigma-Aldrich (now Merck KGaA)

- 1,2-Bis(triethoxysilyl)ethane (95%), BTSE, $[-CH_2Si(OC_2H_5)_3]_2$, CAS 16068-37-4, Alfa Aesar

- 1-(3-Dimethylaminopropyl)-3-ethylcarbodiimide hydrochloride, ECD, $CH_3CH_2N=C=N(CH_2)_3N(CH_3)_2 \cdot HCl$, CAS 25952-53-8, Alfa Aesar

- (3-Aminopropyl)triethoxysilane (98%), APTES, $H_2N(CH_2)_3Si(OCH_2CH_3)_3$, CAS 919-30-2, Alfa Aesar

- 1-Decyl-3-methylimidazolium *bis*(trifluoromethanesulfonyl)imide, CAS 433337-23-6, Combi-Blocks

- Acetonitrile (sure seal), ACN, CH_3CN, CAS 75-05-8, Sigma-Aldrich (now Merck KGaA)

- Ammonium thiocyanate, NH_4SCN, CAS 1762-95-4, Merck KGaA

- Benzoic acid, ($\geq$99.5%), C_6H_5COOH, CAS 65-85-0, Sigma-Aldrich (now Merck KGaA)

- Chromotropic acid disodium salt, $(HO)_2C_{10}H_4(SO_3Na)_2 \cdot 2H_2O$, CAS 5808-22-0, Sigma-Aldrich (now Merck KGaA)

- Disodium phosphate (analytical grade), Na_2HPO_4, CAS 7558-79-4, POCH

- Ethanol (analytical grade), CH_3CH_2OH, CAS 64-17-5, STANLAB

- Glass beads, SiO_2, CAS 65997-17-3, Potters Industries

- Glutaraldehyde, $OHC(CH_2)_3CHO$, CAS 111-30-8, Merck KGaA

- Hexaammineruthenium(III) chloride (98%), $[Ru(NH_3)_6]Cl_3$, CAS 14282-91-8, Sigma-Aldrich (now Merck KGaA)

- Isopropanol (analytical grade), CAS 67-63-0, CHEMPUR

- Methanol (analytical grade), CH_3OH, CAS 67-56-1, STANLAB

- Monopotassium phosphate (analytical grade), KH_2PO_4, CAS 7778-77-0, POCH

- *N*-(2-Aminoethyl)-3-aminopropyltrimethoxysilane, AAPS, $C_8H_{22}N_2O_3Si$, CAS 1760-24-3, Merck KGaA

- *N*-[3-(Trimethoxysilyl)propyl]ethylenediamine, $(CH_3O)_3Si(CH_2)_3NHCH_2CH_2NH_2$, CAS 1760-24-3, Sigma-Aldrich (now Merck KGaA)

- *N*,*N*-diethyldithiocarbamic acid benzyl ester, $C_{12}H_{17}NS_2$, CAS 3052-61-7, TCI Europe

- *N*-Hydroxysuccinimide ($\geq$97%), NHS, $C_4H_5NO_3$, CAS 6066-82-6, Sigma-Aldrich (now Merck KGaA)

- Pentaerythritol tetrakis(3-mercaptopropionate), (>95%), $(HSCH_2CH_2COOCH_2)_4C$, CAS 7575-23-7, Sigma-Aldrich (now Merck KGaA)

- Potassium chloride (analytical grade), KCl, CAS 7447-40-7, POCH

- Potassium nitrate (analytical grade), KNO_3, CAS 7757-79-1, CHEMPUR

- Potassium hexacyanoferrate(III), $K_3Fe(CN)_6$, CAS 13746-66-2, Sigma-Aldrich (now Merck KGaA)

- Potassium hexacyanoferrate(II), $K_4Fe(CN)_6$, CAS 14459-95-1, CHEMPUR

51

- Sodium chloride (analytical grade), NaCl, CAS 7647-14-5, POCH

- Sodium cyanoborohydride (≥95%), $NaBH_3CN$, CAS 25895-60-7, Sigma-Aldrich (now Merck KGaA)

- Sodium dodecyl sulfate, SDS, $C_{12}H_{25}NaO_4S$, CAS 151-21-3, Merck KGaA

- Sodium hydroxide (analytical grade), NaOH, CAS 1310-73-2, POCH

- Tetra-*n*-butylammonium perchlorate (electrochemical grade), $(TBA)ClO_4$, $(CH_3CH_2CH_2CH_2)_4N(ClO_4)$, CAS 1923-70-2, Merck KGaA

- Tetra-*n*-ethylammonium perchlorate (electrochemical grade), $(TEA)ClO_4$, $(CH_3CH_2)_4N(ClO_4)$, CAS 2567-83-1, Merck KGaA

- Triethylamine (≥ 99%), Et_3N, $(C_2H_5)_3N$, CAS 121-44-8, Sigma-Aldrich (now Merck KGaA)

- Tetra-*n*-butylammonium hydroxide solution, (TBA)OH, $(CH_3CH_2CH_2CH_2)_4N(OH)$, CAS 2052-49-5, Sigma-Aldrich (now Merck KGaA)

- Toluene (sure seal), $C_6H_5CH_3$, CAS 108-88-3, Sigma-Aldrich (now Merck KGaA)

2.2 Procedures and instrumentation

This section describes MIP chemosensors' preparation procedures and the instrumentation used.

2.2.1 Procedures and instrumentation for chemosensors based on MIP films

2.2.1.1 The general procedure for preparing films of MIPs templated with food toxins and NIPs

The general procedure of MIPs' preparation comprised complementarily and successively implemented following steps.

(1) Studying the properties of electroactive cross-linking and functional monomers from the group of thiophene derivatives bearing functional groups recognizing chosen toxin analytes selectively.

(2) Computational modeling the structures of analyte-(functional monomer) pre-polymerization complexes and testing their properties.

(3) Depositing thin films of MIPs on electrodes' surfaces and then optimizing deposition procedures.

(4) Studying morphology and physicochemical properties of MIP films.

(5) Applying the MIP films for selective chemosensors fabrication for determining chosen toxin analytes selectively. Determining analytical parameters of these chemosensors. Elaborating determination procedures.

The preliminary step of the research was selecting the appropriate functional monomers bearing functionalities capable of recognizing functionalities of the molecules of given toxin templates to form pre-polymerization complexes in solutions. Then, these complexes were potentiodynamically electropolymerized in the presence of cross-linking monomers and simultaneously deposited as thin MIP films on electrodes. Subsequent removal of the toxin template molecules from these MIPs vacated molecular cavities capable of selectively recognizing these toxins as analytes. Thus, these films played the chemosensor recognition units' role in the selective determination of food toxins.

Control NIP films were prepared under the same conditions as the MIP films but without templates in the solutions. Comparison of the MIP with NIP performance allows for verifying the extent of imprinting.

2.2.1.2 *Quantum-chemistry calculations and selecting appropriate functional monomers for synthesizing (food toxin)-templated MIP films*

The computational calculations were performed with Gaussian 09 software98 (Gaussian, Inc., CT, USA), installed on the high-performance computer with the 16-core Intel Xeon E5620 2.4 GHz processor and 8 GB RAM, to choose appropriate functional monomers that can interact with template molecules and form stable pre-polymerization complexes. The computational density functional theory (DFT) modeling at the B3LYP/3-21G level was applied to calculate values of Gibbs free energy changes, ΔG, accompanying complex formation. The 3-D structures of the template, functional monomers' molecules, and their complexes were visualized with GaussView software. Then, DFT calculations were performed on their optimized structures using Gaussian 09 software, and the ΔG values were acquired.

2.2.1.3 *Confirming complex stability by UV-vis spectroscopy*

UV-vis spectroscopy titration confirmed stable pre-polymerization complex formation of the chosen functional monomers with the *N*-nitroso-L-proline (Pro-NO) template, optimized by computational calculations. A UV-2550 spectrophotometer of Shimadzu Corp. controlled by UVProbe 2.21 software of the same manufacturer was used for the

53

experiments. UV-vis spectra were recorded with 0.1 nm resolution. Moreover, the stoichiometry of the pre-polymerization complex was determined by plotting functional monomer absorbance at 320 nm versus the concentration of Pro-NO, c_{Pro-NO}. The stability constant, K_s, was calculated with the Scatchard method[353] using the following equation:

$$\frac{(Abs_{(FM)} - Abs_{(FM)_0})}{2\,c_{(Pro-NO)}^2} = -K_s\left(Abs_{(FM)} - Abs_{(FM)_0}\right) + K_s c_{(FM)_0} \Delta\varepsilon_{[2(FM)-(Pro-NO)]} \quad \text{(Equation 2.2-1)}$$

where $Abs_{(FM)_0}$ and $Abs_{(FM)}$ represent functional monomer absorbance before and after Pro-NO addition, respectively; $c_{(FM)_0}$ stands for the initial functional monomer concentration, equal to 31.25 µM. The $\Delta\varepsilon_{[2(FM)-(Pro-NO)]} = \varepsilon_{(FM)} - \varepsilon_{(Pro-NO)}$ dependence links the $\varepsilon_{[2(FM)-(Pro-NO)]}$ molar complex absorptivity with that of the functional monomer, $\varepsilon_{(FM)}$, and Pro-NO, $\varepsilon_{(Pro-NO)}$. The K_s value was determined from the slope of the linear dependence of $\frac{(Abs_{(FM)} - Abs_{(FM)_0})}{2\,c_{(Pro-NO)}^2}$ on $\left(Abs_{(FM)} - Abs_{(FM)_0}\right)$, according to Equation 2.2-1.

2.2.1.4 *Preparing electrodes before measurements*

Before depositing an MIP film on the surface of a disk electrode, this surface was cleaned in the "piranha" solution for 10 min, then consecutively polished with the alumina slurries of the 1.0, 0.3, 0.05-µm diameters and rinsing with deionized water. Finally, electrodes were sonicated in ethanol for 10 min. (*Warning. Piranha solution is dangerous upon contact with the skin or eyes*).

Au-layered glass slides with a 100-nm thick Au film vapor deposited over a 15-nm thick Ti underlayer (Institute of Electronic Materials Technology, Warsaw, Poland) were cleaned by 10-min ultrasonication (160 W power IS-3R of InterSonic, Olsztyn, Poland) in acetone, then isopropanol, and then dried in an argon stream. Later, the polymer films were deposited on these slides under conditions like those used for disk electrodes. Those MIP film-coated slides were applied for polymer characterization with XPS, AFM, SEM, and polarization-modulation infrared reflection-absorption spectroscopy (PM-IRRAS).

Commercial BK7 24-mm diameter Au-layered glass disks (Autolab-Metrohm) were used in SPR spectroscopy measurements. Before the experiments, the disks were cleaned with methanol, then isopropanol, and then dried in an argon stream.

AT-cut plano-plano 10-MHz quartz crystal resonators (QCRs), coated with a 100-nm thick Au layer over a 10-nm thick Ti underlayer, were cleaned with methanol, then dried in an Ar stream.

2.2.1.5   Instrumentation for imprinted and non-imprinted polymer films preparation

Polymers were deposited on electrodes by oxidative electropolymerization under potentiodynamic conditions using a computerized electrochemistry system of AUTOLAB, composed of a PGSTAT12 potentiostat/galvanostat equipped with a FRA2 frequency response analyzer controlled by GPES 4.9 software, all from the Eco Chemie manufacturer.

A platinum disk electrode was used as the working electrode placed in a three-electrode, one-compartment V-shaped glass electrochemical minicell (Scheme 2.2-1) with an Ag wire coated with the AgCl and a coiled Pt wire serving as the quasi-reference and counter electrode, respectively.
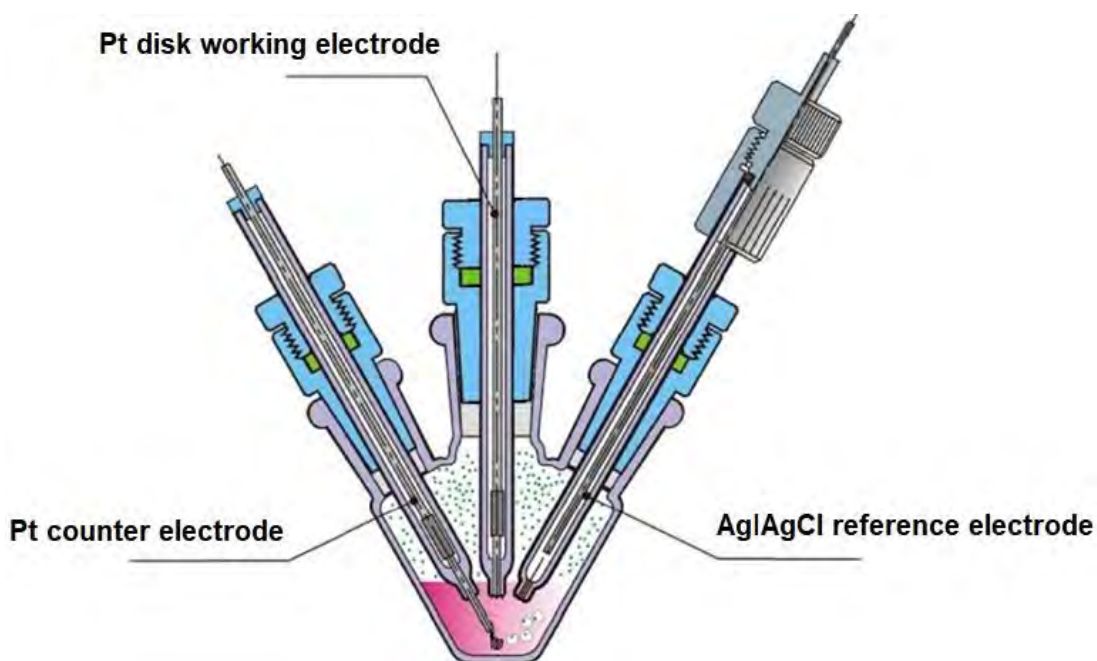
Scheme 2.2-1. The cross-sectional view of a V-shaped three-electrode electrochemical glass minicell.

Furthermore, Au electrodes of QCRs were coated with MIP or NIP films by oxidative polymerization under potentiodynamic conditions using the EP-20 Potentiostat coupled with the EQCM 5710 model quartz crystal microbalance controlled by EQCM 5710-S2 software, all of the IPC PAS, Warsaw. A quartz crystal holder

(Scheme 2.2-2a) was clamped horizontally with its QCR positioned upwards to deposit an MIP film on the surface of the resonator's electrode. An Ag|AgCl and coiled Pt wire used as a quasi-reference and auxiliary electrode, respectively, were mounted close to the working electrode of the QCR (Scheme 2.2-2b).

1. O-ring 9/1 mm (Viton® or silicon rubber)
2. Contacting spring (Au-plated bronze)
3. Quartz crystal
4. Crystal adapter (Au-plated brass)
5. O-ring 15/1mm (Viton®)
6. Back cover (Kel-F®)
7. Quartz crystal tightening screw (stainless steel or Kel-F®)
8. O-ring 2/1 mm (Viton®)
9. Sleeve for fastening of the back cover (Kel-F®)
10. Main body sleeve (PTFE)
11. Conical joint 29/25 mm (PTFE)
13. Conical joint threaded sleeve (Tarnamid™)
14. End cover of the main body (PTFE)
15. Cable fastening screw (Ni-plated brass)
24. Cable

Scheme 2.2-2. (a) The expanded view of the EQCM holder and (b) arrangement of the coiled Pt wire auxiliary electrode and the Ag|AgCl quasi-reference electrode in the vicinity of QCR, mounted in the EQCM holder cavity.[354]

Moreover, an Au-layered glass disk was coated with an MIP film for the SPR spectroscopy measurements. For polymer deposition, an SPR chip serving as the working electrode was placed in a cuvette close to the Ag|AgCl quasi-reference and Pt wire counter electrodes. Electropolymerization was performed using the Autolab ESPRIT instrument of Eco Chemie (Utrecht, The Netherlands), equipped with a computerized PGSTAT128N potentiostat/galvanostat and controlled by the AUTOLAB SPR Data Acquisition and GPES 4.9 software of the same manufacturer.

2.2.1.6   *Preparing MIP film templated with N-nitroso-L-proline*

For depositing a (Pro-NO)-templated MIP film, the 1-mm diameter Pt disk electrode was first cleaned, as described in Section 2.2.1.4. Afterward, an acetonitrile solution of 50 μM Pro-NO template, 100 μM *p-bis*(2,2'-bithien-5-yl)-methylphenol (FM 1) functional monomer, 500 μM 5,5',5"-methanetriyltris(2,2'-bithiophene), CM 1 cross-linking monomer, and 100 mM (TBA)ClO$_4$ supporting electrolyte was used as the pre-polymerization complex solution. For polymer film deposition, the pre-polymerization complex formed was oxidatively electropolymerized under potentiodynamic conditions within five potential cycles at a scan rate, v, of 50 mV s^{-1} at the potential range of 0 to 1.30 V vs. Ag quasi-reference electrode. Then, the Pro-NO template was removed from the resulting MIP film by immersing the electrode coated with this film in 0.1 M NaOH for 20 min with magnetic stirring. Additionally, an NIP film was prepared under the same conditions as the (Pro-NO)-MIP film, but in the template absence, to assess imprinting efficiency.

Afterward, the (Pro-NO)-templated MIP film was deposited on QCR in the same way as described above for PM experiments.

2.2.1.7   *Synthesizing MIP film imprinted with p-synephrine*

An acetonitrile solution of the 10 μM *p*-synephrine (SYN) template, 30 μM 2,2'-bithiophene-5-carboxylic acid (FM 3) functional monomer, 300 μM 2,3'-bithiophene (CM 2) cross-linking monomer, and 100 mM (TBA)ClO$_4$ supporting electrolyte was prepared toward the formation of the pre-polymerization complex. Afterward, this complex was deposited as a thin MIP film on the 1-mm Pt disk electrode by potentiodynamic electropolymerization with five potential cycles at a scan rate of 50 mV s^{-1} over the potential range of 0 to 1.30 V vs. Ag quasi-reference electrode. Finally, the template was removed from the film, leaving molecular voids capable of interacting with the SYN molecules, allowing the determination of this toxin. Control NIP was also prepared as a proof of the imprinting concept.

Furthermore, an SYN-templated MIP film was deposited on the Au-layered glass slides as described for disk electrodes for AFM and UV-vis spectroscopy measurements.

Moreover, SPR chips were coated with SYN-templated MIP films and NIP control films under the same conditions as those mentioned above for SPR measurements.

Five different MIP films, namely (SYN-Fc)-(MIP-1), (SYN-Fc)-(MIP-2), (SYN-Fc)-(MIP-3), (SYN-Fc)-(MIP-4), and (SYN-Fc)-(MIP-5), were synthesized, then examined.

For the (SYN-Fc)-(MIP-1) film formation, an acetonitrile solution of 10 μM SYN template, 30 μM FM 3 functional monomer, 100 μM *bis*-(2,2'-bithienyl)-4-ferrocenylphenyl methane Fc, and 0.1 M (TBA)ClO$_4$ supporting electrolyte was prepared. The (SYN-Fc)-(MIP-1) film was deposited on the Pt disk electrode surface by potentiodynamic electropolymerization with five potential cycles from 0 to 1.30 V vs. Ag quasi-reference electrode and at a potential scan rate of 50 mV s^{-1}.

The (SYN-Fc)-(MIP-2) film was prepared similarly to the (SYN-Fc)-(MIP-1) film but with 100 μM sodium thiophen-2-yl methanesulfonate present in the pre-polymerization complex solution.

The (SYN-Fc)-(MIP-3) film was likewise formed as (SYN-Fc)-(MIP-1) film but with 100 μM chromotropic acid disodium salt in the solution for electropolymerization.

For the (SYN-Fc)-(MIP-4) film synthesis, a solution of 10 μM SYN, 30 μM functional monomer FM 3, 100 μM ferrocene derivative Fc, 100 μM sodium thiophen-2-ylmethanesulfonate, and 0.1 M (TBA)ClO$_4$ in toluene, the 1-decyl-3-methylimidazolium *bis*(trifluoromethanesulfonyl) imide ionic liquid, and acetonitrile at the ratio of 1 : 2.5 : 6.5 (*v* : *v* : *v*) was prepared. The (SYN-Fc)-(MIP-4) film was deposited on the Pt disk electrode by potentiodynamic electropolymerization at a potential scan rate of 50 mV s^{-1} with three potential cycles in the range of 0 to 1.10 V vs. Ag quasi-reference electrode.

Finally, to prove the validity of applying sodium thiophen-2-yl methanesulfonate, the (SYN-Fc)-(MIP-5) film was prepared under similar conditions as the (SYN-Fc)-(MIP-4) film but without the monomer mentioned above. Thus, 10 μM SYN, 30 μM FM 3, 100 μM Fc, and 0.1 M (TBA)ClO$_4$ in a mixture of the 1-decyl-3-methylimidazolium *bis*(trifluoromethanesulfonyl)imide ionic liquid and acetonitrile, 1 : 3 (*v* : *v*), was prepared. The (SYN-Fc)-(MIP-5) film was deposited on the electrode surface by electropolymerization under potentiodynamic conditions with three potential cycles at a potential scan rate of 50 mV s^{-1} in the range of 0 to 1.10 V vs. Ag quasi-reference electrode.

For SYN template extraction from the (SYN-Fc)-(MIP-1), (SYN-Fc)-(MIP-2), and (SYN-Fc)-(MIP-3) films, the electrodes with deposited polymers were immersed in 0.1 M NaOH for 60 min under magnetic stirring. For SYN template extraction from the (SYN-Fc)-(MIP-4) and (SYN-Fc)-(MIP-5) films, the electrodes with deposited polymers were dipped in 0.01 M Et_3N for 5 min under stirring conditions. Moreover, a control (SYN-Fc)-(NIP-4) film was prepared under the same conditions as the (SYN-Fc)-(MIP-4) film but without the template.

Furthermore, for PM measurements, QCRs were coated with (SYN-Fc)-(MIP-4) films by potentiodynamic electropolymerization with one cycle in the range of 0 to 1.20 V vs. Ag quasi-reference electrode at a potential scan rate of 50 mV s^{-1}. For that, 100 μM SYN, 300 μM FM 3, 1 mM Fc, 1 mM sodium thiophen-2-ylmethanesulfonate, and 0.1 M $(TBA)ClO_4$ in the mixture of toluene, the 1-decyl-3-methylimidazolium *bis*(trifluoromethanesulfonyl) imide ionic liquid, and acetonitrile at the ratio of 1 : 2.5 : 6.5 (*v*: *v* : *v*) was used for electropolymerization.

For SPR experiments, the (SYN-Fc)-(MIP-4) film was deposited on an Au-layered glass disk under the same conditions as above, optimized for piezomicrogravimetric measurements.

2.2.1.9   *Instrumentation and procedures for MIP and NIP films' characterization by spectroscopic and microscopic techniques*

XPS measurements were performed to unravel the surface chemical composition of MIP and NIP films and confirm that extraction of the templates from the MIPs was successful. The XPS spectra were recorded on a PHI 5000 Versa Probe-Scanning ESCA microprobe (ULVAC-PHI) by applying monochromatic Al Kα radiation (hv = 1486.4 eV). The data were evaluated using Casa XPS software. The Shirley and mixed Gaussian-Lorentzian methods were used for background subtraction and peak fitting, respectively. The electron binding energy (BE) of the C 1s peak (BE = 284.6 eV) was selected as the internal binding energy reference.

Infrared (IR) spectroscopy measurements were performed to compare the MIP film before and after template removal and with the NIP film. IR spectra were recorded with 2-cm^{-1} resolution for the films using a Fourier-transform infrared (FTIR) spectrometer Vertex 80v (Bruker Corporation, USA) controlled by Opus 6.5 software from the same manufacturer. The instrument was equipped with a (liquid nitrogen)-cooled MCT (Hg-Cd-Te) detector and the PMA50 module to conduct PM-IRRAS experiments. Au-

layered glass slides coated with polymer films were placed in a dedicated holder. The incidence angle of the p-polarized light beam was set at 83° to the normal to the slides. 1024 scans were recorded for each spectrum. The IR spectroscopy data recorded for a bare Au-layered glass slide was used as the background for further measurements of polymer film-coated samples. Moreover, spectra were recorded in a reflection mode with the 2-cm^{-1} resolution using the same spectrometer, except for Monolayer/Grazing Angle Specular Reflectance Accessory type GS19650 (Specac, UK). For fitting the IR spot's dimension to the sample's dimension, the incident and reflection angles were set to 60º. The spectrometer operated under low pressure to minimize the influence of different atmosphere components. During measurements, the pressure inside the sample chamber was kept below 5 hPa.

Further, MIP and NIP films were imaged with a MultiMode 8 AFM microscope of Bruker with the Peak Force Quantitative Nanomechanical properties mapping and equipped with a Nanoscope V controller. Au-layered glass slides were scanned applying the Peak Force Tapping mode™ as well as ScanAssyst™ mode. The calibrated rotated tapping etched silicon probe Sb-doped Si cantilevers featuring the force constant of 52.2 N m^{-1} were used for the experiments. For evaluation of average polymer film thickness, scratches were made with a Teflon spatula in different places of the films deposited on Au-layered glass slides, and then the height of the resulting steps was determined far from a partially detached front of the step. Finally, the mean of step heights measured for scratches was calculated, resulting in an average film thickness. Moreover, AFM measurements were performed to assess the polymer films' thickness in the solution. For that, Au-glass slides coated with polymer films were scanned using an HQ-NSC35 B cantilever with a spring constant of 16 N m^{-1}.

Self-reporting MIP films were characterized with SEM imaging by a NanoSEM 450 microscope (FEI Nova, U.K.) equipped with an energy-dispersive X-ray (EDX) spectroscopy spectrometer for the EDX analysis.

2.2.1.10 General procedures and instrumentation for MIP and NIP films characterization by CV, DPV, and EIS measurements

The CV, DPV, and EIS measurements were performed using an AUTOLAB computerized electrochemistry system controlled by GPES 4.9 software. The system comprised a PGSTAT12 potentiostat/galvanostat and a FRA2 frequency response analyzer from Eco Chemie. For the experiments, a V-shaped glass minicell was

employed with an MIP film-coated Pt disk electrode, an Ag wire coated with the AgCl film, and a coiled Pt wire, serving as the working, quasi-reference, and auxiliary electrode, respectively (Scheme 2.2-1). The minicell was filled with 0.1 M $K_3[Fe(CN)_6]$ and 0.1 M $K_4[Fe(CN)_6]$ redox probe in a 0.1 M phosphate buffer, PB (pH = 7.0) solution or 0.1 M $K_3[Fe(CN)_6]$ and 0.1 M $K_4[Fe(CN)_6]$ redox probe in 0.1 M PBS (pH = 7.4) for characterization of the (Pro-NO)-MIP or SYN-MIP film, respectively. For self-reporting MIP films' characterization, either (redox probe)-free PBS (pH = 7.4) or 0.1 M $(TBA)ClO_4$ in acetonitrile was applied.

After polymer film deposition on the electrode surface using potentiodynamic electropolymerization, templates were removed from MIPs by immersing the MIP film-coated electrodes in dedicated extracting solutions under stirring. After each extraction step, a DPV voltammogram and EIS spectrum were recorded at the electrode dipped in a blank supporting electrolyte solution. The potential was scanned within 30 cycles from 0 to 0.6 V vs. Ag quasi-reference electrode before each measurement to attain steady-state conditions. Template extraction from the MIP film was seized when the redox probe DPV peak reached a constant height. In the DPV experiments, the potential was scanned from 0 to 0.60 V vs. Ag quasi-reference electrode with a potential step of 5 mV, a pulse width of 50 ms, and an amplitude of 25 mV. The EIS spectra were recorded in the frequency range of 1 MHz to 100 mHz with 10-mV sinusoidal amplitude of an alternating voltage applied to the working electrode at the open circuit or the potential of 0.20 V vs. quasi-reference electrode. Results obtained from the EIS experiments were fitted with parameters of equivalent circuits using Z-View software of the Scribner Associates, Inc. NIP film-coated electrodes were also dipped in an appropriate extraction solution to check if the extraction influences polymer morphology.

Food toxins' DPV and EIS determinations were performed under conditions like those for the polymer films' characterization. Analyte samples of known concentrations were added to the respective supporting electrolyte solution, and then the solution was magnetically stirred for 10 min allowing the analyte to interact with the polymer. DPV voltammograms and EIS spectra were consecutively recorded at (template extracted)-MIP film-coated electrode. For DPV chemosensors, calibration curves were plotted based on the difference or relative difference between the DPV peak current for different analyte concentrations. For EIS chemosensors, data were fitted using an equivalent circuit provided by Z-View software. Subsequently, R_{ct} values determined

61

for different analyte concentrations were applied to construct calibration curves. The chemosensors' selectivity was determined by analyzing the sensitivity of structurally and functionally similar interferences under the same DPV and EIS experimental conditions.

2.2.1.11 General procedures and instrumentation for MIP chemosensors characterization by piezoelectric microgravimetry (PM) at an electrochemical quartz crystal microbalance (EQCM)

The Pro-NO analyte in a PB (pH = 7.0) solution was determined by PM under flow-injection analysis (FIA) conditions. For that, a (Pro-NO)-MIP film-coated QCR was mounted in a flow-through EQCM 5610 holder (Scheme 2.2-3a), interfaced with a KDS100 syringe pump (KD Scientific, Inc.), and then rinsed with 0.1 M NaOH to extract the Pro-NO template from the MIP. Subsequently, PB (pH = 7.0) was pumped through the holder at 30 μL min^{-1}, maintaining a laminar flow of the carrier solution to the MIP film. Then, samples of Pro-NO were injected into the PB solution, and the resonant frequency changes with time generated because of the analyte presence were recorded. The PM setup applied for the Pro-NO determination under FIA conditions is presented in Scheme 2.2-3b.

Further, the (SYN-Fc)-(MIP-4) film was characterized by PM at EQCM under stagnant-solution conditions. Toward that, a QCR holder with a template-free self-reporting MIP film-coated QCR mounted was immersed in a V-shaped electrochemical glass cell (Scheme 2.2-4) filled with 0.1 M (TEA)ClO$_4$ in acetonitrile. A coiled Pt wire and an Ag wire coated with Ag|AgCl were used as the respective counter and quasi-reference electrodes. The current was recorded simultaneously with the resonance frequency change and the dynamic resistance change during potential cycling between 0.2 to 0.65 V vs. Ag quasi-reference electrode in the absence and then in the presence of the SYN analyte in the test solution.

62
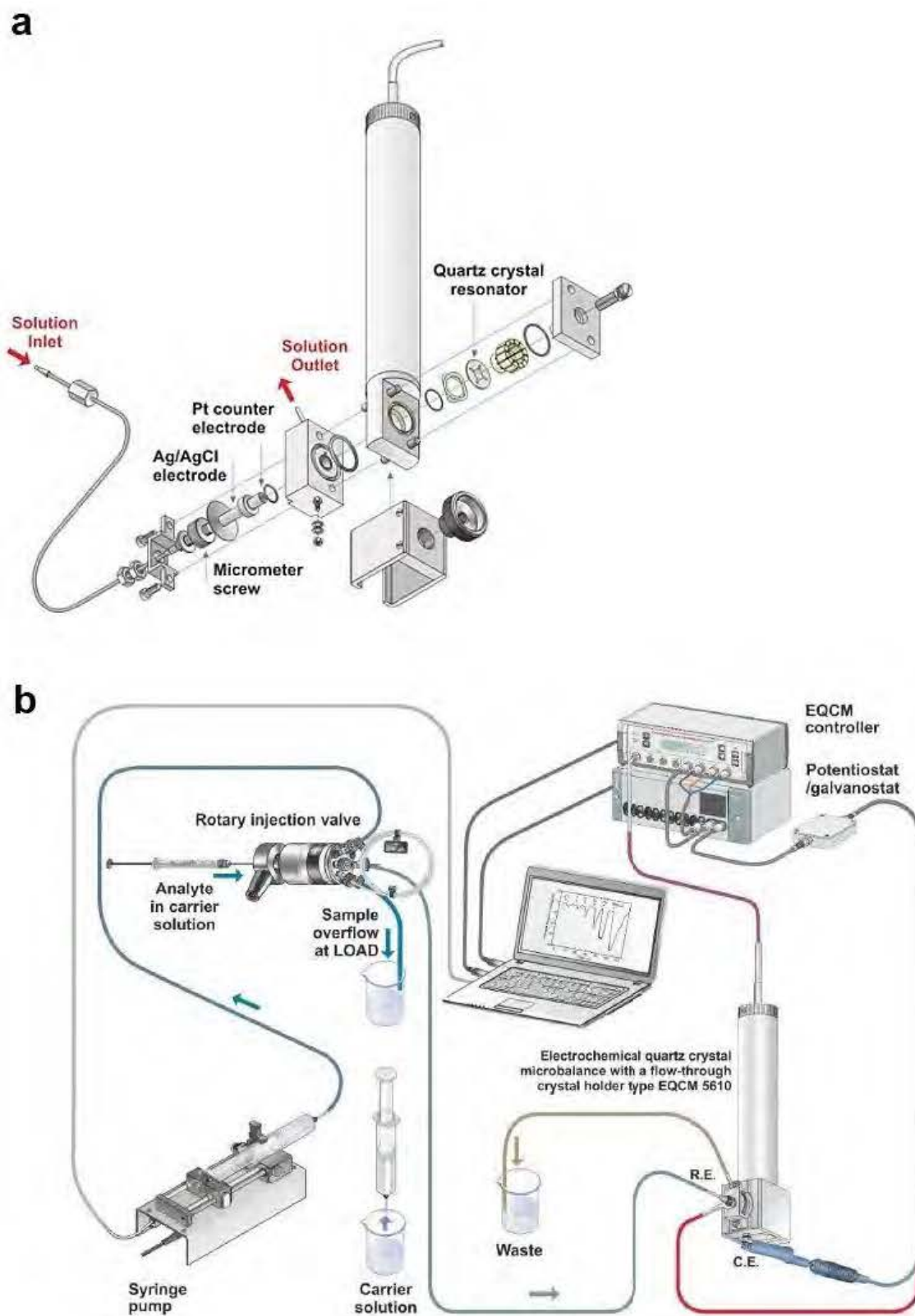
Scheme 2.2-3. Scheme of (a) a flow-through holder for a quartz crystal resonator for FIA measurements using EQCM 5610 microbalance and (b) a setup used for PM experiments under FIA conditions using QCR coated with either (Pro-NO)-extracted MIP film or NIP film.[355]
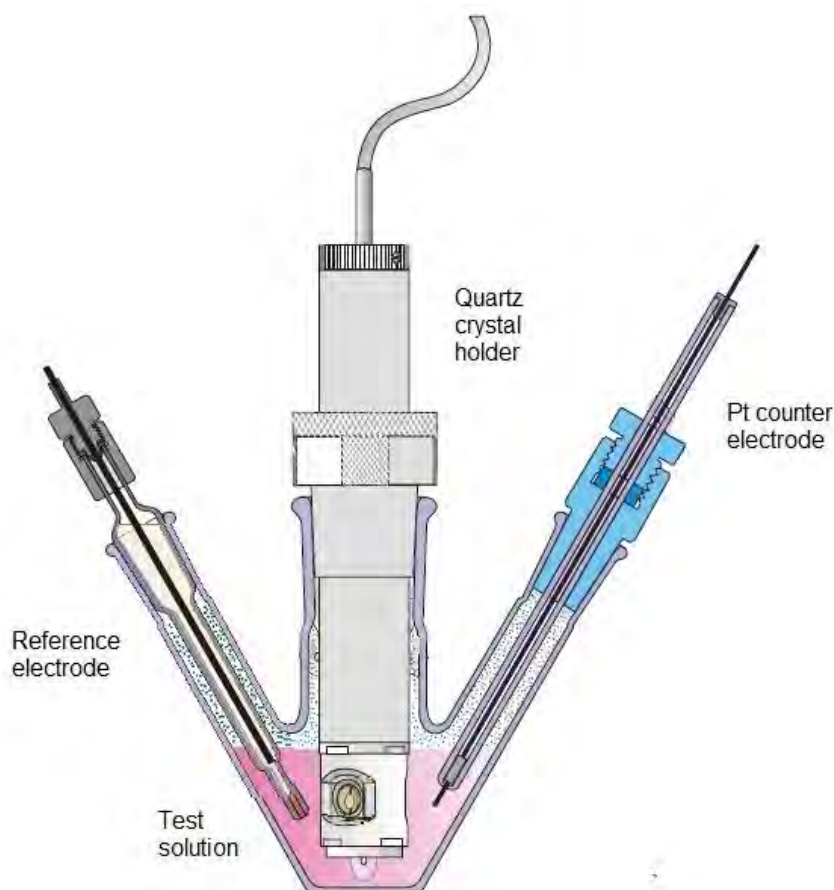
Scheme 2.2-4. Cross-sectional view of the V-shaped electrochemical glass cell for the EQCM holder assembly.

2.2.1.12 *Procedures and instrumentation for MIP and NIP film characterization by surface plasmon resonance (SPR) spectroscopy*

Additionally, SYN-MIP and (SYN-Fc)-MIP-4 films were examined with SPR. For the experiments, the Autolab Esprit instrument, connected to a PGSTAT128N potentiostat/galvanostat and controlled by AUTOLAB SPR Data Acquisition and GPES 4.9 software, all from the same Eco Chemie (Utrecht, The Netherlands) manufacturer, was used. For measurements, (template extracted)-MIP film-coated SPR chip was placed in the cuvette and then filled with the PBS (pH = 7.4) solution. The minimum of resonance was recorded vs. the laser beam angle reflected from the Au surface after injections of the solution of the SYN analyte of different concentrations. The same procedure was applied to the NIP film-coated SPR chips. Measurements were performed at a constant temperature of 20 (±1) °C.

64

2.2.1.13   Determining food toxins in real samples

The Pro-NO was determined in grilled pork neck to confirm that the (Pro-NO)-MIP film chemosensor is an appropriate tool for real sample analysis. For that purpose, the meat was purchased in a local butcher shop, followed by grilling and blending with water. The pork processed that way was mixed with 0.1 M in $K_3[Fe(CN)_6]$ and 0.1 M $K_4[Fe(CN)_6]$ redox probe in the PB (pH = 7.0) solution and then ultrasonicated for 10 min. Afterward, the sample was centrifuged for 15 min. The supernatant was recovered and then spiked with Pro-NO samples of known concentrations. After each Pro-NO sample solution was injected, DPV curves were recorded, and then DPV peaks were normalized against the voltammogram for the lowest analyte concentration. Finally, recovery was determined.

The SYN analyte was determined in a dietary supplement to demonstrate the self-reporting MIP chemosensor applicability for SYN determining in real samples. For that, the SYN-containing product, SYNEPHRINE EXTREME dietary supplement, was purchased from GymBeam s.r.o. Company. Five tablets from the dietary supplement (10 mg SYN each) were grounded in a mortar to a fine powder. Next, 1 mg of this powder was dissolved in 10 mL of methanol, then filtered. A 10 µL sample of the filtrate was diluted with 0.1 M (TBA)ClO$_4$ in acetonitrile, reaching the volume of 10 mL. After that, the DPV signal of the self-reporting MIP chemosensor was recorded for 0.1 M (TBA)ClO$_4$ in acetonitrile and after each addition of a stock solution of SYN. Lastly, recovery values were calculated using the calibration curve constructed.

2.2.2   Procedures and instrumentation for preparation and characterization of chemosensors based on glyphosate-templated MIP nanoparticles (MIP NPs)

2.2.2.1   Computational simulations for the preparation of glyphosate-templated MIP nanoparticles (MIP NPs)

2.2.2.1.1   Sybyl calculations

The Leapfrog algorithm available in Sybyl 7.3 software (Tripos Inc., USA) was applied to the preliminary screening of a library of monomers frequently used for MIP NPs' preparation.[170, 356] Powell's minimization method was used with Tripos force fields and Gasteiger-Hückel charges to minimum energy of 0.0042 kJ mol^{-1}. For an aqueous

environment stimulation, the electric permittivity of 80 was applied. Molecular modeling was performed using an HP Elite-Desk with two Intel Core™ Duo CPU E8400 and 3 GHz processors running on a CentOS Linux 7 operating system. The database included neutral and charged forms of 60 functional monomers. The screening was conducted for 60 000 iterations, searching for possible interactions between the functional monomers and the GLY template. Results were evaluated based on the binding scores.[357]

2.2.2.1.2 DFT calculations

The DFT calculations were carried out using the DFT b3lyp functional with a 6-31g(d) basis set at room temperature. Gaussian 16 software and multicore PC were used to simulate structures of GLY, functional monomers, and their complexes. The input files and the output data visualization were prepared using ChemCraft 1.8 software. The presence of the solvent, DMF, was simulated with the polarizable continuum model (PCM).

2.2.2.2 *General procedure of glyphosate-templated MIP nanoparticles (MIP NPs) synthesis*

The solid-phase synthesis of the MIP NPs used herein involved preparing a template-derivatized solid-phase and synthesizing MIP NPs around these surface-immobilized template molecules by free radical polymerization (Scheme 2.2-5). This procedure was adapted from Canfarotta et al.[358] and Garcia-Cruz et al.[348] and then modified. It is based on the covalent immobilization of the GLY template on a solid support.

Its first step consisted of glass beads' surface activation. That was accomplished by boiling the beads in NaOH to prepare beads bearing $-NH_2$ groups. This activation facilitated subsequent surface silanization by increasing the number of silanol groups.

To more detail, glass beads with a diameter ranging from 70 to 100 μm were boiled in 4.0 M NaOH for 15 min. Next, they were washed with deionized water under a vacuum, then immersed in 10 mM PBS (pH = 7.4) for 5 min. Subsequently, the beads were separated on a Büchner funnel, then washed with deionized water under vacuum until the final pH was between 6 and 8. Afterward, the beads were rinsed with acetone, then dried in an oven for 15 min at 50 °C and then for 2 h at 150 °C.

Subsequently, the activated beads were silanized. For that, the beads were immersed in an anhydrous toluene solution of 3% (*v*/*v*) (3-aminopropyl)triethoxysilane

(APTES) and 2.4% (*v/v*) 1,2-*bis*(triethoxysilyl)ethane (BTSE) to introduce amino groups on their surface. A closed bottle with this mixture was kept overnight at 80 °C. Subsequently, the beads were separated, then rinsed with methanol, and then with acetone, followed by drying in an oven for 15 min at 50 °C and then for 2 h at 150 °C. Next, the beads were analyzed using the dansyl method. Toward that, they were immersed in 1 mg/mL l-dimethylaminonaphthalene-5-sulfonyl chloride (dansyl chloride) in acetonitrile, then kept in the dark for 1 h. Non-silanized beads were treated the same way and used as a control. After this treatment, the beads were washed with acetonitrile, then placed under a UV lamp to check if they were fluorescent, thus evidencing the –NH$_2$ groups' immobilization on their surface.

Then, GLY was immobilized on silanized glass beads by *N*-(3-dimethylaminopropyl)-*N′*-ethylcarbodiimide (ECD) with *N*-hydroxysuccinimide (NHS) coupling. This coupling afforded GLY molecules attachment via their –COOH groups to amino groups on the beads' surface (Scheme 2.2-5). First, GLY was activated by adding ECD (10 mg mL^{-1}, 64 mM) and NHS (15 mg mL^{-1}, 130 mM) to the GLY solution (1 mg mL^{-1}, 5.92 mM) in deionized water. The silanized beads were immersed in PBS (pH = 7.4), then added to the activated GLY solution. Next, the reaction mixture was left for 4 h at room temperature. Finally, the beads were rinsed with water, then dried under a vacuum, and then stored at 4 °C until used for polymerization.
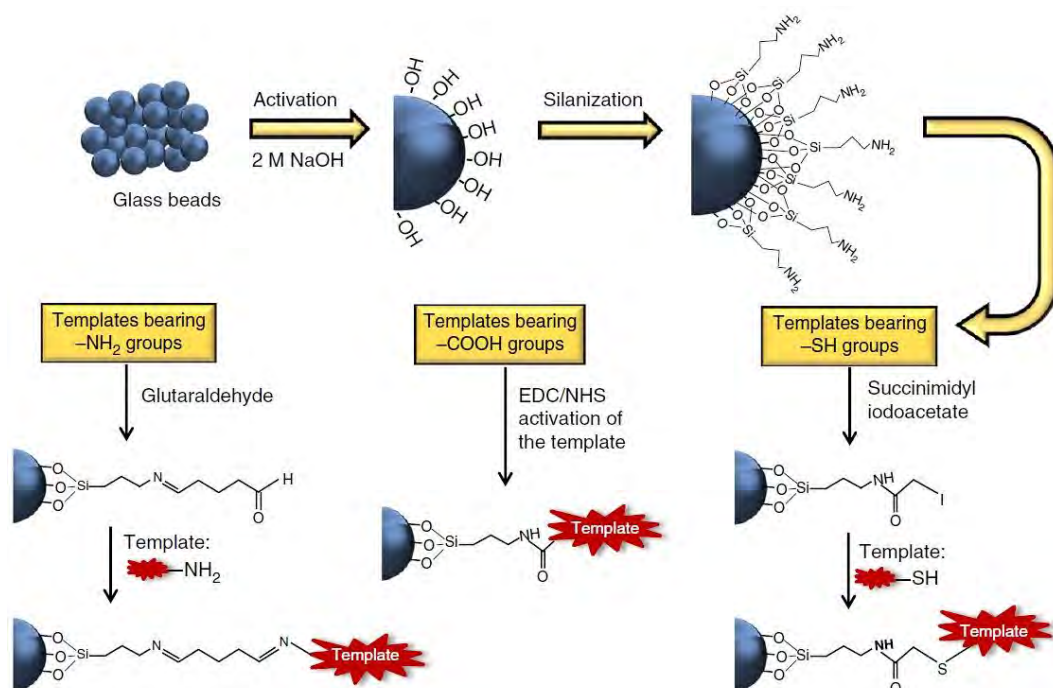
Scheme 2.2-5. The flowchart of template tethering to glass beads for surface immobilizing of common functional groups.[358]

67

Next, polymerization was performed. Because of the small size of imprinted GLY molecules, low number of sites of interaction with the monomers, and possible competitive interaction with water molecules through hydrogen bonding, GLY-MIP NPs were synthesized using an organic solvent. Usually, a pre-polymerization complex in an organic solvent solution contains acrylic and other monomers with functionalities capable of recognizing the template binding sites. EGDMA and trimethylolpropane trimethacrylate (TRIM) are commonly used as cross-linking monomers because their combination leads to polymers with superior recognition capability.[359] Here, *N,N'*-diethyldithiocarbamic acid benzyl ester was applied as the iniferter. That is, it functioned as the initiator, transfer agent, and terminator as well.[360] Moreover, iniferter polymerization enables reasonable particle size and chain length control because it is slower than conventional radical polymerization.[361] Furthermore, a pentaerythritol *tetrakis*(3-mercaptopropionate) chain transfer agent was employed to improve polymerization control. Finally, a polymerizable ferrocene derivative, ferrocenylmethyl methacrylate (FMAA), was added to the pre-polymerization complex mixture as the internal redox probe. Introducing an electroactive ferrocene monomer resulted in the fabrication of a self-reporting electrochemical chemosensor based on electroresponsive MIP NPs. Therefore, MIP NPs were used as both selective recognition units and reporters.[345, 347-349]

Four different pre-polymerization complex mixtures were designed and analyzed to devise a chemosensor based on electroresponsive MIP NPs. All mixtures comprised the same FMAA ferrocene derivative as the redox probe, the same EGDMA and TRIM cross-linking monomers, the same *N,N*-diethyldithiocarbamic acid benzyl ester iniferter, and the same pentaerythritol tetrakis(3-mercaptopropionate) chain transfer agent. Moreover, the following functional monomers were added to the pre-polymerization complex mixtures, including itaconic acid (ITA) in the first one and AAm and ethylene glycol methacrylate phosphate (EGMP) in the second. *N*-Allylurea (AU), 2,2,2-trifluoroethyl methacrylate, and methacrylic acid (MAA) were in the third, and a squaramide-based monomer (SQ6), allylamine (AAm), and hydroxyethyl methacrylate in the fourth. Scheme 2.2-6 compares formulations of all pre-polymerization complex mixtures.
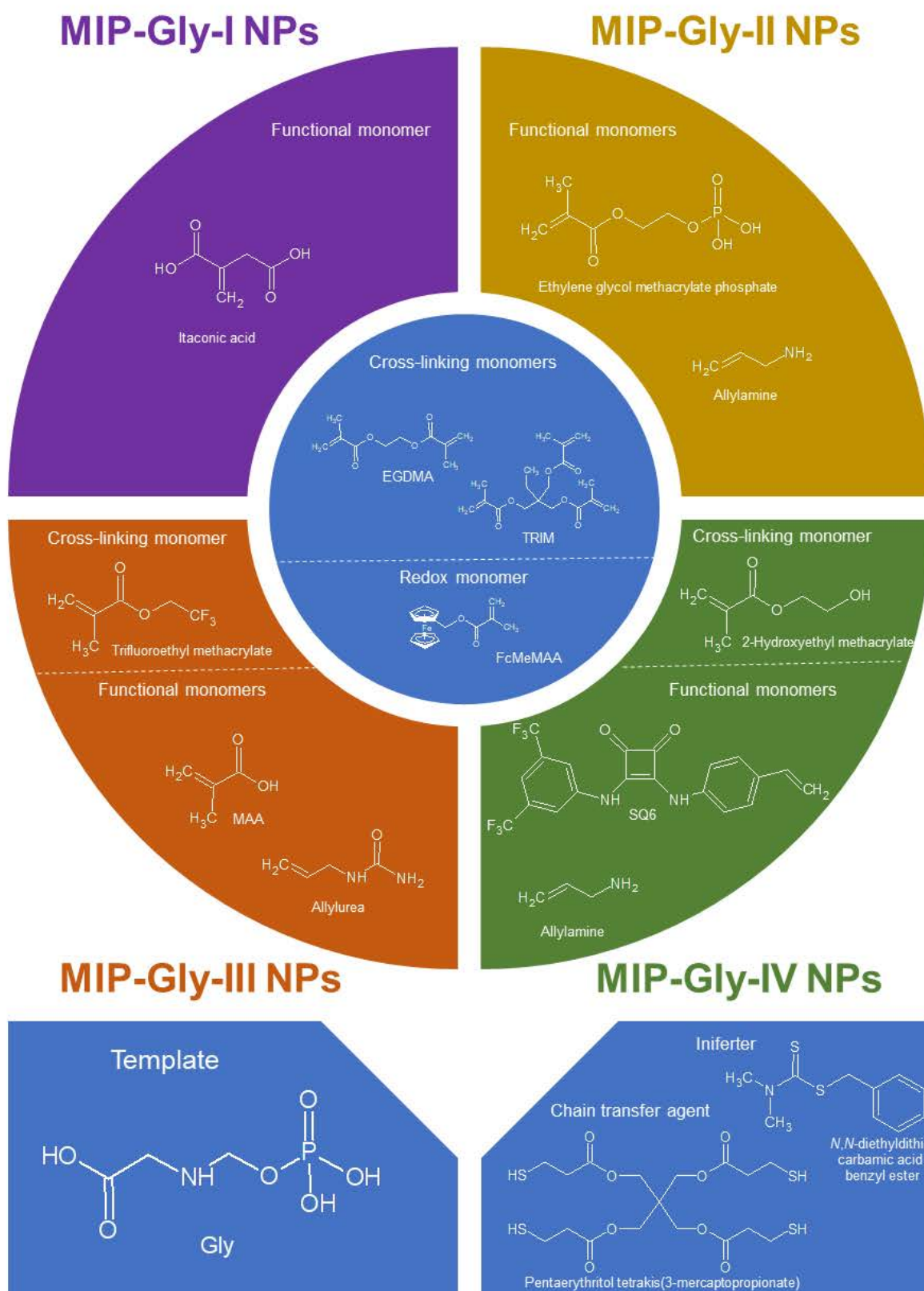
Scheme 2.2-6. Structural formulas of the functional and cross-linking monomers, as well as the GLY template, the iniferter, and the chain transfer agent used to prepare all Gly-MIP NPs.

69

The components of each polymerization were dissolved in dimethylformamide (DMF). The resulting mixtures were placed in vials and purged with a slow stream of nitrogen for 10 min to remove oxygen. Then, GLY-(glass beads) were placed separately in four flat-bottom glass vessels, and all four polymerization mixtures were poured into these vessels. The reactions were initiated by placing the vessels between two UV light sources (Philips model HB/171/A, 4×15 W/cm) for 1 min for the first and second polymerization, as well as 1 min and 20 s for the third and fourth polymerization, under a nitrogen stream.

The final solid-phase MIP NPs synthesis step involved selecting and separating high-affinity MIP NPs. Significantly, the beads also fulfilled the role of an affinity resin to separate high-affinity MIP NPs from unreacted monomers, oligomers, and low-affinity MIP NPs. After the synthesis, the entire content of the vessels was transferred into solid-phase extraction (SPE) cartridges fitted with a 20-μm porosity polyethylene frit. The SPE cartridges were placed in ice baths at 0 °C for 10 min. Then, supernatants were removed using vacuum suction. The solids were washed at a low temperature to eliminate low-affinity MIP NPs and non-polymerized monomers. Toward that, four-bed volumes of DMF at 0 °C, then three volumes of DMF/EtOH, 50 : 50 (v : v) solutions, and then three volumes of EtOH at 0 °C were used. After washing at a low temperature, the SPE cartridges were immersed in baths at 60 °C. Washing the beads at a higher temperature permits the collection of high-affinity MIP NPs because stronger interactions between MIP NPs and the template can be cleaved under these conditions.

High-affinity MIP NPs were collected by washing the solids with ethanol. Subsequently, the eluted MIP NPs were purified by dialysis. For that, 100 mL of the MIP NPs suspensions in EtOH were concentrated to 10 mL and then diluted 10 times with deionized water. The MIP NPs were purified using SnakeSkin dialysis membrane tubing (Spectra/Por 7, regenerated cellulose, 10 kDa MWCO, 11 cm tubing length, 32 mm flat width, 20.4 mm diameter, 3.3 mL cm^{-1}). The MIP NPs suspensions were dialyzed for 8 h, and the water was changed every 2 h. The resulting high-affinity MIP NPs were stored at 4 °C, then used to modify the screen-printed Pt electrodes (SPPtEs).

2.2.2.3 General procedure for electrode functionalizing with MIP NPs for determining glyphosate

Synthesized MIP NPs were covalently immobilized on SPPtEs. For that, SPPtEs were cleaned in isopropanol, then in deionized water. Next, the electrodes' surfaces were

activated using argon plasma for 10 min. Afterward, SPPtEs were immersed in a solution of 5% water in ethanol with 6% (*v/v*) either (3-aminopropyl)triethoxysilane (APTES) or *N*-(2-aminoethyl)-3-aminopropyltrimethoxysilane (AAPS) for 1 h. Finally, electrodes were rinsed with ethanol, then heated in the oven at 120 °C for 30 min.

ECD and NHS were used to immobilize MIP NPs bearing –COOH groups (MIP NPs-1 obtained from the first synthesis) on the surfaces of electrodes. To this end, the ECD and NHS ethanol solutions were mixed with high-affinity GLY-MIP NPs and left for 10 min. Subsequently, the solution was deposited on the surfaces of silanized SPPtEs, then left overnight. Next, the electrodes were rinsed with deionized water and stored at room temperature in the dark for further use.

For MIP NPs bearing –NH₂ groups (MIP NPs-2, -3, and -4, obtained from the second, third, and fourth synthesis, respectively) immobilizing on SPPtEs, silanized SPPtEs were immersed in a solution of 10% glutaraldehyde in PBS (pH = 7.4) for 1 h, and then the electrodes were rinsed with deionized water. Subsequently, high-affinity MIP NPs were deposited onto the surfaces of electrodes and left for 1 h. Next, MIP NPs-coated SPPtEs were rinsed with water, then immersed in 0.1 mM ethanolamine solution of PBS (pH = 7.4) for 15 min to block unreacted groups. Afterward, SPPtEs were rinsed with water, and a sodium cyanoborohydride solution was drop-cast on the surfaces of electrodes, then left for 20 min (Scheme 2.2-7). Finally, SPPtEs were rinsed with deionized water and stored at room temperature in the dark for the next step.
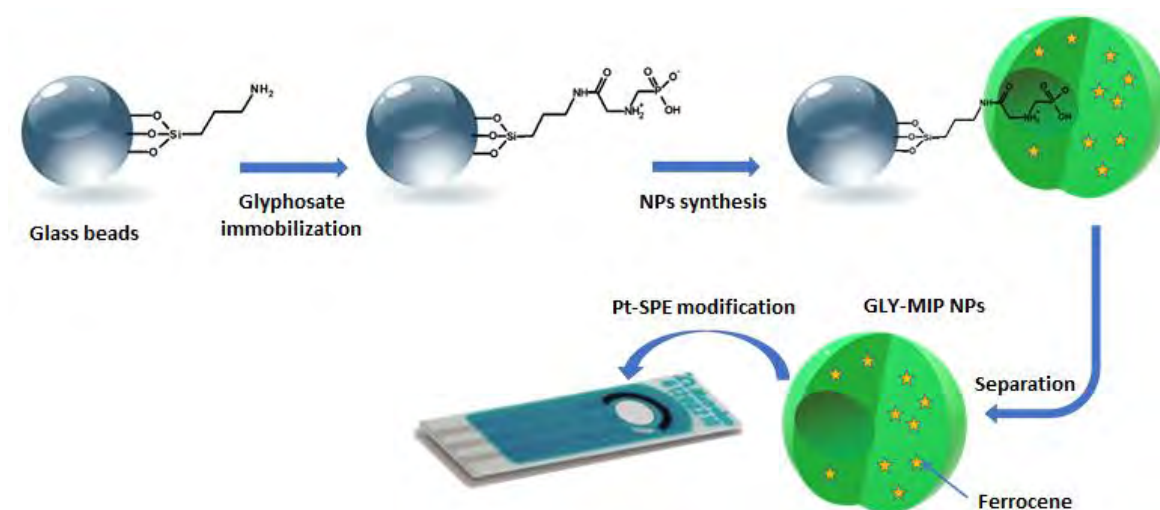
Scheme 2.2-7. A flowchart of the MIP NPs synthesis, then elution, followed by their immobilization on the screen-printed platinum electrode (SPPtE) surface using insulin as a model template.[348]

2.2.2.4   Optimizing electrode modification conditions

Most parameters of the electrode modification with MIP NPs, including silane concentration, MIP NPs immobilization time, and concentration, were the same as in the previous report.[349]   Additionally, two silanes, vis., (3-aminopropyl)triethoxysilane (APTES) and *N*-(2-aminoethyl)-3-aminopropyltrimethoxysilane (AAPS), used for the electrodes' silanization were tested in DPV measurements. The chemosensors prepared using either APTES or AAPS were examined by comparing their DPV peaks for different concentrations of GLY in 10 mM PBS (pH = 7.4).

2.2.2.5   Electrochemical characterizing the MIP NPs chemosensor

DPV and EIS were used to characterize the chemosensor, in 10 mM PBS (pH = 7.4), at each step of its fabrication. DPV measurements were carried out in a range of −0.25 V to 0.80 V vs. Ag quasi-reference electrode. Moreover, the EIS spectra in the range of 10 MHz to 100 mHz at 0.10 V vs. Ag quasi-reference electrode were recorded.

2.2.2.6   Analytical performance of MIP NPs chemosensors

After the electrode surface coating with MIP NPs, all four MIP NPs chemosensors in 10 mM PBS (pH = 7.4) were tested with DPV in a range of −0.25 V to 0.8 V vs. Ag quasi-reference electrode. GLY samples were drop-cast on the surface of SPPtEs coated with MIP NPs, and DPV measurements were trice repeated for each GLY concentration.

2.2.2.7   Preparation of real water samples

Water samples were collected from a river near farmland located close to Warsaw, Poland. First, 2 mL of this water was filtered by syringe with a PTFE microfiltration membrane (pore diameter of 0.45 μm, 25-mm diameter, at 87 psi) of Corning, Inc. Then, 100 μL of the filtered sample was diluted with PBS (pH = 7.4) to a volume of 10 mL. Finally, the samples were spiked with the GLY stock solution, resulting in GLY concentrations in the 0.05 to 100 nM range. GLY was determined using DPV in a potential range of −0.15 V to 0.55 V vs. Ag quasi-reference electrode.

2.2.2.8 *Instrumentation and procedures for characterizing GLY-MIP NPs*

2.2.2.8.1 Dynamic light scattering (DLS) analysis

The dynamic light scattering (DLS) measurements were performed to determine the size of the MIP NPs synthesized. Experiments were carried out with Zetasizer Nano (Nano-S) particle-size analyzer from Malvern Instrument Ltd. Before each measurement, the MIP NPs stock ethanol solution was vortexed for 20 min, then ultrasonicated for 5 min and then analyzed at 25 °C by DLS using a disposable polystyrene cuvette. The instrument automatically selected the duration of the measurement and the number of runs. As a dimensionless measure of particles' size distribution, the *Z*-average hydrodynamic diameter of nanoparticles and the polydispersity index (PdI) were calculated from the cumulants analysis. The values were recorded as an average of at least three measurements.

2.2.2.8.2 Scanning electron microscopy (SEM) imaging

GLY-MIP NPs were imaged with SEM using a Nova NanoSEM 450 microscope of the FEI Nova.

2.2.2.8.3 X-ray photoelectron spectroscopy (XPS)

The elemental composition of MIP NPs' surfaces was determined using XPS. The XPS spectra were recorded with monochromatic Al Kα ($h\nu$ = 1486.4 eV) radiation using a PHI 5000 Versa Probe-Scanning ESCA Microprobe instrument (ULVAC-PHI). The background was subtracted using the Shirley method, and peaks were fitted with (Gaussian-Lorentzian)-shaped profiles. The electron binding energy (*BE*) of the C 1s peak with *BE* = 284.6 eV was chosen as the internal *BE* reference. The XPS spectra were analyzed with CASA XPS software.

2.2.2.9 *Instrumentation and procedures for electrochemical determining glyphosate with MIP NPs chemosensors*

SPPtEs' surfaces were cleaned and activated using a Zepto model plasma cleaner (100 W) from Diener Electronic.

All electrochemical measurements were carried out using PalmSens4 potentiostat from PalmSens, controlled by PSTrace Version 5.7 software of the same manufacturer. Experiments were performed using Drop-Sense SPPtEs (C550) with dimensions of 33 × 10 × 0.5 mm (length × width × height). The SPPtE consisted of a 4-mm diameter

platinum working electrode, platinum film auxiliary electrode, and silver film quasi-reference electrode.

In the DPV measurements, the potential was scanned from −0.25 to 0.80 V vs. Ag quasi-reference electrode, with a potential step of 5 mV and a pulse duration of 100 ms. The amplitude of 7-ms width pulses applied was 25 mV.

The EIS experiments used an alternating current (ac) excitation signal in the frequency range of 10 MHz to 100 mHz and 10-mV sinusoidal amplitude at 0.1 V vs. Ag quasi-reference electrode.

2.3 Experimental techniques

This subchapter describes the principles of experimental techniques for devising and testing selective chemosensors for chosen toxins.

2.3.1 Cyclic voltammetry (CV) Cyclic voltammetry (CV) is one of the main electroanalytical techniques commonly used to study the electrooxidation and electroreduction of organic and inorganic compounds, their adsorption on electrodes, and the mechanism and kinetics of electrochemical reactions. Moreover, it is employed to analyze (electron transfer)-initiated chemical reactions. CV is often the first-choice technique applied to investigate a new system, beneficial for evaluating mechanisms of reactions. The current is measured as a function of the potential applied to the working electrode against the reference electrode. This potential is linearly changed with time from the initial potential, E_i, through the vertex potential, E_v, to the final potential, equal to the initial potential (Scheme 2.3-1).

Considering the model system of the electroreduction of oxidized species (Ox) to its reduced form (Red), where both are soluble, and only Ox is initially present in the solution (Equation 2.3-1), the equilibrium between these two species is described by the Nernst equation (Equation 2.3.2) if this redox system is reversible. It relates the potential of the working electrode, E, to the formal potential of the redox reaction, E_f^0, and the concentrations of the Ox, c_{ox}, and Red, c_{red}, in the system at equilibrium.

$$Ox + e^- \leftrightarrows Red \qquad \text{(Equation 2.3-1)}$$

$$E = E_f^0 + \frac{RT}{F}\ln\frac{c_{ox}}{c_{red}} = E_f^0 + 2.3026\,\frac{RT}{F}\log\frac{c_{ox}}{c_{red}} \qquad \text{(Equation 2.3-2)}$$

74

where R is the ideal gas constant, T is the absolute temperature, and F stands for the Faraday constant. The Nernst equation predicts the system's response to redox species' concentration change in solution or the electrode potential applied.
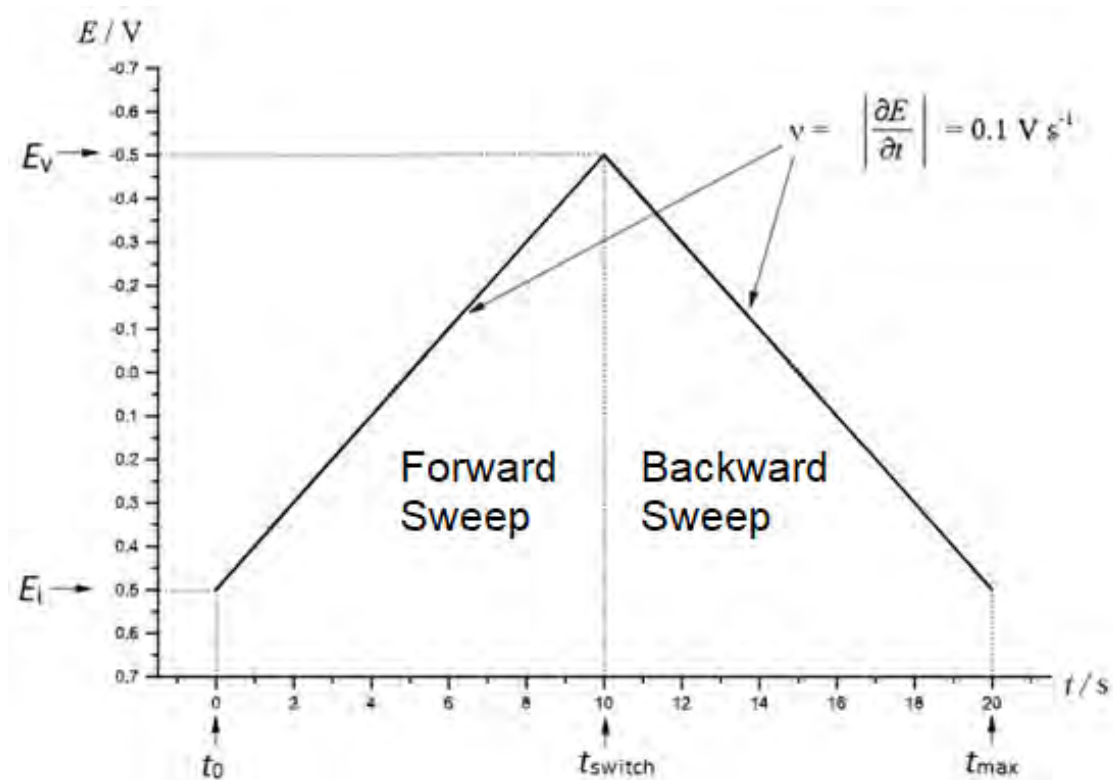
Scheme 2.3-1. The potential change with time in cyclic voltammetry. In this case, the initial potential, E_i, is set at 0.5 V, the vertex potential, E_v, is −0.5 V, and the scan rate, v, is 0.1 V s^{-1}.[362]

For the one-electron diffusion-controlled system, e.g., ferrocenium (Fc$^+$) and ferrocene (Fc), a typical cyclic voltammogram recorded at an inert planar electrode and the concentration-distance profiles for Fc$^+$ and Fc for selected points at the voltammogram, are presented in Scheme 2.3-2.

Importantly, the concentrations of ferrocenium vs. ferrocene in relation to the distance from the electrode surface depend on the applied potential changes with time and species transport (diffusion) between the electrode surface and the bulk solution. Thus, the shape of the voltammogram originates from the evolution of these concentration profiles resulting from the potential sweep and a planar diffusion. According to Fick's first law of diffusion, the current is proportional to the species' concentration gradient at the electrode surface. Scanning the system toward negative potentials from point A to D causes consumption of Fc$^+$ at the electrode, resulting in its reduction to Fc. That

generates a reduction current in the voltammogram (Scheme 2.3-2h). At point C, where the cathodic peak current (I_{pc}) appears, the rate of diffusional delivery of additional Fc^+ from the bulk solution governs the current. Upon scanning in the negative direction from point C to D, the rate of diffusion of Fc^+ from the bulk solution to the electrode surface becomes slower, leading to the current decrease. When point D of potential switching is reached, the scan direction is opposite, and the potential is scanned positively. While the concentration of Fc^+ at the electrode surface was depleted, the concentration of Fc at the electrode surface increased, satisfying the Nernst equation. Scanning the potential positively from point D to G leads to the regeneration of the Fc^+ by oxidation of Fc, and then the oxidation current at the voltammogram is recorded. At points B and E, the concentrations of Fc^+ and Fc at the electrode surface are equal. Following the Nernst equation, at these points $E = E_f^0$, which means that the potential, E, equals the average potential of the cathodic and anodic peaks.
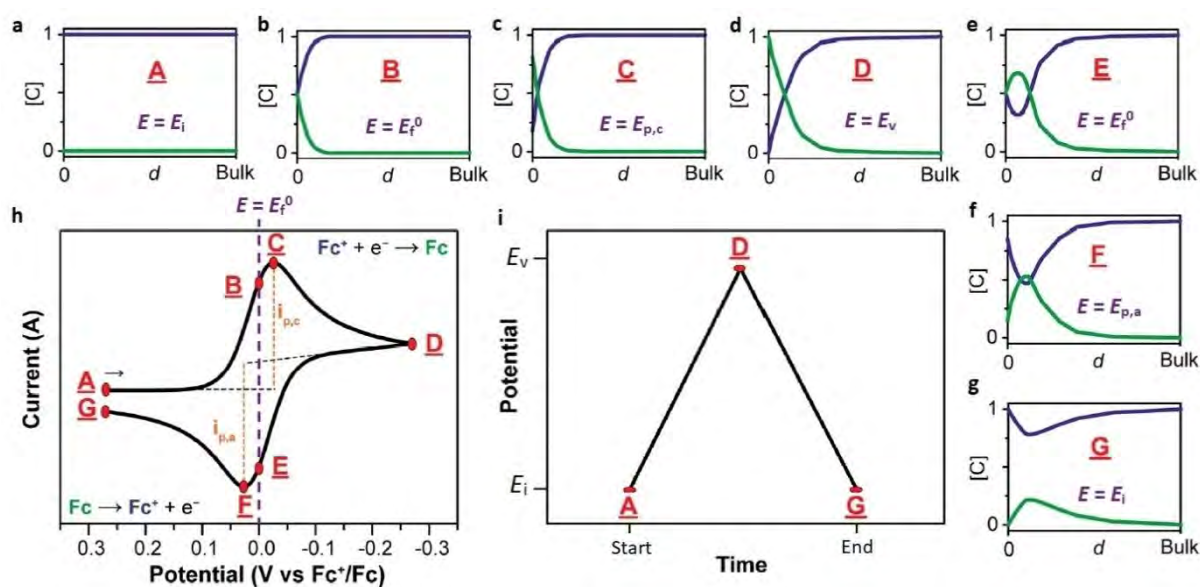
Scheme 2.3-2. (a−g) Concentration profiles for (blue curves) ferrocenium and (green curves) ferrocene as a function of the distance from the electrode surface to the bulk solution, d, for selected points at the voltammogram. (h) Cyclic voltammogram recorded for the reversible Fc^+/Fc electrode reaction. (i) Applied potential as a function of time for typical CV measurement with the initial, vertex, and end potentials defined as A, D, and G, respectively.[362]

One of the voltammogram's main features is the peak height. For a reversible redox couple, the peak current is described by the Randles-Ševčik equation (Equation 2.3-3).[363]

76

$$I_p = 0.4463nFAc \left(\frac{nFvD}{RT} \right)^{1/2} \qquad \text{(Equation 2.3-3)}$$

This equation linearly relates the peak current, I_p, to the square root of the scan rate, v. In this equation, n is the number of electrons transferred in the redox event, A stands for the electrode surface area, usually treated as the projected surface area, D, and c is the diffusion coefficient and the bulk concentration of the electroactive species.

The system is considered reversible if it meets the following criteria:

$$I_p \propto v^{1/2} \qquad \text{(Equation 2.3-4)}$$

$$\Delta E_p = E_{pa} - E_{pc} = \frac{59}{n} \text{ mV at } T = 298 \text{ K} \qquad \text{(Equation 2.3-5)}$$

$$\left| E_p - E_{p/2} \right| = \frac{59}{n} \text{ mV at } T = 298 \text{ K} \qquad \text{(Equation 2.3-6)}$$

$$\left| \frac{I_{pa}}{I_{pc}} \right| = 1 \text{ for } D_{Ox} = D_{Red} \qquad \text{(Equation 2.3-7)}$$

where E_{pa} and E_{pc} represent the potential of the anodic and cathodic peak, respectively, ΔE_p stands for the difference between the anodic and cathodic peak potentials, E_p is the peak potential, $E_{p/2}$ represents the potential where the current is at a half-peak height, I_{pa} and I_{pc} denote the current of the anodic and cathodic peak, and D_O and D_R signifies the diffusion coefficient of the oxidized and reduced redox species, respectively. Moreover, the peak potential should be independent of the scan rate.

For a quasi-reversible system, the diffusion rate is comparable to the electron transfer rate, and the peaks' separation is higher than for the reversible system (curve b in Scheme 2.3-3). For an irreversible system, i.e., controlled by the electron transfer rate, the peak separation is even higher than for a quasi-reversible process (curves c–d in Scheme 2.3-3), or the peak in the backward scan disappears for a very low rate of electron transfer. Moreover, E_p shifts to higher overpotentials as the scan rate increases.

For an irreversible electrode reaction, the peak current at a planar electrode at 298 K is described by Equation 2.3-8.[363]

$$I_p = 2.99 \times 10^5 \alpha^{1/2} n^{3/2} AD^{1/2} c v^{1/2} \qquad \text{(Equation 2.3-8)}$$

where α is the charge transfer coefficient; its value can be determined from the slope of the linear dependence of the I_p on $v^{1/2}$.

The charge transfer coefficient can also be determined from Equation 2.3-9.

$$\alpha = \frac{47.7}{|E_p - E_{p/2}|} \text{ mV at } T = 298 \text{ K} \qquad \text{(Equation 2.3-9)}$$
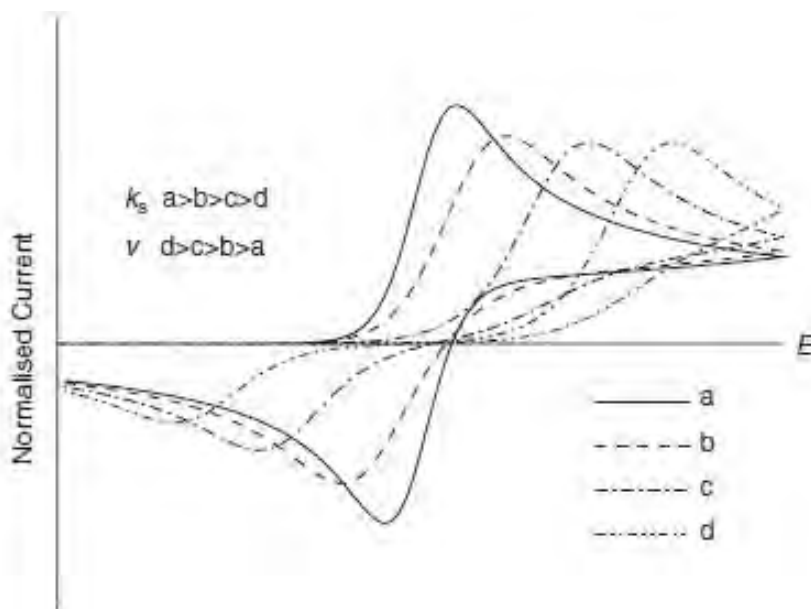
Scheme 2.3-3. Cyclic voltammograms under the electrode reaction rate control. (a) Voltammogram for the diffusion rate of the electroactive species to the electrode surface lower than the electron transfer rate. (b–d) Voltammograms for the diffusion rate increasingly larger than the electron transfer rate. k_s is the standard electron transfer rate constant, and v is the potential scan rate.[363]

Furthermore, an electroactive reactant and/or a product can adsorb on the electrode surface. A voltammogram typical for a reversible redox process with oxidized and reduced species adsorbed on the electrode surface is depicted in Scheme 2.3-4. Its shape is characteristic of an ideal Nernstian electron transfer with the Langmuir isotherm describing the adsorption. Since all the adsorbed species are being reduced/oxidized, two symmetrical peaks with equal charges for oxidation and reduction are produced in the voltammogram.

Then, the peak current is defined by Equation 2.3-10:

$$I_p = \frac{n^2 F^2}{4RT} v A \Gamma_o^* \qquad \text{(Equation 2.3-10)}$$

where Γ_o^* represents maximum electrode coverage with the oxidized species.

78
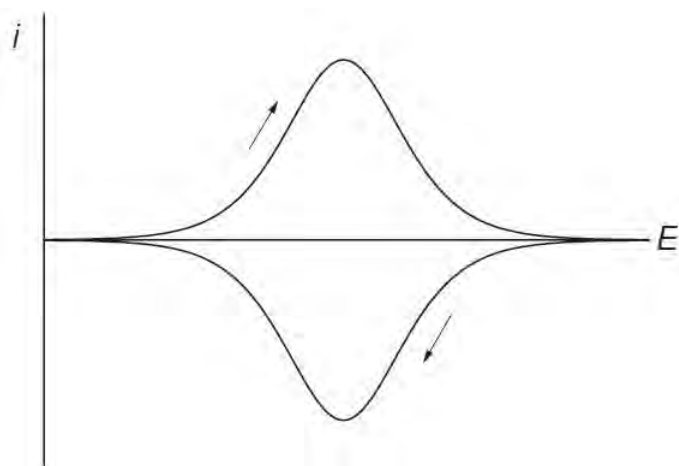
Scheme 2.3-4. The cyclic voltammogram for the reversible electrode process with oxidized and reduced species adsorbed on the electrode surface.[363]

CV is often used to study electron transfer-related chemical reactions. It is less useful for analytical purposes because the undesired capacity current interferes with the faradaic current proportional to the redox analyte concentration.

2.3.2 Differential pulse voltammetry (DPV)

Pulsed techniques, including DPV, were developed to improve the determination sensitivity. In these techniques, the capacity current is largely eliminated, thus improving the signal-to-noise ratio, hence, sensitivity.

In the DPV technique, currents are measured just before applying the pulse, $I(1)$, and just before the end of the pulse, $I(2)$. Near the end of the pulse, the capacity current originating from the charging of the electric double layer is negligible. Pulses of constant height, usually of the 10 to 100 mV amplitude, are superimposed on the base potential, which increases in a linear or staircase manner (Scheme 2.3-5a). The pulse width is at least ten times shorter than the period of the staircase waveform. The pulse duration is generally chosen from the 5 to 100 ms range.[364] The measured current difference is plotted against the staircase potential applied, resulting in a peak-shaped voltammogram (Scheme 2.3-5b). Importantly, the potential of the DPV peak for a reversible system is described by Equation 2.3-11.[365]

$$E_\mathrm{p} = E_{1/2} - \frac{\Delta E}{2}$$
(Equation 2.3-11)

where E_p is the peak potential, $E_{1/2}$ is the half-wave potential, and ΔE stands for the pulse amplitude.

79

The E_p differs from the $E_{1/2}$ for fast kinetics since the current is plotted as a function of the base potential, not as a function of the potential halfway up the pulse.
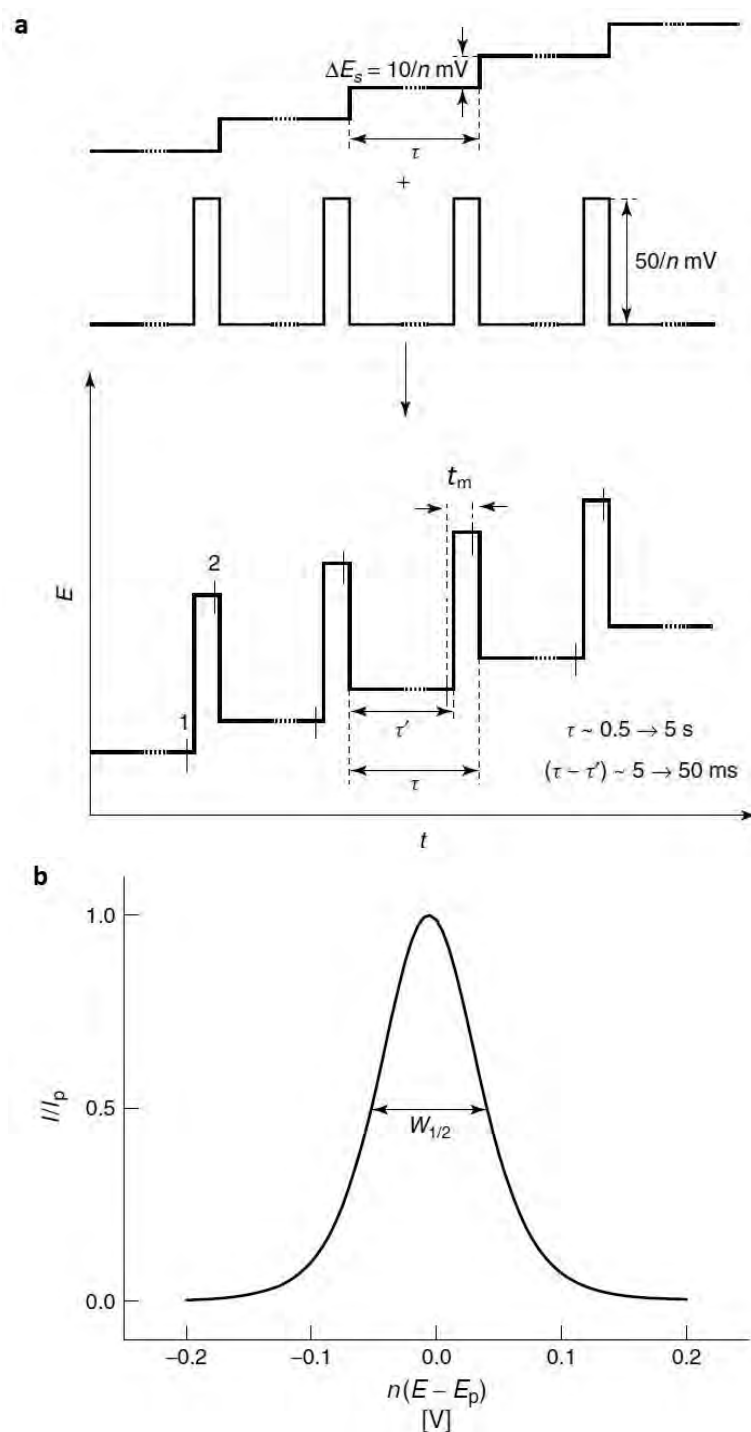
Scheme 2.3-5. (a) Potential-time waveform resulting from superimposing pulses on a staircase waveform and (b) schematic differential pulse voltammogram originating from the plot of the difference between two sampled currents and staircase potential. ΔE_s is the potential step height, τ is the staircase period, τ' stands for the step width, and $W_{1/2}$ is the peak width at its half height.[365]

The DPV peak current, I_p, is defined by the following equation:[365]

$$I_p = -\frac{nFAD^{1/2}c}{(\pi t_m)^{1/2}}\left(\frac{1-\sigma}{1+\sigma}\right) \hspace{2cm} \text{(Equation 2.3-12)}$$

where t_m is the sampling time after pulse application (pulse duration), whereas σ can be calculated as

$$\sigma = \exp\left(\frac{nF}{RT}\frac{\Delta E}{2}\right) \hspace{2cm} \text{(Equation 2.3-13)}$$

The DPV peak is also characterized by its width at half height, $W_{1/2}$:[364]

$$W_{1/2} = \frac{3.52RT}{nF} \hspace{2cm} \text{(Equation 2.3-14)}$$

As can be seen from Equation 2.3-14, $W_{1/2}$ depends on the number of electrons transferred in the electrode process. At 298 K, $W_{1/2}$ equals $\frac{90.4}{n}$ mV. Moreover, the DPV peak height decreases, and its width increases if the system becomes more irreversible as the difference between $E_{1/2}$ for a reversible system and E_p increases.

2.3.3 Electrochemical impedance spectroscopy (EIS)

Electrochemical impedance spectroscopy (EIS) is one of the most complex electrochemical techniques used to study the nature of electrochemical processes. This technique is frequently applied to examine electrochemical mechanisms regarding the corrosion of metals and alloys, as well as batteries and sensors characterization. In contrast to most electrochemical techniques, the frequency-dependent ac potential is used in EIS, in which direct current (dc) constant potential is applied. An alternating voltage of small amplitude, usually 10–20 mV, is applied to the working electrode to obtain a pseudo-linear relationship between current and potential. This potential is defined by Equation 2.3-15:

$$E(t) = E_0 \sin(\omega t) \hspace{2cm} \text{(Equation 2.3-15)}$$

where E_0 stands for the potential amplitude, $\omega = 2\pi f$ is the angular frequency of the alternating voltage applied, and t is the time.

In consequence, the current signal is generated. Typically, it is shifted by the phase angle, φ, against the potential, as shown by Equation 2.3-16.

$$I(t) = I_0 \sin(\omega t + \varphi) \qquad \text{(Equation 2.3-16)}$$

where I_0 is the current amplitude. The sinusoidal potential and current dependence on time at a 20 Hz frequency, f, is presented in Scheme 2.3-6a. The result of plotting the output signal as a function of the input signal at a given frequency graph is called a Lissajous plot (Scheme 2.3-6b).
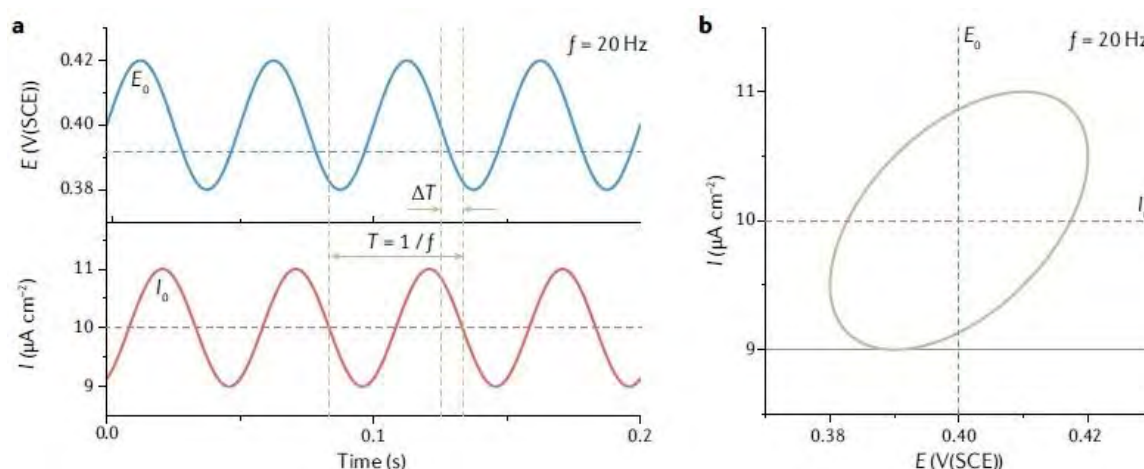
Scheme 2.3-6. (a) Sinusoidal potential (blue curve) and current density (red curve) change with time at a frequency, f, of 20 Hz, and (b) Lissajous plot constructed from these results.[366]

Repeating the measurement for a given frequency range enables the construction of the electrochemical impedance spectrum. The equation for impedance, Z, is analogous to Ohm's law, which is applied to dc measurements. Thus, the impedance of the system is defined as:

$$Z = \frac{E(t)}{I(t)} = \frac{E_0 \sin(\omega t)}{I_0 \sin(\omega t + \varphi)} = |Z| \frac{\sin(\omega t)}{\sin(\omega t + \varphi)} \qquad \text{(Equation 2.3-17)}$$

where $|Z|$ stands for the magnitude of impedance.

The impedance can also be represented as a complex function. Then, the potential is defined as:

$$E(t) = E_0 \exp(j\omega t) \qquad \text{(Equation 2.3-18)}$$

and the current is described as:

$$I(t) = I_0 \exp(j\omega t - \varphi) \qquad \text{(Equation 2.3-19)}$$

where $j = \sqrt{-1}$ is the imaginary unit.

Therefore, the impedance is then expressed as:

$$Z = \frac{E(t)}{I(t)} = \frac{E_0 \exp(j\omega t)}{I_0 \exp(j\omega t - \varphi)} = |Z| \exp(j\varphi) = |Z|(\cos\varphi + j\sin\varphi) \qquad \text{(Equation 2.3-20)}$$

Moreover, impedance can be expressed in the complex plane as:

$$Z = Z_{\text{real}} - jZ_{\text{im}} \qquad \text{(Equation 2.3-21)}$$

where Z_{real} and Z_{im} are the real and imaginary components of Z, respectively.

The magnitude of impedance can be described as the vector sum of Z_{real} and Z_{im}:

$$|Z| = \sqrt{Z_{\text{real}}^2 - jZ_{\text{im}}^2} \qquad \text{(Equation 2.3-22)}$$

Physically, Z_{real} is a frequency-dependent resistance defined as:

$$Z_{\text{real}} = |Z|\cos\varphi \qquad \text{(Equation 2.3-23)}$$

while Z_{im} is a frequency-dependent reactance defined as:

$$Z_{\text{im}} = |Z|\sin\varphi \qquad \text{(Equation 2.3-24)}$$

The most commonly used graphical EIS data representations are Nyquist and Bode plots. The Nyquist plot is constructed by plotting $-Z_{\text{im}}$ against Z_{real}. A typical Nyquist plot is shown in Scheme 2.3-7a. In the Bode plot, $\log|Z|$ and φ are plotted versus frequency, which can help analyze the capacitive or inductive effects of electrochemical systems.[296] A typical Bode plot is depicted in Scheme 2.3-7b. The phase angle, φ, generally tends towards 0° at high frequency because of the ohmic electrolyte resistance, R_s, (blue squares Scheme 2.3-7b). The phase angle φ is then adjusted according to R_s, asymptotically approaching $-90°$ in a high-frequency range for the ideally polarizable electrode (red dots in Scheme 2.3-7b).

83
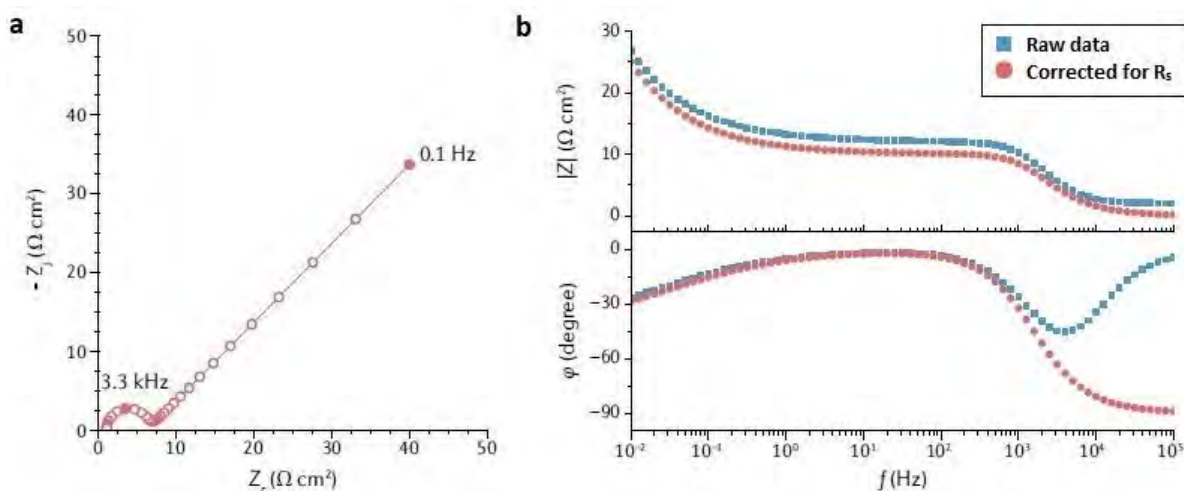
Scheme 2.3-7. EIS data of an ideally polarizable electrode for a redox couple in solution represented by (a) the Nyquist plot, in which the imaginary impedance component, Z_j, is plotted against the real impedance component, Z_r, in a complex plane with frequency as a parameter and (b) the Bode plot where the phase angle, φ, and modulus of impedance, $|Z|$, are plotted against frequency, f.[366]

EIS measurements can be performed to analyze complex electrochemical systems. For that, equivalent electrical circuits involving passive electrical elements, including resistors, inductors, and capacitors, are constructed. The essential electrical components of equivalent circuits and the equations describing their impedances are as follows:

$$Z_R = R \qquad \text{(Equation 2.3-25)}$$

$$Z_C = \frac{1}{j\omega C} = -\frac{j}{\omega C} \qquad \text{(Equation 2.3-26)}$$

$$Z_L = j\omega L \qquad \text{(Equation 2.3-27)}$$

where R, C, and L are the resistance, capacitance, and inductance, respectively.

Typical Nyquist plots for different equivalent circuits are shown in Scheme 2.3-8. Suppose a sinusoidal voltage is applied to a pure resistor of the R resistance value. In that case, impedance can be calculated according to Equation 2.3-25, and the phase angle is equal to 0 for all frequencies (Scheme 2.3-8a). If a sinusoidal voltage is applied across a pure capacitor, the impedance depends on the frequency and is entirely imaginary (Scheme 2.3-8b). This impedance is determined according to Equation 2.3-26. The total impedance for the resistor and capacitor in series can be calculated according to Equation 2.3-28, whereas the total impedance for the resistor and capacitor in parallel is described by Equation 2.3-29.

84

$$Z = R - \frac{j}{\omega C} \qquad \text{(Equation 2.3-28)}$$

$$Z = \left(\frac{1}{R} - \frac{\omega C}{j}\right)^{-1} \qquad \text{(Equation 2.3-29)}$$

The Nyquist plots for the resistor and capacitor in series and parallel are shown in Scheme 2.3-8c and 2.3-8d, respectively.
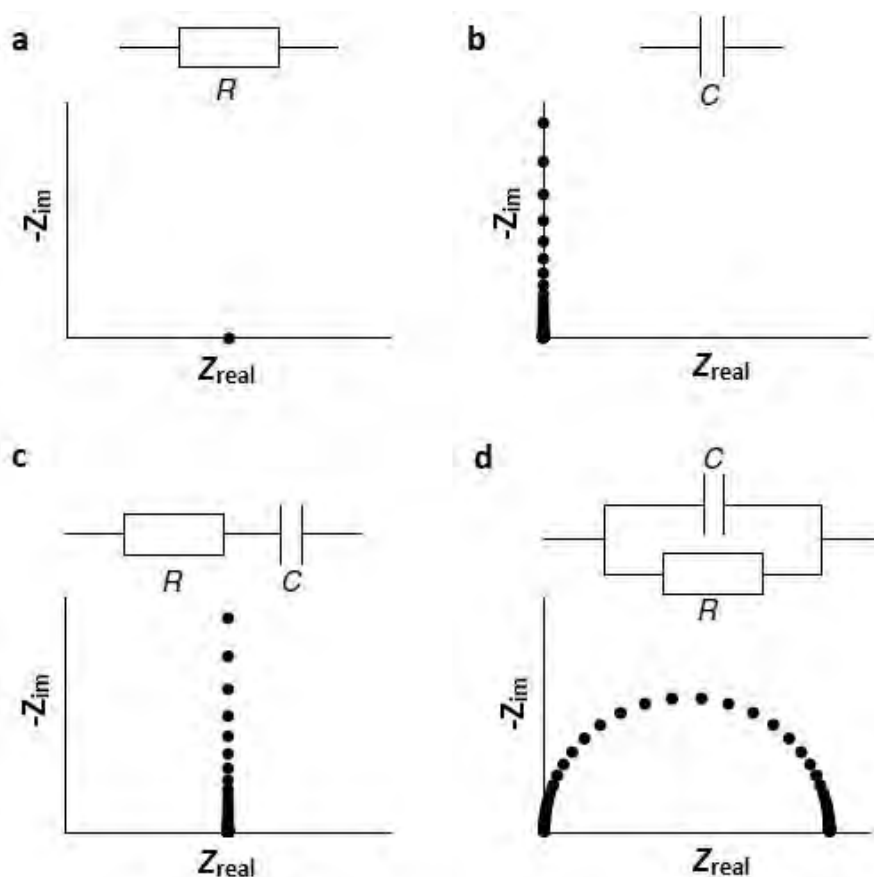
Scheme 2.3-8. Nyquist plots for (a) resistance R, (b) capacitance C, (c) resistance and capacitance in series, and (d) resistance and capacitance in parallel.[365]

A sketch of a simple conventional electrochemical cell where a working electrode is immersed in an electrolyte solution of a redox couple is shown in Scheme 2.3-9. A positive potential is applied to the working electrode, which attracts anions to the electrode surface. That leads to forming the electrochemical double-layer, i.e., a capacitor type at the electrode-solution interface. Each component in the equivalent circuit describes corresponding activity in the electrochemical cell, such as resistance of electrolyte solution, R_s, which should be included in modeling a circuit, electrochemical double-layer capacitance, C_{dl}, and R_{ct}.
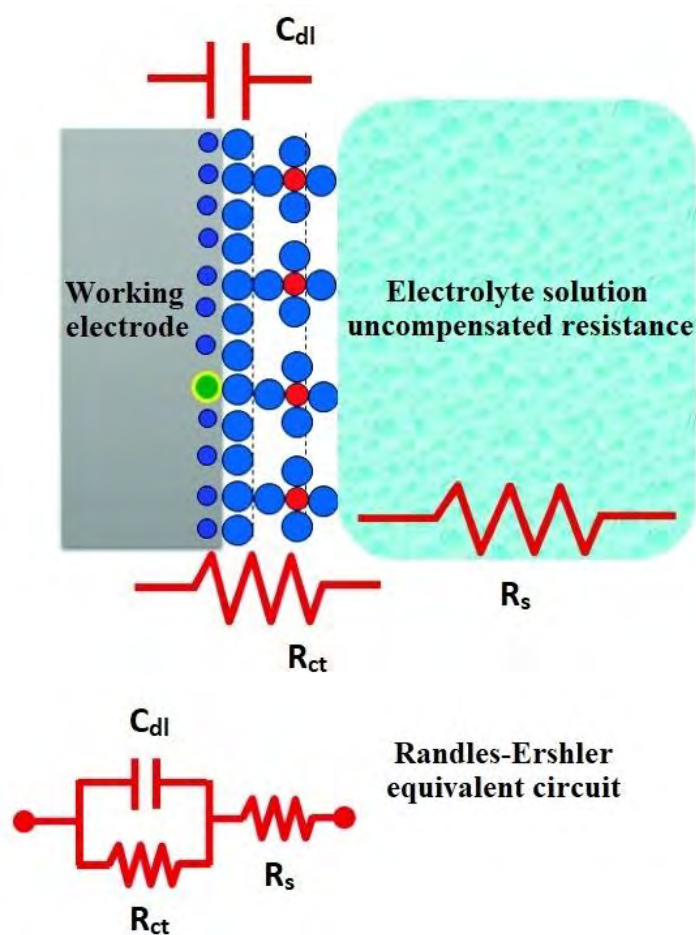
Scheme 2.3-9. A depiction of the electrochemical system described by the Randles-Ershler electric equivalent circuit. C_{dl} stands for the capacitance of the electrical double layer, R_{ct} is the charge transfer resistance, and R_s is the electrolyte solution resistance.[367]

For analyzing electrochemical systems embracing the working electrode coated with a porous polymer film, a modified Randles-Ershler equivalent circuit is often applied (Scheme 2.3-10). In this circuit, a constant phase element, CPE, is frequently used instead of the double-layer capacitance, C_{dl}, because the polymer film does not behave like an ideal capacitor. Thus, a real component of impedance does not equal zero. The impedance of CPE, Z_{CPE}, is defined by Equation 2.3-30.

$$Z_{CPE} = \frac{1}{(j\omega)^{\phi}T'}$$ (Equation 2.3-30)

where ϕ is an exponent with values of $0 \leq \phi \leq 1$. If ϕ equals 1, the system behaves as an ideal capacitor, while for ϕ equal 0, the system behaves as an ideal resistor. The T' symbol represents the frequency-independent proportionality factor; its physical meaning is associated with the diffusion coefficient.

86
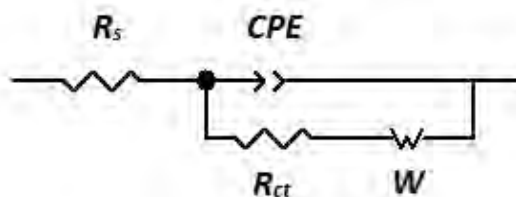
Scheme 2.3-10. A modified Randles-Ershler equivalent circuit frequently applied to model an electrochemical system embracing the working electrode coated with a polymer film. R_s is the solution resistance, CPE stands for the constant phase element, R_{ct} is the charge transfer resistance, and W is the Warburg impedance.

Another parameter that is introduced to the modified Randles-Ershler equivalent circuit is R_{ct}, relevant to electrode reactions. It represents the resistance of the electron transfer between the redox species in the solution and the electrode. The R_{ct} is sensitive to any changes in the electrode surface causing blocking of the electrode, e.g., deposition of a less conductive polymer. Moreover, the Warburg impedance, W, is considered in the equivalent electric circuit describing the (polymer film)-coated electrode. The Warburg impedance characterizes the mass transport to the electrode related to the faradaic process modeling the semi-infinite diffusion of electroactive species. The contribution of the Warburg impedance to the total impedance is defined by Equation 2.3-31.

$$Z_W = \frac{B\tanh(jT\omega)}{(jT\omega)^{\phi}}$$ (Equation 2.3-31)

where B is a fitted parameter.

A Nyquist plot of the impedance spectrum for this electrochemical system is presented in Scheme 2.3-11. The semicircle in this plot originates from an electrode reaction controlled by the charge transfer rate, whereas a straight line with a unit slope is derived from the Warburg impedance. It indicates a reaction with its rate controlled by the rate of diffusion in the low-frequency range.

Suppose no faradaic process occurs in the system because of no redox species in the solution. In that case, the imaginary impedance component is inversely proportional to the double-layer capacitance (Equation 2.3-32)

$$Z_{im} = \frac{1}{\omega A C_{dl}}$$ (Equation 2.3-32)

where A is the surface area of the electrode.

According to Equation 2.3-32, the C_{dl} value is higher at low frequencies. The phase angle, φ, can be determined by applying Equation 2.3-33.

$$\varphi = \tan^{-1}\left(\frac{Z_{im}}{Z_{real}}\right) \qquad \text{(Equation 2.3-33)}$$

According to Equation 2.3-33, a more negative value of φ means a more capacitive behavior of the electrical circuit.
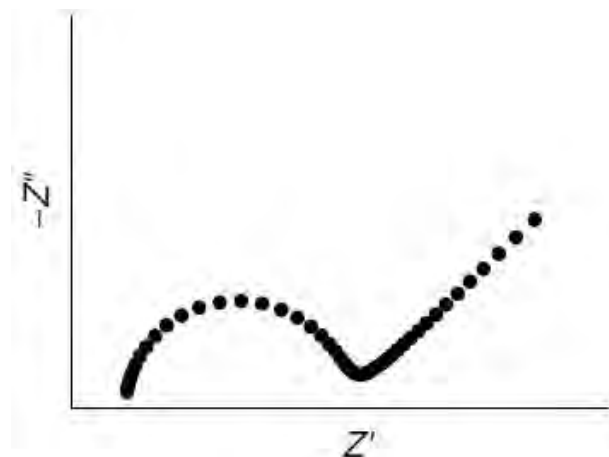
Scheme 2.3-11. The Nyquist plot for an electrochemical system controlled by the charge transfer rate and the diffusion rate at high and low frequencies, respectively.

The equivalent circuit for an electrode coated with a polymer film immersed in a supporting electrolyte solution is described by a solution resistance, R_s, and electrochemical double-layer capacitance, C_{dl}, in series (Scheme 2.3-12).
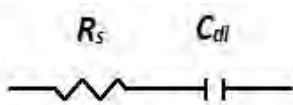
Scheme 2.3-12. The equivalent circuit used to model an electrochemical system based on a non-faradaic process for the working electrode coated with a polymer film and immersed in a solution of the supporting electrolyte. R_s and C_{dl} is the solution resistance and electrical double-layer capacitance, respectively.

2.3.4 Piezoelectric microgravimetry (PM) at a quartz crystal microbalance (QCM)

Piezoelectric microgravimetry (PM) is a technique that uses a QCM to measure small changes in the mass of solids deposited on the surface of a QCR. The deposition of a thin film on the QCR surface and subsequent interaction of the analyte with this film

88

changes the resonant frequency of the QCR. Then, these changes can be converted to changes in the mass deposited.

The piezoelectric effect occurs if pressure is applied to a piezoelectric crystal, i.e., a crystal with no symmetry center. That leads to the deformation in this crystal lattice. This deformation causes the separation of centers of opposite charges producing dipole moments of molecules, separating electric charges. The converse piezoelectric effect, adopted in PM, arises from an alternating voltage applied to the electric contacts attached to opposite faces of a piezoelectric crystal. Then, mechanical oscillations occur within the piezoelectric s crystal lattice oscillating at the resonance frequency proportional to the crystal's thickness.[368] Moreover, the oscillation mode is determined by a crystal cut. The AT-cut quartz crystals that vibrate in a thickness shear mode are the most frequently used in the PM technique. They produce BAW, which propagates from the QCR surface to the solution bulk.

If QCR is loaded with mass, its vibrational frequency will decrease. This mass can be determined using the Sauerbrey relation (Equation 2.3-34).[369-370]

$$\Delta f_{\text{mass}} = -\frac{2f_0^2 \Delta m}{A'(\mu_q \rho_q)^{1/2}} \qquad \text{(Equation 2.3-34)}$$

where f_0 stands for the fundamental resonance frequency of the QCR, Δm is the resonator's mass change, A' is the resonator's acoustically active area, μ_q is the shear modulus of quartz (2.947×10^{11} g s^{-2} cm^{-1}), and ρ_q is the density of quartz (2.648 g cm^{-3}).

Notably, the Sauerbrey equation can be applied if the deposited film is rigid, i.e., it should not exhibit visco-elastic properties ($\Delta f_{\text{vis}} \approx 0$).

For the QCR contacting a viscous medium, the difference in the frequency measured in air and a viscous medium is defined by Equation 2.3-35, which includes visco-elastic parameters of the medium, i.e., dynamic viscosity, η_L, and density, ρ_L:[371-372]

$$\Delta f_{\text{vis}} = (-f_0^{3/2}) \left(\frac{\rho_L \eta_L}{\pi \rho_q \mu_q} \right)^{1/2} \qquad \text{(Equation 2.3-35)}$$

Therefore, Equation 2.3-35 can be combined with the Sauerbrey equation to result in the total frequency change (Equation 2.3-36) containing contributions of the

frequency change due to viscous liquid loading and surface mass changes related to a rigid film.

$$\Delta f_{\text{total}} = \Delta f_{\text{mass}} + \Delta f_{\text{vis}} = -\left[\frac{2f_0^2}{(\mu_q \rho_q)^{1/2}}\right]\left[\frac{\Delta m}{A'} + \left(\frac{\rho_L \eta_L}{4\pi f_0}\right)^{1/2}\right] \quad \text{(Equation 2.3-36)}$$

If the $\rho_L \eta_L$ is constant, Equation 2.3-36 simplifies to the Sauerbrey equation, whereas, in the absence of mass changes, the frequency will be affected only by the density and viscosity of the medium. Then, Equation 2.3-36 simplifies to Equation 2.3-35.[373]

Visco-elastic properties can also be determined using another variable, namely, the dynamic resistance, $\overline{R}$:

$$\overline{R} = \frac{A'}{k^2}(2\pi f_0 \eta_L \rho_L)^{1/2} \quad \text{(Equation 2.3-37)}$$

where $k^2 = 7.74 \times 10^{-3}$ (A^2 s^2 cm^{-2}) represents the electromechanical coupling factor of the resonator.

Therefore, by substituting Equation 2.3-37 into Equation 2.3-35, a relation between Δf_{vis} and $\overline{R}$ can be determined (Equation 2.3-38):

$$\Delta f_{\text{vis}} = -\frac{k^2 \overline{R} f_0}{\pi A'(2\mu_q \rho_q)^{1/2}} \quad \text{(Equation 2.3-38)}$$

2.3.5 Surface plasmon resonance (SPR) spectroscopy

Surface plasmon resonance (SPR) is a phenomenon occurring at a metal (usually gold and silver) and dielectric interface if an incident light beam hits the surface at a particular angle. A portion of the light energy at a certain angle of incidence can interact with the delocalized electrons in the metal film (called plasmons), thus decreasing the reflected light intensity.[374] Surface plasmons are considered surface electromagnetic waves that move in a direction parallel to the metal-dielectric interface. The wave is located on the boundary of the external medium and the metal. Therefore, it is sensitive to any change of this boundary originating from, e.g., molecules' adsorption on the metal surface. Applying p-polarized light of a given wavelength on the dielectric medium prism coated with a thin metal film causes surface plasmons

excitation at a specific wavelength and angle. The incident beam must match its momentum to that of the plasmon.[375]

SPR as a charge-density oscillation occurs at the interface of two media with electric permittivity values of opposite signs, e.g., a metal and a dielectric. This charge density wave is related to an electromagnetic wave, whose field vectors approach their maxima at the interface and decrease evanescently into both media. These propagating surface plasmons (PSPs) are considered transverse magnetic polarized waves, meaning that the magnetic vector is perpendicular to the propagation direction of the surface plasmon wave and parallel to the interface's plane. The propagation constant of the PSP, β, propagating at the interface between a metal and a semi-infinite dielectric, is represented by Equation 2.3-39.

$$\beta = k' \sqrt{\frac{\varepsilon_m n_s^2}{\varepsilon_m + n_s^2}} \qquad \text{(Equation 2.3-39)}$$

where k' stands for the free-space wavenumber, ε_m is the electric permittivity of the metal, and n_s denotes the refractive index of the dielectric.

Because of the limitation of the penetration length of the PSP, the sensing is carried out directly in the area where the PSP is excited by an optical wave. According to Equation 2.3-39, the PSP propagation constant is always higher than that of optical wave propagation in the dielectric. Therefore, the PSP cannot be excited directly by an incident optical wave at a planar metal-dielectric interface. Thus, the incident optical wave's momentum must be enhanced to match that of the surface plasma wave. This momentum change is commonly achieved using attenuated total reflection (ATR) in prism couplers and optical waveguides, then diffraction at the surface of diffraction gratings.

Optical excitation of surface plasmons by the ATR method was originally developed by Otto,[376] as well as Kretschmann and Raether.[377] The method of the latter authors is more versatile.[377] Therefore, the Kretschmann configuration of the ATR method has become the most frequently used geometry in SPR-based sensors. In this geometry, light passes through a high-refractive index prism and excites a PSP on the outer boundary of the metal layer deposited on the prism (Scheme 2.3-13a).
The PSP excitation causes a decrease in the intensity of the reflected light. The refractive index change of the dielectric medium in the evanescent wave of the PSP leads to a change in the PSP propagation constant, thus resulting in modification of the

91

condition of coupling the PSP and the light wave. That causes a change in the optical wave characteristic, including coupling wavelength, coupling angle of incidence, intensity, and phase (Scheme 2.3-13b). Target analyte molecules binding to probe molecules immobilized on the sensor surface leads to a refractive index change at the SPR chip surface, resulting in a change in the SPR angle (Scheme 2.3-13c and d). If binding to the immobilized ligand occurs, the local effective refractive index changes, resulting in a change in the SPR angle.[150]
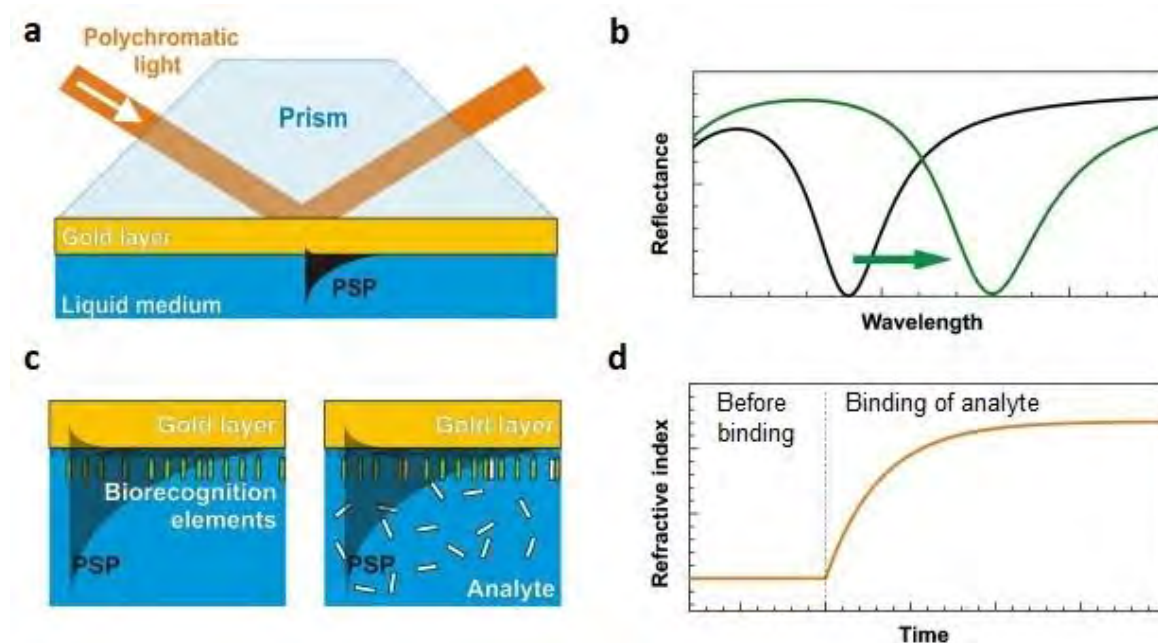
Scheme 2.3-13. Principle of operation of a surface plasmon resonance (SPR) biosensor. (a) Propagating surface plasmons (PSPs) excitation by a polychromatic light in the Kretschmann configuration of the attenuated total reflection (ATR) method, (b) spectrum of reflected light with a characteristic SPR dip for two different refractive index values at the gold layer, (c) binding of an analyte to biorecognition units immobilized on the SPR biosensor surface, and (d) refractive index changes due to analyte binding.[378]

2.3.6 Ultraviolet-visible (UV-vis) spectroscopy

Ultraviolet-visible (UV-vis) spectroscopy is an optical technique that utilizes a light source to illuminate samples with light across the UV to visible wavelength range (190 to 1100 nm), exciting electrons. Various processes may occur when this electromagnetic radiation interacts with matter, including reflection, absorption, scattering, fluorescence or phosphorescence (absorption and re-emission), and

photochemical reactions. Usually, absorbance is measured if analyzing samples by UV-vis spectrophotometry to determine their UV-vis spectrum.[379]

A UV-vis spectrophotometer mainly comprises a light source, a sample holder, and a light dispersive device to separate light of the different wavelengths, i.e., a monochromator using a prism or diffraction grating, as well as a detection system (Scheme 2.3-14).
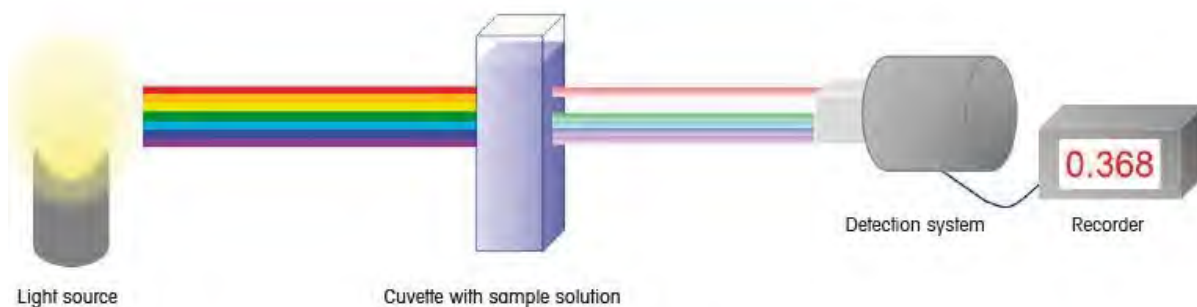
Scheme 2.3-14. The principle of operation of UV-vis spectroscopy.[379]

This spectrophotometer measures the intensity of light passing through a sample solution in a cuvette and compares it to the intensity of the light before it passes through the sample (Scheme 2.3-15). Light with the original intensity, Int_0, is partially absorbed by the sample at specific wavelengths. The remaining light, i.e., the transmitted light with an intensity Int, is recorded as a function of wavelength by a detector, providing a UV-vis spectrum of the sample.
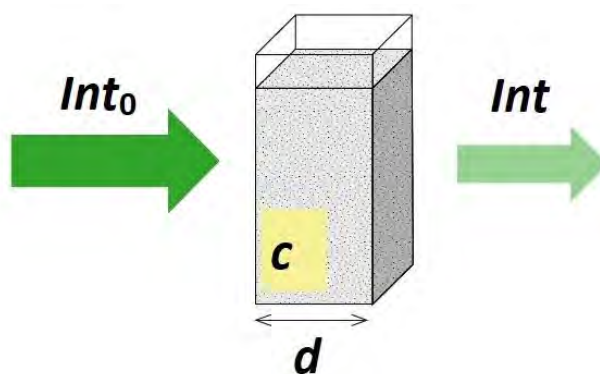
Scheme 2.3-15. A sketch of absorption of the incident light of intensity Int_0 at specific wavelengths by a sample solution of the concentration c; the solution is in the cuvette of the length d.[379]

The ratio of the transmitted light intensity, Int, to the incident light intensity, Int_0, is called transmittance, $Trans$. It is described by Equation 2.3-40:

$$Trans = \frac{Int}{Int_0}$$
(Equation 2.3-40)

On the other hand, absorbance is defined as the negative logarithm of $Trans$:

$$Abs = -\log(Trans)$$
(Equation 2.3-41)

The light intensity is attenuated proportionally to the sample concentration, c, when light passes through a transparent cuvette filled with the sample solution. Moreover, the attenuation is proportional to the cuvette length, d. This dependence can be expressed by absorbance Abs as a function of the concentration and the cuvette length (Equation 2.3-42).

$$Abs = c\,\varepsilon\,d$$
(Equation 2.3-42)

Equation 2.3-42 is the Lambert-Beer law where c is the sample concentration in M or g mL^{-1}, d stands for the path length of the cuvette (in cm), and ε is the molar absorptivity coefficient denoting a sample-specific constant that describes how much the sample is absorbing at a given wavelength (in M^{-1} cm^{-1} or mL cm^{-1} g^{-1}). The Lambert-Beer law predicts a linear relationship between the sample concentration and the amount of light the sample absorbs as it passes through the sample.

2.3.7 Polarization-modulation infrared reflection-absorption spectroscopy (PM-IRRAS)

Infrared (IR) spectroscopy is a technique that studies the interaction of infrared radiation with matter. Most molecules can absorb infrared radiation, and this absorption is measured as a function of the radiation wavelength. This absorption is characteristic of the nature of the chemical bonds of a given compound. The IR spectrum of a sample is obtained by passing a beam of IR light through the sample and recording the light intensity against the wavenumber. IR spectroscopy is mainly applied to analyze and identify functional groups and interactions between them and estimate the structures of the compounds. Infrared reflection-absorption spectroscopy (IRRAS) involves IR measurements with a p-polarized light parallel to the plane of incidence applied. It is

used to characterize adsorbed matter, like thin films including monolayers, deposited on reflective substrates like metals. IRRAS measures the change in the reflectance spectrum caused by this adsorption. The sample is usually analyzed in reflection geometry under grazing incidence to enhance sensitivity. The main drawback of IRRAS is the interference of strong IR absorption of water and carbon dioxide from an aqueous electrolyte solution and air, respectively, during in situ studies of solid-liquid interfaces. IRRAS absorption peaks are usually small; therefore, they frequently require a long acquisition time.

Additionally, not only sample absorption but also that of the reference must be measured. For enhancing the IRRAS sensitivity, a procedure of the polarized radiation modulation between the orthogonal states was developed and utilized in a PM-IRRAS technique.[380-381] In this technique, polarized IR radiation is modulated between the parallel (p-) and perpendicular (s-) states against the incident-reflection plane using a high-frequency photoelastic modulator (PEM).[382] The PM-IRRAS takes advantage of different absorptions of p- and s-polarized light at large ranges of angles of incidence. Since s-polarized light does not generate an electric field of stationary vibration, the absorption is much smaller than that of p-polarized light. The PM-IRRAS technique analyzes the high-frequency modulation between s- and p-polarization, allowing the simultaneous measurement of two signals: the difference spectrum between s- and p-polarized light and the corresponding sum spectrum. The s- and p- polarization signals sum is used as the reference. Thus, a reference measurement is not needed. Hence, employing the polarization-modulation technique to IRRAS eliminates interference caused by CO_2 and water.

2.3.8   X-ray photoelectron spectroscopy (XPS)

X-ray photoelectron spectroscopy (XPS) is one of the most frequently used surface-sensitive techniques to determine, among others, a thin film's elemental composition. Its principle of operation is based on the photoelectric effect, discovered by Heinrich Hertz[383] and later described by Albert Einstein in quantum mechanical terms.[384] The physical phenomenon behind XPS is the emission of electrons from surfaces irradiated by soft X-rays (energy lower than ~6 keV). The sample surface is irradiated with photons of characteristic energy (usually MgKα radiation is used). The interaction of photons with core electrons of the sample atoms leads to the formation of ionized atom states and photoelectrons emission. Since the kinetic energy of emitted photoelectron is

95

related to the difference between the incident photon energy and the electron binding energy (BE), the resulting photoelectron spectrum indicates the binding energies of the different atomic electron levels. In other words, X-ray energy is a sum of the BE, the kinetic energy (KE) of the emitted photoelectron, and the spectrometer work function (Φ_{spec}):

$$hv = BE + KE + \Phi_{spec} \qquad \text{(Equation 2.3-43)}$$

Binding energy can be calculated via transformation of Equation 2.3-43, as follows.

$$BE = hv - KE - \Phi_{spec} \qquad \text{(Equation 2.3-44)}$$

The photoelectron emission produces a core "hole," generating an excited ionized state. An electron located in an upper shell fills the hole to release the excess energy of this ion in one of the two processes: X-ray fluorescence or an Auger electron emission (Scheme 2.3-16). Released Auger electrons are often used in XPS for qualitative analysis.
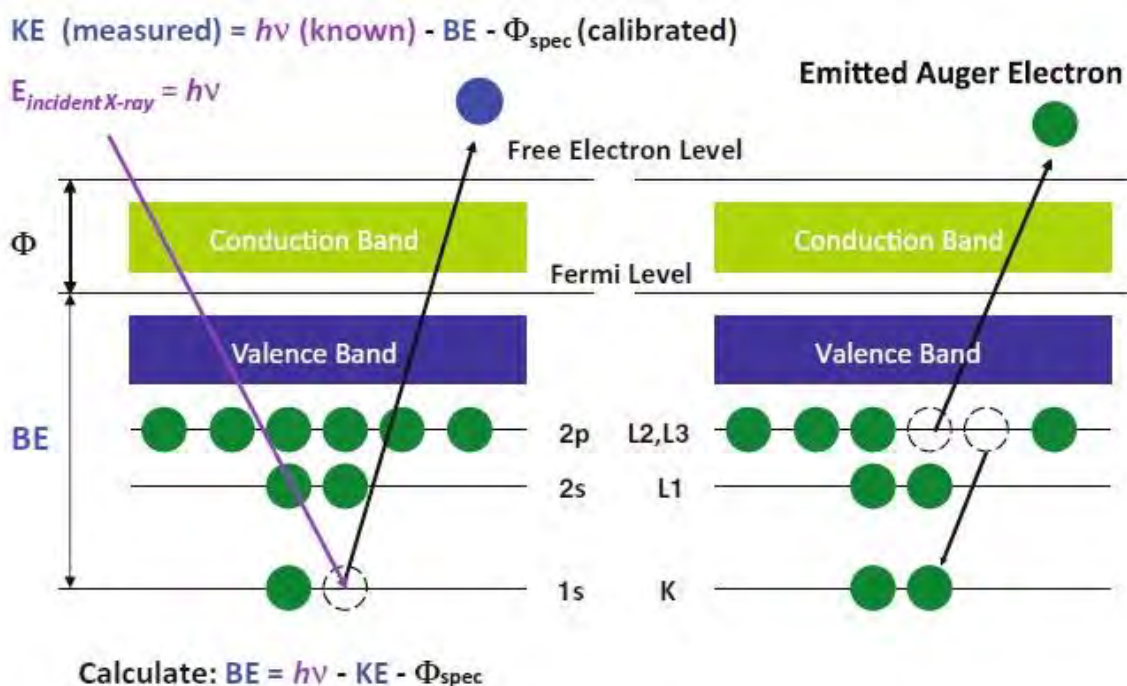
Scheme 2.3-16. The principle of emission of a photoelectron and an Auger electron.[385]

An XPS instrument consists of a monoenergetic X-ray source, sample stage, extraction lenses, analyzer, and detector housed in an ultra-high vacuum (UHV) environment. A sketch of an XPS system is depicted in Scheme 2.3-17.
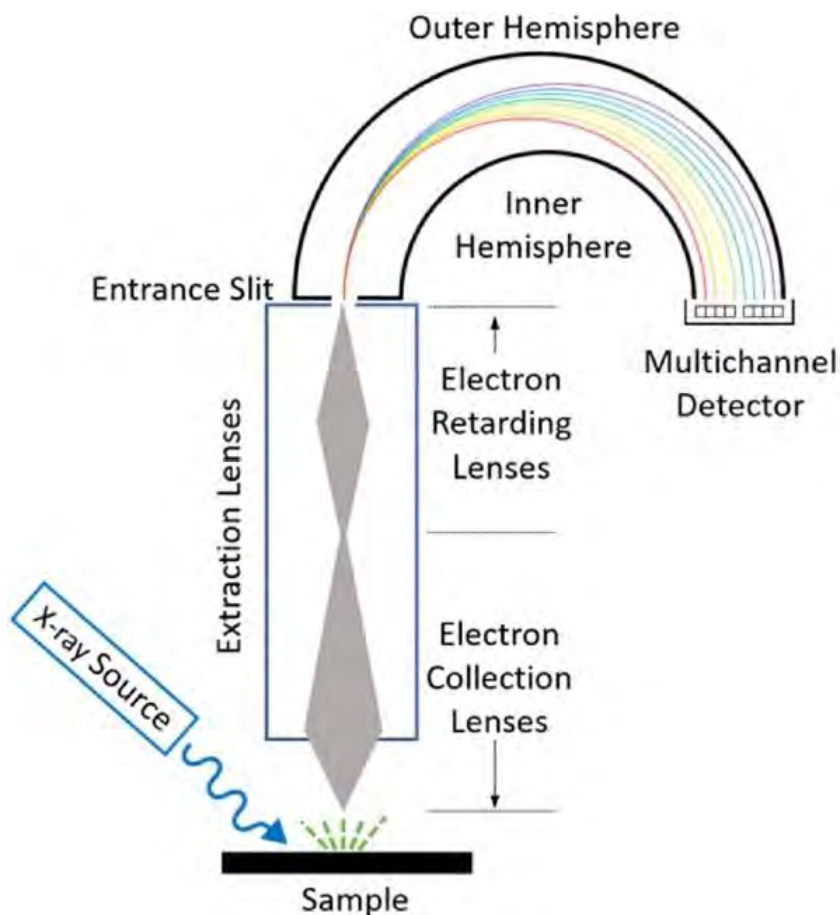
Scheme 2.3-17. Schematic illustration of the XPS setup main components.[386]

The UHV is applied to eliminate air molecules that may hamper the emitted electrons from getting to the analyzer because of their scattering on gas molecules. Moreover, since XPS is a surface-sensitive technique, the UHV is necessary to decrease contamination of the sample surface exposed to the chamber atmosphere.

2.3.9   Atomic force microscopy (AFM)

Atomic force microscopy (AFM) is a technique mainly used for high-resolution imaging of surfaces of materials. It is a valuable tool for direct measuring intermolecular forces with atomic resolution, which helps characterize polymers, semiconductors, electronic materials, and biomaterials. The concept of AFM is shown in Scheme 2.3-18.
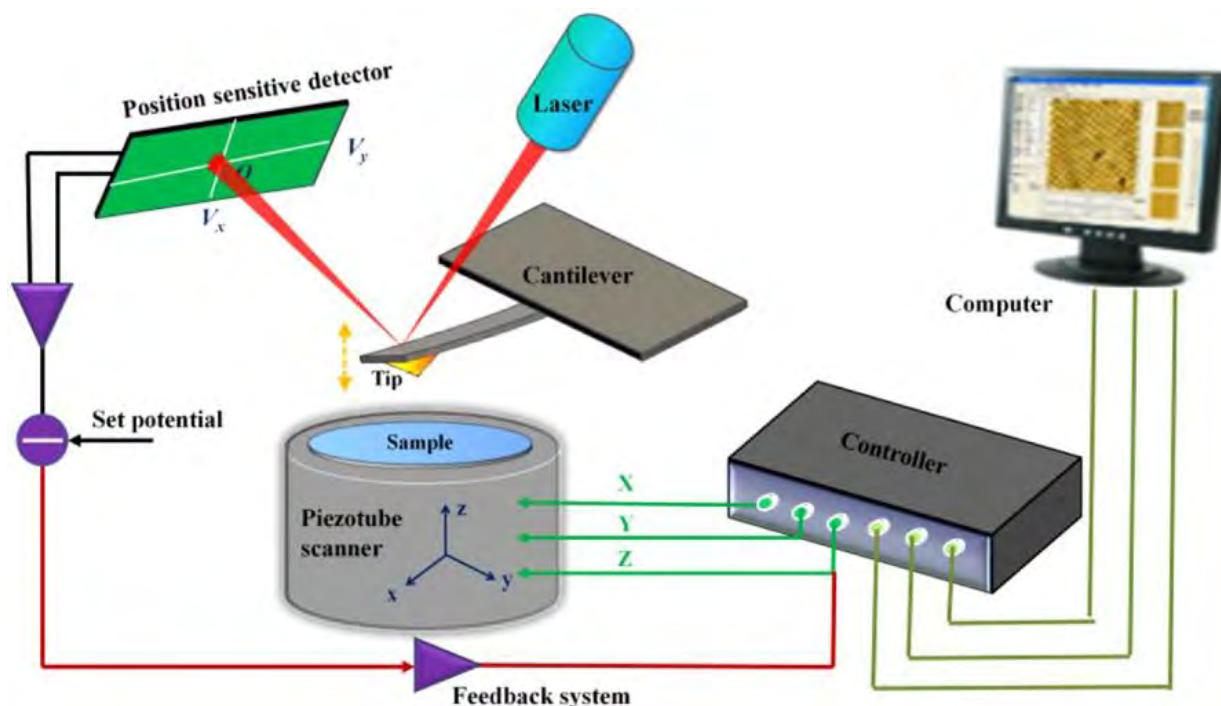
Scheme 2.3-18. The schematic depiction of the AFM setup and operation principle.[387]

The instrumentation mainly comprises a cantilever with a sharp tip on its end, a piezoelectric scanner, scanning and feedback systems, a laser, a photoelectric detector, and a computer. The sharp tip of the cantilever scans over the sample mounted on a piezoelectric scanner, and then the cantilever deflects in response to the force between the tip and the sample. This deflection is measured using a laser beam reflecting off the cantilever's surface. Any deflection leads to a change in the direction of the reflected beam, which is then registered and converted into an electric signal by the photoelectric detector. The piezotube scanner controls the movements between the tip and the sample in the x, y, and z directions.

The AFM operates in two general modes, the static mode (contact mode) and the dynamic mode (the non-contact mode and the tapping mode). Each mode has a dominant interaction force between the tip and the sample, namely the repulsive forces in the contact mode and the attractive forces in the non-contact mode. When the tip is brought into contact with the sample in the static mode, the repulsive force deflects the cantilever away from the sample. Two main types of imaging in the static mode are the constant force mode and the constant height mode. In the former, the feedback system maintains the cantilever deflection. Thus, scanner displacement is related to sample topography. The constant height mode, where the cantilever maintains a fixed height above the sample surface, is convenient for smooth sample imaging at high resolution.

98

The cantilever is mechanically vibrated in the dynamic mode, leading to tip oscillation at a small distance above the sample surface. The attractive force bends the cantilever toward the sample.

Moreover, both the repulsive and attractive modes can be exploited in the tapping mode at high frequencies. In the tapping mode, the cantilever oscillates at its resonance frequency, and the tip taps the sample surface for a short time. Since tip interaction with the sample damps this oscillation down, the tip position is adjusted to keep the amplitude of the oscillation constant. The relation between the interatomic force and the distance is presented in Scheme 2.3-19.
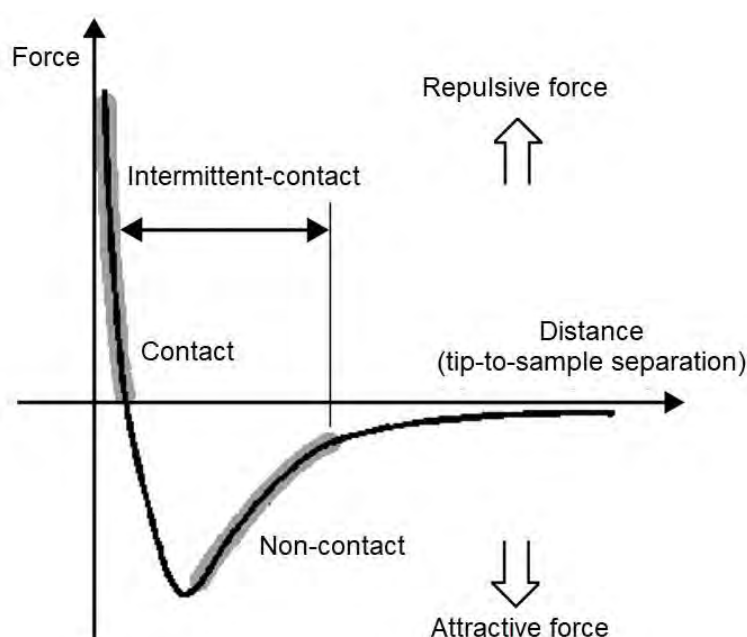
Scheme 2.3-19. Typical curve of interatomic force vs. distance in AFM. The regions of AFM modes are indicated: contact mode (or static mode) operating in the repulsive region and non-contact mode (dynamic mode) operating respectively in attractive/repulsive and attractive regions.[388]

AFM can be used not only for imaging the surface topography of various materials but also for measuring the physical properties of these materials, including magnetic, mechanical, electrical, and electromechanical properties.[389] Moreover, it enables determining the thickness of films coating conductive substrates. The film deposited on the surface must gently be scratched using a soft spatula for that purpose. Then, the edge of the scratch is imaged.

99

2.3.10 Scanning electron microscopy (SEM)

Electron microscopy can be divided into two main classes: scanning electron microscopy (SEM) and transmission electron microscopy (TEM). Basic SEM and TEM imaging principles are shown in Scheme 2.3-20.
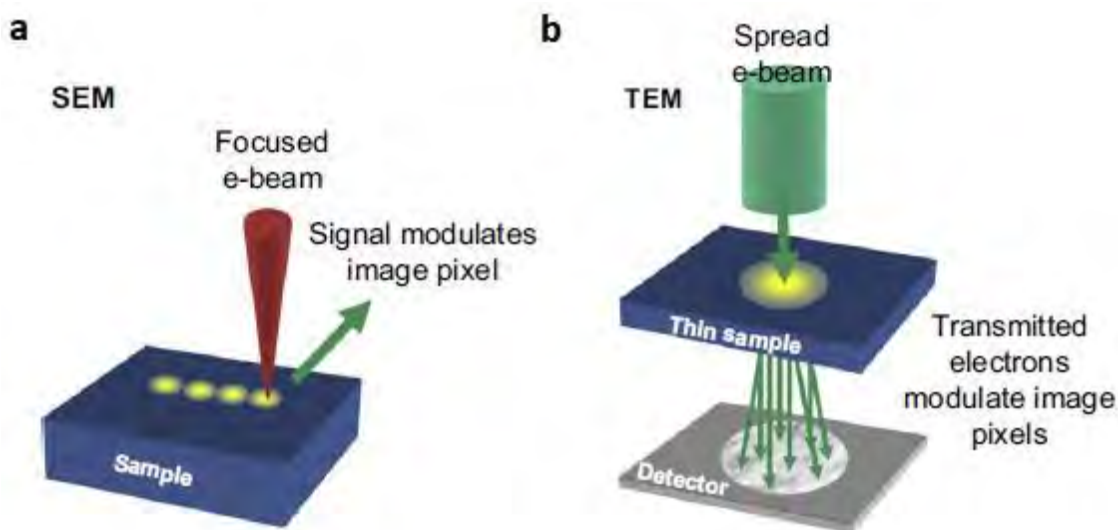
Scheme 2.3-20. Operation principles of scanning electron microscopy (SEM) and transmission electron microscopy (TEM) presenting (a) serial collection of data points in SEM and (b) parallel image acquisition in TEM.[390]

In both a scanning electron microscope and a transmission electron microscope, the electron beam is generated from the electron source, then used to bombard the sample. Both SEM and TEM microscopes work under vacuum conditions to eliminate interactions between molecules present in the microscope column and the electron beam, as well as to protect the electron gun from noise and vibrations.

After bombarding a sample with electron beams, the most important signals emitted are scattered primary electrons, secondary electrons, and X-rays (Scheme 2.3-21a). These signals are abundant and easy to collect. They form the basis of most microstructural characterization studies by SEM. The transmitted primary electron signal, used in TEM, will only be abundant if the sample is ultrathin.

Two main inelastic scattering mechanisms are involved in generating X-rays. Bremstrahlung X-rays are generated by the slowing down of primary electrons as they pass through atoms and have a continuous range of energies up to the primary electron incident energy. Characteristic X-rays are generated when primary electrons knock an electron out of an atom, and the subsequent transition of a second electron between

100

energy levels leads to an emission of an X-ray of specific energy, which is the difference in energy states (Scheme 2.3-21a). These X-rays of specific energy are attributed to the specific elements in the sample by comparing their energy with elemental standards in energy dispersive X-ray (EDX) spectroscopy analysis (Scheme 2.3-21b).
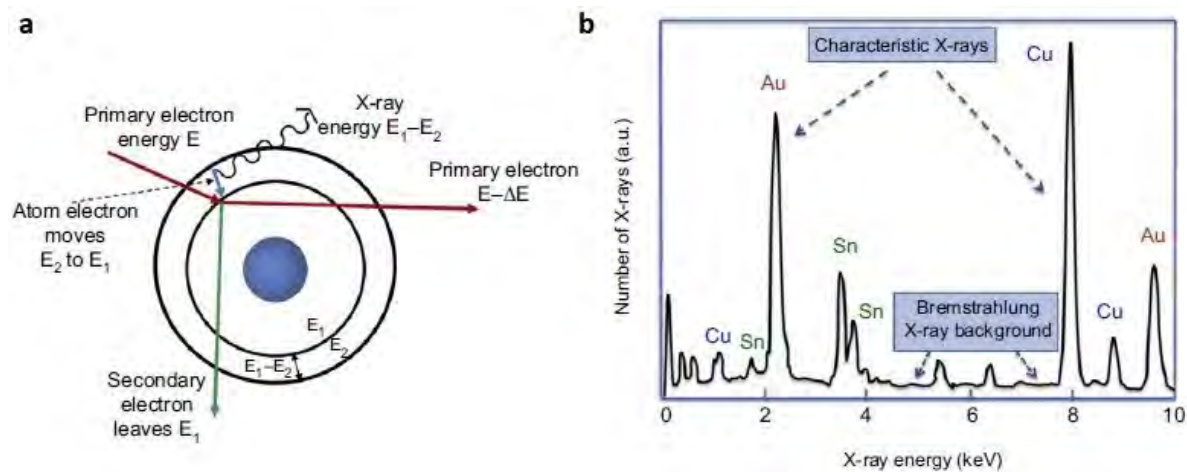
Scheme 2.3-21. (a) A principle of emission of characteristic X-rays. (b) An example of an energy dispersive X-ray (EDX) spectrum showing X-ray peaks at energies characteristic for a given element.[390]

In EDX spectroscopy, X-ray spectra are acquired by bombarding the sample with the electron beam and counting the number of X-rays reaching the detector according to their energy. EDX spectroscopy in SEM has found application in the nondestructive chemical analysis of materials.

SEM microscopes are mainly applied to analyze material surfaces (similar to reflection light microscopes). Moreover, SEM is one of the most commonly used techniques for the examination and chemical composition characterization of inorganic and heterogeneous organic materials on a nanometer to micrometer scale. The area to be analyzed is bombarded by a focused beam of electrons that scans the sample surface (Scheme 2.3-20a). The interaction between the electron beam and the atoms from the sample causes the emission of secondary and backscattered electrons, characteristic X-rays, and other photons of various energies. Detectors collect signals in the form of electrons and rays characteristic of the sample. The detector signal is synchronized with the electron beam location on the sample. The signal's intensity is adjusted to the corresponding image pixel. The signals collected in series are combined to form the images. The resulting images reveal information about the composition and topography

101

of the sample. Signals originating from secondary and backscattered electrons differ mainly due to differences in surface topography. Thus, they are mostly used in SEM imaging.

Main SEM microscope components include an electron source, anode, condenser lens, scanning coils, objective lens, and a detector (Scheme 2.3-22).
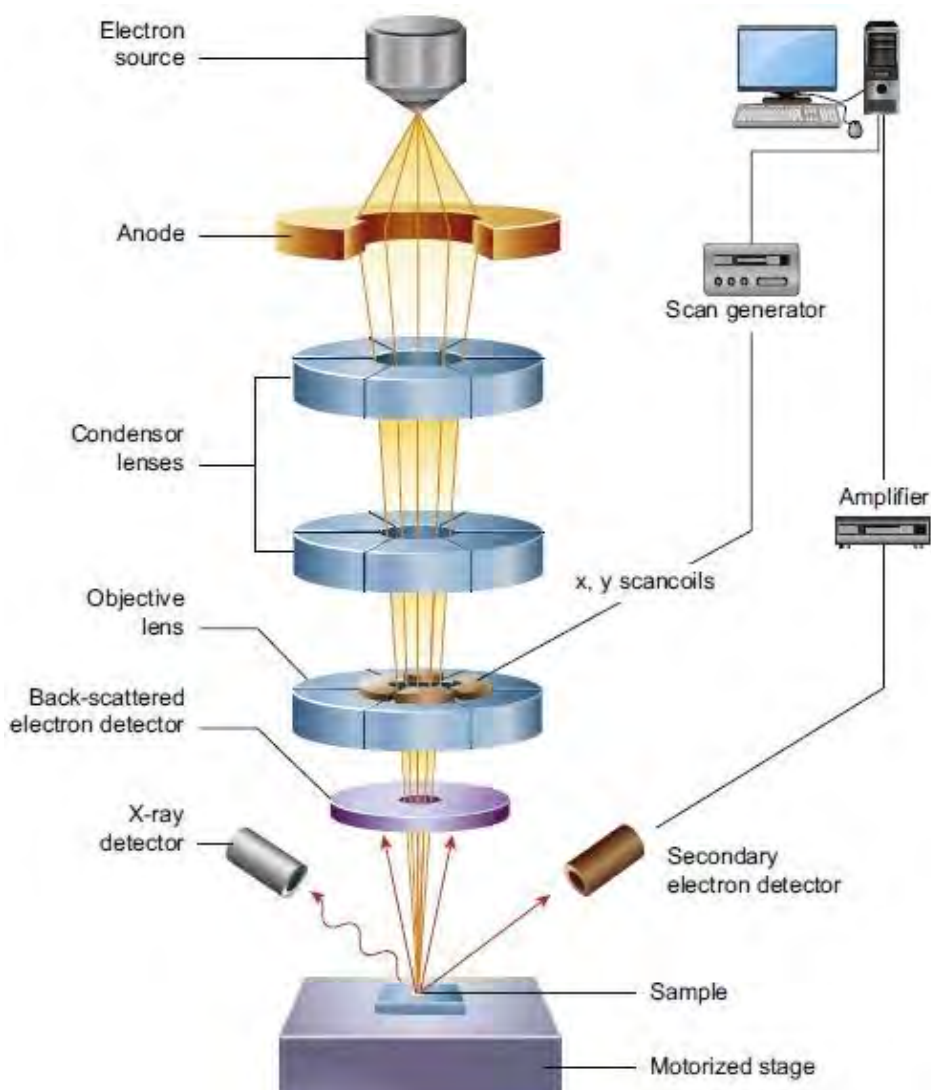
Scheme 2.3-22. Schematic view of main components of a scanning electron microscope.[390]

Electron beams are emitted from the electron source and accelerated down the microscope column by the anode, passing through lenses and apertures responsible for focusing the electrons into a narrow beam. The electron beams either scan the sample's surface in a raster pattern or are static to analyze the sample at one position. Electrons' energy usually ranges from 1 to 30 keV.

102

2.3.11 Dynamic light scattering (DLS) analysis

The operation principle of dynamic light scattering (DLS) is based on the changes in scattered light intensity due to the Brownian motion of particles dispersed in solution. Macromolecules in a liquid move randomly in all directions, colliding with solvent molecules, thus transferring energy, which also induces the movement of particles. Since such an energy transfer is relatively constant, the impact on small particles is bigger, resulting in faster movements of small than big particles. Therefore, it is possible to determine particles' hydrodynamic diameters by monitoring their speed, which is expressed by their diffusion coefficient, D.

In a DLS instrument, a monochromatic light beam hits particles dispersed in solution, then scatters in all directions. A spontaneous movement of these particles causes fluctuation in scattered light intensity because the distance between particles and the detector changes constantly. Measurement of these intensity fluctuations against time leads to the determination of the diffusion coefficient, which depends on the size and shape of the particles.[391]

The relation between the diffusion coefficient of the particles and the particle size is described by the Stokes-Einstein equation:

$$d(H) = \frac{kT}{3\pi\eta_L D}$$
(Equation 2.3.45)

where $d(H)$ stands for hydrodynamic particle diameter, k is Boltzmann constant, T is absolute temperature, η_L is the dynamic viscosity of the dispersant (solvent), and D stands for the diffusion coefficient.

The movement of particles depends on temperature and dispersant viscosity. The Stokes-Einstein equation includes these two parameters. Significantly, particles' movement should solely be based on Brownian motion. Otherwise, processes like particle sedimentation may lead to false results.

Chapter 3

3. Results and discussion

The present chapter covers several complementary topics. First, it describes the experiments performed to devise electrochemical sensors with MIP film recognition units that are selective to chosen food and dietary supplement contaminants, namely *N*-nitroso-L-proline (Pro-NO) and *p*-synephrine (SYN). Second, the chapter details the so-called "gate effect" mechanism for the electrodes coated with conductive MIP films. Conclusions drawn from these analyses allowed the fabrication of a redox self-reporting MIP chemosensor with the covalently immobilized ferrocene redox probe for label-free electrochemical determination of SYN. Moreover, the chapter describes experiments conducted for devising self-reporting chemosensors based on electroresponsive MIP nanoparticles (MIP NPs) for GLY sensing.

3.1 MIP chemosensor for selective determining *N*-nitroso-L-proline

The first section of the present chapter focuses on devising, characterizing, and fabricating an MIP film chemosensor for selective electrochemical determination of Pro-NO, a food toxin that might cause chronic diseases, including severe hormonal dysfunctions and cancer. Toward that, a thiophene-based polymer molecularly imprinted with Pro-NO was used as the chemosensor's recognition unit. The pre-polymerization complex of the DFT-optimized structure was potentiodynamically electropolymerized to form and subsequently deposit a (Pro-NO)-MIP film on the electrode surface. After removing the Pro-NO template molecules from the imprinted cavities of the (Pro-NO)-MIP, the analytical performance of the (Pro-NO)-MIP film chemosensor was analyzed using electrochemical techniques, i.e., DPV and EIS, as well as PM using an EQCM. Moreover, the MIP film chemosensor was successfully applied to determine Pro-NO in grilled pork neck samples, revealing its usefulness in Pro-NO determination in real samples (Scheme 3.1-1).
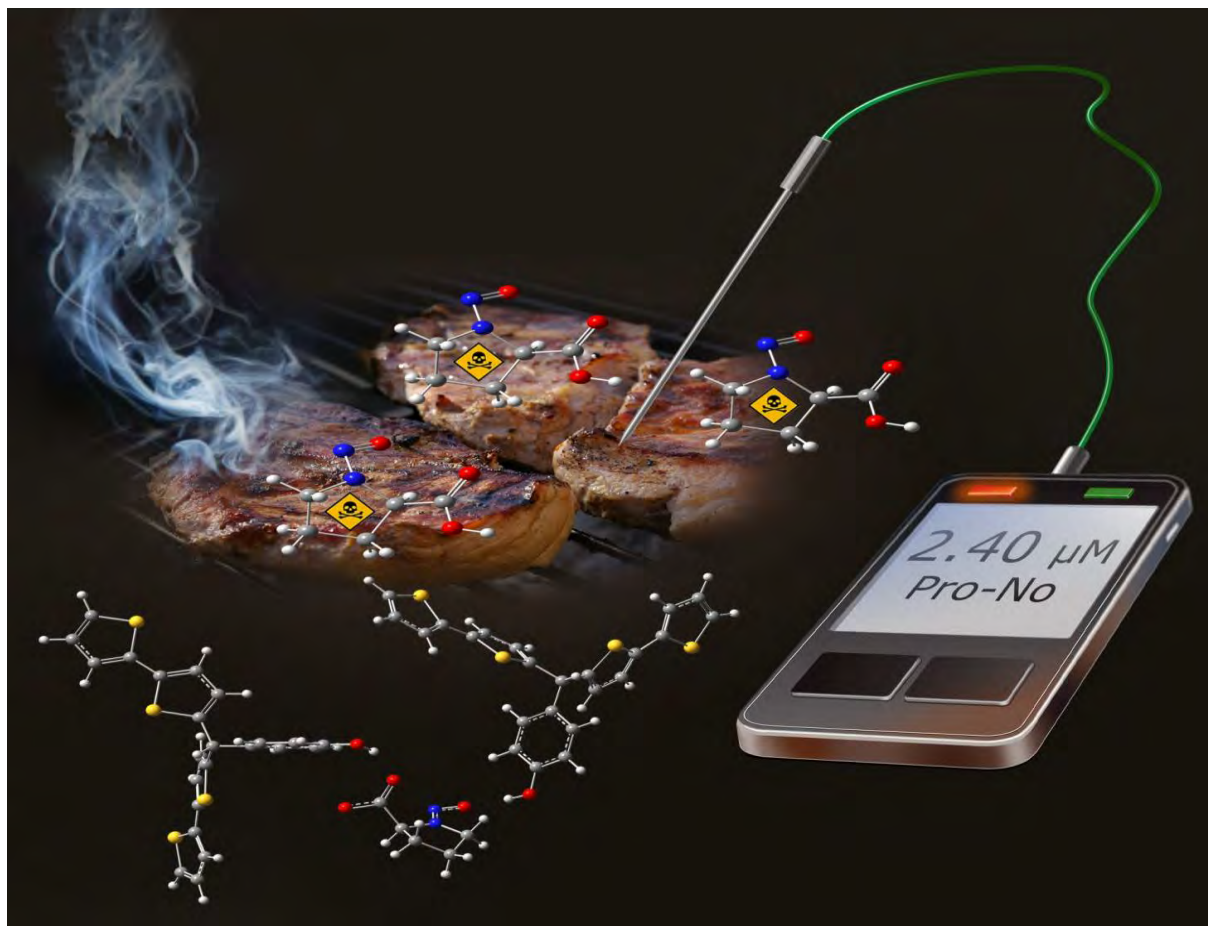
Scheme 3.1-1. An illustration of the future application of (Pro-NO)-MIP film chemosensor.

3.1.1 Quantum-chemical modeling of the pre-polymerization complexes

Computational modeling allowed for predicting the formation of a stable pre-polymerization complex of the Pro-NO template with selected functional monomers. The Pro-NO template (Scheme 3.1-2), classified as an *N*-nitrosamine, is a derivative of the L-proline amino acid bearing carboxyl and nitroso groups in its structure. Additionally, a non-toxic "dummy" template *N*-acetyl-L-proline, Ac-Pro (Scheme 3.1-2), with functional groups similar to those of Pro-NO, was analyzed. Based on the possible templates' binding sites, two different functional monomers, namely, *p-bis*(2,2'-bithien-5-yl)-methyl-*o*-catechol, FM 1, and *p-bis*(2,2'-bithien-5-yl)methylphenol, FM 2 (Scheme 3.1-2), bearing functionalities capable of interacting with functional groups of the templates, were selected for computational modeling (Schemes 3.1-3 and 3.1-4).
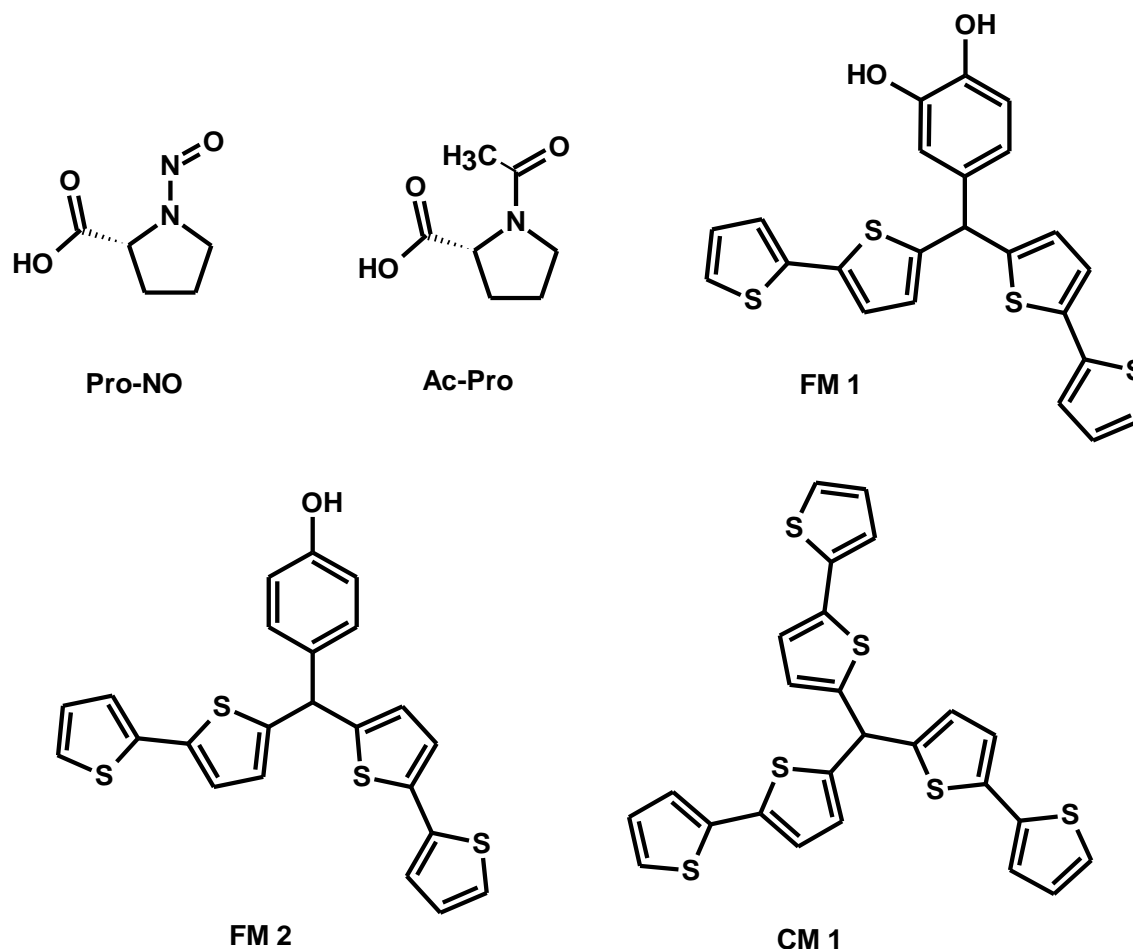
Scheme 3.1-2. Structural formulas of Pro-NO and Ac-Pro templates, FM 1 and FM 2 functional monomers, and CM 1 cross-linking monomer.

The pre-polymerization complexes structures were optimized using DFT calculations at the B3LYP/6-31G(d) level. Then, the Ac-Pro template complexation with FM 1 was first molecularly modeled to select the "dummy" template appropriately. In the DFT-optimized structure of the pre-polymerization complex, two molecules of FM 1 bound the Ac-Pro molecule through hydrogen bonds (Schemes 3.1-3a and 3.1-3b). The negative Gibbs free energy gain (ΔG) corresponding to the template interacting with the imprinted cavity was equal to −296.3 kJ mol^{-1}. Then, the structure-optimized complex was modified by introducing the target analyte Pro-NO molecule instead of the Ac-Pro molecule. Moreover, bithienyl moieteies were "frozen" to simulate their immobilization in polymer matrix (Schemes 3.1-3c and 3.1-3d). The negative ΔG value of this complex formation was as high as −278 kJ mol^{-1}.
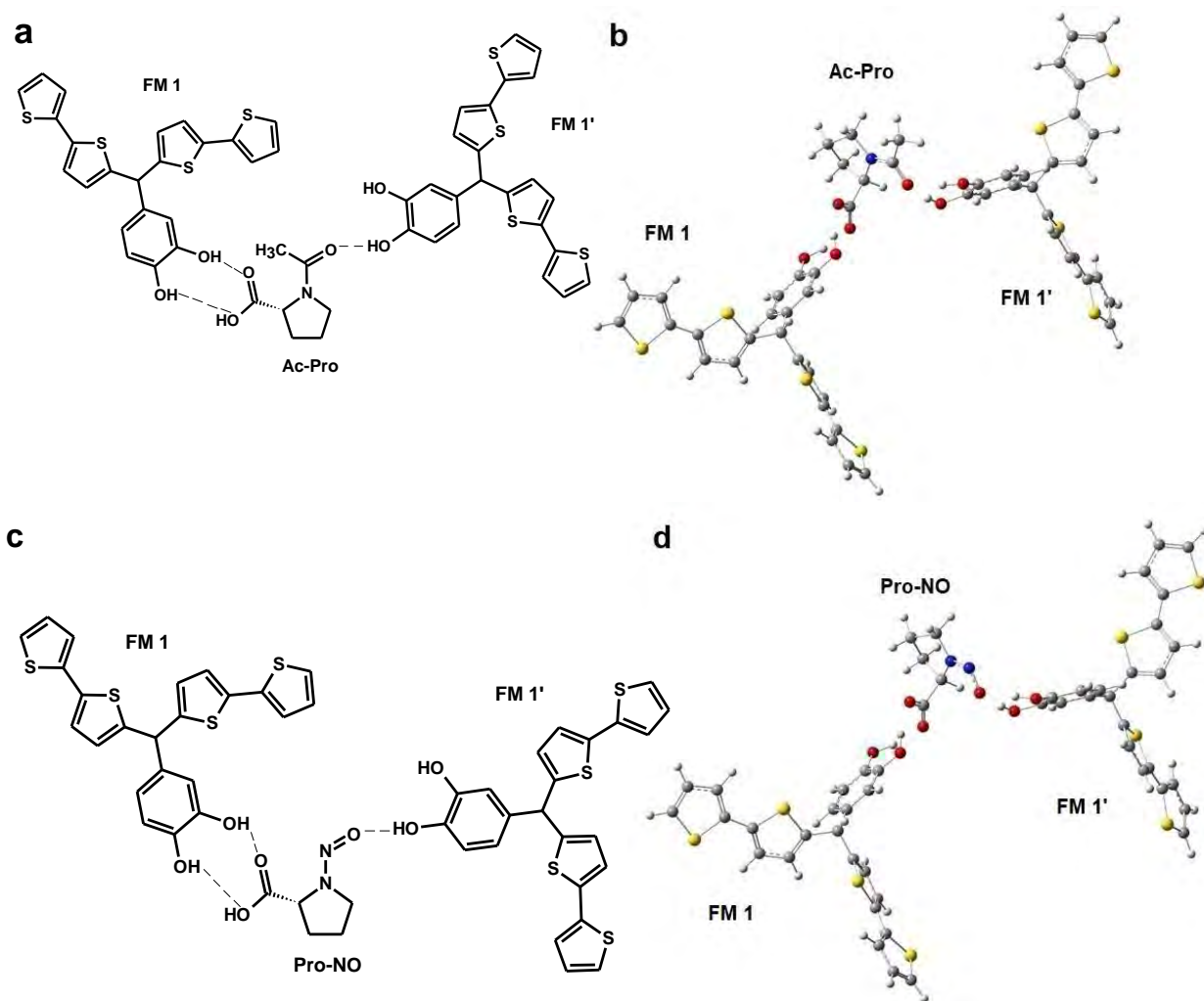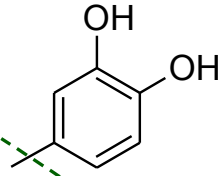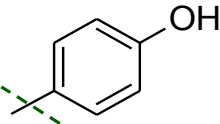
Scheme 3.1-3. The pre-polymerization complex of one molecule of the Ac-Pro "dummy" template with two FM 1 functional monomer molecules (a) structural formula and (b) DFT-optimized structure. (c) The pre-polymerization complex of one molecule of the Pro-NO template with two FM 1 functional monomer molecules (c) structural formula and (d) DFT-optimized structure. Calculations were performed for 298 K in a vacuum with the B3LYP functional and the 6-31G(d) basis set using Gaussian 09 software.

107
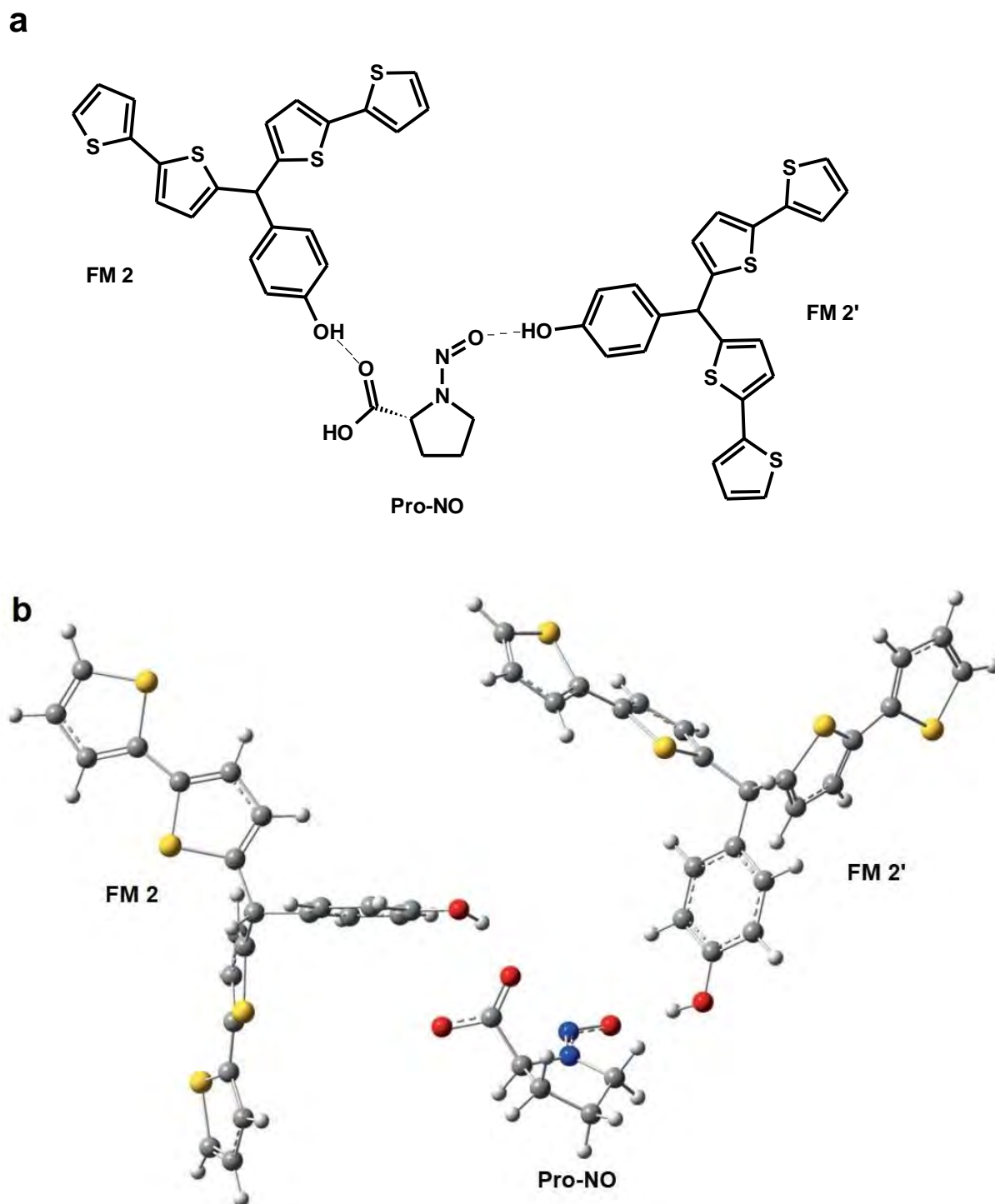
Scheme 3.1-4. (a) The structural formula and (b) the DFT-optimized structure of the pre-polymerization complex of one Pro-NO molecule with two FM 2 molecules. Calculations were performed for 298 K in a vacuum with the B3LYP functional and the 6-31G(d) basis set using Gaussian 09 software.

Table 3.1-1. Gibbs free energy change, ΔG, of chosen functional monomers and templates.

Functional monomer	Template	Gibbs free energy change of complex formation with a template (ΔG), kJ/mol	Gibbs free energy of change of binding Pro-NO in the created cavity (ΔG), kJ/mol
OH OH **FM 1**	*N*-nitroso-L-proline	−278,2	
	N-acetyl-L-proline	−302,7	−296,3
OH **FM 2**	*N*-nitroso-L-proline	−130,4	

3.1.2 Experimental confirming the stability and stoichiometry of the DFT-optimized pre-polymerization complex of Pro-NO with FM 2

Among all three tested MIP chemosensors based on pre-polymerization complexes mentioned above, the selectivity in DPV measurements was the highest if using the chemosensor with the (Pro-NO)-MIP film formed from the FM 2 functional monomer and the Pro-NO template in the presence of the CM 1 cross-linking monomer (Figure 3.1.9b). Therefore, this polymer was selected for further investigations.

The DFT-determined stoichiometry and stability of the pre-polymerization complex of Pro-NO with FM 2 were experimentally verified by UV-vis spectroscopy titration (Figure 3.1-1a). The UV-vis absorbance spectra (Figure 3.1-1a) recorded for FM 2 were quenched with the Pro-NO solution of acetonitrile and toluene at the 1 : 4 (*v*/*v*) ratio. Thus, the FM 2 absorbance at $\lambda = 320$ nm dependence on the Pro-NO concentration ranging from 4.95 to 23.81 µM was plotted (Figure 3.1-1a, inset). The stoichiometry of the pre-polymerization complex was determined as 2 : 1. Moreover, the stability constant of the complex, K_s, was calculated from the slope of the

linear $\frac{(Abs_{(FM)} - Abs_{(FM)_0})}{2\, c^2_{(Pro-NO)}}$ vs. $\left(Abs_{(FM)} - Abs_{(FM)_0}\right)$ dependence using Equation 2.2-1 (Figure 3.1-1b). The obtained K_s value as high as $(3.14\pm0.71)\times10^9$ M proved the formation of a stable pre-polymerization complex of Pro-NO with FM 2.
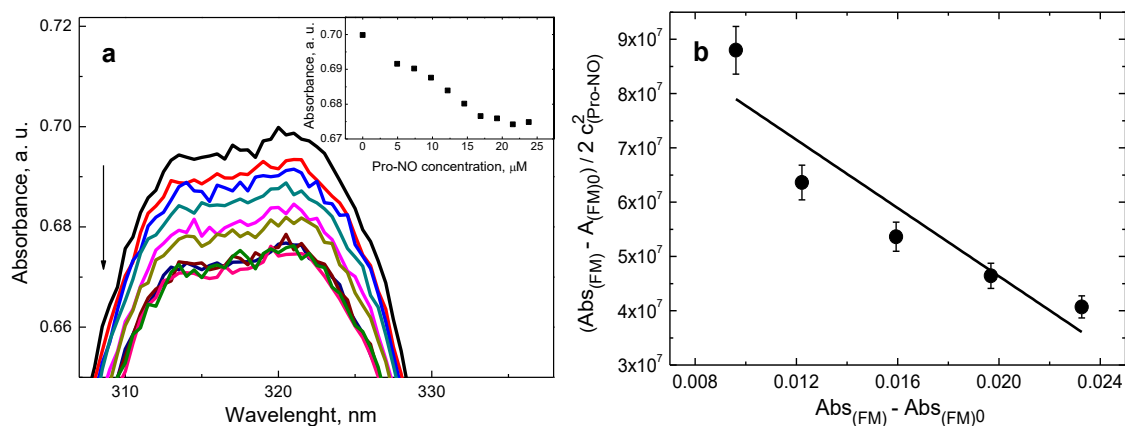
Figure 3.1-1. (a) The steady-state UV-vis spectra for the FM 2 quenched with the Pro-NO titrant at the Pro-NO concentration of 4.95 to 23.81 µM. The initial FM 2 concentration was 31.25 µM. Inset is the FM 2 absorbance dependence on the Pro-NO concentration at $\lambda = 320$ nm. (b) The Scatchard plot for the Pro-NO concentration range of 4.95 to 14.56 µM.

3.1.3 Preparing (Pro-NO)-templated MIP film

For the synthesis of a (Pro-NO)-templated MIP film and this film's simultaneous deposition on a 1-mm diameter Pt disk electrode surface (Figure 3.1-2) or a QCR surface (Figure 3.1-3), the pre-polymerization complex solution of FM 2, Pro-NO, CM 1, and (TBA)ClO$_4$ in acetonitrile was prepared as described in Section 2.2.1.6 above. Then, this solution was used for potentiodynamic electropolymerization in the potential range of 0 to 1.3 V vs. Ag quasi-reference electrode. The anodic peak at ~1.20 V vs. Ag quasi-reference electrode during polymer formation could be attributed to the electro-oxidation of bithiophene moieties of the FM 2 and CM 1 as thiophenes can electropolymerize in the positive potential range via the formation of a radical cation.[307] Moreover, the peak current increase in each consecutive current-potential cycle demonstrated that the electrode was coated with a conductive MIP film. The (Ac-Pro)-templated MIP films were deposited on the electrodes' surfaces under conditions the same as the (Pro-NO)-MIP films (data not shown).

110
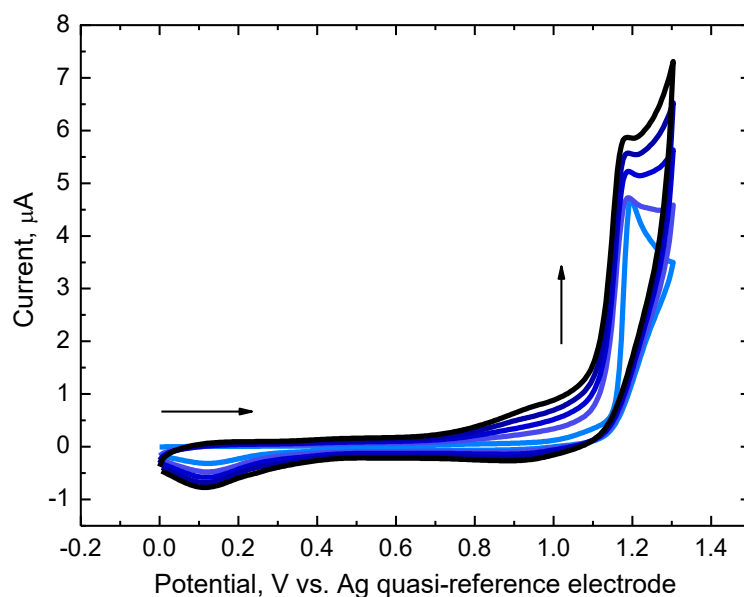
Figure 3.1-2. The current-potential curves for simultaneous electropolymerization and (Pro-NO)-templated MIP film deposition on a 1-mm diameter Pt disk electrode from 50 μM Pro-NO, 100 μM FM 2, and 500 μM CM 1 in 100 mM (TBA)ClO$_4$ in acetonitrile solution. The potential scan rate was 50 mV s^{-1}.

Moreover, the (Pro-NO)-MIP film was deposited on the gold electrode of the QCR under conditions the same as those described above for PM experiments. The resonance frequency and dynamic resistance changes were simultaneously recorded during potentiodynamic electropolymerization. The decrease in the oscillation frequency (Figure 3.1-3b), i.e., the QCR mass increase at positive potentials, indicated successful polymer film deposition on the QCR. These changes were comparable in each consecutive cycle, demonstrating that similar polymer mass was deposited in each polymerization cycle. The frequency drop was accompanied by a slight increase in dynamic resistance ranging several dozen ohms (Figure 3.1-3c). The latter indicated a slight change in viscosity and (or) polymer density. Evidently, MIP film rigidity did not change significantly after electropolymerization. Then, the mass of the deposited (Pro-NO)-MIP film was calculated (~3.19 μg) using the Sauerbrey equation (Equation 2.3-34 in Section 2.3.4 above) derived for rigid thin films with viscoelasticity effects ignored.[373, 392-394]

Furthermore, control NIP films were deposited on the surface of the Pt disk electrode and Au electrode of QCR in the same manner as MIP films but without the Pro-NO template in the pre-polymerization complex solutions.

For XPS, PM-IRRAS, and AFM measurements, (Pro-NO)-MIP and NIP films were prepared and deposited on Au-layered glass slides similarly to that for polymers deposited on the Pt disk and Au-QCR electrodes.
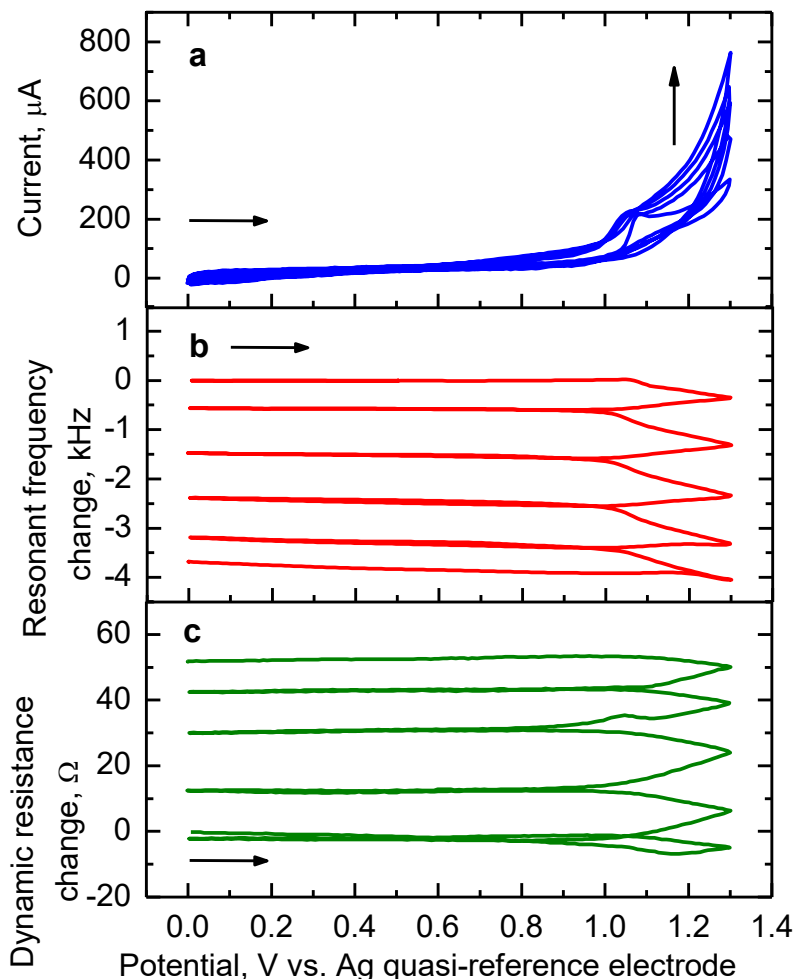
Figure 3.1-3. Simultaneously recorded five-cycle curves of (a) current, (b) resonant frequency change, and (c) dynamic resistance change vs. the potential for potentiodynamic electropolymerization, leading to deposition of the (Pro-NO)-MIP film on the gold electrode of QCR from a solution of 50 µM Pro-NO, 100 µM FM 2, 500 µM CM 1, and 100 mM (TBA)ClO$_4$ in acetonitrile.

3.1.4 Template extracting from (Pro-NO)-MIP films

The Pro-NO template was removed from the (Pro-NO)-MIP film deposited on the Pt disk electrode surface by extraction with a basic solution for subsequent determining the Pro-NO analyte. For that, first, the DPV peak was recorded at the (Pro-NO)-MIP film-coated electrode immersed in the 0.1 M K$_4$[Fe(CN)$_6$] and 0.1 M K$_3$[Fe(CN)$_6$] redox probe in 0.1 M phosphate buffer, PB (pH = 7.0). Then, the electrode coated with

112

the (Pro-NO)-MIP film was transferred to 0.1 M NaOH for a predetermined time and then again immersed in a solution of the redox probe. The procedure was repeated until the DPV peak height remained constant (Figure 3.1-4). Apparently, the Pro-NO template presence in molecular cavities of the MIP film hampered the redox probe diffusion to the surface of the electrode (curve *1* in Figure 3.1-4). Nonetheless, template extraction from the MIP film resulted in the increase of faradaic current for the redox probe oxidation (curves *2* and *3* in Figure 3.1-4), suggesting enhanced diffusion of the $[Fe(CN)_6]^{4-}/[Fe(CN)_6]^{3-}$ probe to the surface of the electrode. The DPV peak of the probe did not change after 20 min of extraction with 0.1 M NaOH (curve *4* in Figure 3.1-4). Therefore, DPV measurements were used as indirect confirmation for Pro-NO removal from MIP film, and thus a 20 min time was selected for extraction before further measurements.

The Ac-Pro "dummy" template was removed from the polymer film in the same manner as the Pro-NO template from (Pro-NO)-MIP film (data not shown).
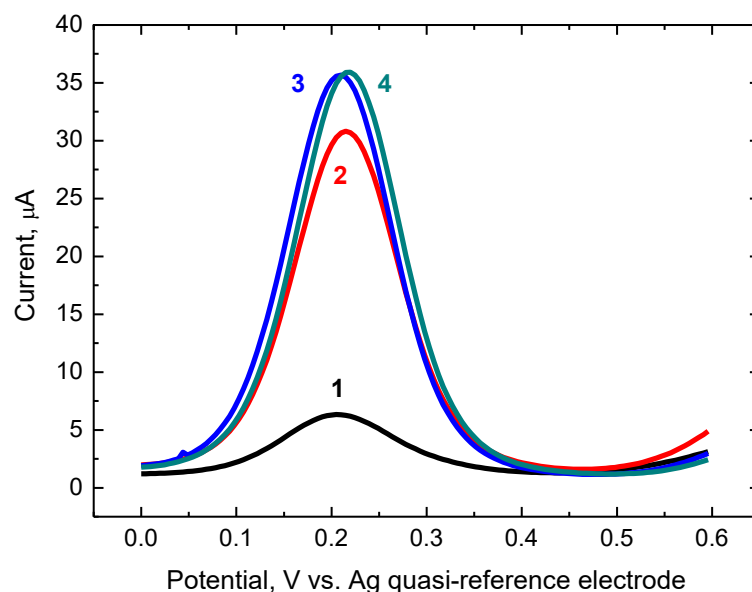
Figure 3.1-4. Differential pulse voltammograms recorded at the 1-mm diameter Pt disk electrode coated with the (Pro-NO)-MIP film in the presence of 0.1 M K$_3$[Fe(CN)$_6$] and 0.1 M K$_4$[Fe(CN)$_6$] redox probe in 0.1 M PB (pH = 7.0) (curve *1*) before and after (curve *2*) 10, (curve *3*) 20, and (curve *4*) 30 min of Pro-NO template extraction with 0.1 M NaOH.

Moreover, XPS experiments (Figure 3.1-5) were performed for the (Pro-NO)-MIP film to confirm the complete removal of the template from the polymer. Two N 1s peaks in the electron binding energy (*BE*) region of ca. 398 to 400 eV were present

in the XPS spectrum of the Au-layered glass slide coated with the (Pro-NO)-MIP film (Figure 3.1-5a). They revealed successful Pro-NO imprinting because only the Pro-NO molecule contains the nitrogen atom in its structure. The disappearance of these nitrogen peaks from the XPS spectrum for the MIP film-coated slide after 20-min extraction with 0.1 M NaOH confirmed that the Pro-NO template was entirely removed from the film (Figure 3.1-5b).
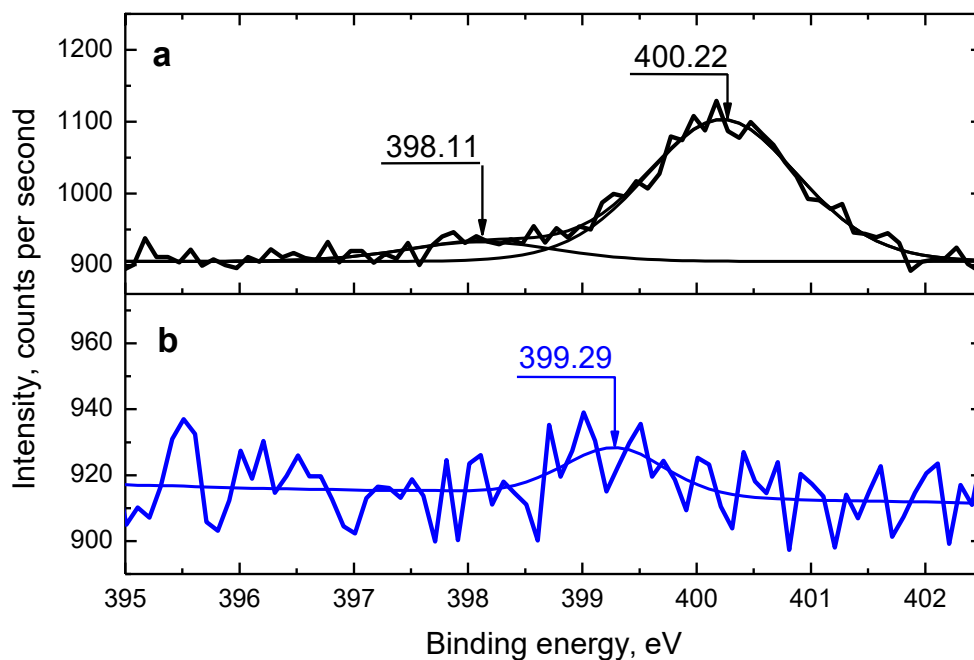
Figure 3.1-5. The high-resolution XPS spectra of nitrogen 1s for the (Pro-NO)-MIP film deposited on the Au-layered glass slide (a) before and (b) after Pro-NO template extraction with 0.1 M NaOH for 20 min.

3.1.5 AFM and PM-IRRAS characterizing the (Pro-NO)-MIP and NIP films

The AFM imaging unraveled (Pro-NO)-MIP and NIP films' morphology (Figures 3.1-6a to 3.1-6c). The surface of polymers deposited on the Au-layered glass slide was somewhat irregular, composed of many grains with diameters ranging from 20 to 60 nm. The AFM imaging demonstrated that the MIP film morphology only slightly changed after Pro-NO template extraction. The thickness and roughness of the MIP film before Pro-NO template removal were estimated as 154 ($\pm$8) and 29.3 nm, respectively, whereas the thickness and roughness of the (Pro-NO)-extracted MIP film were 161 ($\pm$5) and 26.2 nm, respectively.

114
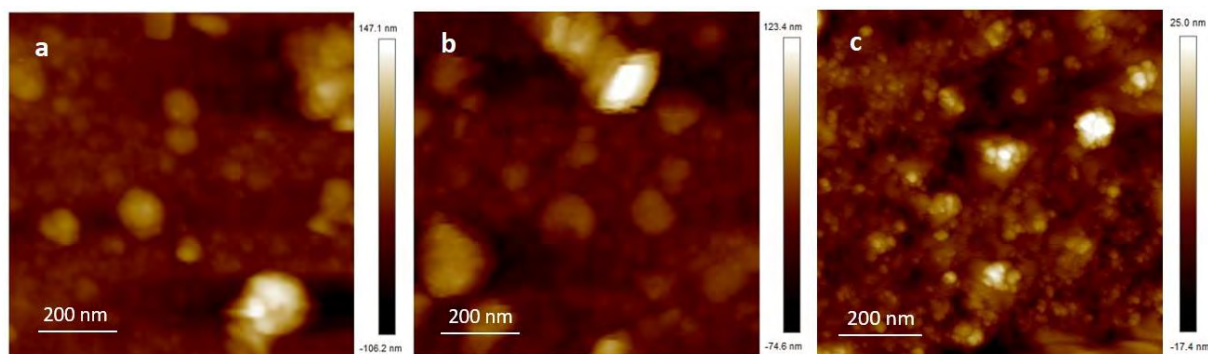
Figure 3.1-6. The (1.0×1.0) μm^2 AFM images of the (Pro-NO)-MIP film (a) before and (b) after Pro-NO template extraction with 0.1 M NaOH for 20 min, as well as (c) corresponding non-imprinted polymer (NIP) deposited on Au-layered glass slides.

Advantageously, PM-IRRAS spectra recorded for (Pro-NO)-MIP and NIP films (Figures 3.1-7a to 3.1-7c) revealed the presence of a band at ~2900 cm^{-1} characteristic for C–H aromatic stretching vibrations, as well as bands at 1250–1100 and 780 cm^{-1} typical for in-plane and out-of-plane C–H aromatic bending vibrations of the thiophene ring.[395-396]
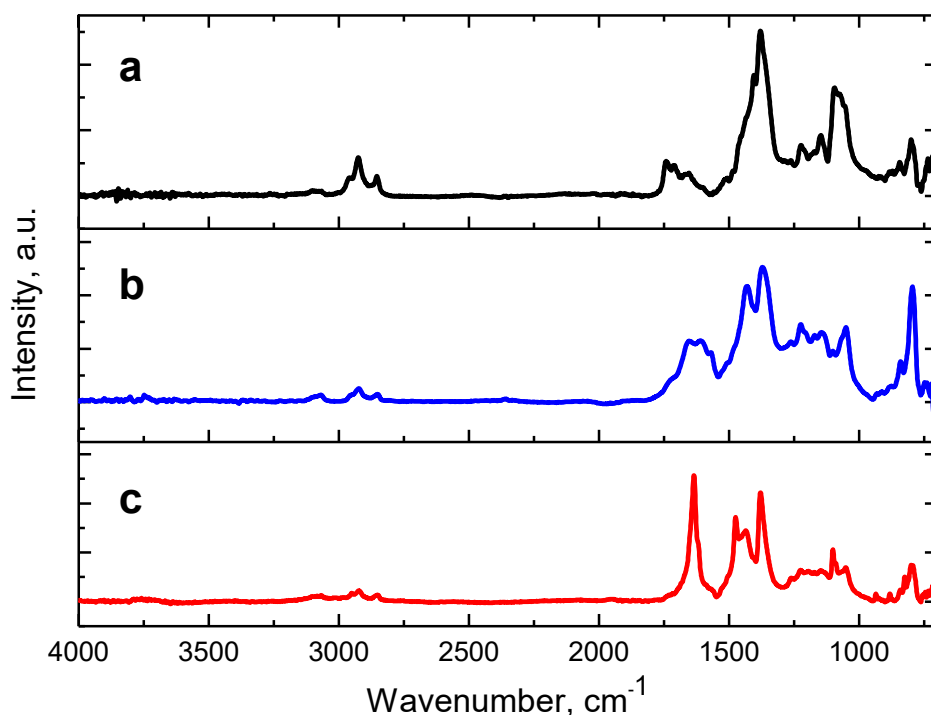
Figure 3.1-7. The PM-IRRAS spectra of the (Pro-NO)-MIP film (a) before and (b) after the Pro-NO template removal from the MIP film with 0.1 M NaOH for 20 min, as well as the PM-IRRAS spectrum of (c) the control NIP film.

The appearance of these bands in spectra confirmed the presence of the polythiophene chains of the polymers deposited on the Au-glass slides. Moreover, an intensive band in the 1100–1050 cm^{-1} region characteristic for N–N stretching vibration of template's *N*-nitroso group[397] was present in the spectrum for the MIP film imprinted with (Figure 3.1-7a). Importantly, PM-IRRAS spectra for the (Pro-NO)-extracted MIP and NIP films showed that the relative intensity of this band markedly decreased (Figures 3.1-7b and 3.1-7c), signifying that Pro-NO was extracted from the film. Additionally, the intensity of the band at 1320 cm^{-1}, typical for N=O stretching vibration of nitrosamines,[395, 397] was weakened in PM-IRRAS spectra recorded for (Pro-NO)-extracted MIP and NIP films, confirming the removal of the Pro-NO template from the (Pro-NO)-MIP film (Figures 3.1-7a and 3.1-7b).

3.1.6 Analytical performance of the (Ac-Pro)-MIP and (Pro-NO)-MIP chemosensors

3.1.6.1 *Selectivity of different pre-polymerization complexes*

Different functional monomers and templates were examined during the initial research stage regarding MIP films' preparation. The performance of MIP sensors based on Ac-Pro "dummy" template complexes with two different functional monomers, vis., FM 1 and FM 2, was analyzed by DPV. Even though computational calculations' results were promising (Table 3.1-1), the MIP chemosensor prepared with the Ac-Pro template and FM 1 was not selective in DPV measurements (Figure 3.1-8a). Presumably, the FM 1 molecule bearing two binding sites might adjust its conformation inside the MIP cavity and effectively interact not only with the Ac-Pro analyte but also with compounds of similar structures. Furthermore, the MIP chemosensor prepared with the Ac-Pro template and FM 2 proved more selective than the former chemosensor (Figure. 3.1-8b). However, the geometric fit of the Pro-NO analyte molecule to the imprinted cavity, thus the highest selectivity, was the best for the MIP film prepared with FM 2 as the functional monomer, Pro-NO as the template, and 5,5',5"-methanetriyltris(2,2'-bithiophene), CM 1, as the cross-linking monomer (Figure 3.1-9). Thus, this optimized MIP composition was chosen for further experiments.
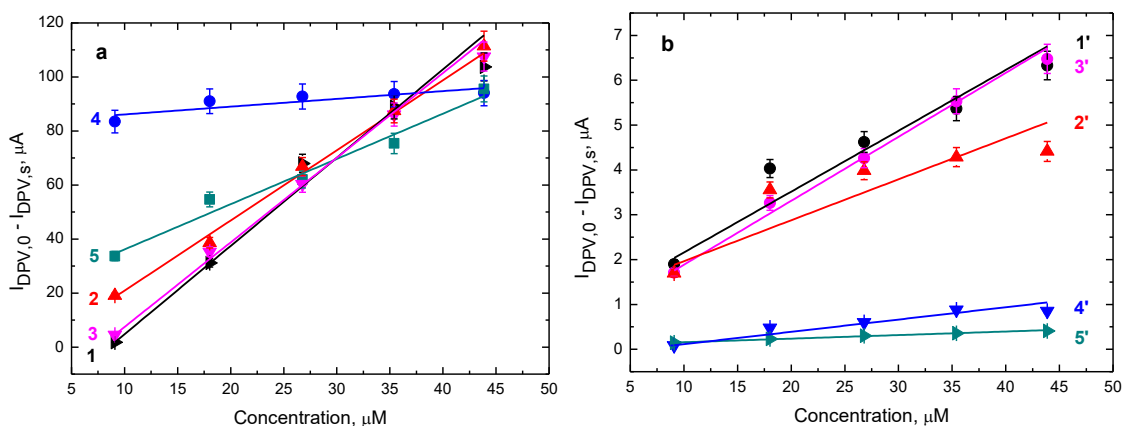
Figure 3.1-8. Calibration plots for (curves *1* and *1'*) Ac-Pro, (curves *2* and *2'*) creatinine, (curves *3* and *3'*) adrenalin, (curves *4* and *4'*) urea, (curve *5* and *5'*) glucose constructed for the Pt disk electrodes coated with MIP films prepared using either (a) FM 1 or (b) FM 2 as functional monomers and Ac-Pro as the template. The experiments were performed in the presence of the redox probe, 0.1 M $K_3[Fe(CN)_6]$ and 0.1 M $K_4[Fe(CN)_6]$, in 0.1 M PB (pH = 7.0).

3.1.6.2 *Differential pulse voltammetry (DPV) determining the Pro-NO with the (Pro-NO)-MIP film chemosensor*

DPV measurements were performed to determine the Pro-NO analyte under stagnant-solution conditions. The DPV peaks (Figure 3.1-9a) were recorded at the Pt disk electrode coated with the template-extracted (Pro-NO)-MIP film after each addition of a Pro-NO solution sample to the test solution of 0.1 M $K_4[Fe(CN)]_6$ and 0.1 M $K_3[Fe(CN)]_6$ in PB (pH = 7.0). The DPV peak of the redox probe decreased with the Pro-NO concentration increase (Figure 3.1-9a). Apparently, the interaction of Pro-NO binding sites with molecular cavities in the MIP limited the diffusion of the redox probe through the MIP film, resulting in a drop in the faradaic current of the redox probe. The "gate effect" was used for signal transduction to determine the analyte indirectly.[398] In the DPV experiments, the (Pro-NO)-MIP chemosensor response to the analyte was linear in the concentration range of 9.1 to 43.9 μM (Figure 3.1-9b). It obeyed the linear regression equation of $I_{DPV,0} - I_{DPV,s}$ [μA] = 3.0 (±0.2) [μA] + 0.094 (±0.008) $c_{(Pro-NO)}$ [μM] with the correlation coefficient, $R^2 = 0.971$, and LOD = 80.9 nM at a signal-to-noise ratio, $S/N = 3$. Furthermore, the apparent *IF* was determined to confirm the formation of selective molecular cavities in the (Pro-NO)-MIP film. Since the NIP chemosensor DPV response was completely insensitive to Pro-NO, the *IF* calculated as the ratio of the MIP chemosensor's

117

sensitivity to the NIP chemosensor's sensitivity exceeded 20. This enormously high value implied the polymer matrix's homogenous distribution of recognition sites. Moreover, the (Pro-NO)-MIP chemosensor selectivity was examined. The selectivity for interferences that can accompany Pro-NO in real samples or have similar structures to Pro-NO, namely, creatinine, adrenalin, urea, and glucose, were determined as 2.1, 2.0, 6.6, and 13.2, respectively. The DPV chemosensor's selectivity to urea and glucose was high because these compounds are structurally different from the analyte. However, selectivity to interferences with a size and arrangement of functional groups similar to Pro-NO, i.e., creatinine and adrenalin, were lower.
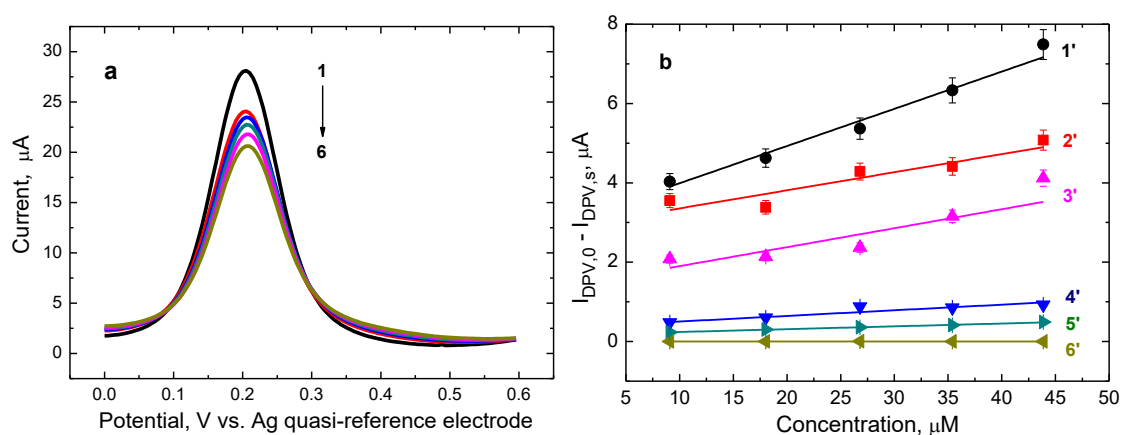
Figure 3.1-9. (a) The DPV curves for the redox probe, 0.1 M $K_3[Fe(CN)_6]$ and 0.1 M $K_4[Fe(CN)_6]$, in 0.1 M PB (pH = 7.0), recorded at the Pt disk electrode coated with the (Pro-NO)-MIP film (curve *1*) after extraction of Pro-NO template with 0.1 M NaOH for 20 min, and then in the presence of (curve *2*) 9.09, (curve *3*) 18.02, (curve *4*) 26.79, (curve *5*) 35.40, and (curve *6*) 43.86 μM Pro-NO. (b) Calibration plots for the (Pro-NO)-MIP film coated electrode for (curve *1′*) Pro-NO, (curve *2′*) creatinine, (curve *3′*) adrenalin, (curve *4′*) urea, (curve *5′*) glucose, and (curve *6′*) Pro-NO at the electrode coated with the control NIP film.

3.1.6.3 *Electrochemical impedance spectroscopy (EIS) determining the Pro-NO analyte with the (Pro-NO)-MIP chemosensor*

Moreover, EIS experiments were conducted to determine Pro-NO and analyze the chemosensor's response mechanism. EIS spectra were recorded at the (Pro-NO)-extracted MIP film-coated electrode under stagnant-solution conditions in the presence of the 0.1 M $K_4[Fe(CN)_6]/K_3[Fe(CN)_6]$ redox probe in 0.1 M PB (pH = 7.0). Nyquist plots constructed for the Pro-NO determination comprised well-pronounced semicircles with diameters representing the R_{ct} of the redox probe faradaic process in the high-frequency ranges and straight lines corresponding to the Warburg impedance in the low-

118

frequency region of spectra (Figure 3.1-10a). Notably, the slopes of these lines were independent of the Pro-NO concentration, suggesting that Pro-NO binding to the MIP film did not affect the redox probe diffusion through the polymer to the electrode surface. The EIS data were interpreted using a modified Randles-Ershler equivalent circuit, $R_s + CPE/(R_{ct} + W)$, where R_s, CPE, R_{ct}, and W are solution resistance, constant phase element, charge transfer resistance, and Warburg impedance, respectively. The R_{ct} of the MIP film linearly increased with the Pro-NO analyte concentration increase from 9.1 to 43.9 μM (Figure 3.1-10b). This dependence was characterized by the linear regression equation of ΔR_{ct} [Ω] = 112 (±12) [Ω] + 8.6 (±0.4)$c_{(Pro-NO)}$ [μM] with the correlation coefficient, $R^2 = 0.991$. For Pro-NO, LOD was equal to 36.9 nM at $S/N = 3$. The selectivity factors for urea, adrenalin, glucose, and creatinine were 2.3, 2.6, 2.3, and 3.2, respectively.
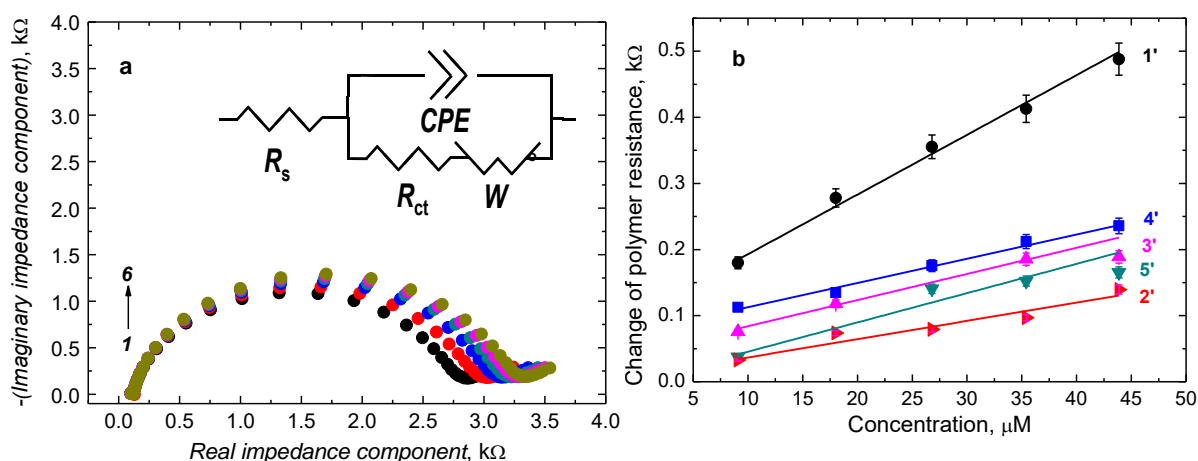
Figure 3.1-10. (a) The EIS spectra recorded in the presence of the redox probe, 0.1 M $K_3[Fe(CN)_6]$ and 0.1 M $K_4[Fe(CN)_6]$, in 0.1 M PB (pH = 7.0), for the Pt disk electrode coated with (Pro-NO)-MIP film (curve *1*) after extraction of Pro-NO template with 0.1 M NaOH for 20 min, and then in the presence of (curve *2*) 9.09, (curve *3*) 18.02, (curve *4*) 26.79, (curve *5*) 35.40, and (curve *6*) 43.86 μM Pro-NO. (b) Calibration plots for (Pro-NO)-MIP coated electrode for (curve *1'*) Pro-NO, (curve *2'*) creatinine, (curve *3'*) adrenalin, (curve *4'*) urea, and (curve *5'*) glucose.

3.1.6.4 Piezoelectric microgravimetry (PM) determining Pro-NO under flow-injection analysis (FIA) conditions

Moreover, the (Pro-NO)-MIP chemosensor analytical performance was studied with PM under FIA conditions. With time, resonance frequency changes were consecutively recorded at QCRs coated with (Pro-NO)-extracted MIP and NIP films. Resonance

119

frequency decreased after each injection of the Pro-NO solution sample to the 0.1 M PB, pH = 7.0, carrier solution (Figure 3.1-11a). This decrease indicates analyte binding to MIP cavities and, thus, a polymer mass increase, according to the Sauerbrey equation (Equation 2.3-34 in Section 2.3.4). After reaching the minimum at −5.5 Hz for the 2-mM Pro-NO injection, corresponding to polymer mass increase by 0.48 ng, the frequency returned to its baseline level, confirming Pro-NO elution from the MIP film by the carrier solution. Resonant frequency changes were linearly dependent on the Pro-NO concentration in the range of 0.125 to 2.0 mM, satisfying the linear regression equation of Δf [Hz] = $-0.9(\pm0.1)$ [Hz] $- 2.3(\pm0.1)\,c_{(Pro-NO)}$ [mM] with the correlation coefficient, $R^2 = 0.989$ and LOD $= 10\,\mu M$ at $S/N = 3$ (curve *1* in Figure 3.1-11b). Notably, the response of the NIP film deposited on the QCR was very low (curve 2 in Figure 3.1-11b). Thereby, the *IF*, calculated as the ratio of calibration curves' slopes constructed for MIP and NIP films, exceeded 20, thus indicating the formation of MIP cavities with a high affinity to Pro-NO molecules.
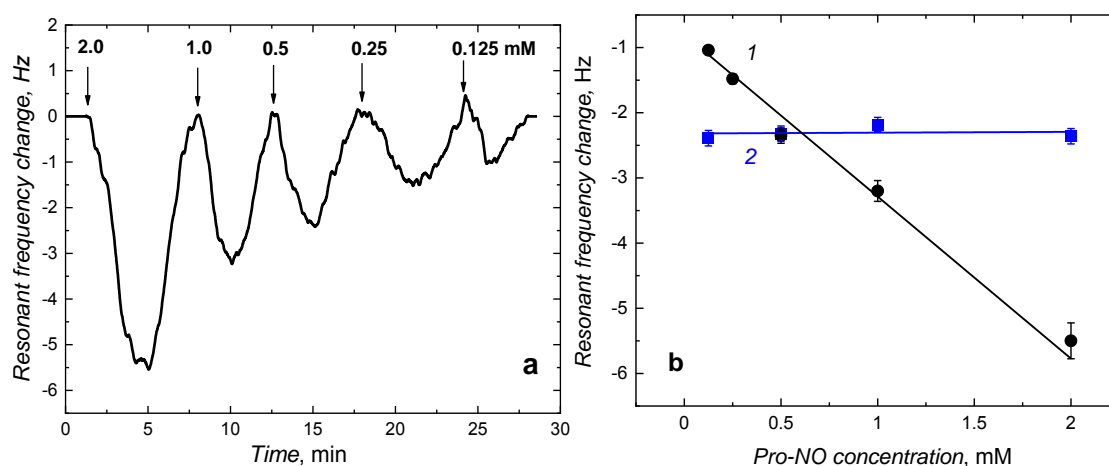
Figure 3.1-11. (a) The resonant frequency changes with time for consecutive FIA injections of 100 mL Pro-NO samples for (Pro-NO)-MIP film-coated Au-QCR. (b) Calibration curves for Pro-NO determined at the (curve *1*) MIP and (curve *2*) NIP films. The flow rate of the 0.1 M PB (pH = 7.4) carrier solution was 35 μL min^{-1}.

3.1.7   Pro-NO determining in real samples of meat

Finally, Pro-NO was determined in grilled pork neck samples to verify the usefulness of the devised (Pro-NO)-MIP film chemosensor in analyzing food of animal origin. DPV peaks were recorded after adding Pro-NO solution to the real sample prepared according to the procedure described in Section 2.2.1.13 above. The analyte concentration determined in meat samples was compared to those obtained in PB and

summarized in Table 3.1-2. The calculated Pro-NO recovery ranged from 77% to 118%, demonstrating that (Pro-NO)-MIP film chemosensor is a sufficient tool for Pro-NO determination in food samples.

Table 3.1-2. Pro-NO determination in grilled pork neck samples with the (Pro-NO)-MIP film chemosensor.

Sample No.	Known Pro-NO concentration, µM	DPV peak recorded at the electrode coated with (Pro-NO)-MIP film, µA	Determined Pro-NO concentration, µM	Recovery, %
1.	8.66	11.7 ± 0.6	-	-
2.	17.21	12.8 ± 0.6	20 ± 7	118 ± 39
3.	25.27	13.2 ± 0.7	25 ± 7	98 ± 27
4.	33.80	13.6 ± 0.7	29 ± 7	87 ± 21
5.	42.37	13.9 ± 0.7	33 ± 7	77 ± 17

3.2 MIP-based electrochemical sensor for selective *p*-synephrine determining and detailed investigating the "gate effect" mechanism

The present section of Chapter 3 covers our results of both calculations and experiments performed to devise an MIP film chemosensor for the potentially hazardous dietary supplement, *p*-synephrine (SYN), and a comprehensive investigation of the "gate effect" mechanism related to conductive MIP film-coated electrodes. Electrochemical determination of electroinactive analytes generally requires using an external redox probe that generates an electrochemical signal. Presumably, an MIP film may swell or shrink as a result of analyte binding, thus leading to changes in the permittivity of a redox probe through the film and, consequently, changes in the redox probe faradaic current in CV and DPV measurements.[267-269, 399] This phenomenon, the so-called "gate effect," responsible for enhanced or, more frequently, hindered diffusion of the redox probe, accounts for the operation of all chemosensors based on MIP films. Furthermore, the adsorption of large nonconductive molecules on the electrode surface,

121

leading to physical electrode blocking, may be responsible for another possible mechanism for the hindered diffusion of redox probes through a polymer.[280-282] Nevertheless, the above mechanisms do not include all conceivable phenomena that might explain electrochemical signal change due to MIP binding of the analyte. Therefore, to study the "gate effect," a functionalized polythiophene imprinted with SYN was used as a model MIP film. For analyzing possible mechanisms responsible for current changes recorded at the SYN-MIP film-coated electrode corresponding to SYN analyte binding, several techniques, including CV, DPV, EIS, SPR, and UV-vis spectroscopy, were engaged.

Moreover, in situ AFM imaging determined the MIP film thickness in both the absence and presence of the SYN. Furthermore, the decrease in the signal for the redox probe, recorded at the semiconductive SYN-MIP film-coated electrode, with the increase in the SYN analyte concentration did not originate from swelling or shrinking of the polymer but from the decrease in the polymer's conductivity. Presumably, this effect resulted from the decrease in the mobility of SYN-MIP film's radical cations (polarons).

3.2.1 Quantum-chemical modeling of the structure of the pre-polymerization complex of SYN with chosen functional monomers

The structure of a stable pre-polymerization complex of the SYN template with selected functional monomers was predicted via computational modeling. To this end, 2,2'-bithiophene-5-carboxylic acid (FM 3) was chosen as the functional monomer capable of interacting with the SYN binding sites. FM 3 bears a carboxyl group that can be dissociated in an aprotic polar solvent solution, e.g., acetonitrile, and the resulting carboxylate group may form hydrogen bonds with SYN hydroxyl groups. Moreover, FM 3's carboxylate group and SYN's positively charged amine group may interact electrostatically. Therefore, structures of pre-polymerization complexes of the SYN template with the FM 3 functional monomer at different molar ratios and interacting compounds' arrangements were computationally modeled (Scheme 3.2-1) to validate the above assumptions. The calculated negative ΔG value was the highest in forming the pre-polymerization complex at the SYN : FM 3 molar ratio of 1 : 3 (-227.4 kJ mol^{-1}), indicating that the complex is sufficiently stable to survive electropolymerization and subsequent SYN template extraction. The structural formula and the DFT-optimized

122

structure of the pre-polymerization complex selected for further studies are shown in Scheme 3.2-2.
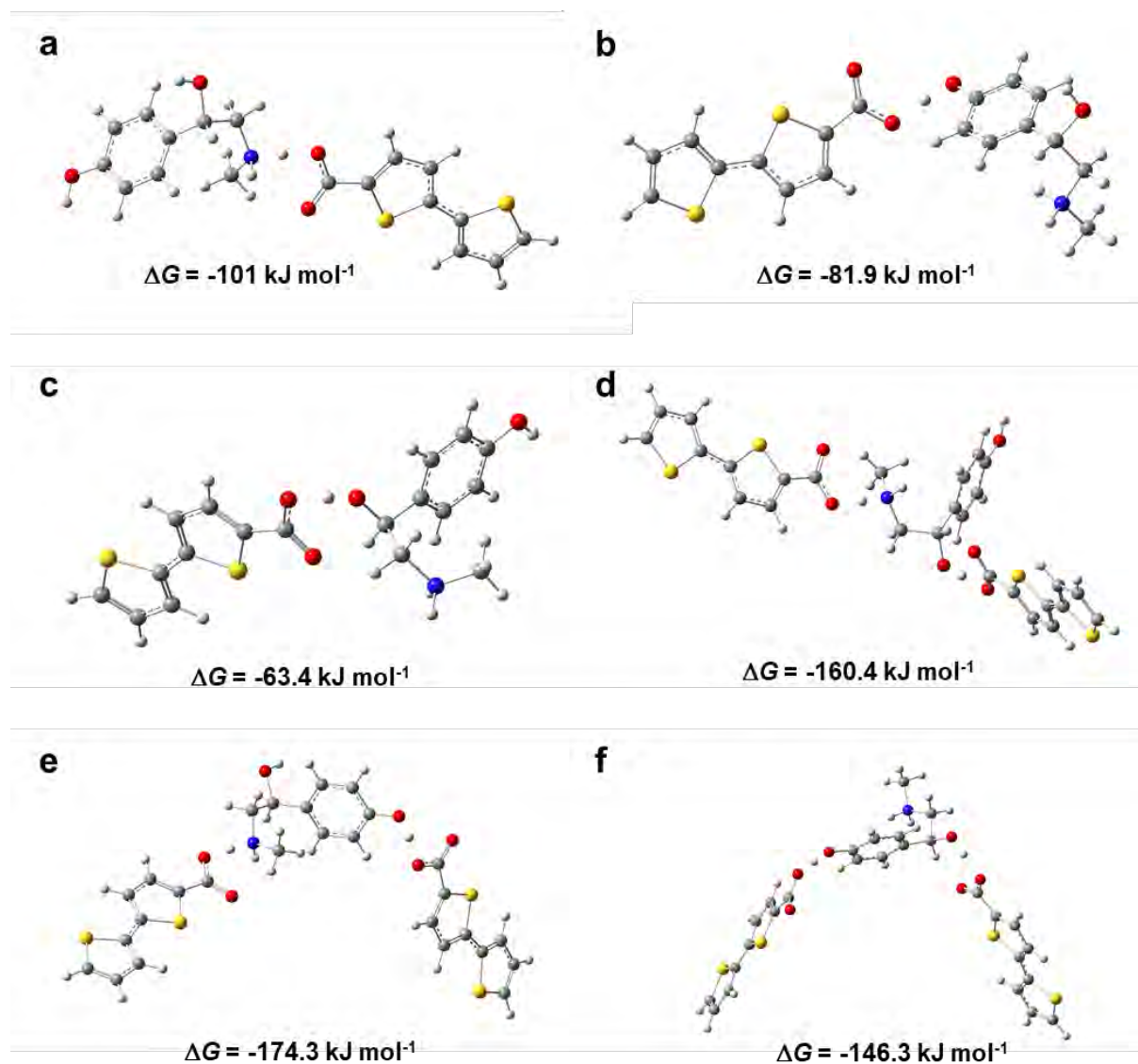
Scheme 3.2-1. The DFT-optimized structures of pre-polymerization complexes of the SYN template with the FM 3 functional monomer at (a–c) 1 : 1 and (d–f) 1 : 2 molar ratios with different spatial configurations of the molecules, as well as their corresponding Gibbs free energy changes. DFT calculations were performed for room temperature in acetonitrile using the B3LYP/6-31g(d) basis set of Gaussian 09 software.
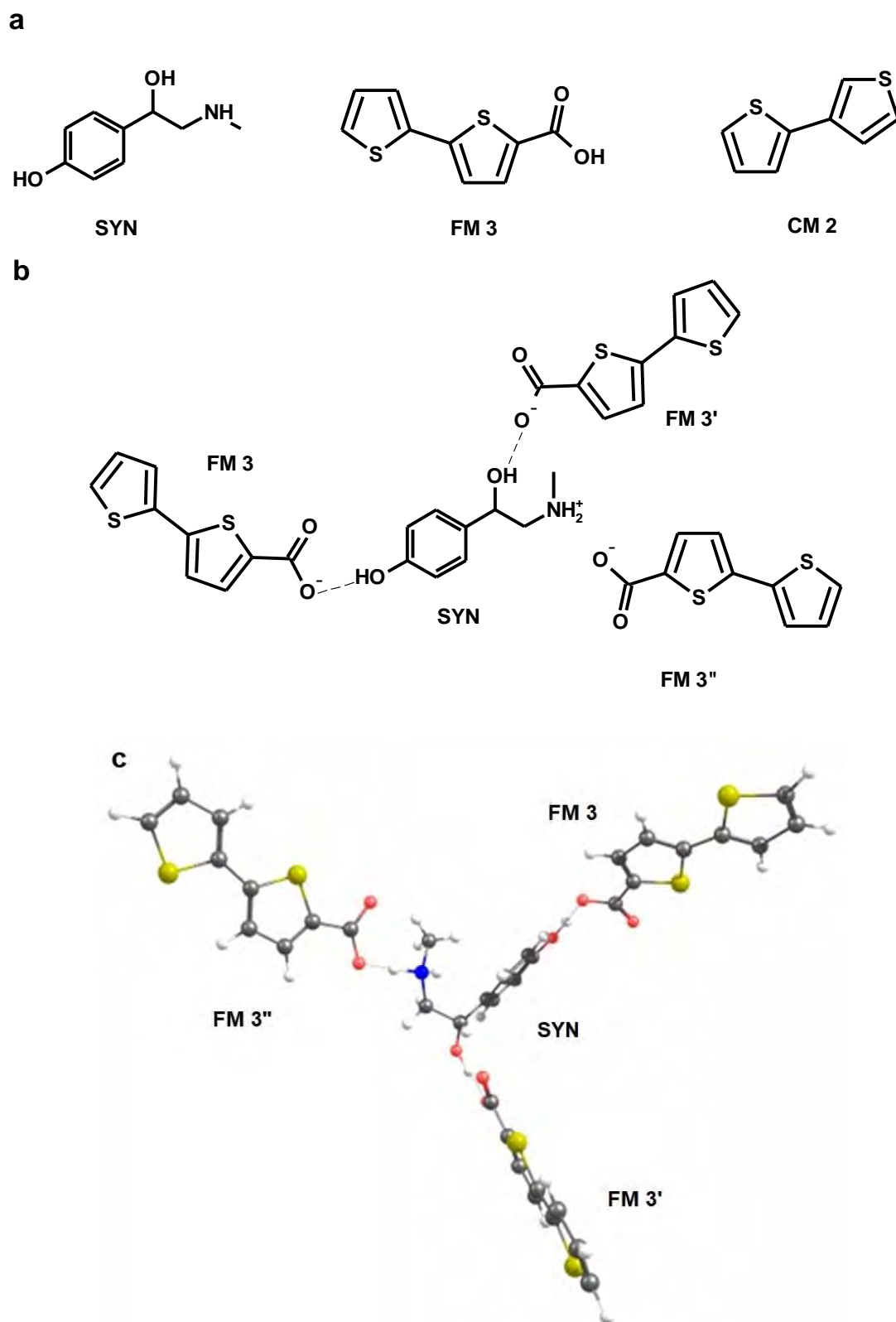
Scheme 3.2-2. (a) Structural formulas of the SYN template, FM 3 functional monomer, and CM 3 cross-linking monomer. (b) The structural formula, and (c) the DFT-optimized structure of the pre-polymerization complex of one SYN molecule with three FM 3 molecules. DFT calculations were performed for room temperature in acetonitrile at the B3LYP/6-31g(d) level using Gaussian 09 software.

124

3.2.2 SYN-MIP film preparation and subsequent SYN template removal from the SYN-MIP film

At an early research stage, before preparing the SYN-MIP film, the target SYN analyte electroinactivity was demonstrated with CV experiments (Figure 3.2-1). Otherwise, if the analyte was electroactive in a potential range similar to that of the functional monomer's electro-oxidation, there would be a high possibility that the product of the electrochemical reaction was imprinted instead of the analyte itself during the electropolymerization.[400-402] Moreover, such products might adsorb on the electrode surface, contaminating it. Thus, imprinting of electroactive analytes without any pretreatment is undesirable.

However, no peaks were observed on the CV curve recorded at the bare electrode immersed in an SYN solution of 0.1 M (TBA)ClO$_4$ in acetonitrile (Figure 3.2-1), indicating that SYN was not electro-oxidized or electroreduced in the potential range of 0 to 1.3 V vs. Ag quasi-reference electrode.
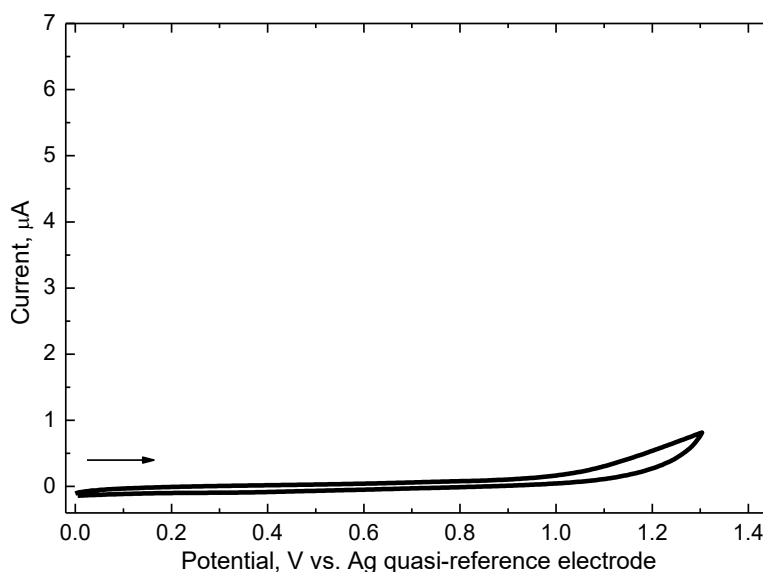
Figure 3.2-1. Cyclic voltammogram for 10 μM SYN in 0.1 M (TBA)ClO$_4$ in acetonitrile recorded at a 1-mm diameter Pt disk electrode at a 50-mV s^{-1} scan rate.

For the simultaneous preparation of SYN-templated MIP film and its deposition on the 1-mm diameter Pt disk electrode (Figure 3.2-2), a pre-polymerization complex of the SYN template with the FM 3 functional monomer was electropolymerized under potentiodynamic conditions in the presence of the CM 2 cross-linking monomer in (TBA)ClO$_4$ in acetonitrile, as described in Section 2.2.1.7 above. The anodic peak

125

at 1.20 V vs. Ag quasi-electrode in the first cycle in the curve in Figure 3.2-2 corresponds to electro-oxidation of the 2,2′- and 2,3′-bithiophene moieties of the FM 3 and CM 2, resulting in the formation of radical cations.[307] Afterward, the current increased in the potential range of 1.0 to 1.10 V vs. Ag quasi-reference in consecutive current-potential curves, manifesting the readily electro-oxidizable oligothiophene and (or) polythiophene chains formation. Moreover, the current increase in subsequent cycles during the SYN-MIP film deposition on the electrode surface demonstrated that the deposited polymer was conductive.
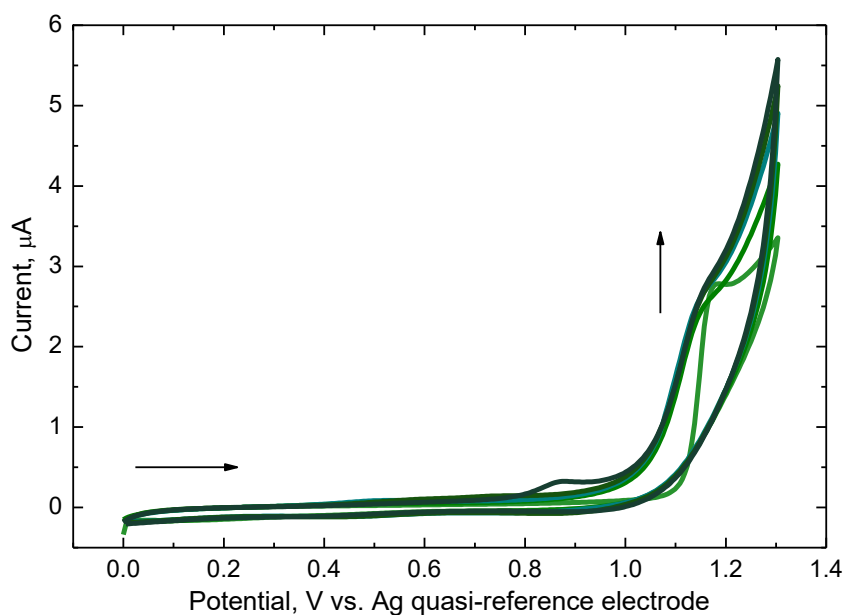
Figure 3.2-2. Five-cycle current vs. potential curves for SYN-templated MIP film deposition on a 1-mm diameter Pt disk electrode by potentiodynamic electropolymerization at 50 mV s^{-1} from the acetonitrile solution of 10 μM SYN template, 30 μM FM 3, 300 μM CM 2, and 100 mM (TBA)ClO$_4$.

Further, the Pt disk electrode and the Au-layered glass slide were coated with corresponding NIP films under conditions the same as for MIP films but in the SYN absence in the pre-polymerization complex solutions.

Subsequently, the SYN template was extracted from the SYN-MIP film to vacate its imprinted cavities. For that, the (SYN-MIP film)-coated electrode was immersed in 0.1 M NaOH for 80 min. DPV measurements of 0.1 M K$_4$[Fe(CN)$_6$] and 0.1 M K$_3$[Fe(CN)$_6$] redox probe in PBS (pH = 7.4) monitored the extraction progress using the "gate effect" described in Section 3.1-4 above. The probe DPV peak remained the same after 60-min SYN extraction, indicating successful SYN removal from the MIP film (Figure 3.2-3).

126
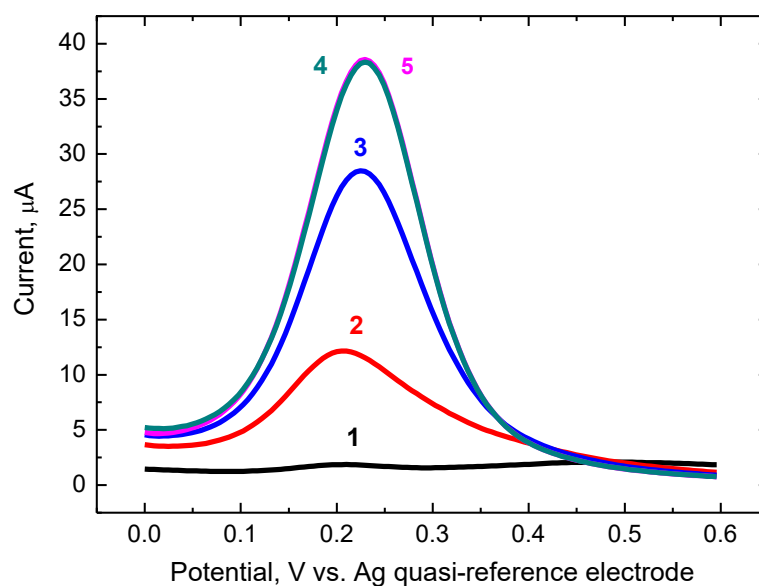
Figure 3.2-3. DPV curves recorded for the SYN-MIP film-coated Pt disk electrode (curve *1*) before and after SYN template extraction with 0.1 M NaOH for (curve *2*) 20, (curve *3*) 40, (curve *4*) 60, and (curve *5*) 80 min. Measurements were carried out in the presence of the 0.1 M $K_4[Fe(CN)_6]$ and 0.1 M $K_3[Fe(CN)_6]$ redox probe in 0.1 M PBS (pH = 7.4).

For SPR measurements, SYN-MIP and NIP films were potentiodynamically deposited on Au-glass disks (Figures 3.2-4a and 3.2-4c). The acetonitrile solution for SYN-MIP preparation comprised a 5 μM SYN template, 15 μM FM 3, 150 μM CM 2, and 0.1 M (TBA)ClO$_4$. The NIP film was prepared under conditions like the MIP film but without the SYN template in the solution for electropolymerization. The current-potential curves recorded in the potential range of 0 to 1.30 V vs. Ag|AgCl corresponded to those for SYN-MIP deposition on the Pt disk electrode. The anodic peaks of electropolymerization appearing at ~1.20 V vs. Ag quasi-reference electrode indicated the electro-oxidation of the bithiophene moieties of the FM 3 and CM 2. However, the current decreased in subsequent cycles, substantiating the formation of comparatively resistive MIP and NIP films. Moreover, the polymer films' average thickness was estimated based on the SPR angle changes recorded during the deposition of SYN-MIP and NIP films (Figures 3.2-4b and 3.2-4d). The SYN-templated MIP film and NIP film thicknesses were determined as 17.6 and 27.1 nm, respectively.

Furthermore, the SYN template was removed from the SYN-MIP film by immersing the SYN-MIP film-coated SPR chip in 0.1 M NaOH for 60 min, as described above.

127
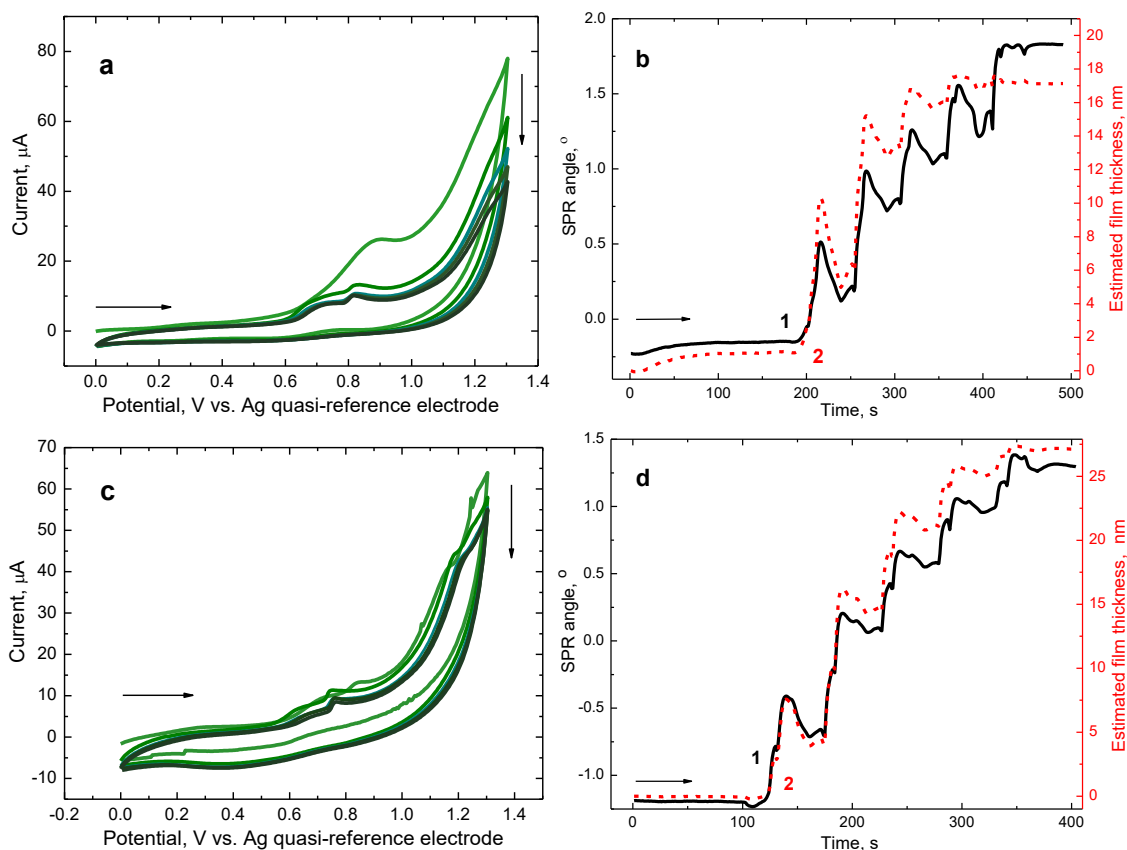
Figure 3.2-4. Five-cycle potentiodynamic curves for deposition of (a) the SYN-MIP film and (c) the corresponding NIP film on Au-layered SPR chips at a scan rate of 50 mV s^{-1} from the solution of 5 μM SYN template, 15 μM FM 3, 150 μM CM 2 and 0.1 M (TBA)ClO$_4$ in acetonitrile. (b) SYN-MIP and (d) NIP films' changes of (curves *1* and *1'*) SPR angle and (curves *2* and *2'*) estimated films' thickness with time during (b) SYN-MIP film and (d) NIP film potentiodynamic electrodeposition on the Au-glass disks.

For XPS, PM-IRRAS, and AFM measurements, Au-layered glass slides were coated with SYN-MIP and NIP films in the manner mentioned above for polymer films deposition on the disk and Au-QCR electrodes.

3.2.3 Characterizing SYN-MIP film and control NIP film

The MIP film imprinted with the SYN template before and after template extraction and the corresponding NIP film were examined by PM-IRRAS (Figure 3.2-5) and XPS (Table 3.2-1) to verify the films' chemical compositions. Moreover, the morphology of the MIP and NIP films was examined with AFM imaging (Figures 3.2-6a to 3.2-6c).

Advantageously, both PM-IRRAS and XPS experiments confirmed the deposition of MIP and NIP films on Au-layered glass slides. PM-IRRAS spectra recorded for SYN-MIP and NIP films (Figures 3.2-5a, 3.2-5b, and 3.2-5d) showed a strong band

128

at ~1700 cm^{-1}, corresponding to C=O stretching vibration[403] originating from the carboxyl group of FM 3. Importantly, this band is absent in the spectrum of SYN, drop-cast on the glass slide (Figure 3.2-5c). Moreover, bands in the region of ~2900 cm^{-1} and 1550–1200 cm^{-1} characteristic of C–H aromatic stretching vibrations and in-plane ring vibrations of thiophenes, respectively,[395-396] were present in PM-IRRAS spectra of MIP and NIP films (Figures 3.2-5a, 3.2-5b, and 3.2-5d). The presence of these bands confirmed the formation of the pre-polymerization complex and subsequent deposition of polymers on electrodes. Further, the MIP film spectrum after template removal (Figure 3.2-5b) was similar to that of the control NIP film (Figure 3.2-5d).
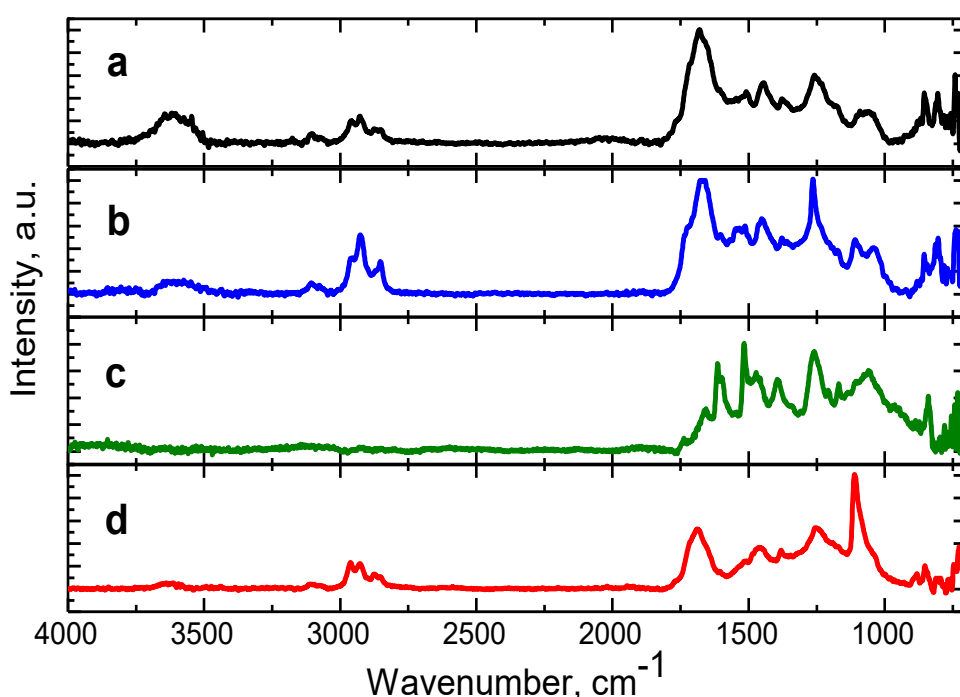
Figure 3.2-5. The PM-IRRAS spectra of the SYN-MIP film (a) before and (b) after removal of the SYN template from the polymer with 0.1 M NaOH for 60 min as well as the PM-IRRAS spectra of (c) SYN drop-cast on the surface of Au-layered glass slide and (d) the control non-imprinted polymer (NIP).

Moreover, XPS measurements showed that after 60 min of SYN extraction, the relative content of nitrogen and sulfur atoms in the SYN-MIP film respectively decreased and increased, thus confirming template removal from the polymer. That was because SYN was the only nitrogen source in the MIP.

Furthermore, SYN-templated MIP, SYN-extracted MIP, and NIP films were AFM imaged in the air to determine their morphology (Figures 3.2-6a to 3.2-6c). All samples were composed of well-defined grains with diameters of ~55 nm. Significantly, SYN

template extraction from the polymer did not influence the film's topography (Figure 3.2-6b).
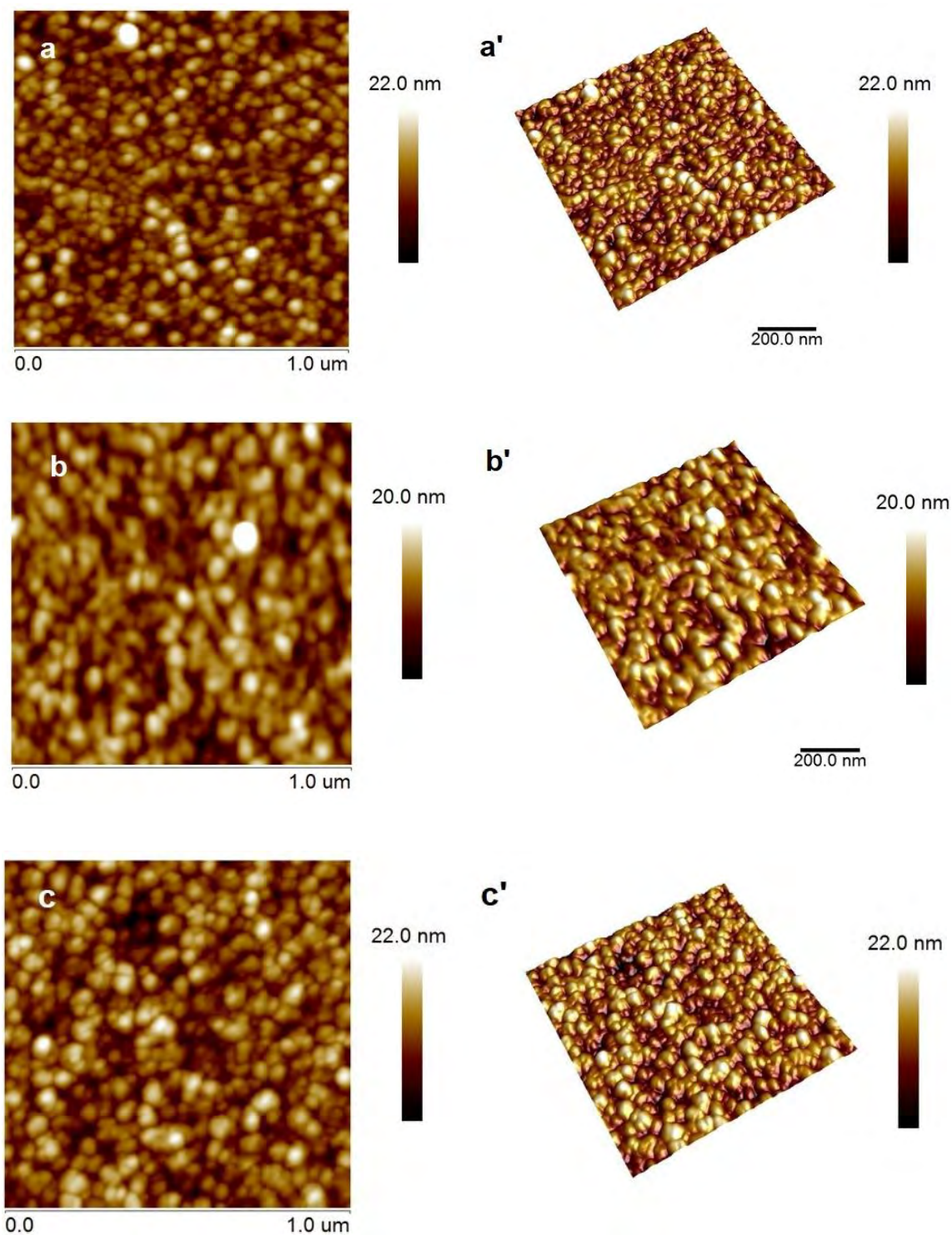
Figure 3.2-6. The (1 × 1) μm^2 AFM (a and b) 2-D and (a' and b') pseudo-(3-D) images of the SYN-MIP film before and after SYN template extraction, respectively, as well as the (1 × 1) μm^2 AFM (c) 2-D and (c') pseudo-(3-D) images of the NIP film.

Table 3.2-1. Surface elemental composition of the SYN-MIP and NIP films.

Element	NIP film	SYN-MIP film	
		before SYN template extraction	after SYN template extraction
		Concentration (atomic %)	
O	18.13	17.52	17.43
N	4.63	2.86	2.10
C	72.65	74.84	72.34
S	0.31	4.77	8.12
Cl	4.27		

3.2.4 Analytical performance of SYN-MIP chemosensor for SYN determination

3.2.4.1 *DPV determining the SYN analyte*

The MIP with emptied molecular cavities was used as the chemosensor recognition unit to determine the SYN analyte. DPV measurements were conducted for the indirect determination of SYN in 0.1 M PBS (pH = 7.4), actuating the "gate effect". In these measurements, a 0.1 M $K_4[Fe(CN)_6]/K_3[Fe(CN)_6]$ redox probe was used. The DPV peak of this redox couple at the SYN-extracted MIP film-coated Pt disk electrode decreased with the increase of the SYN concentration (Figure 3.2-7a). According to the previously-mentioned mechanism,[267-269, 399] analyte molecules enter MIP molecular cavities, hampering the redox probe diffusion through the polymer. The linear dynamic concentration ranged from 0.1 to 0.99 µM SYN (Figure 3.2-7b), with the calibration plot obeying the linear regression equation of $(I_{DPV,0} - I_{DPV,s})/I_{DPV,0} = 12 \times 10^{-2}(\pm 1 \times 10^{-2}) + 3.2 \times 10^{-4}(\pm 0.2 \times 10^{-4})\, c_{SYN}$ [nM]. The correlation coefficient and LOD at $S/N = 3$ was 0.979 and 12.2 nM, respectively. Notably, the SYN-MIP chemosensor was moderately selective to common interferences. That is, DPV-determined selectivity for urea, creatinine, adrenalin, and glucose were 2.05, 2.08, 2.63, and 2.46, respectively (Figure 3.2-7b). Moreover, SYN was determined with DPV at the Pt disk electrode coated with the NIP film (Figure 3.2-7c) to demonstrate successful imprinting. The control polymer (NIP) film-coated electrode was immersed in 0.1 M NaOH for 60 min before SYN determination to execute the same extraction procedure

as with the MIP film. The linear regression equation for SYN binding at the NIP was

$$(I_{DPV,0} - I_{DPV,s})/I_{DPV,0} = 7.5 \times 10^{-2}(\pm 0.5 \times 10^{-2}) + 1.19 \times 10^{-4}(\pm 0.08 \times 10^{-4}) \, c_{SYN} \, [nM]$$

with the correlation coefficient, $R^2 = 0.980$. The NIP film sensitivity was lower than that of the SYN-extracted MIP film (curve *2'* in Figure 3.2-7b), thus confirming the formation of high-affinity molecular cavities in the SYN-MIP. The apparent *IF*, calculated as the ratio of MIP and NIP film sensitivity to SYN (curves *1'* and *2'* in Figure 3.2-7b), was *IF* = 2.7.
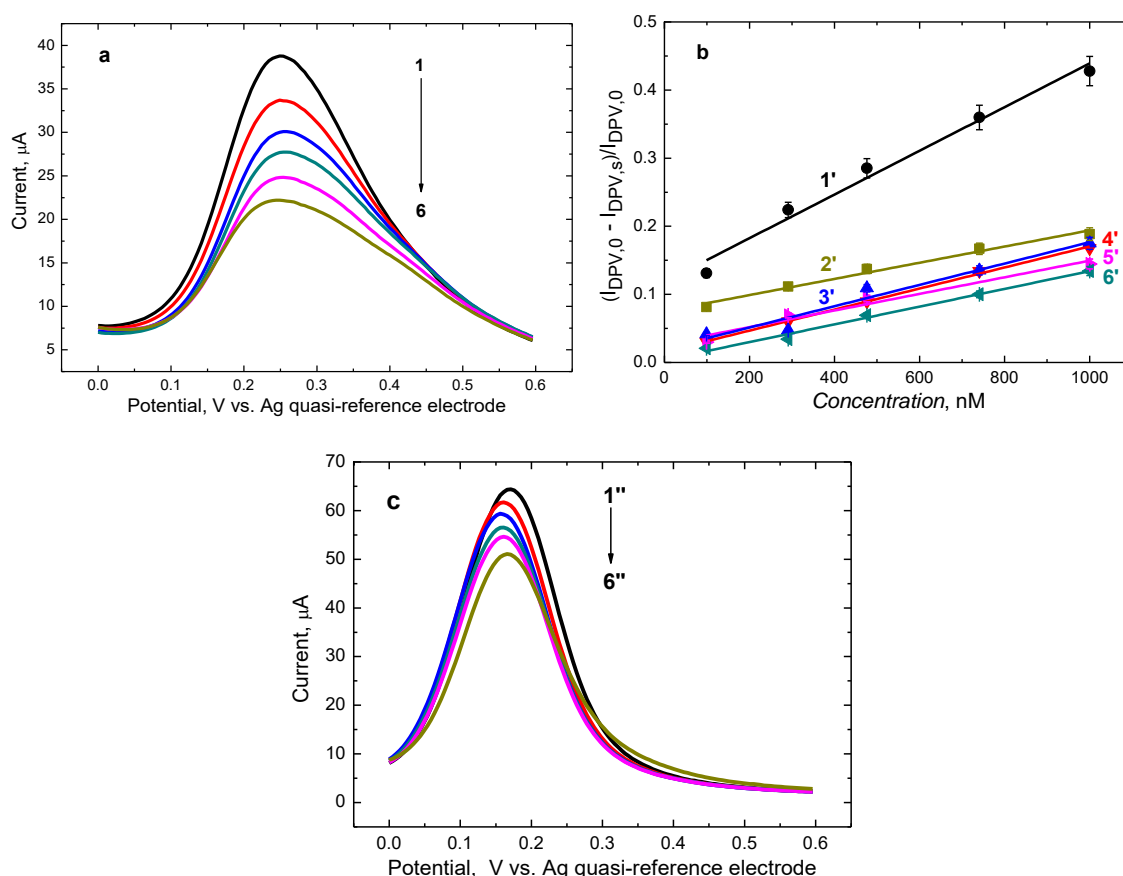
Figure 3.2-7. The DPV curves recorded at (curve *1*) SYN-MIP film-coated Pt disk electrode after SYN template removal with 0.1 M NaOH for 60 min, and then after addition of SYN to result in its solution concentration of (curve *2*) 0.10, (curve *3*) 0.29, (curve *4*) 0.48, (*5*) 0.74, and (curve *6*) 0.99 μM. (b) Calibration plots for electrodes coated with (curves *1* and *3−6*) SYN-MIP and (curve *2*) the NIP film for (curves *1'* and *2'*) SYN, (curve *3'*) urea, (curve *4'*) creatinine, (curve *5'*) adrenalin, and (curve *6'*) glucose. (c) The DPV peak recorded at the control NIP film-coated Pt disk electrode in (curve *1''*) the SYN absence and its presence at the concentration of (curve *2''*) 0.10, (curve *3''*) 0.29 (curve *4''*) 0.48, (curve *5''*) 0.74, and (curve *6''*) 0.99 μM. All DPV experiments were performed in the presence of the 0.1 M $K_4[Fe(CN)_6]$ and 0.1 M $K_3[Fe(CN)_6]$ redox probe in 0.1 M PBS (pH = 7.4) solution.

132

3.2.4.2   EIS determining the SYN analyte

Furthermore, SYN was determined using EIS. Impedance spectra were recorded at the SYN-extracted MIP film-coated Pt disk electrode in the presence of 0.1 M $K_4[Fe(CN)_6]$/$K_3[Fe(CN)_6]$ redox probe in 0.1 M PBS (pH = 7.4). Each Nyquist plot consists of a semicircle and a straight line in the high- and low-frequency region, respectively (Figure 3.2-8a). Such a plot represents a redox process under the control of the charge-transfer rate at a porous film-coated electrode.[364] A modified Randles equivalent circuit was applied to interpret the EIS spectra recorded (inset in Figure 3.2-8a). R_{ct} representing the charge transfer resistance of the electron transfer between the redox probe in solution and the electrode was determined for each SYN addition to the test solution. The MIP film resistance increased with the SYN concentration increase because more and more molecular cavities in the MIP film were occupied by the SYN analyte molecules, causing the polymer to be more insulating. Moreover, the phase angle became increasingly negative within the binding of SYN molecules (Figure 3.2-8b), suggesting a more capacitive nature of the system. The calibration plot constructed for SYN (curve 1^{IV} in Figure 3.2-8d) in the dynamic concentration range of 0.1 to 0.99 μM SYN conformed to the linear regression equation of ΔR_{ct} [Ω] = 75 (±11) [Ω] + 0.47 (±0.02) c_{SYN} [nM] with the correlation coefficient, $R^2 = 0.993$. The LOD for SYN reached 5.69 nM at $S/N = 3$. Moreover, the SYN-MIP chemosensor's selectivity to interferences, determined by EIS, was high. The selectivity for urea, creatinine, adrenalin, and glucose was high, equaling 10.90, 9.97, 9.65, and 11.27, respectively. Additionally, to confirm the imprinting, SYN was determined at the NIP film-coated electrode under the same conditions as the SYN-MIP film (Figure 3.2-8c). The NIP sensitivity, determined from the EIS calibration plot, was much lower than the sensitivity of the SYN-extracted MIP film (curve 2^{IV} in Figure 3.2-8d). The apparent *IF* was 6.31. The linear regression equation of the calibration plot of ΔR_{ct} [Ω] = 13(±3) [Ω] + 7.5×10^{-2} (±0.5×10^{-2}) c_{SYN} [nM], with the correlation coefficient, $R^2 = 0.994$, described the linear dynamic concentration range of 0.1 to 0.99 μM SYN in the case of (NIP film)-coated electrode.

133
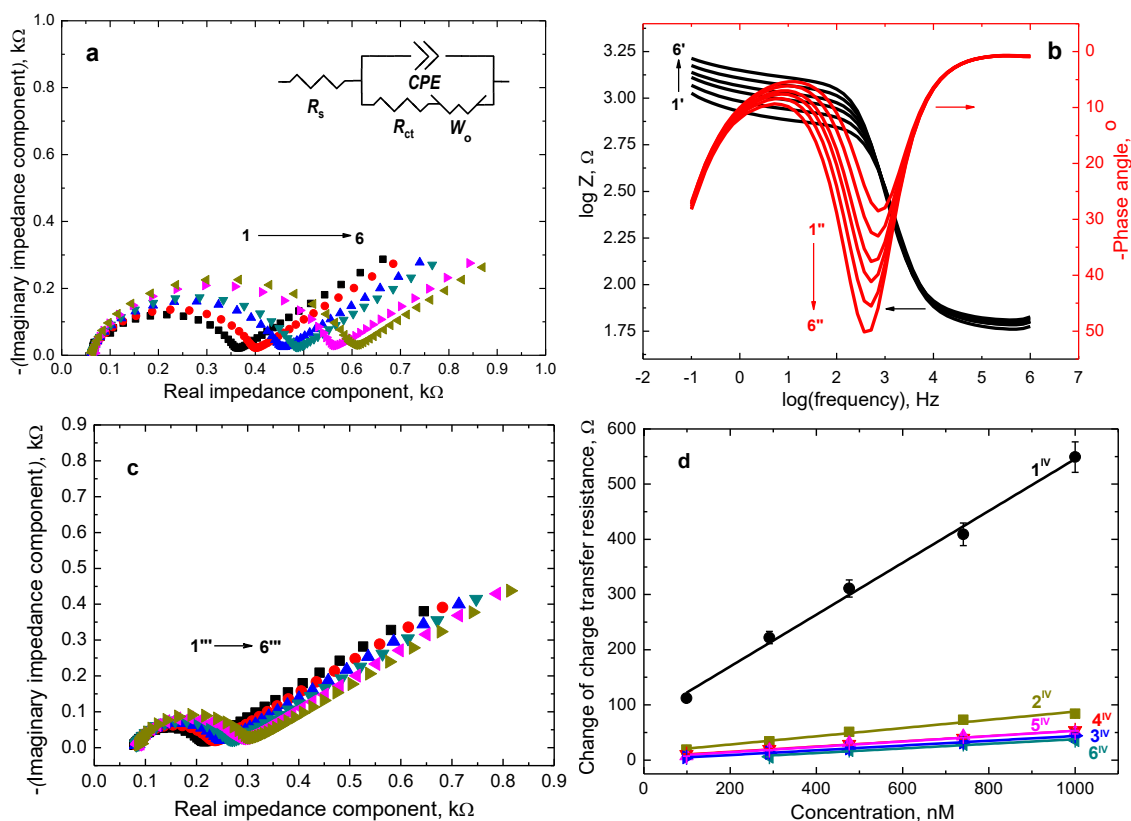
Figure 3.2-8. The (a) Nyquist and (b) Bode plots of impedance spectra recorded at (curves *1, 1′* and *1″*) SYN-MIP film-coated Pt disk electrode after extraction of the SYN template with 0.1 M NaOH for 60 min, and then after the addition of SYN reaching the solution concentration of (curves *2, 2′* and *2″*) 0.10, (curve *3, 3′* and *3″*) 0.29, (curves *4, 4′* and *4″*) 0.48, (curves *5, 5′* and *5″*) 0.74, and (curve *6, 6′* and *6″*) 0.99 μM. (c) Nyquist plots for the NIP film-coated Pt disk electrode (curve *1‴*) in the absence and then in the presence of SYN at a solution concentration of (curve *2‴*) 0.10, (curve *3‴*) 0.29, (curve *4‴*) 0.48, (curve *5‴*) 0.74, and (curve *6‴*) 0.99 μM. (d) The calibration plots constructed for electrodes coated with (curves *1^{IV}* and *3^{IV}−6^{IV}*) SYN-MIP and (curve *2^{IV}*) the NIP film for (curves *1^{IV}* and *2^{IV}*) SYN, (curve *3^{IV}*) urea, (curve *4^{IV}*) creatinine, (curve *5^{IV}*) adrenalin, and (curve *6^{IV}*) glucose. All EIS measurements were performed in the presence of the 0.1 M $K_4[Fe(CN)_6]$ and 0.1 M $K_3[Fe(CN)_6]$ redox probe in 0.1 M PBS (pH = 7.4) in the frequency range of 1 MHz to 0.1 Hz at open circuit potential.

3.2.5 Investigation of the "gate effect" mechanism

Furthermore, the origin of the decrease in the DPV peak of a redox probe recorded at the SYN-MIP film-coated electrode with the SYN concentration increase (Figure 3.2-7a) was investigated in detail. Possible mechanisms accounting for those changes may be divided into two groups. One is related to the change in the rate of the redox probe diffusion through the polymer film, whereas the other group is associated with the change in the electrochemical properties of the MIP film itself.

134

3.2.5.1 *Possible "gate effect" mechanism related to redox probe diffusion*

One of the mechanism hypotheses describing the redox probe diffusion through the MIP film is connected to the swelling or shrinking of the polymer film (Schemes 3.2-3 and 3.2-4). According to this hypothesis, analyte molecules binding by molecular cavities may cause MIP film shrinking or swelling, thus enhancing[267] or hampering[268-269, 399] redox probe diffusion through the film to the electrode surface, resulting in faradaic current changes corresponding to oxidation of the redox probe at the MIP film-coated electrode. Therefore, EIS measurements were performed to analyze the above mechanism. EIS spectra were recorded in the presence of SYN of different concentrations in the test solution (Figure 3.2-8a) because the above changes in the diffusion rate of the redox probe should impact the Nyquist plot in the low-frequency region. However, just straight lines coming from Wartburg impedance were visible in the low-frequency region of EIS spectra.
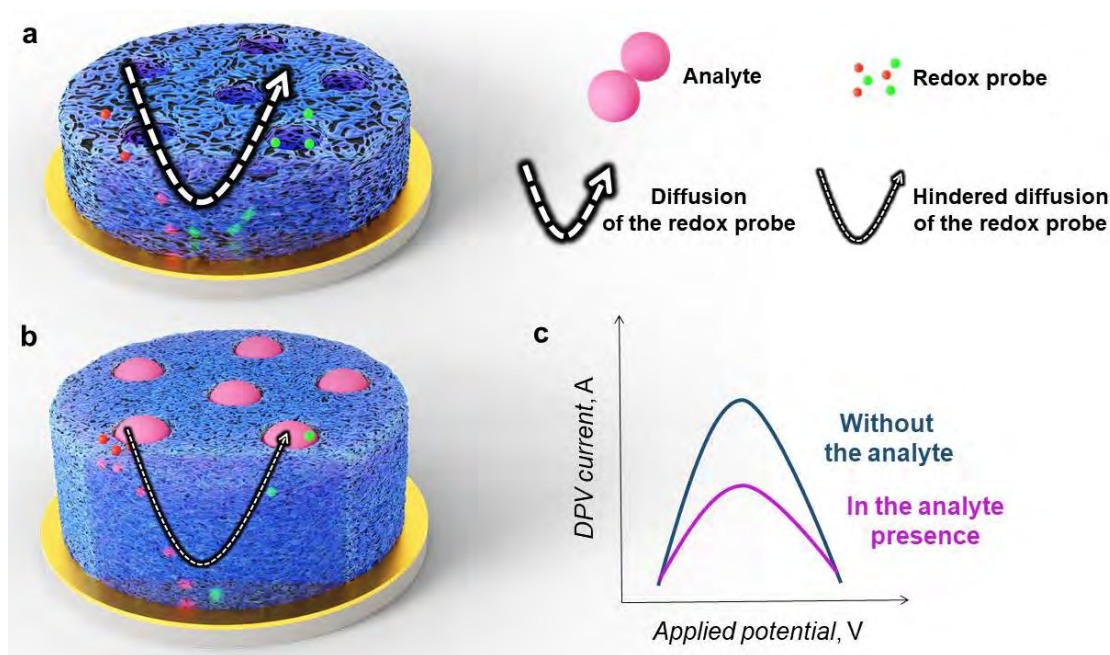
Scheme 3.2-3. Illustration of the possible diffusion-controlled "gate effect" mechanism presenting the MIP film swelling. Polymer film (a) before and (b) after analyte binding, as well as (c) DPV signals recorded at an MIP film-coated electrode in the presence of a redox probe in the test solution.

Moreover, SYN molecules binding to molecular cavities of the MIP film did not influence the slopes of these lines, which were equal to 42 (±1) °. Notably, an increase in the charge transfer resistance in the high-frequency region of EIS spectra with

the SYN concentration increase was substantial. Additionally, Bode plots (Figure 3.2-8b), simultaneously recorded with Nyquist plots, showing the phase angle increase with the SYN concentration increase, suggested changes in the double-layer capacitance. The EIS measurement results indicate that the "gate effect" mechanism related to polymer films' swelling or shrinking does not adequately explain the operation of the SYN-MIP film-coated electrodes.
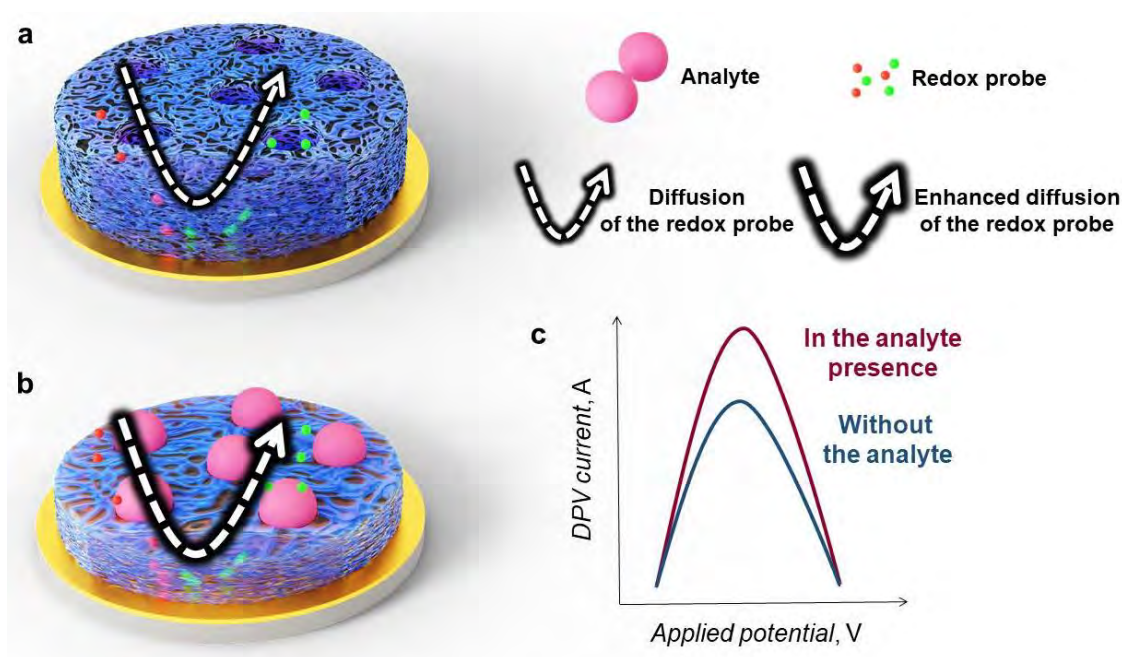
Scheme 3.2-4. Illustration of the possible diffusion-controlled "gate effect" mechanism showing the MIP film shrinking. Polymer film (a) before and (b) after analyte binding, as well as (c) DPV signals recorded at an MIP film-coated electrode in the presence of a redox probe in the test solution.

Afterward, SPR measurements on Au-glass disks coated with SYN-MIP and NIP films were performed to verify the above inference. The SPR signal changes are related to changes in the refractive index of the insulating phase in the close vicinity of the SPR chip gold surface.[364] Thus, MIP film swelling due to analyte binding should push out water from the proximity of the Au-layered glass disk, resulting in a change in the refractive index and then a change in the SPR signal. However, the signal nearly did not change with the SYN concentration change in the 90 to 330 μM range (Figure 3.2-9), manifesting no MIP film swelling due to SYN molecules binding by imprinted cavities.

136
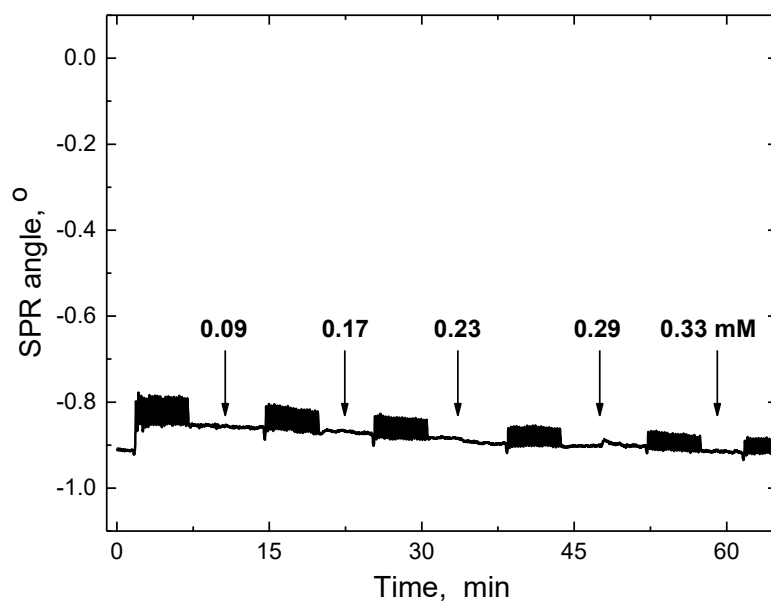
Figure 3.2-9. Changes in the SPR angle with time recorded at the SYN-MIP film-coated SPR chip for the SYN analyte of concentrations indicated with numbers at the curve in 0.1 M PBS (pH = 7.4).

Interestingly, the SPR signals recorded at Au-glass disks coated with SYN-MIP and NIP films were dependent on the only relatively high concentration of SYN ranging from 0.45 to 2.06 mM (Figures 3.2-10a and 3.2-10b), thus indicating that swelling of the polymer film may occur only at such high concentrations of SYN. The increase in the SPR signal for the MIP film with the SYN concentration increase (curve *1* in Figure 3.2-10a) was characterized by the linear regression equation of the calibration plot of $\left(SPR_0 - SPR_S\right)$ [°/mM] $= 10.5 \times 10^2 \, (\pm 0.5 \times 10^2) + 9.6 \times 10^2 \, (\pm 0.4 \times 10^2) c_{SYN}$ [mM] with the correlation coefficient, $R^2 = 0.990$ (calibration plot *1'* in Figure 3.2-10b). The calculated LOD was equal to 6.9 μM SYN at $S/N = 3$. The SPR signal for the NIP film linearly increased with the SYN concentration increase (curve *2* in Figure 3.2-10a), obeying the linear regression equation of the calibration plot of $\left(SPR_0 - SPR_S\right)$ [°/mM] $= 6.6 \times 10^2 \, (\pm 0.2 \times 10^2) + 2.2 \times 10^2 \, (\pm 0.1 \times 10^2) \, c_{SYN}$ [mM] with the correlation coefficient, $R^2 = 0.984$. The apparent *IF* calculated from the ratio of these calibration curves' slopes was 4.4.

137
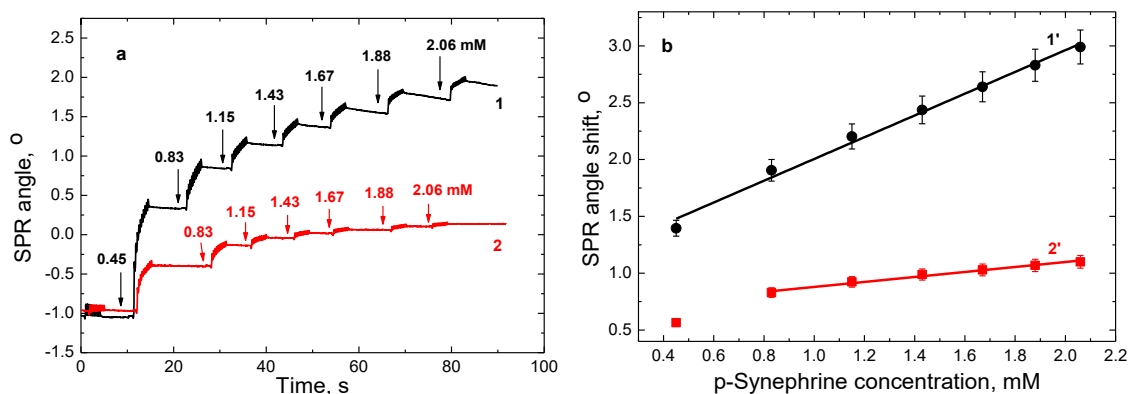
Figure 3.2-10. (a) The SPR angle change with time for SYN in 0.1 M PBS (pH = 7.4) at the (curve *1*) SYN-MIP and (curve *2*) NIP film-coated SPR chip at concentrations indicated with numbers at the curve. (b) The SPR calibration plots for SYN in 0.1 M PBS (pH = 7.4) at the (curve *1'*) SYN-MIP and (curve *2'*) NIP film-coated SPR chip.

Furthermore, in situ AFM imaging was performed to analyze the influence of the SYN binding by molecular cavities on the MIP film swelling (Figure 3.2-11). These in situ AFM experiments allowed verifying whether the polymer swells or not by determining its thickness change accompanying analyte binding. First, the SYN-MIP film-coated Au-layered glass slide was imaged in the air (Figure 3.2-6a). The film thickness and roughness were determined by scratching the polymer with a plastic pipette tip. Then the film was stripped of the gold surface near the scratch, exposing the gold layered intact, allowing to determine the exact film thickness. An example of a similar procedure is depicted in Figure 3.2-12.
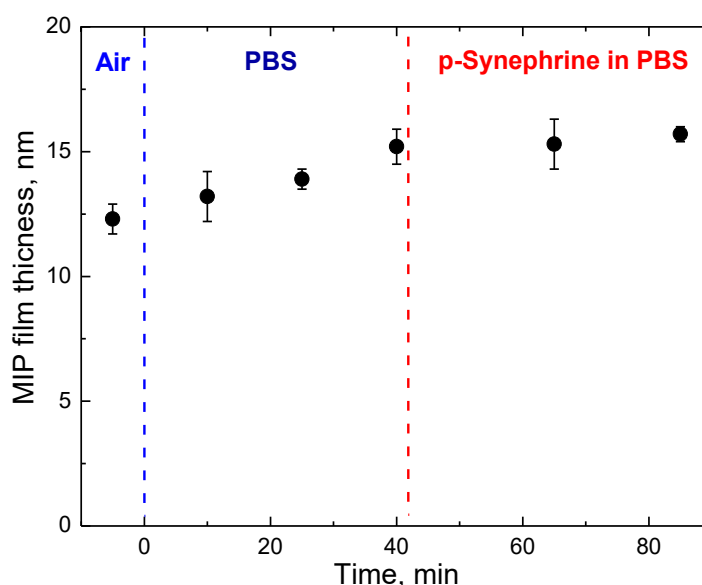
Figure 3.2-11. The SYN-MIP film thickness determined by AFM imaging in the air, then in 0.1 M PBS (pH = 7.4), and then in a solution of 0.5 μM SYN in 0.1 M PBS (pH = 7.4).

138

The polymer's thickness and roughness in the air were determined as 12.3 (±0.6) and 2.4 nm, respectively. Subsequently, the glass slide coated with this MIP film was immersed in 0.1 M PBS (pH = 7.4) for 40 min. The polymer thickness in situ determined using the scratch previously made was equal to 15.2 (±0.7) nm, indicating that the MIP film swelled by ~25% after immersion in the blank PBS. Then, the MIP film coated slide was transferred to a solution of 0.5 μM SYN in 0.1 M PBS (pH = 7.4) and then kept in it for 45 min. Then, the film thickness was again determined by analyzing the same scratch. The obtained value remained nearly the same, equalling 15.7 (±0.3) nm, signifying that SYN-MIP film did not swell due to analyte binding at a given SYN concentration range. The AFM results correspond to SPR experiments' results during SYN-MIP deposition on an Au-layered glass disk (Figure 3.2.4b).
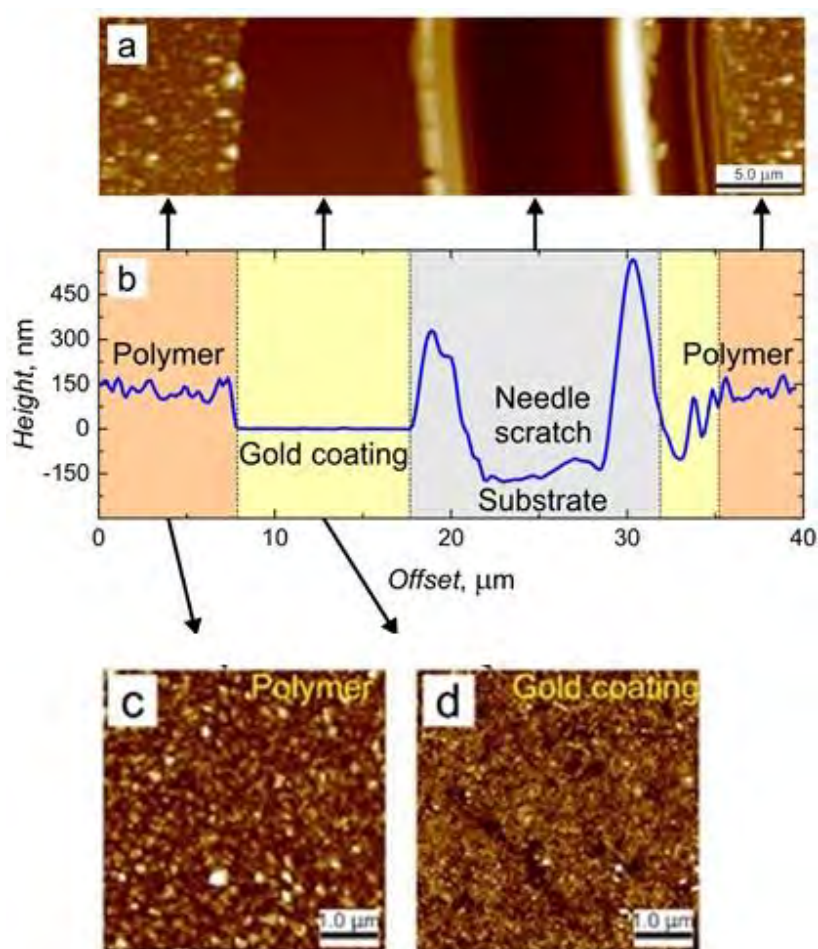
Figure 3.2-12. An example of making a scratch in a polymer film for the determination of the film thickness. (a) The $(10 \times 40)\ \mu m^2$ AFM image displaying the area in the vicinity of a scratch and (b) corresponding film cross-section, including the Au coating and the polymer film. (c) The $(5 \times 5)\ \mu m^2$ AFM image showing the surface of the polymer film, which thickness was determined against the Au coating. (d) The $(5 \times 5)\ \mu m^2$ AFM image presenting an intact Au surface revealed after exfoliation of the polymer film. Reproduced from.[404]

139

Another possible mechanism involves the physical blocking of the redox probe diffusion through the MIP film (Scheme 3.2-5). This mechanism is well suited for thin, nonconductive MIP films imprinted with macromolecules.[280-282] Surface imprinting of those molecules caused the formation of molecular cavities with diameters ranging from 5 to 10 nm, a few times larger than the redox probe diameter. In consequence, redox probe diffusion through these cavities is highly possible.[285, 288-289] If target macromolecules occupy these cavities, the diffusion of the redox probe can be blocked.

Nevertheless, $K_4[Fe(CN)_6]/K_3[Fe(CN)_6]$ redox probe diffusion directly through cavities in SYN-MIP film is unlikely since the diameters of redox probe molecules are similar to those of imprinted cavities. Moreover, cavities interconnection to form channels in the SYN-MIP film protruding to the electrode surface is impossible. Such a polymer structure would be manifested in the low-frequency region of the Nyquist plot by curve deviation from linearity, characteristic of diffusion through porous materials.[282] However, this feature was not observed (Figure 3.2-8a). Therefore, this mechanism may be excluded for the SYN-MIP film-based chemosensor.
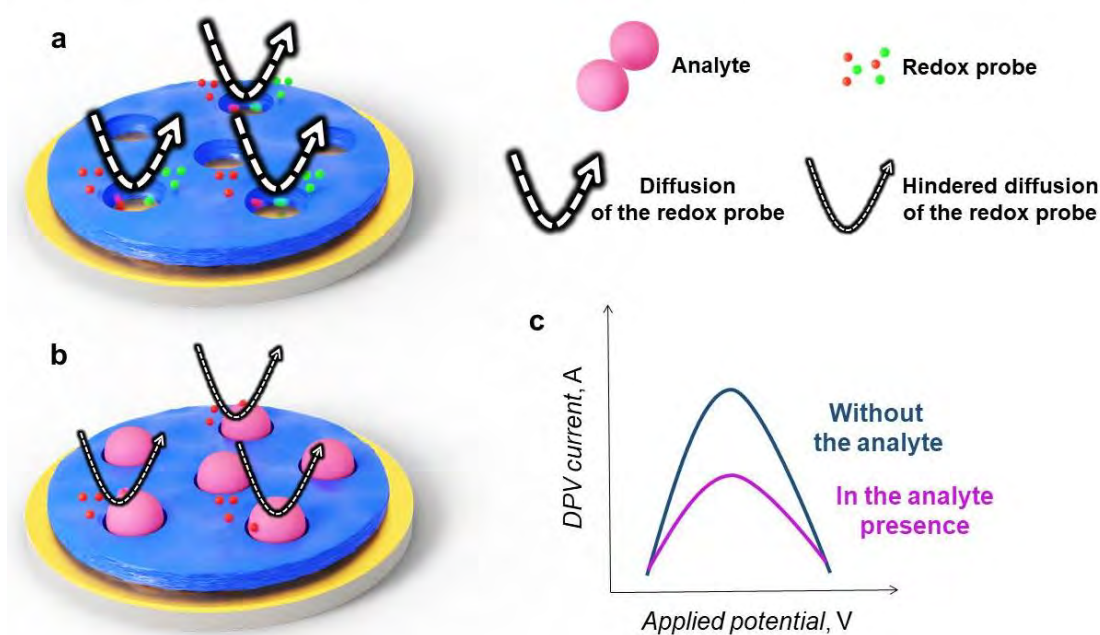
Scheme 3.2-5. Illustration of the possible diffusion-controlled "gate effect" mechanism showing the physical blocking of the redox probe diffusion through the MIP film by analyte molecules filling the imprinted cavities. MIP film (a) before and (b) after analyte binding, as well as (c) DPV signals recorded at an MIP film-coated electrode in the presence of a redox probe in the test solution.

140

The last possible mechanism related to the redox probe diffusion is charge accumulation in the MIP film (Schemes 3.2-6 and 3.2-7.).
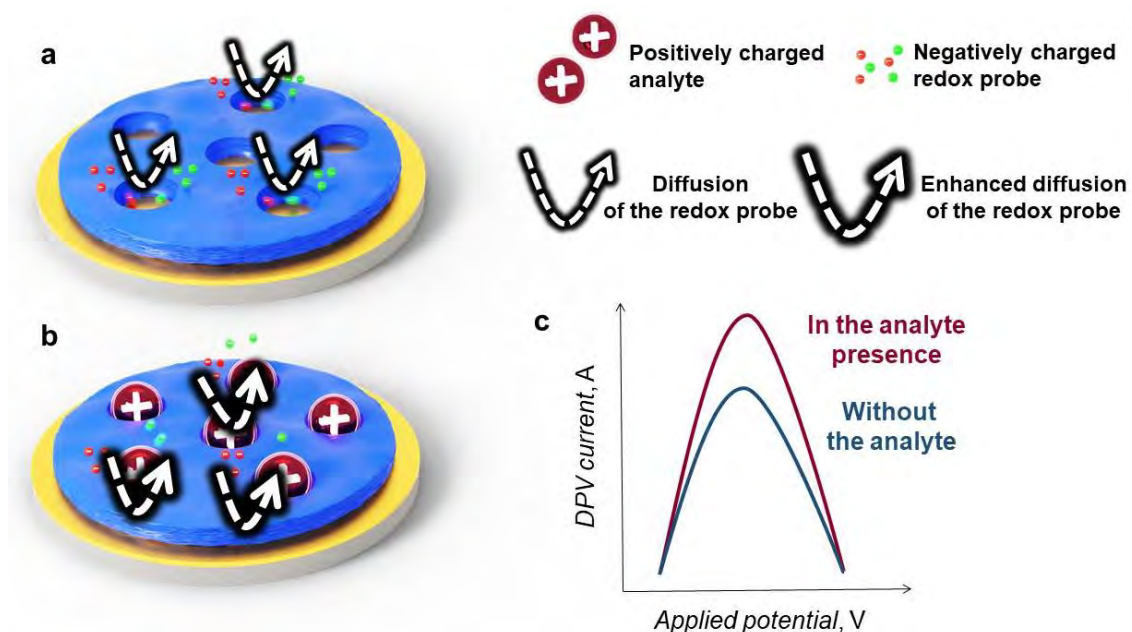
Scheme 3.2-6. Illustration of the possible diffusion-controlled "gate effect" mechanism showing the charge accumulation in the MIP film. MIP film (a) before and (b) after binding of a positively charged analyte, as well as (c) DPV signals recorded at an MIP film-coated electrode in the presence of a negatively charged redox probe in the test solution.
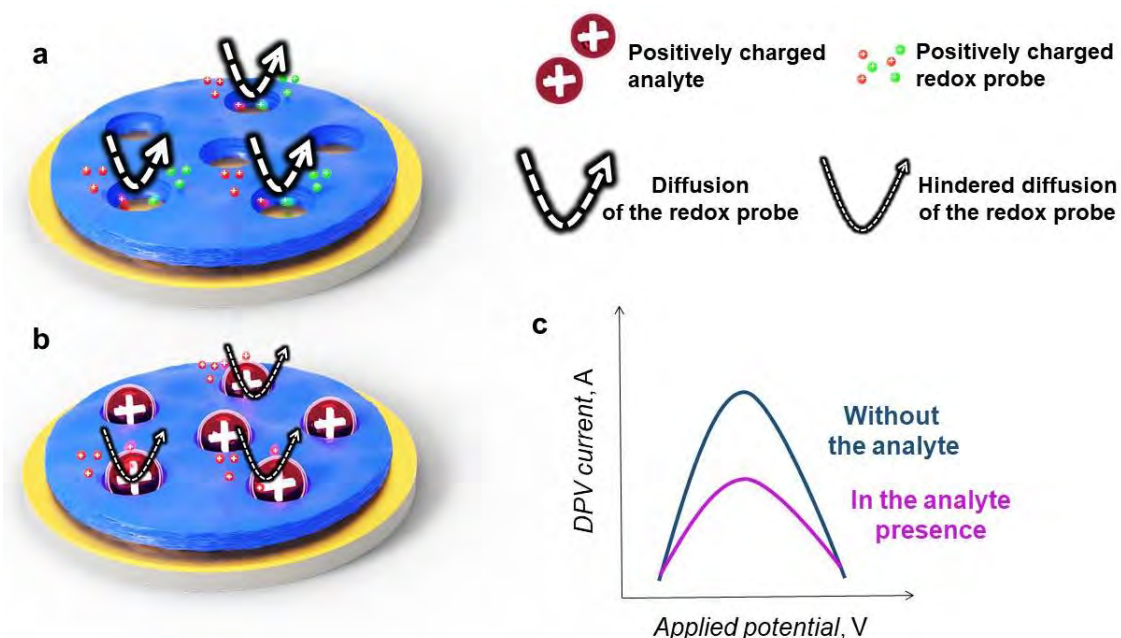
Scheme 3.2-7. Illustration of the possible diffusion-controlled "gate effect" mechanism showing the charge accumulation in the MIP film. MIP film (a) before and (b) after binding of a positively charged analyte, as well as (c) DPV signals recorded at an MIP film-coated electrode in the presence of a positively charged redox probe in the test solution.

141

The SYN-MIP film is formed from the CM 2 cross-linking monomer and FM 3 functional monomer bearing the carboxyl group, deprotonated and thus negatively charged in a neutral solution. In this solution, the SYN amine group is protonated and, hence, is positively charged. Therefore, due to charge accumulation in the SYN-MIP film, the diffusion of the redox probe may be affected via electrostatic interactions. Hence, DPV measurements were performed in the presence of a positively charged redox probe, 0.1 M [Ru(NH$_3$)$_6$]Cl$_3$ in 0.1 M PBS (pH = 7.4) at the electrode coated with SYN-extracted MIP film (Figure 3.2-13).
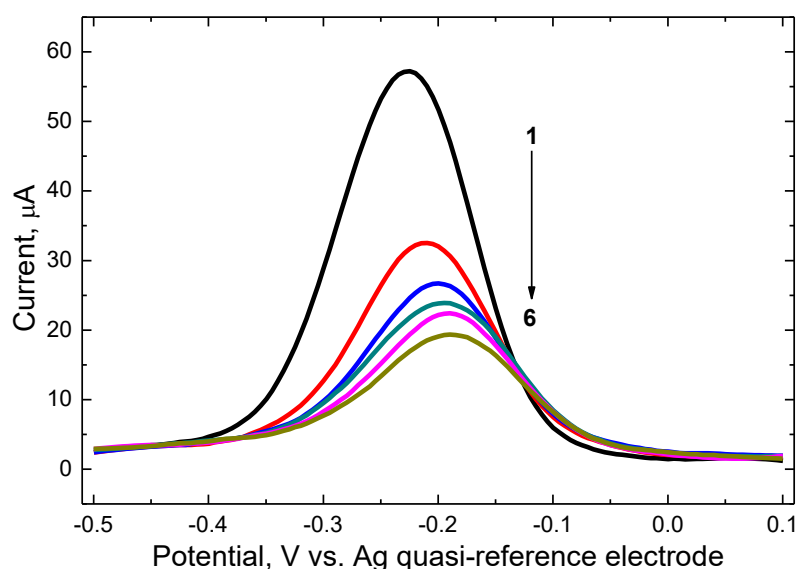
Figure 3.2-13. DPV voltammograms for 0.1 M Ru(NH$_3$)$_6$Cl$_3$ redox probe in 0.1 M PBS (pH = 7.4) recorded at the SYN-MIP film-coated Pt disk electrode (curve *1*) after template extraction with 0.1 M NaOH for 60 min, and then immersion in a solution of (curve *2*) 0.10, (curve *3*) 0.29 (curve *4*) 0.48, (curve *5*) 0.74, and (curve *6*) 0.99 μM SYN in 0.1 M PBS (pH = 7.4).

The occurrence of negatively charged carboxylate groups in the polymer may hinder Fe(CN)$_6^{3-}$ ions diffusion and accumulate Ru(NH$_3$)$_6^{3+}$ cations. Subsequent binding of positively charged SYN in the presence of a negatively charged probe might either facilitate or make transport of the hexacyanoferrate ions less difficult, thus resulting in a DPV peak increase and, presumably, narrowing. The binding of SYN in the presence of the positively charged Ru(NH$_3$)$_6^{3+}$ probe may cause less redox probe accumulation, decreasing and possibly broadening the DPV peak. Using a differently charged redox probe should result in changes in the DPV peak of the Ru(NH$_3$)$_6^{3+}$ probe in the opposite direction than that of the negatively charged Fe(CN)$_6^{3-}$ probe or DPV peak Ru(NH$_3$)$_6^{3+}$ redox probe would not be much affected with the SYN concentration

increase. However, the behavior of the DPV peak of $Ru(NH_3)_6^{3+}$ was similar to that of the negatively charged $Fe(CN)_6^{3-}$. Namely, it decreased with the SYN concentration increase. Similar behavior of DPV peaks originating from differently charged redox probes suggests that PBS ions might compensate for any charge appearing in the MIP film, and therefore, charge accumulation in the MIP film does not affect redox probe diffusion through the SYN-MIP film. Thus, the mechanism involving charge accumulation may also be excluded.

3.2.5.2 Possible "gate effect" mechanism involving the electrical effects of an MIP film

The above experiments demonstrated that the decrease in the DPV peak of the redox probe with the SYN analyte concentration increase, recorded at the conductive SYN-MIP film-coated electrode, does not hamper redox probe diffusion through the MIP but most likely incurs changes in the MIP film electrochemical properties. The Nyquist plots recorded for SYN determination show an increase in the MIP charge transfer resistance with the analyte concentration increase (Figure 3.2-8a). Moreover, the separation of anodic and cathodic peaks in the current-potential curves increased with the SYN concentration increase (Figure 3.2-14), like if the electrochemical reversibility of the $K_4[Fe(CN)_6]/K_3[Fe(CN)_6]$ redox couple electro-oxidation decreased because of analyte binding by the MIP.
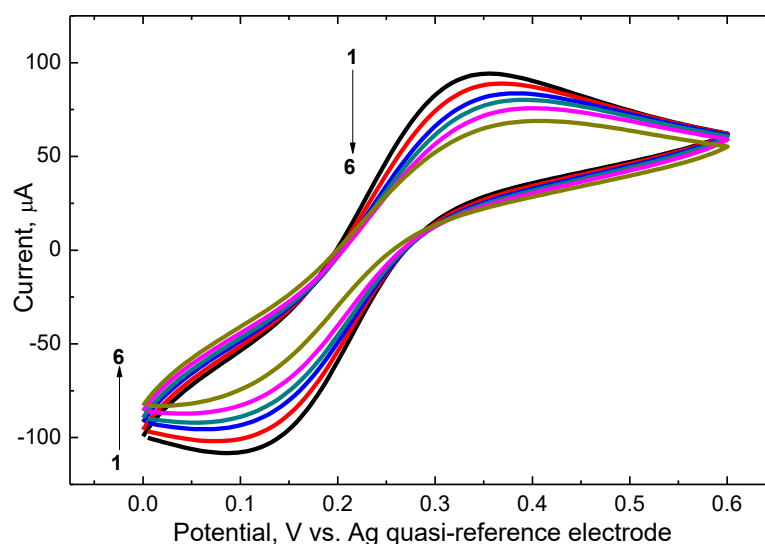
Figure 3.2-14. The current-potential curves in the presence of the 0.1 M $K_4[Fe(CN)_6]$ and 0.1 M $K_3[Fe(CN)_6]$ redox probe in 0.1 M PBS (pH = 7.4) recorded at the SYN-MIP film-coated Pt disk electrode (curve *1*) after extraction of the SYN template from the film, and then the addition of SYN analyte to reach the concentration of (curve *2*) 0.10, (curve *3*) 0.29 (curve *4*) 0.48, (curve *5*) 0.74, and (curve *6*) 0.99 μM.

143

CV results align with the DPV determination of SYN, in which DPV peaks decreased and broadened with the SYN concentration increase (Figure 3.2-7a and Table 3.2-2). This behavior pointed to conductivity changes in the polymer film.

Table 3.2-2. The DPV peak width at half height recorded at the bare Pt disk electrode and the SYN-extracted MIP film-coated Pt disk electrode.

The DPV peak	Peak width at half height ($W_{1/2}$), mV	
	0.1 M K$_3$[Fe(CN)$_6$] and 0.1 M K$_4$[Fe(CN)$_6$] redox probe	0.1 M Ru(NH$_3$)$_6$Cl$_3$ redox probe
Bare Pt disk electrode	171	160
SYN-extracted MIP film-coated Pt disk electrode; the SYN concentration of:		
0	215	136
0.10 µM	225	137
0.29 µM	234	140
0.48 µM	244	142
0.74 µM	249	144
0.99 µM	269	153

Therefore, the current-potential curves were derivatized (Figure 3.2-15) to assess the MIP film's conductivity. Evidently, MIP molecular cavities binding of SYN molecules led to a decrease in MIP film conductivity, decreasing and broadening the DPV peak with the increase in SYN concentration.

Thus, UV-vis spectroscopy measurements were performed to examine the electronic properties of conductive MIP films in detail.[405] UV-vis absorption spectra were recorded for SYN (spectrum *1* in Figure 3.2-16), CM 2 (spectrum *2* in Figure 3.2-16), and FM 3 (spectrum *3* in Figure 3.2-16) in acetonitrile. Moreover, UV-vis reflection spectra were recorded for the control NIP film (spectrum *4* in Figure 3.2-16) and the SYN-extracted MIP film (spectrum *5* in Figure 3.2-16), and then after immersion of the latter film in 0.1 M PBS (pH = 7.4) for 15 min,

144

and subsequently in the solution of 0.5 μM SYN in 0.1 M PBS (pH = 7.4) for 5 min (spectra *6* and *7* in Figure 3.2-16, respectively).
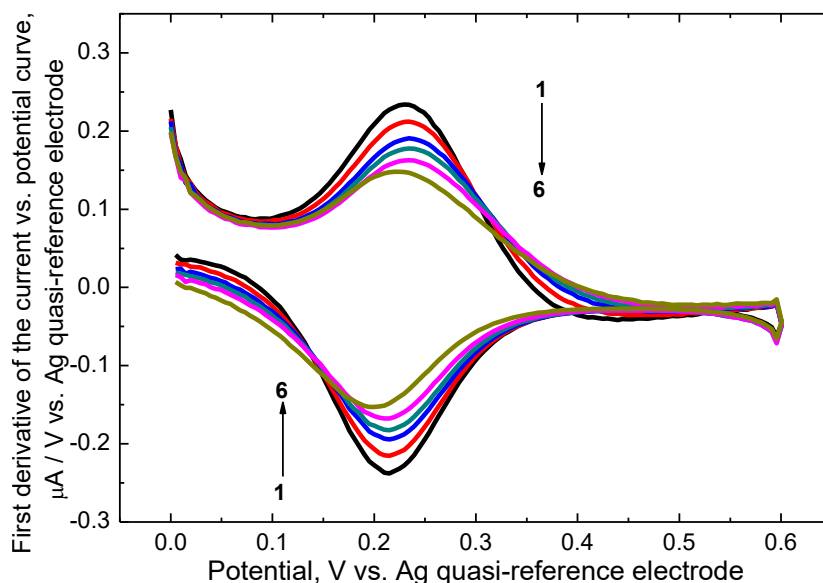
Figure 3.2-15. The first derivatives of CV curves presented in Figure 3.2-14.

The presence of thiophene moieties in cross-linking monomer CM 2 and functional monomer FM 3 resulted in respective absorption bands at ~280 and ~325 nm in spectra *2* and *3* in Figure 3.2-16. A broad red-shifted band extending from ~250 to 600 nm in spectrum *5* for the SYN-extracted MIP film implied the occurrence of polythiophene chains, with various conjugation lengths, formed during the electrodeposition of the MIP film on the electrode.[406-407] A band shift to a longer wavelength in spectrum *5* may also originate from the π−π stacking of neighboring thiophene aromatic rings of the polymer backbone.[263] Moreover, a similar band, ranging from ~250 to 600 nm, is seen in spectrum *4* for the NIP film, indicating the presence of polythiophene chains in the NIP. Additionally, a weak band, presumably originating from partially oxidized polythiophene,[405] is seen between 700 and 730 nm in spectra *4* to *7* (inset in Figure 3.2-16). The appearance of these weak bands signifies the presence of the polythiophene radical cations (polarons) in the MIP film, although in low quantity. Unfortunately, with our spectrophotometer, it was impossible to record spectra for wavelengths exceeding 900 nm, where the presence of dication (bipolaron) bands is expected. Nevertheless, it still may be concluded that the semiconductive MIP and NIP films with just a slight doping were formed. Moreover, similar spectra were recorded for SYN-extracted MIP film-coated electrode immersed in blank PBS

145

(pH = 7.4) for 15 min and then transferred to the solution of 0.5 µM SYN in PBS (pH = 7.4) for 5 min (spectra *6* and *7*, respectively, in Figure 3.2-16).

Furthermore, no significant changes were observed at a wavelength above 600 nm, indicating that the MIP film binding of the SYN analyte did not influence the polymer film doping. Thus, the DPV peak decrease with the SYN concentration increase does not involve changes in the SYN-MIP film doping. Hence, no difference in the population of radical cations (polarons) in the semiconductive SYN-MIP film implies that a decrease in MIP film's conductivity results from the decrease in the mobility of radical cations (polarons) resulting from analyte binding.
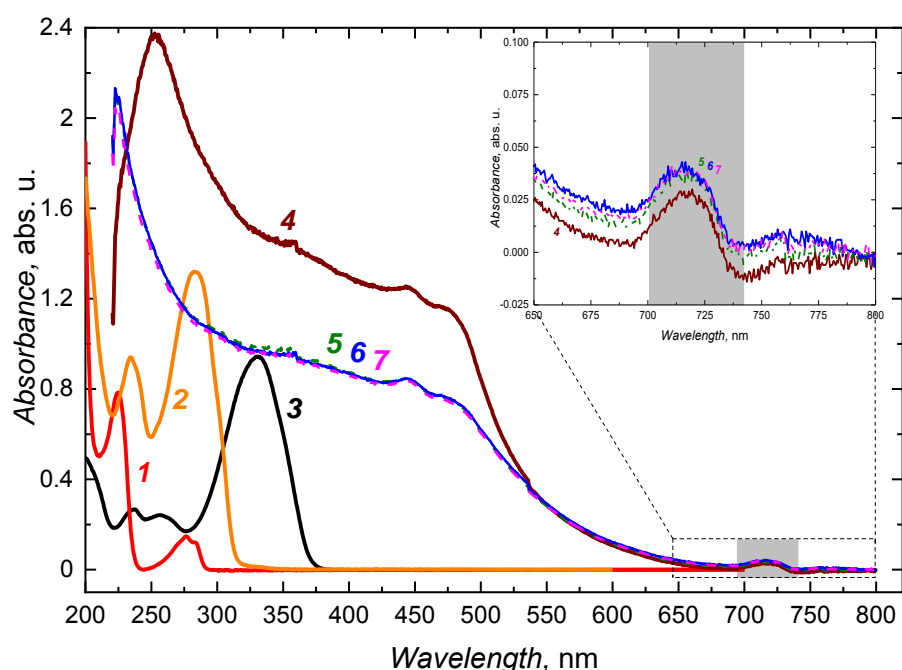
Figure 3.2-16. UV-vis absorption spectra for (spectrum *1*) 100 µM SYN, (spectrum *2*) 50 µM CM 2, and (spectrum *3*) 50 µM FM 3 in acetonitrile, as well as UV-vis reflection spectra for (spectrum *4*) the NIP film and (spectrum *5*) the SYN-MIP film after SYN template removal, and then (curve *6*) immersion in 0.1 M PBS (pH = 7.4) for 15 min, and subsequently (spectrum *7*) in the solution of 0.5 µM SYN in 0.1 M PBS (pH = 7.4) for 5 min.

3.3   Redox self-reporting MIP film-based chemosensor

The present section concentrates on devising a chemosensor involving a film of a redox self-reporting MIP with the covalently immobilized ferrocene redox probe for label-free electrochemical determination of an SYN model analyte.

It has already been demonstrated in Section 3.2 above that a faradaic current decrease correlating with the electro-oxidation of the redox probe due to SYN binding originated from changes in the electrochemical properties of the SYN-MIP film. Since, presumably, the binding of an analyte to the polymer does not affect the diffusion of the redox probe to the electrode, redox probe diffusion might not be a crucial parameter for the involved faradaic current. Thus, it might be excluded in determining electroinactive analytes at electrodes coated with conductive MIP films. In consequence, a redox probe could be embedded inside the MIP matrix. Therefore, a new monomer (FcM), a ferrocene (Fc) derivative, was synthesized and used to prepare self-reporting MIP film. The role of FcM was to provide an internal redox probe and simultaneously act as a cross-linking monomer. Moreover, a well-known pre-polymerization complex of the FM 3 functional monomer with the SYN template was used for constructing a self-reporting MIP film chemosensor. Applying the system same as for the traditional ("gate effect")-operated SYN-MIP film chemosensor described in Section 3.2 above allowed comparing the analytical performance of those two chemosensors. Additionally, the deposition conditions of the self-reporting polymer were optimized because the MIP film morphology and thickness proved to be significant sensing parameters. The analytical performance of the devised chemosensor was examined during SYN determination in the (redox probe)-free test solution. Applying the self-reporting MIP chemosensor for label-free analyte sensing significantly shortens the sample preparation time for analysis. Moreover, such an electrochemical sensor with the immobilized redox probe is easy to miniaturize into a hand-held device useful for in-field measurements.

3.3.1   Selecting components of the pre-polymerization complex solution

For pre-polymerization complex formation, the functional monomer and template were selected the same as those for the SYN-MIP film chemosensor preparation, described in Section 3.2.1 above. That is, FM 3 was chosen as a functional monomer capable of hydrogen bonding and electrostatically interacting with the SYN template

147

(Schemes 3.2-2b and 3.2-2c). The Gibbs free energy gain of such a complex of one molecule of SYN with three molecules of FM 3 was -227.4 kJ mol^{-1}, demonstrating the formation of a stable pre-polymerization complex.

Using a well-known complex of the template with the functional monomer in the preparation of a self-reporting MIP film chemosensor allows for comparing the analytical performance of this sensor with that traditional using the "gate effect." Moreover, for devising a redox self-reporting MIP film-based chemosensor, a specially designed and synthesized monomer, namely *bis*-(2,2'-bithienyl)-4 ferrocenylphenyl methane, FcM (**1** in Scheme 3.3-1a), was also included in the pre-polymerization complex solution. Because of bearing both the ferrocene and *bis*-bithiophene moieties in its structure, FcM provides an internal redox probe and acts as a cross-linking monomer forming a rigid framework of the polymer matrix. Introducing FcM facilitates exchanging electrons between the electrode substrate and the ferrocene moieties, transferred through the polybithiophene backbone, resulting in the faradaic current of the internal redox probe being enhanced compared to formerly reported (internal ferrocene probe)-based MIP chemosensors.[341, 344, 350-351] Those non-conductive MIPs were prepared mainly from vinyl ferrocene monomers and ferrocenylmethyl methacrylate monomers. Therefore, ferrocene moieties from these polyacrylic MIPs located far from the electrode surface could not be electro-oxidized. Thus, a deficient number of ferrocene moieties participated in the MIP chemosensors' responses. In consequence, the generated faradaic currents were small.

148

a

b
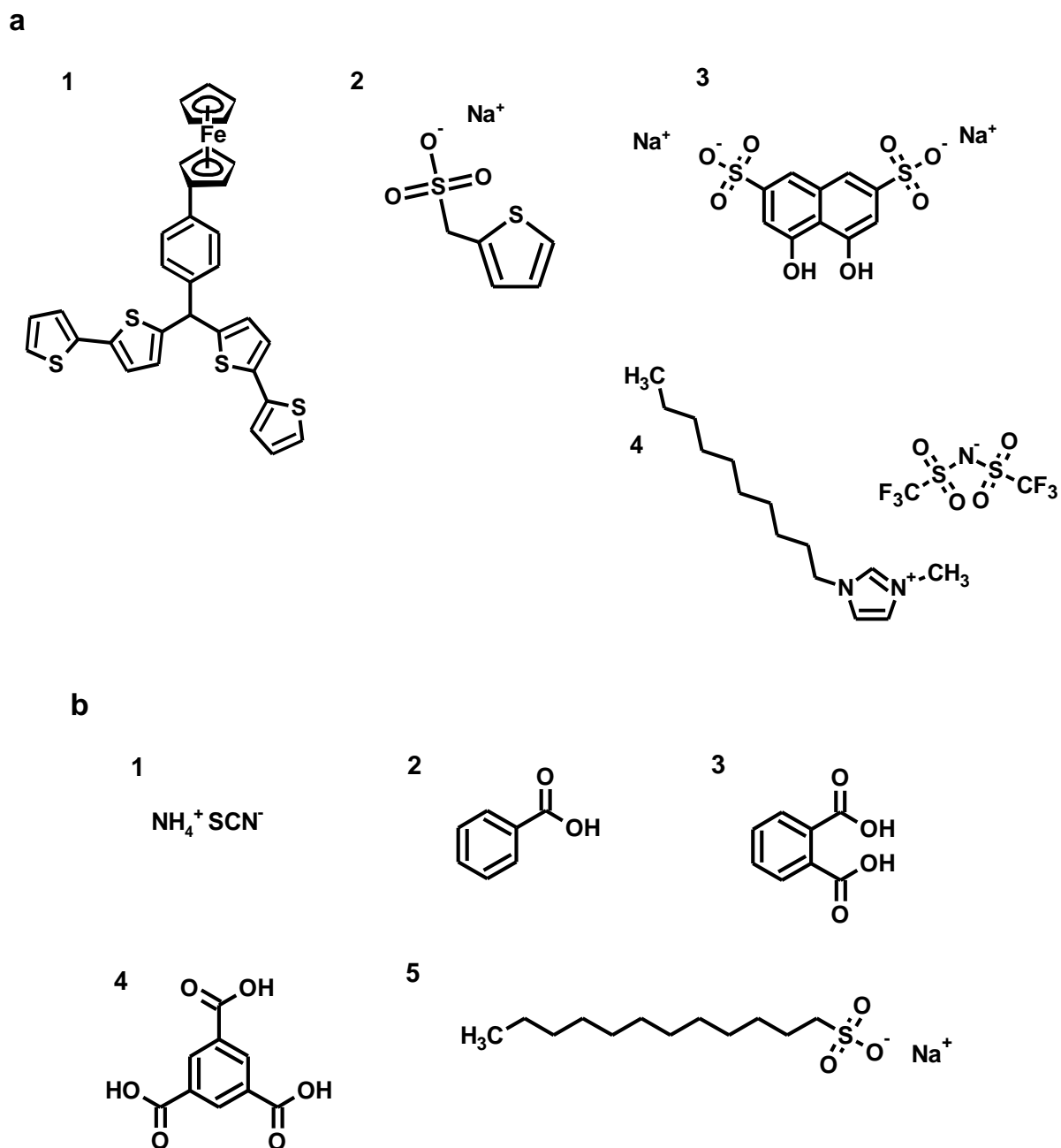
Scheme 3.3-1. (a) The structural formulas of compounds used for electropolymerization: (1) *bis*-(2,2'-bithienyl)-4-ferrocenylphenyl methane (FcM), (2) sodium thiophen-2-ylmethanesulfonate, (3) chromotropic acid disodium salt, (4) 1-decyl-3-methylimidazolium *bis*(trifluoromethanesulfonyl)imide ionic liquid as well as (b) the structural formulas of compounds which provide lipophilic anions: (1) ammonium thiocyanide, (2) benzoic acid, (3) phthalic acid, (4) trimesic acid, (5) sodium dodecyl sulfate.

3.3.2 Optimizing synthesis of redox self-reporting (*p*-synephrine)-templated MIP films for *p*-synephrine determining in aqueous solutions

Different MIP films with covalently immobilized ferrocene redox probes, namely (SYN-Fc)-(MIP-1), (SYN-Fc)-(MIP-2), and (SYN-Fc)-(MIP-3) films, were prepared as described in Section 2.2.1.8 above.

3.3.2.1 Preparing (SYN-Fc)-(MIP-1) film chemosensor and subsequent examining its analytical performance in aqueous solutions

The (SYN-Fc)-(MIP-1) film was deposited on the Pt disk electrode surface by potentiodynamic copolymerizing FM 3 with FcM in the presence of the SYN template (Figure 3.3-1). The appearance of an anodic peak at 1.20 V vs. Ag quasi-electrode during polymer film formation indicated the electro-oxidation of bithiophene moieties of FM 3 and FcM. Moreover, the current increase in subsequent cycles signified the deposition of a conductive MIP film. Importantly, anodic and cathodic peaks of ferrocene in the potential range of 0.40 to 0.50 V vs. Ag quasi-reference electrode were visible during the electropolymerization (Inset in Figure 3.3-1). Peak-to-peak potential separation increased from 88 to 122 mV with successive cycles, implying that either the one-electron electrochemically quasi-reversible process became electrochemically irreversible or the *iR* potential drop increased with the current increase because of the high resistivity of the polymer film.

Figure 3.3-1. Five-cycle potentiodynamic curves for (SYN-Fc)-(MIP-1) film deposition on 1-mm diameter Pt disk electrode from 10 µM SYN, 30 µM FM 3, 100 µM FcM in 0.1 M (TBA)ClO$_4$, in the acetonitrile-dichloromethane 9 : 1 (*v* : *v*) solution.

150

Presumably, the charge provided by the counter ion diffusion in and out of the (SYN-Fc)-(MIP-1) film was insufficient to compensate for the charge appearing on the ferrocene moiety during electropolymerization. Moreover, the height of ferrocene peaks remained almost similar from cycle to cycle, indicating that consecutive polymer layers' deposition nearly did not impact the redox process of ferrocene. Instead, charging and discharging of the ferrocene moiety occurred, presumably, in the pre-polymerization complex solution of acetonitrile only in the electrical double layer at the interface of the electrode-(MIP film) or (MIP film)-(acetonitrile solution).

After (SYN-Fc)-(MIP-1) film deposition, template extraction from the MIP film was optimized using UV-vis spectroscopy (Figure 3.3-2). The MIP film-coated electrode was transferred to the 0.1 M NaOH extraction solution, and then a UV spectrum was recorded after each 10-min interval. The characteristic band at 210 nm corresponding to SYN absorption was visible, implying the presence of SYN in the extraction solution. The band did not increase after 50-min extraction. Apparently, the SYN concentration in the extraction solution remained constant, thus indicating that the template was removed from the MIP film. Therefore, this time was selected for SYN extraction with 0.1 M NaOH.
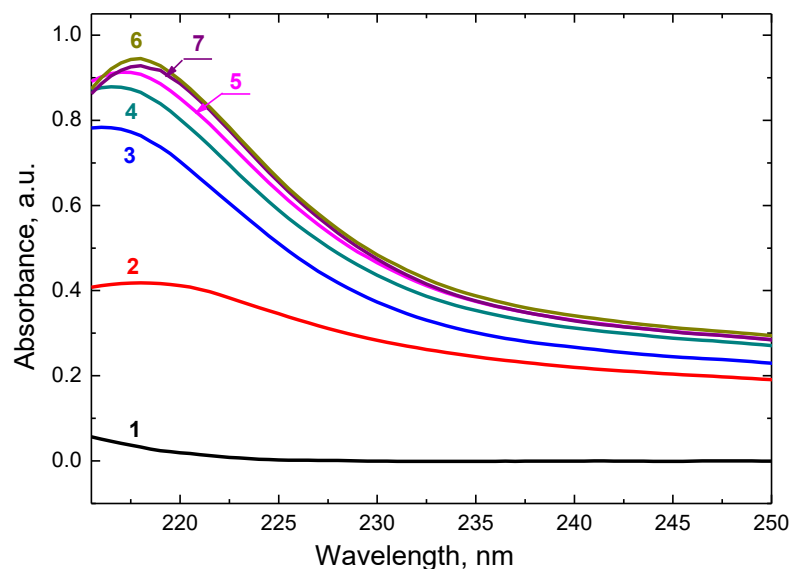
Figure 3.3-2. UV-vis spectra for 0.1 M NaOH extraction solution (spectrum *1*) before and after its application for SYN template removal from the (SYN-Fc)-(MIP-1) film for (spectrum *2*) 10, (spectrum *3*) 20, (spectrum *4*) 30, (spectrum *5*) 40, (spectrum *6)* 50, and (spectrum *7*) 60 min.

After template removal, the Pt disk electrode coated with the SYN-extracted MIP film was transferred to a blank PBS (pH = 7.4), then the DPV current was recorded. However, the DPV peak for the ferrocene internal redox probe was not visible in the potential range of 0 to 0.70 V vs. Ag quasi-reference electrode (Figure 3.3-3a), even though anodic and cathodic peaks were well pronounced during potentiodynamic (SYN-Fc)-(MIP-1) film formation. The phosphate and chloride anions from the PBS solution were presumably too hydrophilic to penetrate the hydrophobic poly(*bis*-bithiophene) MIP film. Therefore, they could not balance the positive charge generated on ferrocene moieties during their electro-oxidation. Hence, different lipophilic salts or acids were added to the test solution, PBS (pH = 7.4), to facilitate the electro-oxidation of the ferrocene internal redox probe.
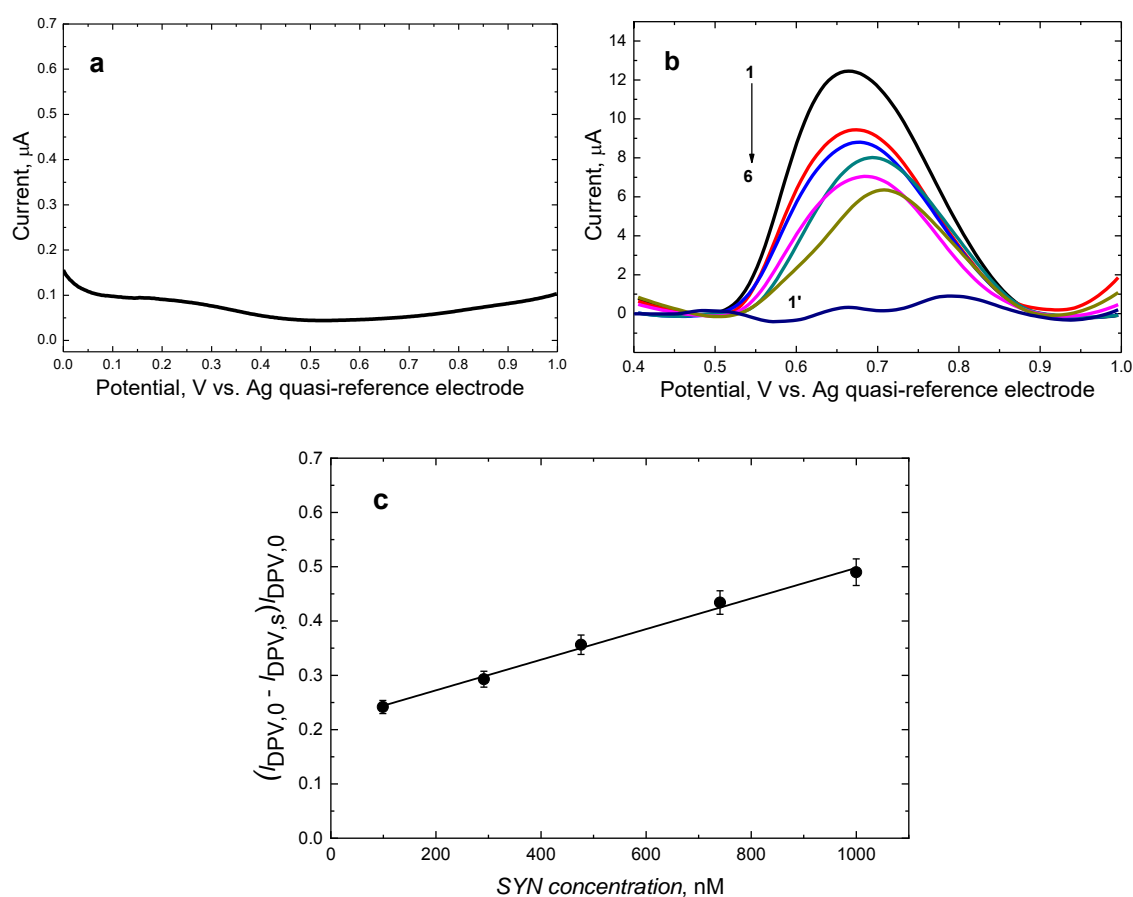
Figure 3.3-3. The DPV curve recorded at the 1-mm Pt disk electrode coated with the SYN-extracted (SYN-Fc)-(MIP-1) film in (a) blank 0.1 M PBS (pH = 7.4) and the presence of (b) 0.1 M NH$_4$SCN in 0.1 M PBS (pH = 7.4) after addition of SYN to reach the concentration of (curve *1*) 0, (curve *2*) 0.10, (curve *3*) 0.29, (curve *4*) 0.48, (curve *5*) 0.74, and (curve *6*) 0.99 µM as well as (*1'*) the current recorded at the blank 1-mm Pt disk electrode in 0.1 M NH$_4$SCN in 0.1 M PBS (pH = 7.4). (c) The calibration plot for the SYN analyte in 0.1 M NH$_4$SCN in 0.1 M PBS (pH = 7.4) at the template-extracted (SYN-Fc)-(MIP-1) film-coated electrode.

152

Unfortunately, applying benzoic acid (**2** in Scheme 3.3-1b), phthalic acid (**3** in Scheme 3.3-1b), trimesic acid (**4** in Scheme 3.3-1b), and sodium dodecyl sulfate (**5** in Scheme 3.3-1b) resulted in no peak during DPV measurements at the (SYN-Fc)-(MIP-1) film-coated electrode (data not shown). Apparently, these electrolytes did not promote ferrocene moiety oxidation in PBS. However, a broad peak of ferrocene appeared at 0.65 V vs. Ag quasi-reference electrode in the presence of 0.1 M NH₄SCN in 0.1 M PBS, pH = 7.4 (curve *1* in Figure 3.3-3b). Notably, such a pronounced DPV peak was not observed in the voltammogram recorded at a bare Pt electrode immersed in the same 0.1 M NH₄SCN solution (curve *1'* in Figure 3.3-3b).

3.3.2.2   *Preparing (SYN-Fc)-(MIP-2) film chemosensor and examining its analytical performance in aqueous solutions*

Adding extra salts to the test solution to facilitate ferrocene moieties' electro-oxidation is inconvenient in SYN analyte determining in a (redox probe)-free test solution. Thus, a film of another polymer, vis., (SYN-Fc)-(MIP-2), was prepared (Figure 3.3-4).
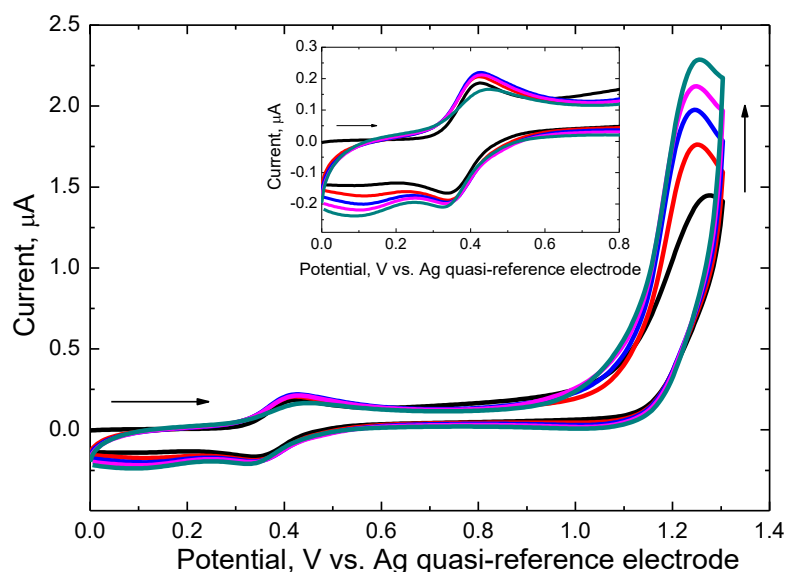
Figure 3.3-4. Potentiodynamic curves for (SYN-Fc)-(MIP-2) film deposition on a 1-mm diameter Pt disk electrode from the acetonitrile-dichloromethane 9 : 1 (*v* : *v*) solution of 10 µM SYN, 30 µM FM 3, 100 µM FcM, 100 µM sodium thiophen-2-ylmethanesulfonate, and 0.1 M (TBA)ClO₄.

This film was synthesized similarly to the (SYN-Fc)-(MIP-1) film, but one more component, vis., sodium thiophen-2-ylmethanesulfonate (**2** in Scheme 3.3-1a), was introduced to the pre-polymerization complex solution. This compound provides an

153

anion that supposedly neutralizes the positive charge generated on the ferrocene moiety during electro-oxidation. Sodium thiophen-2-ylmethanesulfonate was copolymerized with FcM at the molar ratio of 1 : 1 in the presence of FM 3 and SYN. Immobilizing this salt in the MIP film might enable the ferrocene oxidation in the PBS and thus improve the label-free determination of SYN. During potentiodynamic deposition of the (SYN-Fc)-(MIP-2) film on the Pt disk electrode surface, an anodic peak at 1.20 V vs. Ag quasi-reference electrode was well developed. This pronounced peak might be assigned to electro-oxidizing the 2,2′-*bis*-bithiophene moieties of the FcM and FM 3, confirming successful polymer formation on the electrode surface. Moreover, the anodic peak current, I_{pa}, increased in consecutive cycles, suggesting that the synthesized MIP film was conductive. Importantly, anodic and cathodic peaks of the ferrocene moiety were observed in current-potential curves at potentials ranging from 0.35 to 0.40 V vs. Ag quasi-reference electrode, demonstrating that the ferrocene derivative was covalently immobilized along with anion in the (SYN-Fc)-(MIP-2) film structure. In fact, a pronounced DPV peak was recorded in blank PBS (pH = 7.4) at the polymer film-coated electrode after SYN extraction with 0.1 M NaOH (curve *1* in Figure 3.3-5a). This peak originated from the electro-oxidation of the ferrocene moiety embedded in (SYN-Fc)-(MIP-2). Its presence in the voltammogram recorded after transferring the MIP film-coated electrode to blank PBS (pH = 7.4) implied that the deposited polymer containing the internal redox probe was stable and remained at the electrode surface after the SYN extraction. Moreover, sodium and potassium cations were presumably expelled from the MIP film to maintain the polymer's electroneutrality, thus enabling the electro-oxidation of the ferrocene moiety. Furthermore, this DPV peak potential was slightly less positive than that recorded for the (SYN-Fc)-(MIP-1) film-coated electrode.

The DPV peak decreased with the SYN concentration increase (Figure 3.3.5a). The linear dynamic concentration range extended from 10 to 99 nM SYN with the calibration plot described by the linear regression equation of $(I_{DPV,0} - I_{DPV,s})/I_{DPV,0} = 0.16\,(\pm0.02) + 3.8 \times 10^{-3}\,(\pm0.3{\times}10^{-3})\,c_{SYN}$ [nM] with the correlation coefficient, $R^2 = 0.979$ (Figure 3.3.5b).
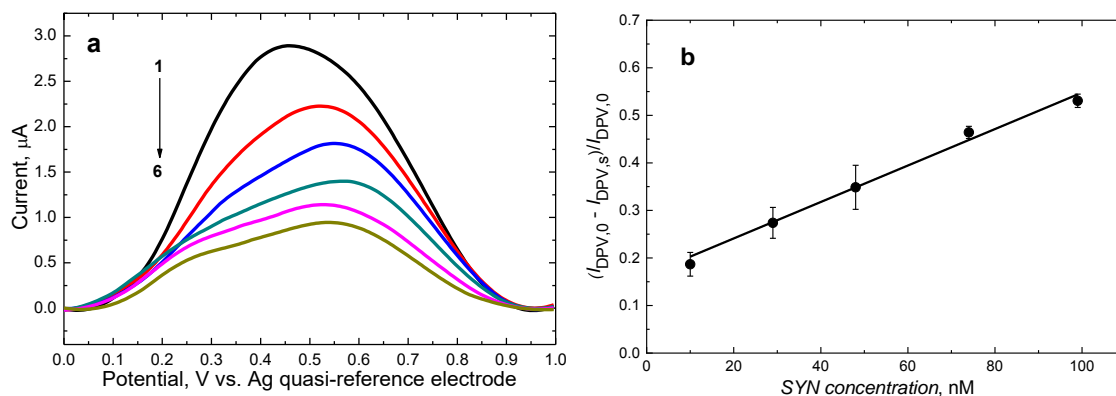
Figure 3.3-5. (a) DPV curves recorded at the 1-mm Pt disk electrode coated with the template-extracted (SYN-Fc)-(MIP-2) film in (curve *1*) blank 0.1 M PBS (pH = 7.4) and then after adding an SYN sample to achieve the concentration of (curve *2*) 10, (curve *3*) 29, (curve *4*) 48, (curve *5*) 74, and (curve *6*) 99 nM. (b) DPV calibration plot for SYN.

3.3.2.3 *Preparing (SYN-Fc)-(MIP-3) film chemosensor and characterizing its analytical performance in aqueous solutions*

Furthermore, another MIP film was synthesized and examined, namely, (SYN-Fc)-(MIP-3) film with entrapped chromotropic acid disodium salt (**3** in Scheme 3.3-1a) as a compound providing the counter ion for ferrocene moiety's electro-oxidation. However, during the polymer formation on the electrode surface, the current decreased in subsequent cycles, signifying that the deposited MIP film was relatively resistive (Figure 3.3-6).
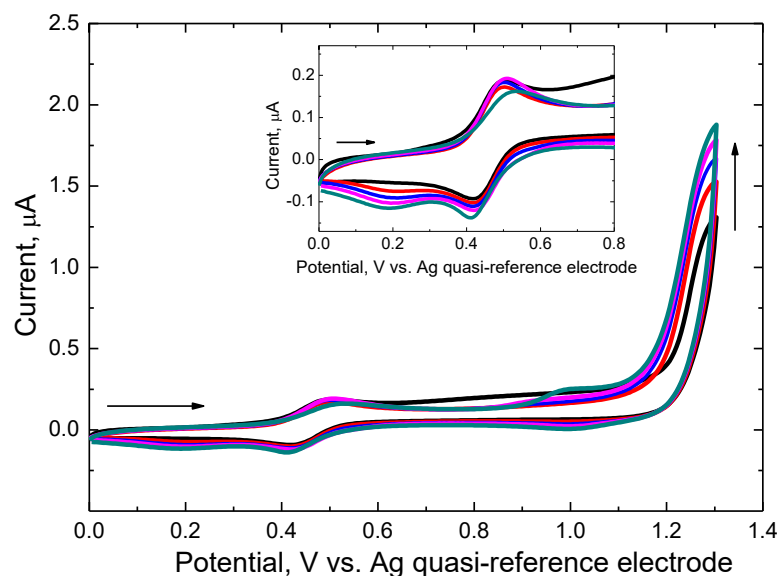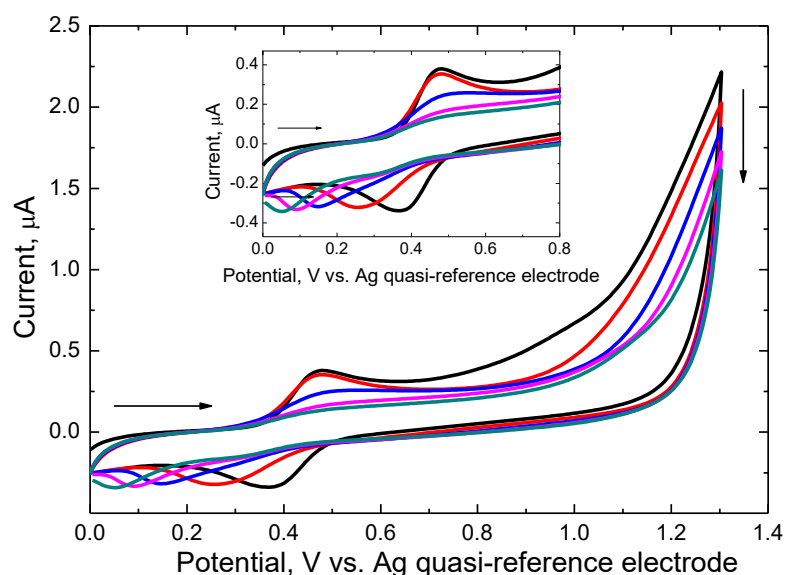

Figure 3.3-6. The five-cycle potentiodynamic curve for (SYN-Fc)-(MIP-3) film deposition on 1-mm diameter Pt disk electrode from 10 μM SYN, 30 μM FM 3, 100 μM Fc, and 100 μM chromotropic acid disodium salt in 0.1 M (TBA)ClO$_4$, in the acetonitrile-dichloromethane 9 : 1 (*v* : *v*), solution.

155

Moreover, anodic and cathodic peak currents originating from the electro-oxidation and electroreduction of the ferrocene moiety, respectively, decreased in consecutive cycles until they disappeared in the last cycle. Besides, the separation of these peaks increased during electropolymerization. Supposedly, (SYN-Fc)-(MIP-3) film was not permeable for perchlorate anions of the supporting electrolyte to penetrate the polymer. That is, the ingress and egress of these ions were impossible. Consequently, the ferrocene internal redox probe could not be electro-oxidized during the deposition of a thicker MIP film. Afterward, the DPV peak recorded at the electrode coated with the SYN-extracted (SYN-Fc)-(MIP-3) film linearly decreased with the increase of the SYN concentration in the range of 0.1 to 0.99 μM (Figure 3.3.7a) obeying the linear regression equation of $(I_{DPV,0} - I_{DPV,s})/I_{DPV,0} = 0.24\,(\pm0.03) + 2.6 \times 10^{-4}\,(\pm0.4 \times 10^{-4})\,c_{SYN}$ [nM] with the correlation coefficient, $R^2 = 0.902$ (Figure 3.3.7b).
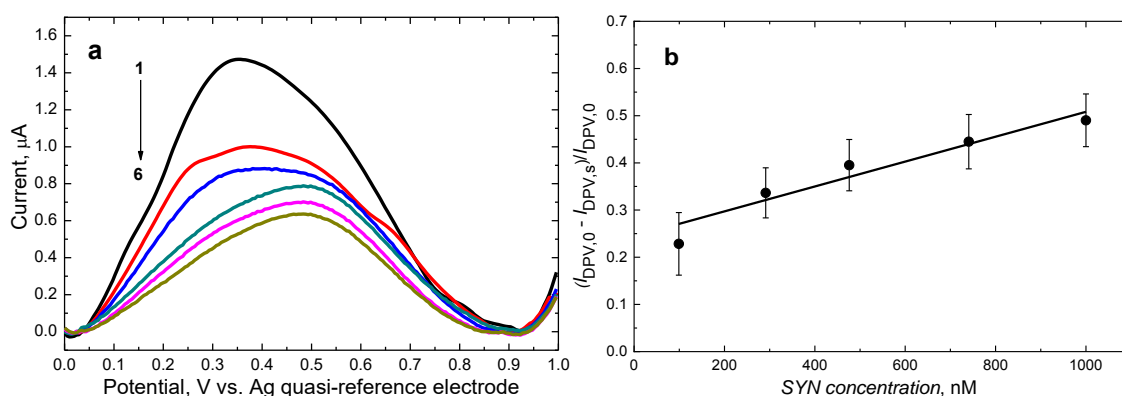
Figure 3.3-7. (a) The DPV curves recorded at the 1-mm Pt disk electrode coated with the (SYN-Fc)-(MIP-3) film after SYN extraction with 0.1 M NaOH in (curve *1*) blank 0.1 M PBS (pH = 7.4) and after subsequent addition of SYN to reach the concentration of (curve *2*) 0.10, (curve *3*) 0.29, (curve *4*) 0.48, (curve *5*) 0.74, and (curve *6*) 0.99 μM in the test solution. (b) The DPV calibration plot for SYN constructed.

DPV signals recorded at electrodes coated with template-extracted (SYN-Fc)-(MIP-2) and (SYN-Fc)-(MIP-3) films during the determination of SYN in blank 0.1 M PBS (pH = 7.4) were, respectively, four- (Figure 3.3-5a) and eight-times (Figure 3.3-7a) lower than that for the (SYN-Fc)-(MIP-1) film-coated electrode recorded in the NH4SCN presence. However, the necessity of introducing an additional salt to the test solution is impractical in terms of label-free sensing of SYN. Thus, studying the chemosensor based on the (SYN-Fc)-(MIP-1) film was abandoned. Moreover, the sensitivity in terms of the relative change of the DPV peak of the (SYN-Fc)-(MIP-2)

film sensor to SYN was ~14 times higher than those for (SYN-Fc)-(MIP-1) and (SYN-Fc)-(MIP-3) film-coated electrodes and ten times higher than that for the SYN-MIP film chemosensor in detail described in Section 3.2 above.

Regrettably, the DPV peaks recorded at the (SYN-Fc)-(MIP-2) and (SYN-Fc)-(MIP-3) film-coated electrode in the aqueous solution, blank 0.1 M PBS (pH = 7.4), were flattened and broadened (Figures 3.3-5a and 3.3-7a, respectively). Those peaks originating from the ferrocene moiety redox probe immobilized in MIP films might be composed of two overlapping peaks, possibly suggesting the presence of two forms of ferrocene moieties in polymer films. One might be localized near the MIP film-solution interface. Thus, it could be easier electro-oxidized because of easier accessibility for counter ions of the test solution. The other form might be immobilized deep inside the MIP film, hence less reachable for counter ions and, consequently, less prone to electro-oxidation.

3.3.3   Optimizing self-reporting MIP films' composition for determining *p*-synephrine in non-aqueous solutions

3.3.3.1   Preliminary studies of the analytical performance of (SYN-Fc)-MIP film-based chemosensors in acetonitrile solution

The broadened and flattened DPV peaks recorded at Pt disk electrodes coated with (SYN-Fc)-MIP films in 0.1 M PBS (pH = 7.4) prompted us to study the analytical performance of the (SYN-Fc)-(MIP-1) and (SYN-Fc)-(MIP-2) film chemosensors in 0.1 M (TBA)ClO$_4$ in acetonitrile. DPV peaks recorded in this hydrophobic supporting electrolyte were narrow and well-pronounced (Figures 3.3-8a and 3.3-8c), suggesting enhanced supporting electrolyte ions diffusion through the MIP film. The DPV peak decreased with the SYN concentration increase from 2 to 75 nM in both cases. The (SYN-Fc)-(MIP-1) film-coated electrode response to SYN in 0.1 M (TBA)ClO$_4$ in acetonitrile obeyed the linear regression equation of $(I_{DPV,0} - I_{DPV,s})/I_{DPV,0} = 0.32\,(\pm0.02) + 2.4\times10^{-3}\,(\pm0.5\times10^{-3})\,c_{SYN}$ [nM] with the correlation coefficient, $R^2 = 0.805$ (Figure 3.3.8b), whereas the (SYN-Fc)-(MIP-2) film-coated electrode response to SYN in 0.1 M (TBA)ClO$_4$ in acetonitrile was described by the equation of $(I_{DPV,0} - I_{DPV,s})/I_{DPV,0} = 0.36\,(\pm0.02) + 3.4\times10^{-3}\,(\pm0.7\times10^{-3})\,c_{SYN}$ [nM] with the correlation coefficient, $R^2 = 0.834$ (Figure 3.3.8d).
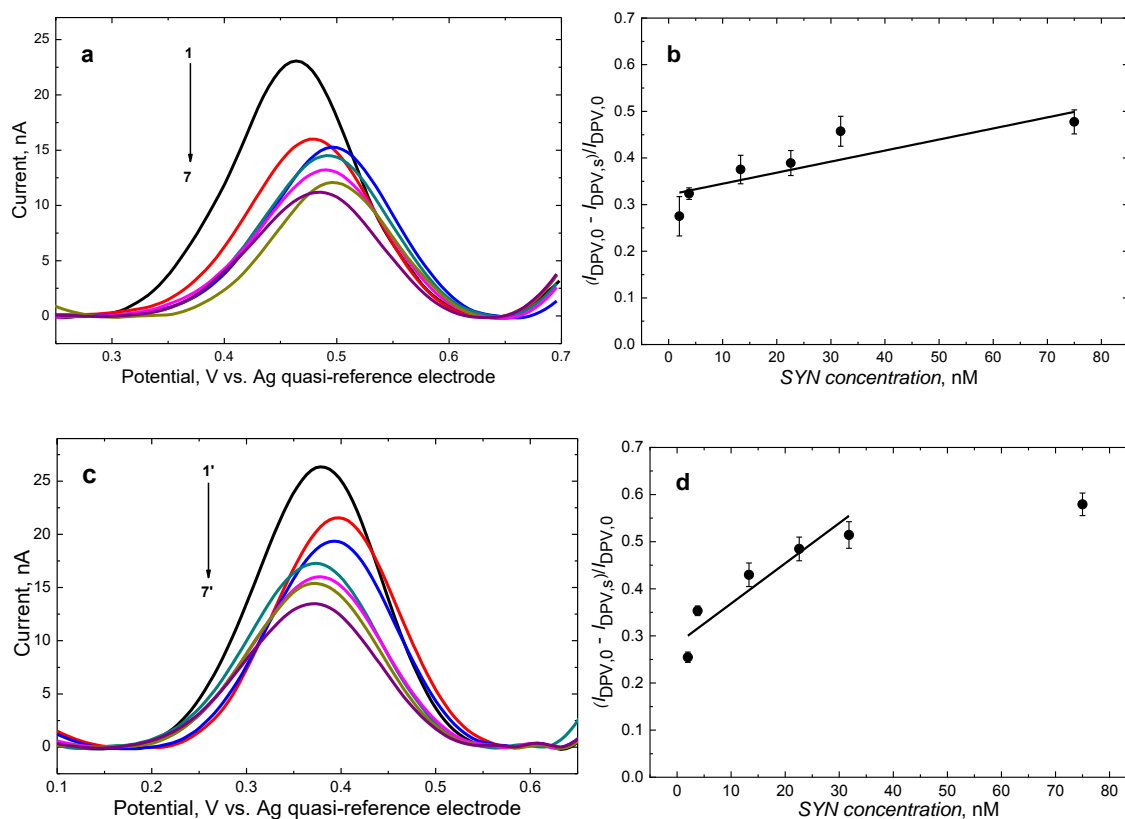
Figure 3.3-8. DPV curves recorded at the 1-mm Pt disk electrode coated with (a) the (SYN-Fc)-(MIP-1) film and (c) the (SYN-Fc)-(MIP-2) film after SYN extraction from the polymer with 0.1 M NaOH in (curves *1* and *1'*) blank 0.1 M (TBA)ClO$_4$ in acetonitrile and then after addition of SYN to reach the concentration of (curves *2* and *2'*) 2.0, (curves *3* and *3'*) 3.8, (curves *4* and *4'*) 13.3, (curves *5* and *5'*) 22.6, (curves *6* and *6'*) 31.7, and (curves *7* and *7'*) 75 nM. (b and d) The calibration curves for the SYN analyte in 0.1 M (TBA)ClO$_4$ in acetonitrile at the electrode coated with template-extracted (b) (SYN-Fc)-(MIP-1) and (d) (SYN-Fc)-(MIP-2) films.

3.3.3.2 *Optimizing electropolymerization of (SYN-Fc)-(MIP-4) film deposition for SYN determining in the acetonitrile solution*

As the DPV peaks recorded at (SYN-Fc)-MIP film-coated electrodes in non-aqueous solution were well-pronounced, in contrast to broad DPV peaks for 0.1 M PBS (pH = 7.4), further experiments were performed for 0.1 M (TBA)ClO$_4$ in acetonitrile. Moreover, the potentiodynamic electropolymerization conditions were carefully optimized because the (SYN-Fc)-MIP film thickness is essential for SYN determination. Two issues were taken into account during film preparation. On the one hand, synthesizing a thick MIP film results in more FcM moieties and more cavities in the polymer. Thus, the current and capacity of the MIP film might increase with the polymer thickness increase. On the other, however, thick MIP film signifies a larger

158

distance between the immobilized FcM moieties and interfaces of the MIP film-(test solution) and MIP film-(electrode surface). Therefore, ion transport and electron transfer may be inhibited for a thicker film, decreasing the current. Hence, the 1-decyl-3-methylimidazolium *bis*(trifluoromethanesulfonyl)imide ionic liquid (**4** in Scheme 3.3-1a) was applied to prepare porous MIP film for balancing the two above effects. For film thickness optimization, different potential ranges and numbers of potentiodynamic cycles for (SYN-Fc)-MIP film deposition were examined (Figure 3.3-9).
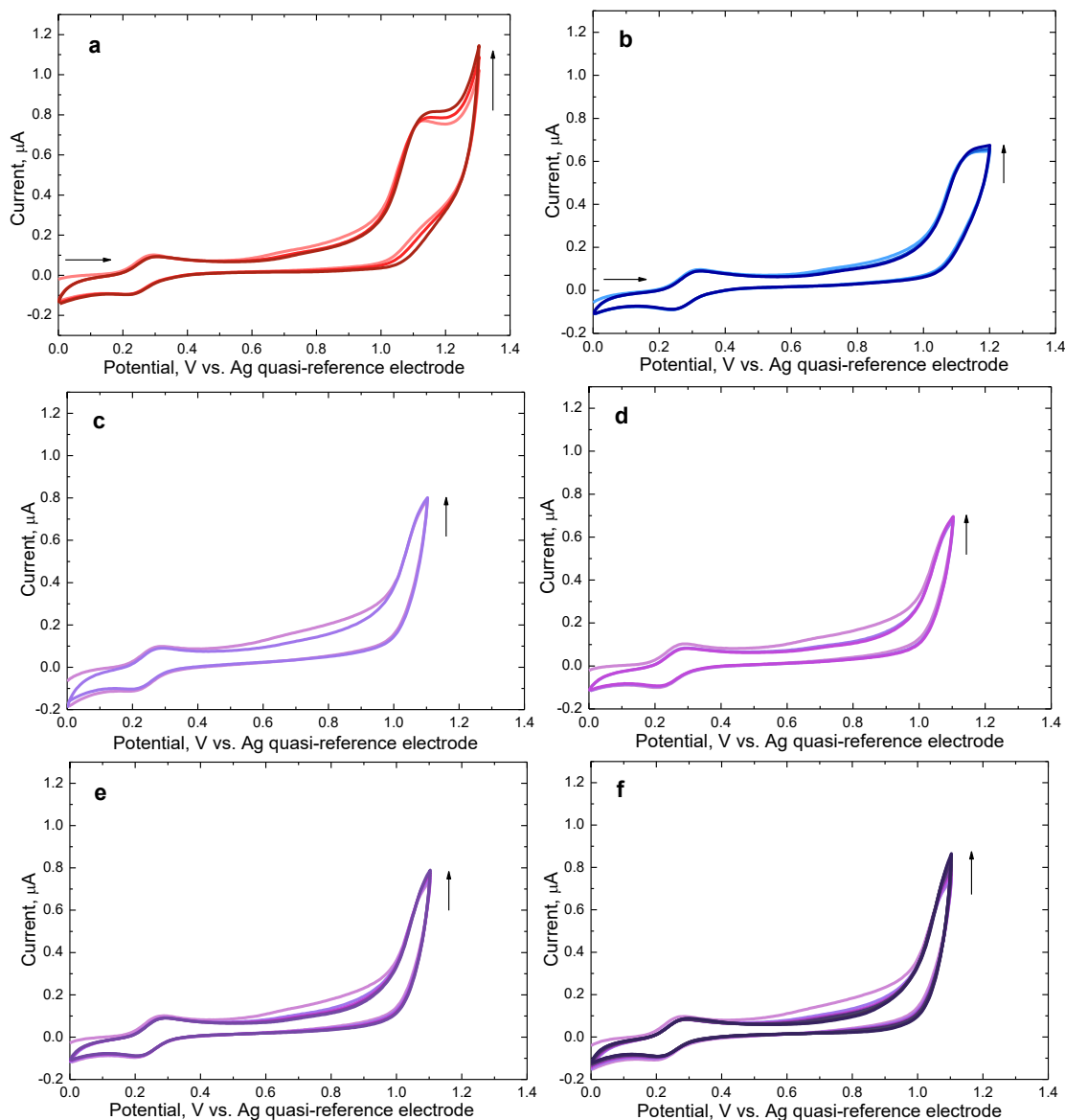
Figure 3.3-9. Optimization of simultaneous potentiodynamic electropolymerization and deposition of the (SYN-Fc)-(MIP-4) film on the 1-mm diameter Pt disk electrode from the solution of 10 µM SYN, 30 µM FM 3, 100 µM Fc, 100 µM sodium thiophen-2-ylmethanesulfonate, and 0.1 M (TBA)ClO$_4$ in toluene, 1-decyl-3-methylimidazolium *bis*(trifluoromethanesulfonyl)imide ionic liquid, and acetonitrile at the 1 : 2.5 : 6.5, *v* : *v* : *v* ratio. The electropolymerization potential range was 0 to (a) 1.30, (b) 1.20, and (c)–(f) 1.10 V vs. Ag quasi-reference electrode within (c) 2, (a), (b), and (d) 3, (e) 5, and (f) 10 current-potential cycles at a scan rate of 50 mV s^{-1}.

159

After electropolymerization under different conditions, polymer film-coated electrodes were transferred to 0.1 M (TBA)ClO$_4$ in acetonitrile, and then DPV peaks were recorded (Figure 3.3-10a). Subsequently, SYN was extracted from the polymers with 10 mM Et$_3$N in acetonitrile for 5 min. Then, electrodes with deposited MIP films were again immersed in the 0.1 M (TBA)ClO$_4$ acetonitrile solution (Figure 3.3-10b). The DPV peak was the highest for the MIP film deposited by applying three current-potential cycles in the potential range of 0 to 1.10 V (curve *4* in Figure 3.3-10a). Moreover, the DPV signal after template extraction was the most pronounced for the same polymer film (curve *4'* in Figure 3.3-10b).
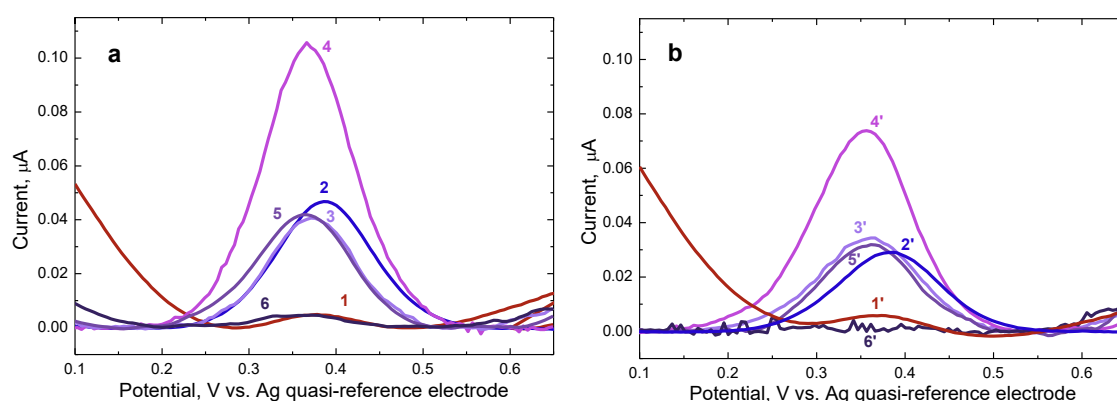
Figure 3.3-10. DPV curves for the deposited, according to electropolymerization procedures shown in Figures 3.3-9a–3.3-9f, MIP film-coated electrodes in 0.1 M (TBA)ClO$_4$ in acetonitrile (a) before and (b) after SYN extraction with 10 mM Et$_3$N in acetonitrile for 5 min. The electropolymerization potential range for MIP films deposition was 0 to (curves *1* and *1'*) 1.30, (curves *2* and *2'*) 1.20, and (curves *3* and *3'*)–(curves *6* and *6'*) 1.10 V vs. Ag quasi-reference electrode within (curves *3* and *3'*) 2, (curves *1* and *1'*), (curves *2* and *2'*), and (curves *4* and *4'*) 3, (curves *5* and *5'*) 5, and (curves *6* and *6'*) 10 current-potential cycles at a scan rate of 50 mV s^{-1}.

The (SYN-Fc)-(MIP-4) polymer prepared under these electropolymerization conditions was applied in a further study.

Using the ionic liquid for the (SYN-Fc)-(MIP-4) preparation led to partial blocking of the electrode surface, and hence currents recorded during electropolymerization were slightly lower than those recorded during (SYN-Fc)-(MIP-2) film deposition. Nevertheless, DPV peaks recorded at the (SYN-Fc)-(MIP-4) film-coated electrode were better defined than those for the (SYN-Fc)-(MIP-2) film.

Moreover, the immobilization of a compound providing sulfonyl groups as counter ions for ferrocene electro-oxidation was validated. For that purpose, another polymer film, namely, the (SYN-Fc)-(MIP-5) film, was deposited under the

160

electropolymerization conditions same as for the (SYN-Fc)-(MIP-4) film but without sodium thiophen-2-ylmethanesulfonate (**2** in Scheme 3.3-1a) in the pre-polymerization complex solution (Figure 3.3-11a).

DPV peaks for the (SYN-Fc)-(MIP-5) film-coated electrode after SYN extraction were significantly lower than those for the (SYN-Fc)-(MIP-4) film-coated electrode with sulfonyl groups present inside the polymer (Figure 3.3-11b).
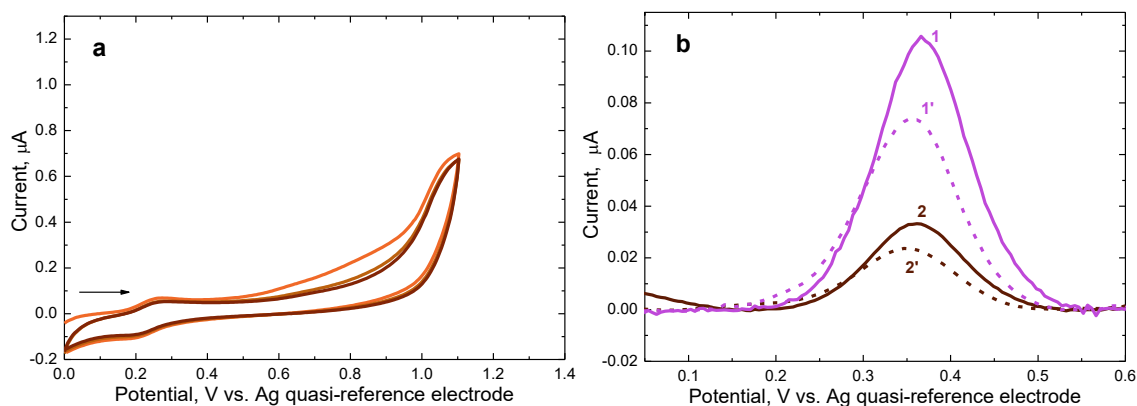
Figure 3.3-11. (a) The multi-cyclic potentiodynamic curve for (SYN-Fc)-(MIP-5) film deposition on the 1-mm diameter Pt disk electrode from the solution of 10 μM SYN, 30 μM FM 3, 100 μM Fc, 100 μM sodium thiophen-2-ylmethanesulfonate, and 0.1 M (TBA)ClO$_4$ in toluene, 1-decyl-3-methylimidazolium *bis*(trifluoromethanesulfonyl)imide ionic liquid, and acetonitrile of the 1 : 2.5 : 6.5, $v : v : v$ ratio. (b) DPV curves recorded at electrodes coated with (curves *1* and *1′*) (SYN-Fc)-(MIP-4) and (curves *2* and *2′*) (SYN-Fc)-(MIP-5) films (curves *1* and *2*) before and (curves *1′* and *2′*) after SYN extraction with 10 mM Et$_3$N in acetonitrile for 5 min.

What is more, further measurements were performed using 0.1 M (TBA)ClO$_4$ in acetonitrile because DPV peaks, recorded at the optimized (SYN-Fc)-(MIP-4) film-coated electrode in 0.1 M PBS (pH = 7.4) during SYN determination, were still flattened and broadened (Figure 3.3-12).

Furthermore, SYN extraction from (SYN-Fc)-(MIP-4) film was examined. The DPV peaks for the ferrocene moiety in 0.1 M (TBA)ClO$_4$ in acetonitrile were measured before and after SYN extraction using different extraction solutions. The DPV peak decreased by 17.45 nA (40.7%) after SYN extraction with 0.1 M NaOH for 60 min (Figure 3.3-13a). However, SYN extraction with 10 mM Et$_3$N for 5 min decreased the DPV peak by 30.1 nA (25%) (Figure 3.3-13b). So, both procedures were nearly equally efficient. Nevertheless, the latter took only 5 min under milder conditions than the former, with 0.1 M NaOH. Thus, 10 mM Et$_3$N was used for further SYN extraction.

Moreover, SYN was extracted with 10 mM tetrabutylammonium hydroxide, (TBA)OH, in acetonitrile. However, there was no DPV peak after SYN template extraction (Figure 3.3-13c). Most likely, this extraction damaged the film. Therefore, it was abandoned.
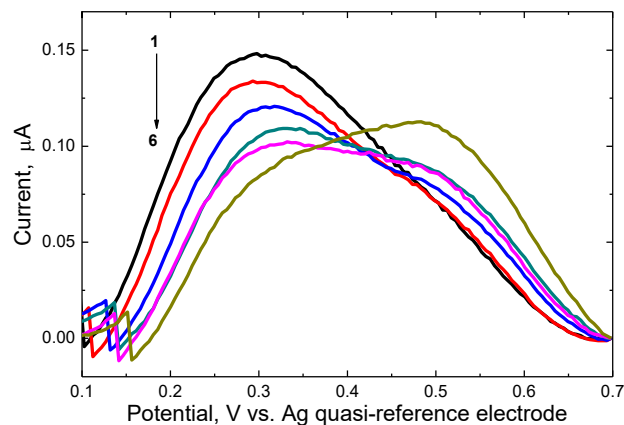
Figure 3.3-12. The DPV curves recorded at the 1-mm Pt disk electrode coated with the SYN template-extracted (SYN-Fc)-(MIP-4) film in blank 0.1 M PBS (pH = 7.4) and then after the addition of SYN resulting in its concentration of (curve *2*) 2.0, (curve *3*) 3.8, (curve *4*) 13.3, (curve *5*) 22.6, and (curve *6*) 31.7 nM in the test solution.
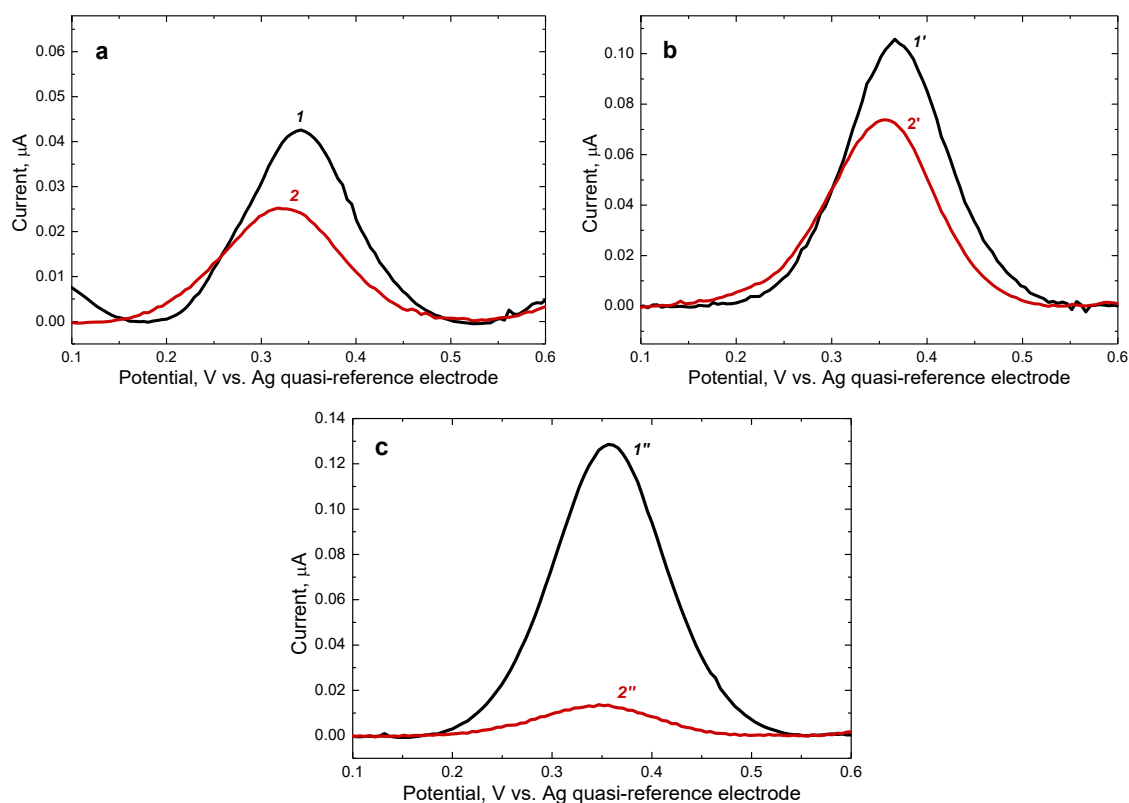
Figure 3.3-13. DPV curves recorded at the (SYN-Fc)-(MIP-4) film-coated Pt electrodes in 0.1 M (TBA)ClO$_4$ in acetonitrile (curves *1*, *1′*, and *1″*) before and (curves *2*, *2′*, and *2″*) after SYN template extraction with (a) 0.1 M NaOH for 60 min, (b) 10 mM Et$_3$N in acetonitrile for 5 min, and (c) 10 mM (TBA)OH in acetonitrile for 5 min.

162

To verify the imprinting, a control polymer film, vis., Fc-(NIP-4), was prepared in the same manner as the (SYN-Fc)-(MIP-4) film but without the SYN template in the pre-polymerization complex solution.

For a direct comparing all MIP film chemosensors prepared, their deposition conditions and analytical parameters are summarized in Table 3.3-1.

Table 3.3-1. Deposition conditions and analytical parameters of synthesized MIP films.

MIP film	Deposition parameter			DPV determined parameter		
	Composition of pre-polymerization complex solution	Number of current-potential cycles	Potential range, V vs. quasi-reference electrode	Supporting electrolyte	Sensitivity to SYN, nM^{-1}	LOD, nM
(SYN-Fc)-(MIP-1)	10 μM SYN, 30 μM FM 3, 100 μM Fc, and 0.1 M (TBA)ClO$_4$ in acetonitrile	5	0 – 1.3	0.1 M PBS (pH = 7.4)	-	-
				0.1 M PBS (pH = 7.4) in the presence of 0.1 M NH$_4$SCN	2.82×10^{-4}	28.93
				0.1 M (TBA)ClO$_4$ in acetonitrile	2.37×10^{-3}	19
(SYN-Fc)-(MIP-2)	10 μM SYN, 30 μM FM 3, 100 μM Fc, 100 μM sodium thiophen-2-ylmethanesulfonate, and 0.1 M (TBA)ClO$_4$ in acetonitrile	5	0 – 1.3	0.1 M PBS (pH = 7.4)	3.8×10^{-3}	17.2
				0.1 M (TBA)ClO$_4$ in acetonitrile	8.53×10^{-3}	10.3
(SYN-Fc)-(MIP-3)	10 μM SYN, 30 μM FM 3, 100 μM Fc, 100 μM chromotropic acid disodium salt, and 0.1 M (TBA)ClO$_4$ in acetonitrile	5	0 – 1.3	0.1 M PBS (pH = 7.4)	2.64×10^{-4}	30.25
(SYN-Fc)-(MIP-4)	10 μM SYN, 30 μM FM 3, 100 μM Fc, 100 μM sodium thiophen-2-ylmethanesulfonate, and 0.1 M (TBA)ClO$_4$ in the solution of toluene, 1-decyl-3-methylimidazolium *bis*(trifluoromethanesulfonyl)imide ionic liquid, and acetonitrile at the 1 : 2.5 : 6.5, *v* : *v* : *v* ratio	3	0 – 1.1	0.1 M (TBA)ClO$_4$ in acetonitrile	3.99×10^{-2}	0.57
SYN-MIP described in Section 3.2	10 μM SYN, 30 μM FM 3, 300 μM CM 2, and 0.1 M (TBA)ClO$_4$ in acetonitrile	5	0 – 1.3	0.1 M PBS (pH=7.4) with 0.1 M K$_4$[Fe(CN)$_6$] and 0.1 M K$_3$[Fe(CN)$_6$]	3.21×10^{-4}	12.2

164

3.3.4 Characterizing (SYN-Fc)-(MIP-4) and Fc-(NIP-4) films

The optimized MIP film and corresponding control NIP film were characterized using AFM, XPS, PM-IRRAS, and EDX spectroscopy. For that purpose, (SYN-Fc)-(MIP-4) and Fc-(NIP-4) films were deposited on the surface of Au-layered glass slides under potentiodynamic conditions, described in Section 3.3.3.2 above.

PM-IRRAS measurements confirmed the successful deposition of (SYN-Fc)-(MIP-4) and Fc-(NIP-4) films on the electrode surface (Figure 3.3-14). Indeed, the band at ~1800 cm^{-1} characteristic of C=O stretching vibration of the carboxyl group[403] of the FM 3 functional monomer was visible in PM-IRRAS spectra for the (SYN-Fc)-(MIP-4) and Fc-(NIP-4) films. The band at ~1100 cm^{-1} in the MIP and NIP film spectra is, presumably, the vibration band of perchlorate ions of the supporting electrolyte that remained in the polymers after their deposition on the electrode surface. The band at ~3100 cm^{-1} is an artifact originating from baseline correction of the spectrum for the (SYN-Fc)-(MIP-4) film.
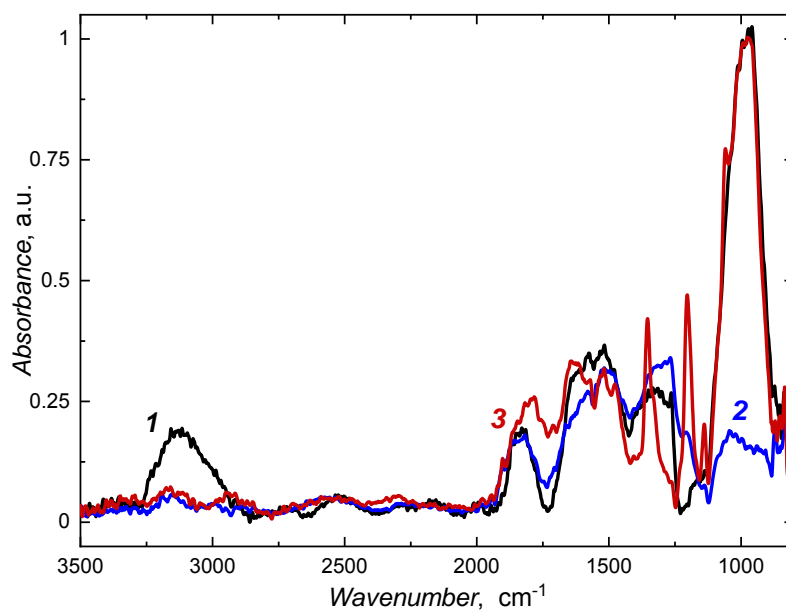
Figure 3.3-14. The PM-IRRAS spectra for (SYN-Fc)-(MIP-4) film recorded (spectrum *1*) before and (spectrum 2) after SYN template extraction with 10 mM Et$_3$N in acetonitrile for 5 min as well as (spectrum *3*) for Fc-(NIP-4) film after treating with the same extraction solution for 5 min.

The XPS measurement results for MIP and NIP films before and after SYN extraction with 10 mM Et$_3$N in acetonitrile indicated low concentrations of iron atoms, ranging from 0.20 atomic % for Fc-(NIP-4) film to 1.68 Fe atomic % for the (SYN-Fc)-(MIP-4) film (Tables 3.3-2 to 3.3-5). Thus, MIP films were then studied with EDX

spectroscopy (Tables 3.3-6 to 3.3-9). Atomic concentrations of iron, based on the Fe L line in the EDX spectra for MIP and NIP films, were substantially higher than those determined by XPS, ranging from 2.7 to 5.7 Fe atomic %. These differences in the EDX spectroscopy and XPS results may, presumably, come from different locations of positively charged ferrocenium moieties in the polymers. Supposedly, they were located deeply inside the polymer matrix instead of being exposed to the (polymer film)|(hydrophobic solvent) interface during electropolymerization. Therefore, their concentration in the polymer bulk might be much higher than that close to the surface, thereby barely detected by XPS.

Moreover, concentrations of fluoride originating from the ionic liquid in MIP and NIP films were low. Evidently, only a tiny ionic liquid amount was entrapped in the polymers during their deposition. Presumably, the ionic liquid was rinsed out after electropolymerization, forming nanopores in the (SYN-Fc)-(MIP-4) and Fc-(NIP-4) films. Therefore, additional ionic liquid removal from the deposited polymer was unnecessary.

Table 3.3-2. The XPS-determined surface elemental composition of the (SYN-Fc)-(MIP-4) film before SYN template removal.

Element	Concentration, atomic %
Na	1.03
Fe	1.63
F	-
O	25.35
N	5.06
C	63.35
S	3.58

Table 3.3-3. The XPS-determined surface elemental composition of the (SYN-Fc)-(MIP-4) film after SYN template extraction with 10 mM Et_3N in acetonitrile for 5 min.

Element	Concentration, atomic %
Na	-
Fe	1.68
F	1.23
O	25.35
N	8.03
C	59.51
S	4.20

166

Table 3.3-4. The XPS-determined surface elemental composition of the Fc-(NIP-4) film.

Element	Concentration, atomic %
Na	-
Fe	0.23
F	7.55
O	9.49
N	7.88
C	71.20
S	3.65

Table 3.3-5. The XPS-determined surface elemental composition of the Fc-(NIP-4) film after treatment with the extraction solution of 10 mM Et$_3$N in acetonitrile for 5 min.

Element	Concentration, atomic %
Na	0.25
Fe	0.20
F	5.95
O	11.52
N	10.02
C	68.89
S	3.17

Table 3.3-6. The (EDX spectroscopy)-determined composition of the (SYN-Fc)-(MIP-4) film before extracting the SYN template.

Element	Concentration, atomic %
Fe	2.78
O	10.5
N	25.5
C	61.15

Table 3.3-7. The (EDX spectroscopy)-determined composition of the (SYN-Fc)-(MIP-4) film after SYN template extraction with 10 mM Et$_3$N in acetonitrile for 5 min.

Element	Concentration, atomic %
Fe	3.49
O	10.1
N	26.6
C	59.8

Table 3.3-8. The (EDX spectroscopy)-determined composition of the Fc-(NIP-4) film.

Element	Concentration, atomic %
Fe	3.24
O	11.1
N	27.0
C	58.7

Table 3.3-9. The (EDX spectroscopy)-determined composition of the Fc-(NIP-4) film after treatment with the extraction solution of 10 mM Et_3N in acetonitrile for 5 min

Element	Concentration, atomic %
Fe	5.26
O	10.1
N	25.8
C	58.8

The results of AFM imaging of the (SYN-Fc)-(MIP-4) film and the control Fc-(NIP-4) film confirmed the EDX spectroscopy and XPS results (Figure 3.3-15 and Table 3.3-10). Moreover, the film morphology before and after treatment with the extraction solution was thus compared. All films contained flattened, round grains much bigger than the Au support grains (Table 3.3-10). Moreover, numerous pores with 150 to 200 nm diameters were randomly located in the (SYN-Fc)-(MIP-4) and Fc-(NIP-4) films (Figures 3.3-15a and 3.3-15c). Extraction of the SYN template from the MIP resulted in the shrinking of some polymer pores (Figures 3.3-15b and 3.3-15d). Nevertheless, most of them stayed intact. The AFM determined (SYN-Fc)-(MIP-4) film thickness and roughness before SYN extraction was 22 ($\pm$6) nm and 10.2 ($\pm$0.7) nm, respectively, whereas the thickness and roughness of the (SYN-Fc)-(MIP-4) film after SYN extraction were 27 ($\pm$7) nm and 5 ($\pm$1) nm, respectively. Moreover, the thickness and roughness of the Fc-(NIP-4) film before treatment with the extraction solution were estimated as 23 ($\pm$6) nm and 8.8 ($\pm$0.2) nm, respectively, whereas thickness and roughness after the treatment were 21 ($\pm$5) nm and 4 ($\pm$2) nm, respectively.

Furthermore, the nanomechanical properties of the polymer films were examined with AFM. The results indicated the average hardness of the (SYN-Fc)-(MIP-4) and Fc-(NIP-4) films with the Young modulus of a few GPa and tip-sample adhesion of

several nN. Interestingly, SYN extraction led to a substantial increase in Young modulus and adhesion parameters of MIP and NIP films, suggesting the formation of rigid polymers. Moreover, Young modulus and adhesion values assessed for the (SYN-Fc)-(MIP-2) film were close to those for the (SYN-Fc)-(MIP-4) and Fc-(NIP-4) films after treating with the extraction solution. All AFM-determined nanomechanical properties of the films are summarized in Table 3.3-10.
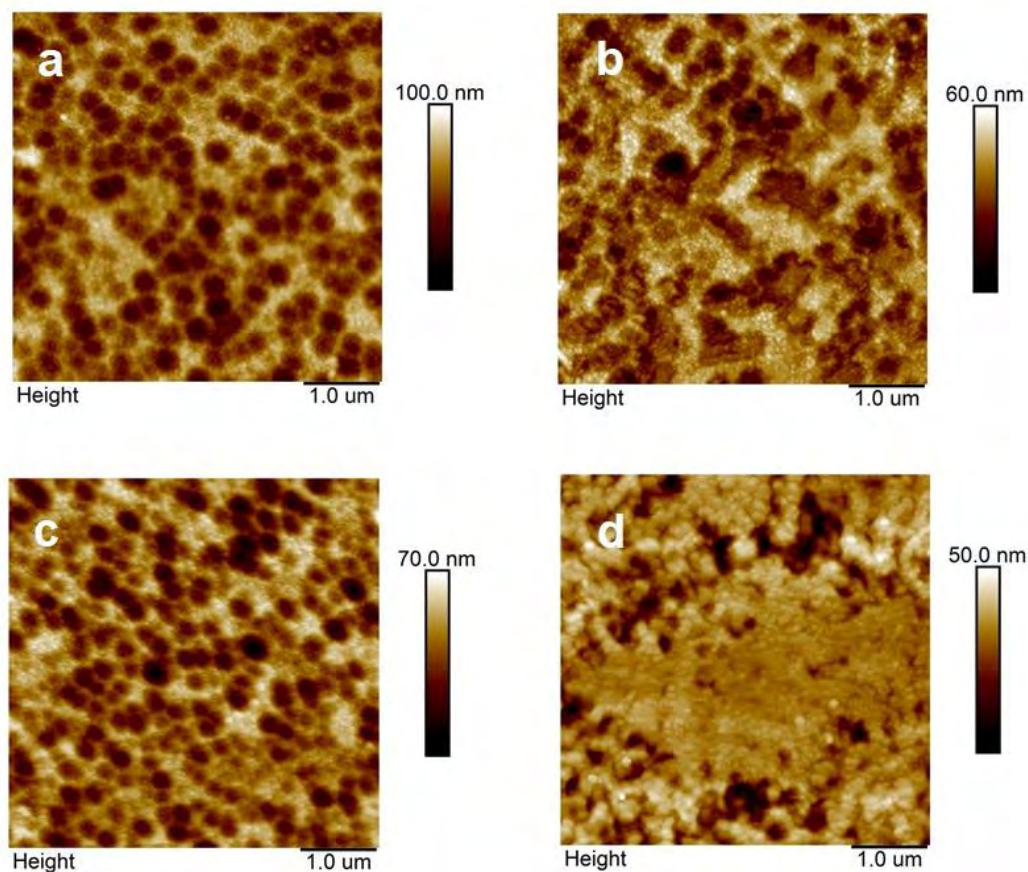
Figure 3.3-15. The (5.0×5.0) μm^2 AFM images of (a) and (b) (SYN-Fc)-(MIP-4) and (c) and (d) Fc-(NIP-4) films imaged (a) and (c) before, as well as after (b) SYN template extraction, and (d) treating with 10 mM Et_3N in acetonitrile for 5 min.

169

Table 3.3-10. The AFM-determined nanomechanical properties of polymer films deposited on gold-layered glass slides.

Sample	Thickness, nm	Roughness (R_a), nm	Average grain size, nm	Young modulus, GPa	Adhesion, nN
(SYN-Fc)-(MIP-4) as prepared	22 ± 6	10.2 ± 0.7	73	9 ± 1	9 ± 5
(SYN-Fc)-(MIP-4) after SYN extraction	27 ± 7	5 ± 1	91	35 ± 2	72 ± 23
Fc-(NIP-4) as prepared	23 ± 6	8.8 ± 0.2	88	4 ± 1	8 ± 4
Fc-(NIP-4) after treatment with extraction solution	21 ± 5	4 ± 2	100	73 ± 16	109 ± 41
Uncoated Au support	-	1.36 ± 0.07	42	-	-

3.3.5 Analysis of the electrochemical response mechanism of the self-reporting chemosensor with the (SYN-Fc)-(MIP-4) film

The EIS experiments in the frequency range of 10 MHz to 100 mHz at $E = 0.20$ V vs. Ag quasi-reference electrode were performed for the (SYN-Fc)-(MIP-4) film-coated electrode in 0.1 M (TBA)ClO$_4$ in acetonitrile before and after SYN template extraction to examine in detail the mechanism of the chemosensor response. Interestingly, instead of the expected Nyquist plots in the form of semicircles representing charge transfer resistance,[258] plots with shapes characteristic of diffusion in thin films with mixed reflecting-absorbing boundary at predomination of the reflecting boundary[408] were recorded (Figure 3.3-16a). These results suggest electron transport through intrinsically conducting polymer film[409] and/or ion diffusion through the porous, semiconductive film.[410-411] Nyquist plots recorded before and after SYN extraction were comparable. However, a substantial difference was in the low-frequency range in the Bode plots (Figure 3.3-16b). A slight "kink-like" feature below ~1 Hz was observed on the curve of the logarithm of impedance modulus vs. the logarithm of the frequency for the electrode coated with the (SYN-Fc)-(MIP-4) film before SYN extraction (black dashed curve *1″* in Figure 3.3-16b). Moreover, a peak at 1 Hz was seen on the plot of the phase angle vs. the logarithm of the frequency (black curve *1′* in Figure 3.3-16b),

substantiating that the prepared MIP film was porous.[412] Furthermore, SYN extraction from the MIP resulted in a peak shift to lower frequencies (red curve *2'* in Figure 3.3-16b). This shift indicates a decrease in pore density in harmony with the AFM results.
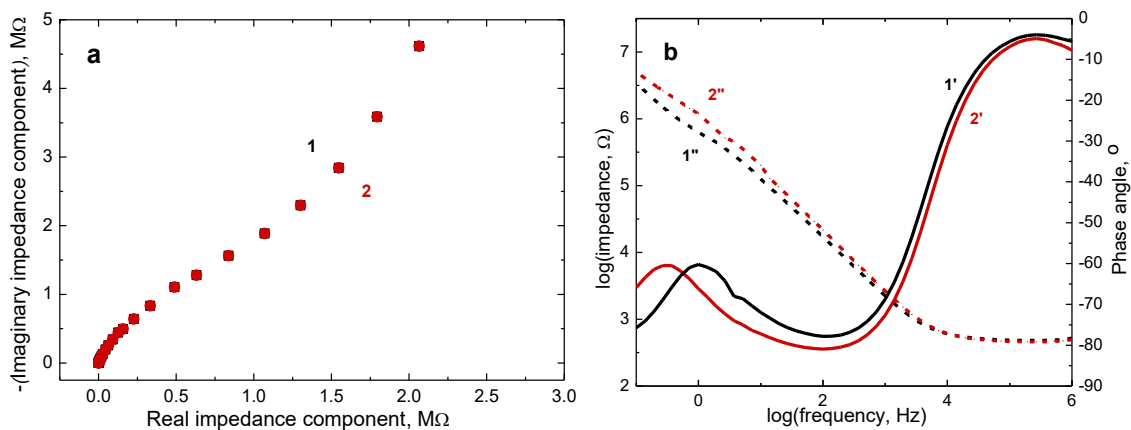
Figure 3.3-16. The EIS (a) Nyquist and (b) Bode plots recorded at the (SYN-Fc)-(MIP-4) film-coated electrode in 0.1 M (TBA)ClO$_4$ in acetonitrile (curves *1*, *1'*, and *1''*) before and (curves *2*, *2'*, and *2''*) after SYN template extraction from the polymer film.

Notably, the decrease in the phase angle peak and its further shift to lower frequencies with the SYN concentration increase (Figure 3.3-17) demonstrate that the (SYN-Fc)-(MIP-4) cavities bound SYN molecules, leading to the film porosity decrease.
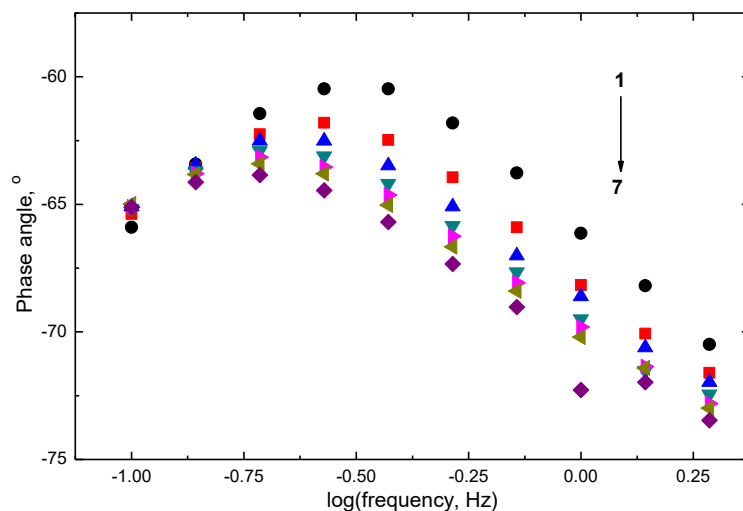
Figure 3.3-17. The EIS phase angle dependence on the logarithm of frequency recorded at the 1-mm diameter Pt disk electrode coated with the (SYN template)-extracted (SYN-Fc)-(MIP-4) film (curve *1*) in 0.1 M (TBA)ClO$_4$ in acetonitrile and after the SYN addition to reaching the concentration of (curve *2*) 2.0, (curve *3*) 3.8, (curve *4*) 13.3, (curve *5*) 22.6, (curve *6*) 31.7, (curve *7*) 75 nM in the test solution.

171

Moreover, the (SYN-Fc)-(MIP-4) film was examined by PM at EQCM. First, the polymer was deposited on the gold film electrode of the QCR under optimized conditions described in Section 3.3.3.2 above. The current of electro-oxidation and electroreduction of the ferrocene moiety was recorded in the potential range of 0.20 to 0.60 V vs. Ag quasi-reference electrode, simultaneously with the resonance frequency and dynamic resistance with the potential change. However, the signal-to-noise ratio was low, and resonance frequency changes were irreproducible (data not shown).

Therefore, the conditions were optimized for MIP film deposition on the gold film electrode of the QCR from the pre-polymerization complex solution of 100 μM SYN, 300 μM FM 3, 1 mM Fc, 1 mM sodium thiophen-2-ylmethanesulfonate, and 0.1 M (TBA)ClO$_4$ in toluene, the 1-decyl-3-methylimidazolium *bis*(trifluoromethanesulfonyl)imide ionic liquid, and acetonitrile at the volume ratio of 1 : 2.5 : 6.5 (Figure 3.3-18). One potentiodynamic cycle in the potential range of 0 to 1.20 V vs. Ag quasi-reference electrode sufficed for this deposition. Moreover, (TEA)ClO$_4$ instead of (TBA)ClO$_4$ was employed as the supporting electrolyte because tetraethylammonium (TEA) cations are smaller and, therefore, more mobile than tetrabutylammonium (TBA) cations. These new conditions resulted in substantial changes in current and resonant frequency associated with electro-oxidation and subsequent electroreduction of the ferrocene moiety in the polymer film (curves *1* and *1'* in Figures 3.3-19a and 3.3-19b, respectively).

Small anodic-to-cathodic peak separation for the ferrocene moiety (curve *1* in Figure 3.19a) signifies the occurrence of a thin-layer electrochemical process. According to the Sauerbrey equation (Equation 2.3-34 in Section 2.3.4), the 37.82 μg mass of the polymer was deposited during the electropolymerization. Then, the current, in the potential range of 0.20 to 0.60 V vs. Ag quasi-reference electrode of potentiodynamic electropolymerization, was integrated, resulting in 1.11 nmol of the ferrocene moiety deposited, calculated using Faraday's law. The charge passed during this moiety electro-oxidation recorded at the electrode of QCR coated with the optimized (SYN-Fc)-(MIP-4') film was 42.77 μC, indicating that 0.44 nmol of positively charged ferrocene moiety was generated. Thus, 40% of the moieties were electro-oxidized, which accounted for the electrochemical response of the chemosensor. Since the dynamic resistance changed only slightly during potential cycling (Figure 3.3-19c), suggesting that the polymer film rigidity was not altered,

the Sauerbrey equation was used to calculate the MIP film mass change after ferrocene moiety electro-oxidation.
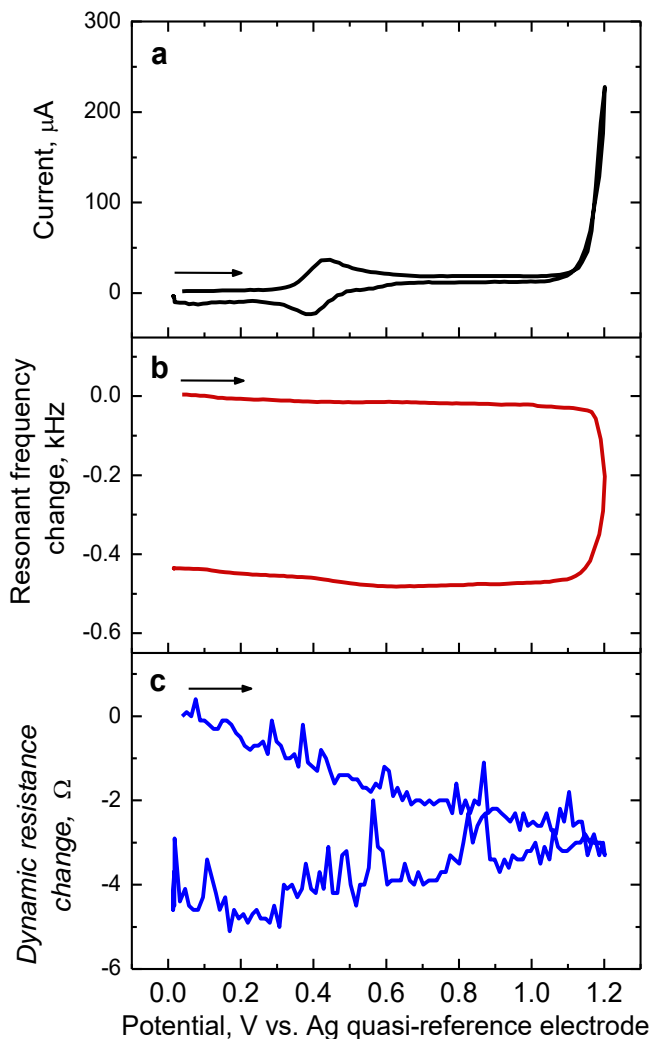
Figure 3.3-18. Simultaneously recorded curves of the potential dependence of (a) current, (b) the resonant frequency change, and (c) the dynamic resistance change for potentiodynamic electropolymerization from the solution of 100 μM SYN, 300 μM FM 3, 1 mM Fc, 1 mM sodium thiophen-2-ylmethanesulfonate, and 0.1 M (TBA)ClO$_4$ in toluene, the 1-decyl-3-methylimidazolium *bis*(trifluoromethanesulfonyl)imide ionic liquid and acetonitrile of the 1 : 2.5 : 6.5 (*v* : *v* : *v*) ratio on a 10-MHz Au-QCR.

The 20.6 (±0.8) Hz resonance frequency decrease after the ferrocene moiety electro-oxidation (curve *1'* in Figure 3.3-19b), signifying an increase in MIP film's mass by 1.79 ng, indicated a mechanism different than that expected. This polymer mass increase may imply that 18 picomoles of perchlorate of the supporting electrolyte entered the MIP film during ferrocene moiety electro-oxidation. However, this number of moles is significantly lower than that of the ferrocene moiety electro-oxidized, suggesting that perchlorate counter-ions may ingress the polymer, whereas cation co-

173

ions may simultaneously egress. Nevertheless, the perchlorate ions ingress slightly prevailed. Then, the resonant frequency increased during the return scan, ending at a level of 6.5 Hz lower than that original (curve *1'* in Figure 3.3-19b). These results meant the entrapment of 5.69 picomoles of perchlorate in the polymer.

Moreover, the CV curve was flattened after adding the SYN sample to the test solution to reach 40 nM of its concentration (curve *2* in Figure 3.3-19a). Although the faradaic current was not pronounced at the potential of the ferrocene moiety electro-oxidation, the resonant frequency increased in this potential range (curve *2'* in Figure 3.3-19b), indicating electroactivity of a tiny amount of the ferrocene moiety. In that case, only cations were expelled from the film, leading to its mass drop. These results might imply that mainly perchlorate diffusion from the solution into the polymer was affected by SYN sorption by the MIP.
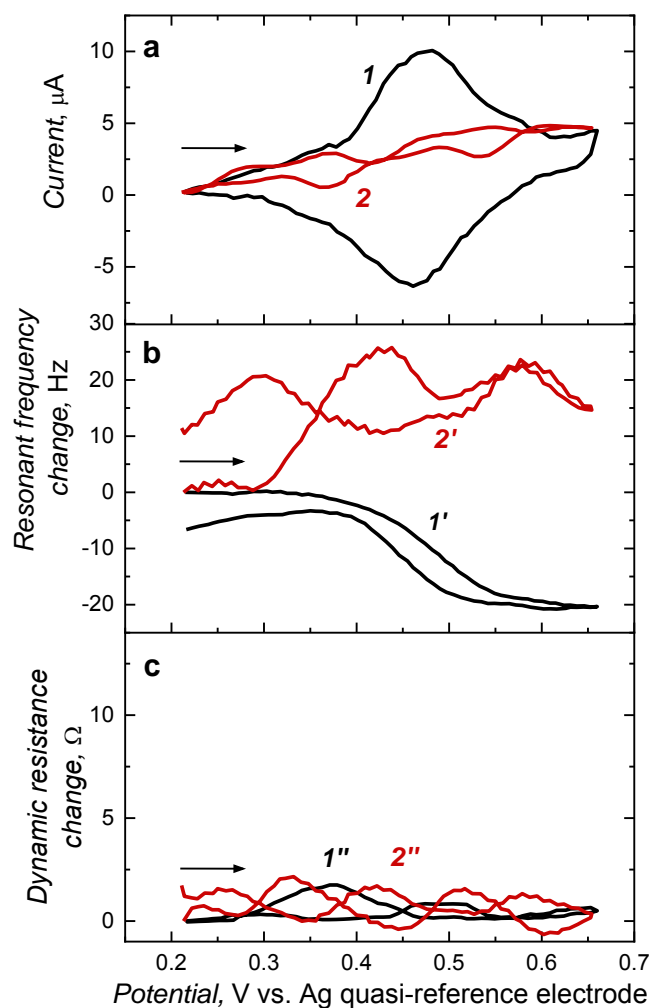
Figure 3.3-19. Simultaneously recorded curves of (a) current, (b) the resonant frequency change, and (c) the dynamic resistance change vs. potential for the Au electrode of QCR coated with the optimized (SYN-Fc)-(MIP-4') film in 0.1 M (TEA)ClO$_4$ in acetonitrile (curves *1, 1',* and *2''*) in the SYN-free solution and (curves *2, 2',* and *2''*) in 40 nM SYN.

174

Furthermore, the (SYN-Fc)-(MIP-4') film chemosensor operation mechanism was studied using SPR spectroscopy. The polymer film was deposited on the Au-SPR chip like that optimized for PM at EQCM measurements. Moreover, current and SPR signal changes were simultaneously recorded during MIP film deposition (Figure 3.3-20) and subsequent CV measurements (Figure 3.3-21).
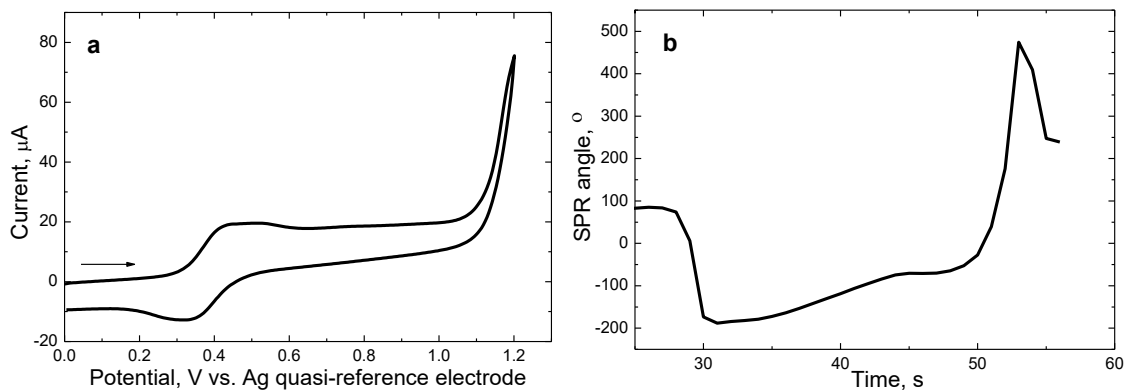
Figure 3.3-20. (a) The potentiodynamic curve and (b) the change in the SPR angle with time during electropolymerization leading to deposition of the (SYN-Fc)-(MIP-4) film on an SPR chip from the 100 μM SYN, 300 μM FM 3, 1 mM Fc, 1 mM sodium thiophen-2-ylmethanesulfonate, and 0.1 M (TBA)ClO$_4$ solution of toluene, 1-decyl-3-methylimidazolium *bis*(trifluoromethanesulfonyl)imide ionic liquid, and acetonitrile of the 1 : 2.5 : 6.5 (*v* : *v* : *v*) ratio on a 10-MHz Au-QCR.

Importantly, well-pronounced peaks of the ferrocene moiety were visible in cyclic voltammograms at the SPR chip coated with the (SYN-Fc)-(MIP-4') polymer (curve *1* in Figure 3.3-21a) together with an increase in the SPR angle due to ferrocene moiety electro-oxidation in each consecutive cycle (curve *1'* in Figure 3.3-21b). After each cycle, the SPR signal returned to its baseline level. The SPR peaks' heights ranged from 220 to 250 m°. Those signal changes may originate from MIP film swelling and shrinking, as well as the changes in its electric permittivity caused by both ferrocenium ions' formation and accompanying counter-ions ingress from the solution to the film and co-ions egress from the film to the solution. Afterward, the SYN sample was added to the solution, substantially decreasing the faradaic current (curve *2* in Figure 3.3-21a). The SPR peaks were still detectable; however, their heights decreased twice compared to those recorded without SYN (curve *2* in Figure 3.3-21b). The SPR results corresponded to those of PM experiments.

175
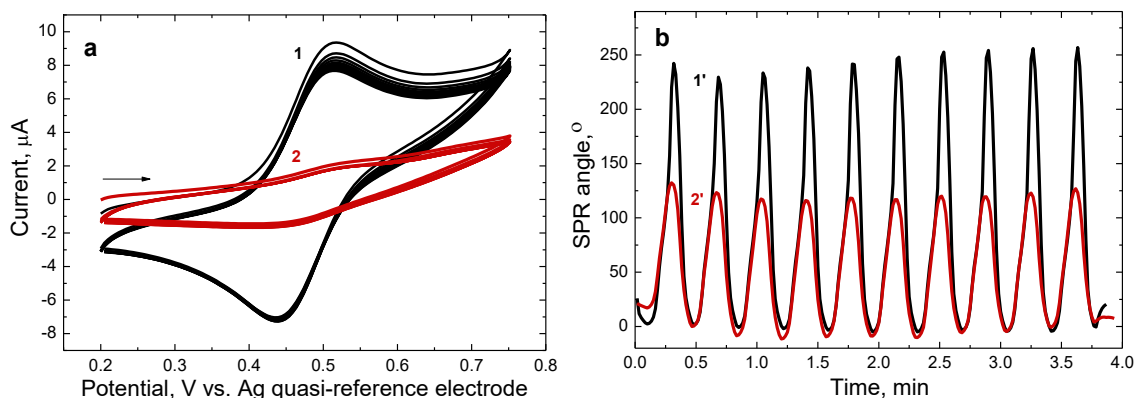
Figure 3.3-21. The simultaneously recorded (a) multi-cyclic CV curve and (b) SPR angle change with time at the Au-SPR chip coated with the (SYN template)-extracted (SYN-Fc)-(MIP-4) film in 0.1 M (TBA)ClO$_4$ in acetonitrile (curves *1* and *1'*) in the SYN-free solution and (curves *2* and *2'*) in 40 nM SYN.

Furthermore, CV curves were recorded at scan rates between 10 and 100 mV s^{-1} at the (SYN-Fc)-(MIP-4) film-coated electrode (Figure 3.3-22a) to reveal the dependence of ferrocene peak currents on the scan rate applied. The logarithms of the current of anodic and cathodic peaks linearly increased with the increase of the logarithm of the potential scan rate (Figure 3.3-22b).
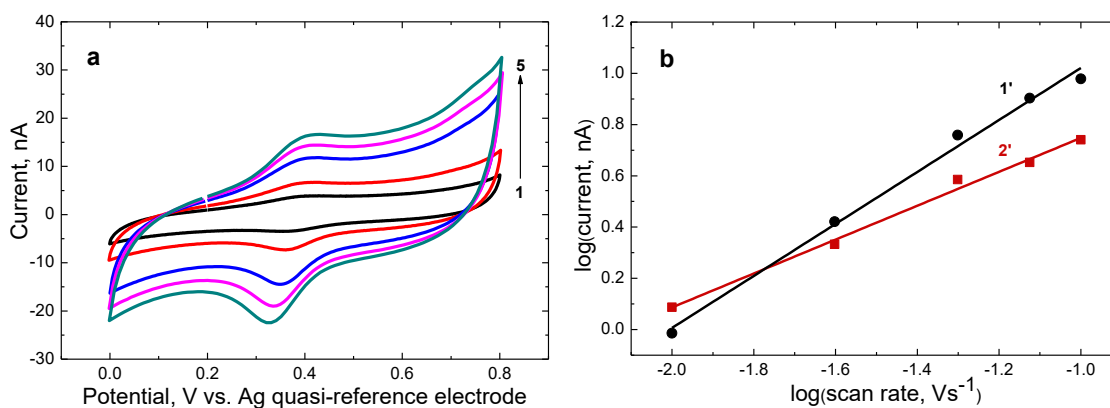
Figure 3.3-22. (a) Cyclic voltammograms for the 1-mm diameter Pt disk electrode coated with the template-extracted (SYN-Fc)-(MIP-4) film in 0.1 M (TBA)ClO$_4$ in acetonitrile at the potential scan rate of (curve *1*) 10, (curve *2*) 25, (curve *3*) 50, (curve *4*) 75, and (curve *5*) 100 mV s^{-1}. (b) The logarithm of the peak current dependence on the logarithm of the potential scan rate for the (curve *1'*) cathodic and (curve *2'*) anodic peak current.

If the slope of the relationship between the logarithm of the ferrocene anodic peak and the logarithm of the potential scan rate were 0.5, it would indicate that the rate of semi-infinite diffusion controlled the overall process rate.[413] However, if the calculated slope were 1.0, it would indicate that the finite diffusion rate governed the process rate.

176

The latter behavior is typical for (electrode surface)-confined redox species. In the studied system, the calibration curve constructed for the anodic process obeyed the linear regression equation of $\log[I_{pa}, nA] = 1.41\ (\pm0.04) + 0.66\ (\pm0.03) \log[v, V\ s^{-1}]$ with the correlation coefficient of $R^2 = 0.991$. In contrast, the calibration plot constructed for the cathodic process was described by the linear regression equation of $\log[I_{pc}, nA] = 2.04\ (\pm0.07) + 1.01\ (\pm0.05) \log[v, V\ s^{-1}]$ with the correlation coefficient of $R^2 = 0.991$. Both equations include I_{pa} and I_{pc} as the CV current of the anodic and cathodic peaks, respectively, and v, which stands for the potential scan rate.

The obtained CV-SPR results agree well with those of PM experiments. Namely, electro-oxidation of the ferrocene moiety led to the perchlorate ions ingress from the solution to the polymer film to compensate positive charge generated on the ferrocene moiety. However, the MIP film mass increase was too low to balance this effect. Hence, the cation was presumably simultaneously released from the MIP to the solution. Therefore, a mixed mechanism controlling the diffusion was most likely responsible for the resulting plot's slope of 0.66. However, finite diffusion during the ferrocene moiety electroreduction, manifested by the 1.01 slope of the constructed plot, indicated that perchlorate was mainly expelled from the (SYN-Fc)-(MIP-4) film during potential backward scanning.

3.3.6 Analytical performance of the self-reporting (SYN-Fc)-(MIP-4) film sensor in the *p*-synephrine determination

(SYN-Fc)-(MIP-4) film-coated electrodes were used for the DPV determination of SYN in 0.1 M (TBA)ClO$_4$ in acetonitrile. The recorded DPV peak decreased with the SYN analyte concentration increase (Figure 3.3-23a). The Langmuir-Freundlich isotherm was fitted to the chemosensor DPV vs. SYN concentration in the 2.0 to 75 nM range (Equation 3.3.1).

$$\Delta I = \Delta I_{max} \frac{K_S\, c_{SYN}^{n'}}{(1 + K_S\, c_{SYN}^{n'})} \qquad \text{(Equation 3.3.1)}$$

In this relationship, ΔI describes a relative change in the DPV peak $[\Delta I = (I_{DPV,0} - I_{DPV,s})/ I_{DPV,0}]$, ΔI_{max} is a maximal relative change in the DPV peak, K_S stands for the stability constant of the imprinted cavity complex with the SYN

molecule, whereas c_{SYN} and *n'* is the concentration of SYN and the homogeneity factor, respectively.

The Langmuir-Freundlich isotherms were applied to describe the dependence of (SYN-Fc)-(MIP-4) film chemosensor DPV peak on the concentration of interfering compounds and SYN analyte at the control Fc-(NIP-4) film-coated electrode (Figure 3.3-23b).
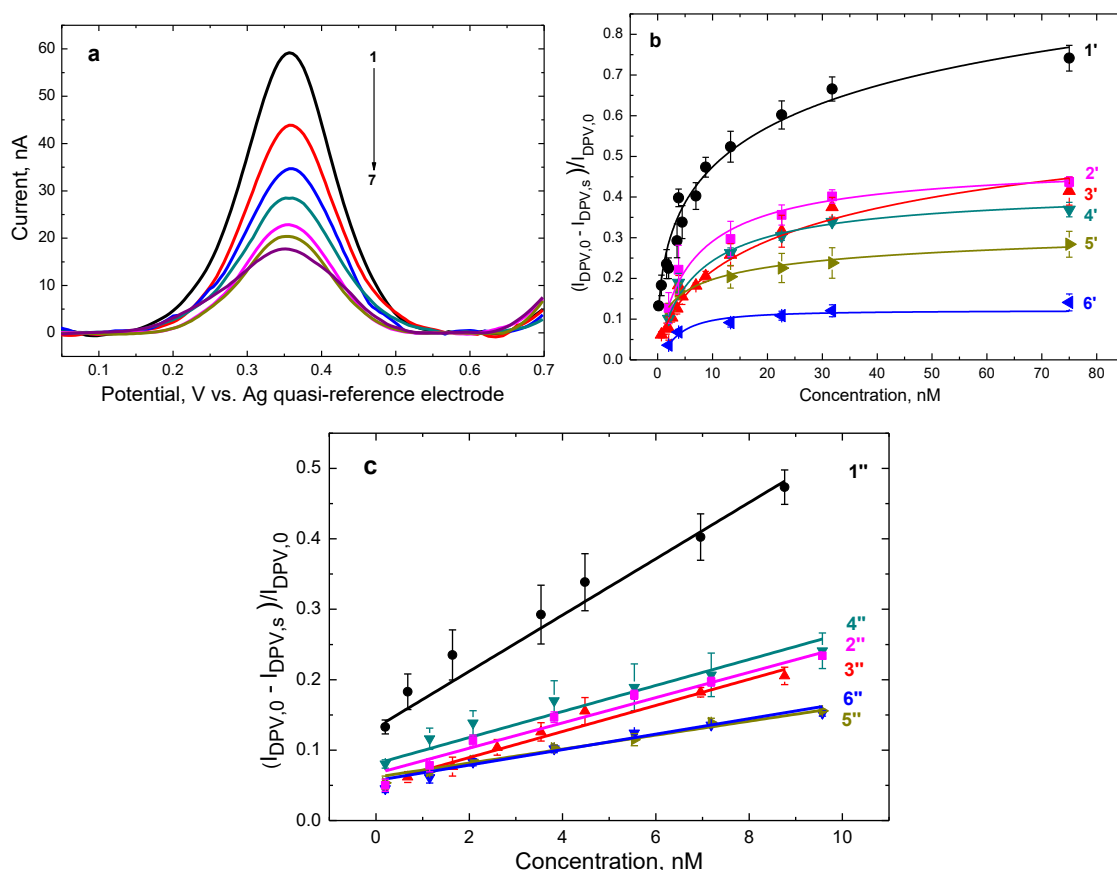
Figure 3.3-23. (a) DPV curves recorded at the 1-mm diameter Pt disk electrode coated with the (SYN-Fc)-(MIP-4) film in 0.1 M (TBA)ClO$_4$ in acetonitrile (curve *1*) after template extraction with 10 mM Et$_3$N in acetonitrile for 5 min, and then after subsequent SYN addition, resulting in its concentration of (curve *2*) 2.0, (curve *3*) 3.8, (curve *4*) 13.3, (curve *5*) 22.6, (curve *6*) 31.7, and (curve *7*) 75 nM. (b) Langmuir-Freundlich isotherm fitting and (c) calibration plots for (curves *1″* and *3″*) SYN analyte, (curve *2″*) penicillin G, (curve *4″*) glucose, (curve *5″*) tyramine, and (curve *6″*) urea at (curves *1″, 2″, 4″–6″*) the (SYN-Fc)-(MIP-4) film- and (curve *3″*) the Fc-(NIP-4) film-coated Pt disk electrode.

All isotherms' parameters determined for the SYN analyte and interferences are summarized in Table 3.3-11. The apparent *IF* calculated as the ratio of the slope of the calibration plot for SYN, constructed for the electrode coated with the MIP, and NIP films, was 1.9. The selectivity for tested interferences, namely, penicillin G, glucose,

tyramine, and urea, calculated as ratios of slopes of the calibration plot for the SYN analyte to that for a given interference at the (SYN-Fc)-(MIP-4) film-coated electrode, was 2.9, 3.3, 3.8, and 11.8, respectively.

Table 3.3-11. Parameters of Langmuir-Freundlich isotherms obtained from DPV measurements for the Pt disk electrodes coated with the (SYN-Fc)-(MIP-4) film.

Analyte/Interference	ΔI_{max}	K_S, nM^{-1}	n'
p-Synephrine	1.4 ± 0.5	0.02 ± 0.03	0.42 ± 0.06
Penicillin G	0.49 ± 0.03	0.15 ± 0.03	0.9 ± 0.2
Glucose	0.42 ± 0.05	0.14 ± 0.05	0.9 ± 0.2
Tyramine	0.4 ± 0.1	0.1 ± 0.2	0.5 ± 0.2
Urea	0.12 ± 0.01	0.27 ± 0.08	1.4 ± 0.4
p-Synephrine at the Fc-(NIP-4) film-coated electrode	0.8 ± 0.2	0.02 ± 0.02	0.63 ± 0.08

Since linear fitting allows for easy comparison of different calibration plots' parameters, linear fitting is more convenient than isotherm fitting. Hence, the SYN analyte and interferences were determined with DPV in the pseudo-linear part of the Langmuir-Freundlich isotherms, namely in a low concentration range of 0.2 to 8.8 nM (Figure 3.3-23c). The calibration plot for SYN obeyed the linear regression equation of $(I_{DPV,0} - I_{DPV,s})/ I_{DPV,0} = 0.130\ (\pm 008) + 4.0 \times 10^{-2}\ (\pm 0.2 \times 10^{-2})\ c_{SYN}$ [nM]. The correlation coefficient, R^2, was 0.982, and the LOD was 0.57 nM at the $S/N = 3$. The calculated apparent *IF* was 2.16. Moreover, the selectivity for glucose, penicillin G, urea, and tyramine was 2.16, 2.22, 3.34, and 4.06, respectively. These results correspond to those obtained from Langmuir-Freundlich isotherm fitting. Notably, the devised self-reporting chemosensor analytical parameters, namely, sensitivity and LOD, were superior to those determined for the SYN-MIP film chemosensor prepared without the immobilized redox probe (described in Section 3.2 above). The sensitivity of the chemosensor with the (SYN-Fc)-(MIP-4) film was 125 times higher, while selectivity and *IF* were slightly lower than those for the mentioned above SYN-MIP film chemosensor.

Additionally, semi-logarithmic calibration plots were constructed for SYN and interferences (Figure 3.3-24) to cover a broader concentration range. The linear

dynamic concentration range of 2.0 to 75 nM SYN was characterized by the equation of the semi-logarithmic calibration curve of $(I_{\text{DPV,0}} - I_{\text{DPV,s}})/I_{\text{DPV,0}} = 0.17 \ (\pm 3.23 \times 10^{-2}) + 0.32 \ (\pm 2.87 \times 10^{-2}) \log[c_{\text{SYN}}, \text{nM}]$. The correlation coefficient, R^2, was 0.968, and the LOD was 0.27 nM at $S/N = 3$. The calculated apparent IF was 1.48, while the selectivity for glucose, penicillin G, tyramine, and urea were 1.68, 1.7, 3.25, and 4.51, respectively.
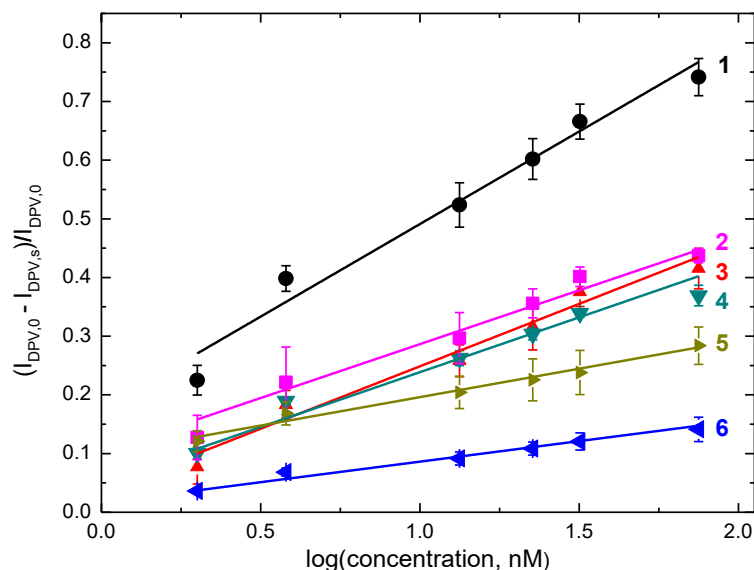
Figure 3.3-24. Calibration plots for (curves *1* and *2*) SYN, (curve *3*) penicillin G, (curve *4*) glucose, (curve *5*) tyramine, and (curve *6*) urea recorded at (curves *1, 3 - 6*) the (SYN-Fc)-(MIP-4) film- and (curve *2*) the Fc-(NIP-4) film-coated Pt disk electrode in 0.1 M (TBA)ClO$_4$ in acetonitrile.

Afterward, the stability of the (SYN-Fc)-(MIP-4) film-coated electrodes was studied (Figures 3.3-25a and 3.3-25b). For that, the chemosensor's response for 31.9 nM SYN in 0.1 M (TBA)ClO$_4$ in acetonitrile was monitored within 98 days. Nearly there were no changes in chemosensor signals for SYN within the first month (Figure 3.3-25a). Moreover, the relative difference in current recorded at the (SYN-Fc)-(MIP-4) film-coated electrode for 31.9 nM SYN after three months decreased merely to ~90% of that recorded on the first day (Figure 3.3-25b). Thus, after subsequent calibration, the chemosensor may still be used for SYN determination.
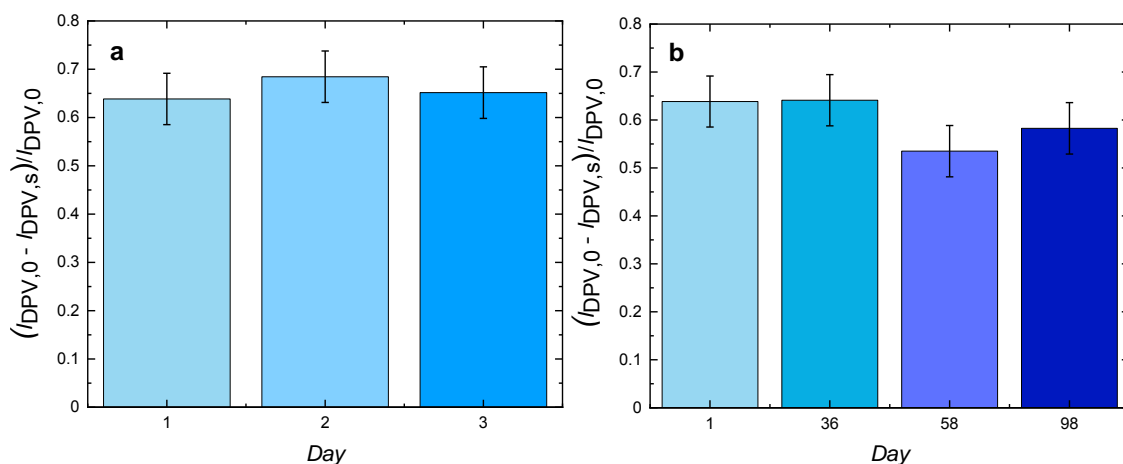
Figure 3.3-25. Histograms of the (SYN-Fc)-(MIP-4) film-coated Pt disk electrode DPV responses to 31.9 nM SYN in 0.1 M $(TBA)ClO_4$ in acetonitrile within (a) 3 days and (b) 98 days.

Furthermore, three electrodes, each coated with (SYN-Fc)-(MIP-4) film, prepared from three pre-polymerization complex solutions, were used to examine the reproducibility of the self-reporting chemosensor (Figure 3.3-26). No significant changes in the relative current difference were observed for the 4.48 nM SYN in 0.1 M $(TBA)ClO_4$ in acetonitrile. The standard deviation of the three DPV electrodes' responses to 4.48 nM SYN was 5.45%.
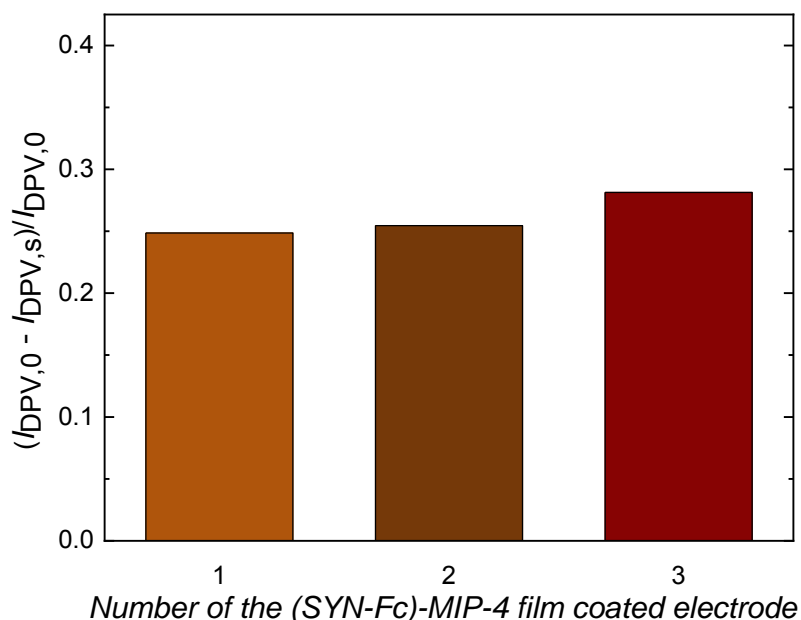
Figure 3.3-26. Histograms of DPV responses to 4.48 nM SYN of three different Pt disk electrodes, coated with the (SYN-Fc)-(MIP-4) films, in 0.1 M $(TBA)ClO_4$ in acetonitrile.

181

3.3.7 *p*-Synephrine DPV determining in real samples using self-reporting MIP chemosensor

Finally, SYN was determined in tablets of SYNEPHRINE EXTREME to check the applicability of the chemosensor featuring the (SYN-Fc)-(MIP-4) film in experiments involving real samples. The real sample preparation procedure was described in detail in Section 2.2.1.13 above. Afterward, electrochemical measurements were performed. A DPV curve was recorded at the (SYN-Fc)-(MIP-4) film-coated electrode in 0.1 M (TBA)ClO$_4$ in acetonitrile. Subsequently, the examined solution was spiked with real samples of the prepared stock solution of known SYN concentration to reach SYN concentration ranging from 0.66 to 10.12 nM. Then, DPV curves were recorded after each SYN sample injection. The results of real sample experiments are summarized in Table 3.3-12. The recovery, calculated by applying the linear calibration plot (curve *1″* in Figure 3.3-23c), was acceptable, signifying that the (SYN-Fc)-(MIP-4) film containing chemosensor is a promising tool for SYN determination in real samples.

Table 3.3-12. SYN determination in tablets of the SYNEPHRINE EXTREME dietary supplement.

Sample No.	Known SYN concentration, nM	Relative change of DPV peak current (±st.dev.)[a]	Determined concentration of SYN (±st.dev.), nM	Recovery (±st.dev.), %
1	0.66	0.16 ± 0.02	0.8 ± 0.4	102 ± 55
2	1.64	0.20 ± 0.02	1.8 ± 0.4	112 ± 25
3	3.54	0.26 ± 0.02	3.2 ± 0.5	90 ± 14
4	4.48	0.32 ± 0.02	4.6 ± 0.4	103 ± 9
5	6.96	0.386 ± 0.004	6.4 ± 0.1	91 ± 2
6	8.76	0.44 ± 0.02	7.7 ± 0.4	88 ± 5
7	10.12	0.49 ± 0.02	9.0 ± 0.5	89 ± 5

3.4 Electrochemical chemosensors with MIP NPs for selective determining of glyphosate

This section focuses on preparing and characterizing the (MIP NPs)-containing chemosensors selective for glyphosate (GLY).

3.4.1 Selecting the most appropriate monomers for glyphosate imprinting

Choosing appropriate functional and cross-linking monomers is crucial for GLY-MIP NPs preparation. Therefore, computational calculations were performed to select these monomers. Since methacrylate-based monomers are preferable for polymerization triggered by UV light, these monomers were chosen for nanoparticle synthesis. Sybyl calculations showed that the most promising Gibbs free energy changes due to GLY complexation are for EGMP, AAm, and ITA, namely, −77.0, −60.10, and −34.60 kJ mol^{-1}, respectively (Scheme 3.4-1). Thus, these functional monomers may form the most stable pre-polymerization complexes with the GLY template. Importantly, the solvation effects and interactions at pH = 7.45 were considered during calculations.
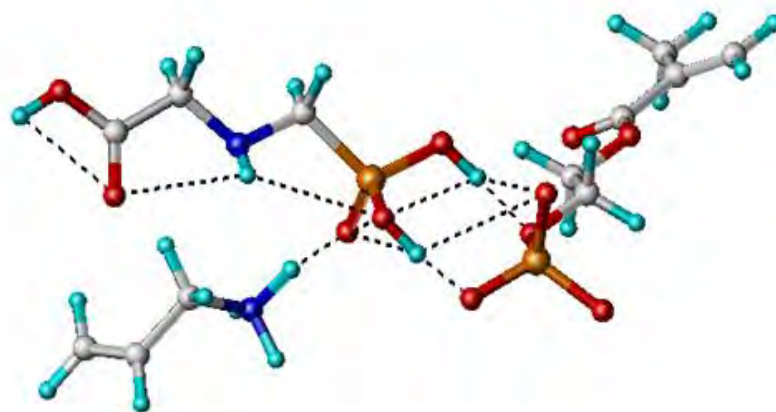
Scheme 3.4-1. The structure of the GLY complex with EGMP and AAm optimized by Sybyl calculations.

After the initial screening of suitable monomers, computational DFT modeling at the B3LYP/6-31G(d) level of complex formation was performed to investigate the interaction between the GLY molecule and functional monomers' molecules further. The highest negative gain of Gibbs free energy change was for seven functional

monomers. These monomers can form stable complexes with the GLY template. Therefore, they were chosen for GLY-MIP NPs synthesis (Schemes 3.4-2 to 3.4-7).

a ΔG = - 27.9 kJ/mol

b ΔG = - 5.6 kJ/mol

c ΔG = - 40.7 kJ/mol

d ΔG = - 38.4 kJ/mol

e ΔG = - 34.4 kJ/mol

f ΔG = - 12.2 kJ/mol

g ΔG = - 6.7 kJ/mol
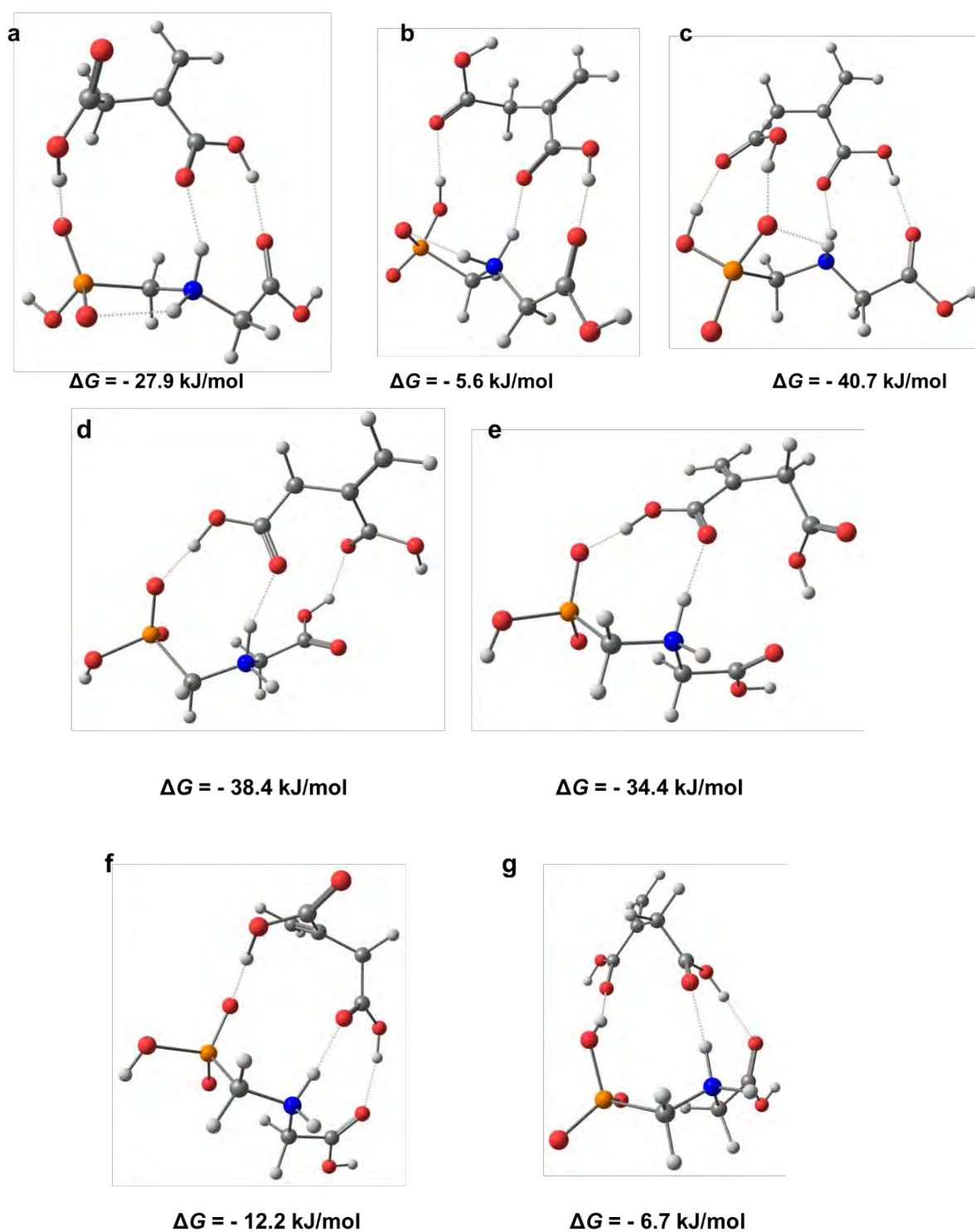
Scheme 3.4-2. The DFT-optimized structures of the complexes of GLY with ITA.

a   **b**   **c**

ΔG = - 2.6 kJ/mol ΔG = - 9.6 kJ/mol ΔG = - 14.3 kJ/mol
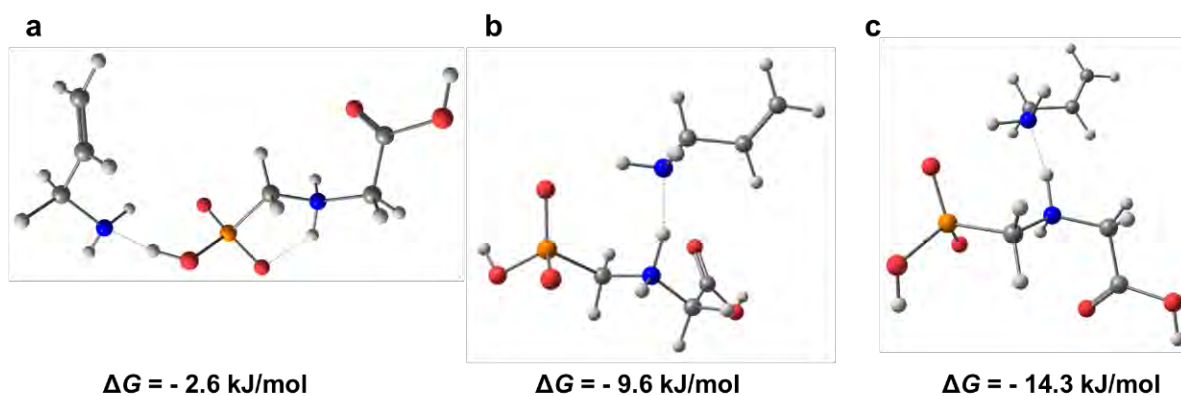
Scheme 3.4-3. The DFT-optimized structures of the complexes of GLY with AAm.

a   **b**

ΔG = - 40 kJ/mol ΔG = - 48.8 kJ/mol

c   **d**

ΔG = - 44.1 kJ/mol ΔG = - 39.5 kJ/mol
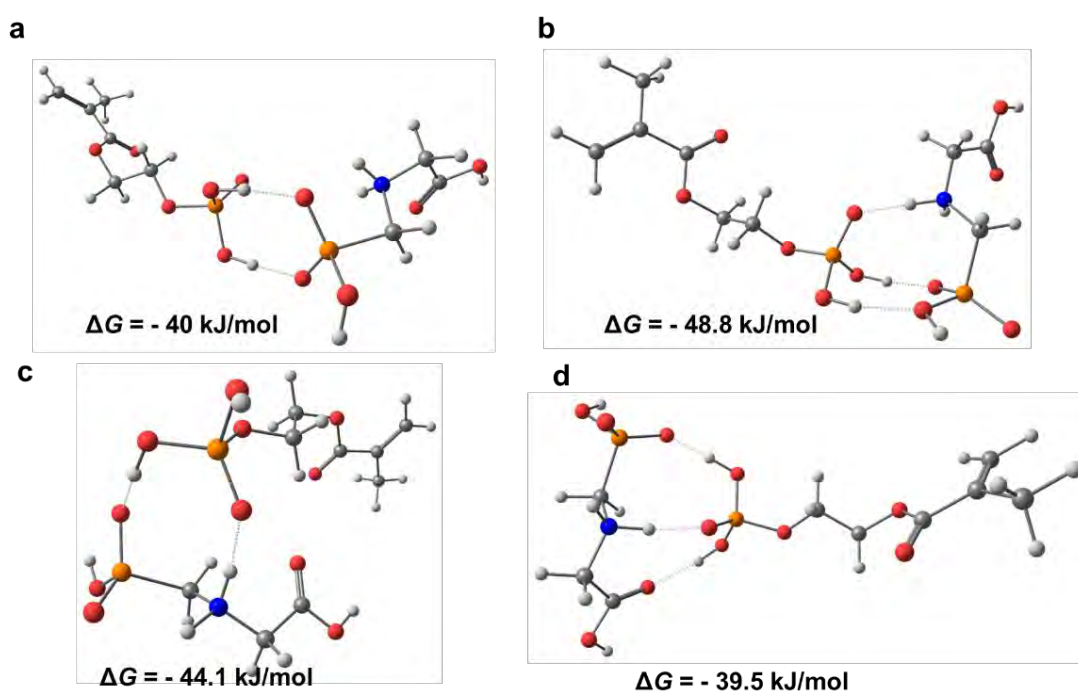
Scheme 3.4-4. The DFT-optimized structures of the complexes of GLY with EGMP.

ΔG = - 20.8 kJ/mol
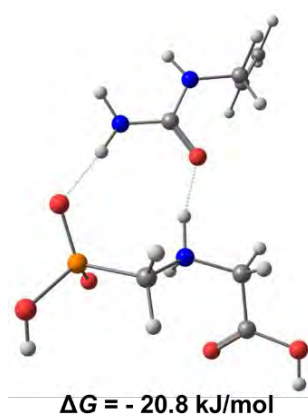
Scheme 3.4-5. The DFT-optimized structure of the complex of GLY with AU.

185

ΔG = - 25.6 kJ/mol   ΔG = - 27.4 kJ/mol   ΔG = - 30.9 kJ/mol
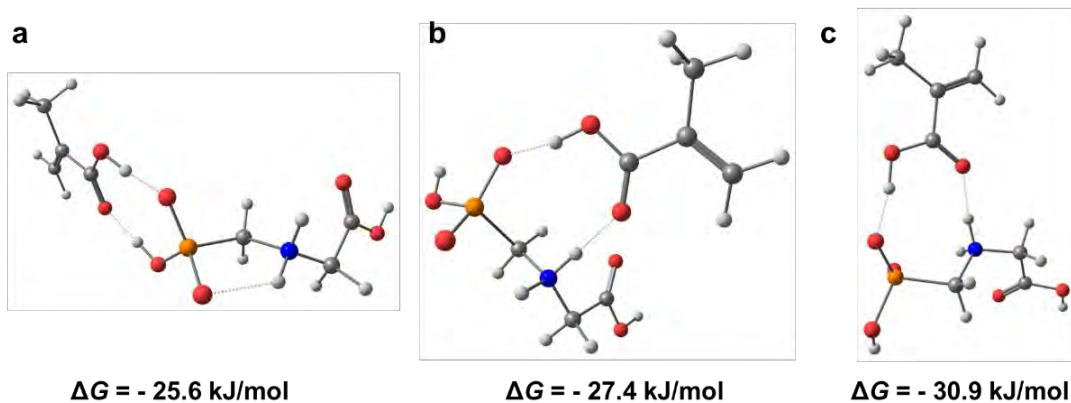
Scheme 3.4-6. The DFT-optimized structures of the complexes of GLY with MAA.

ΔG = - 16.9 kJ/mol
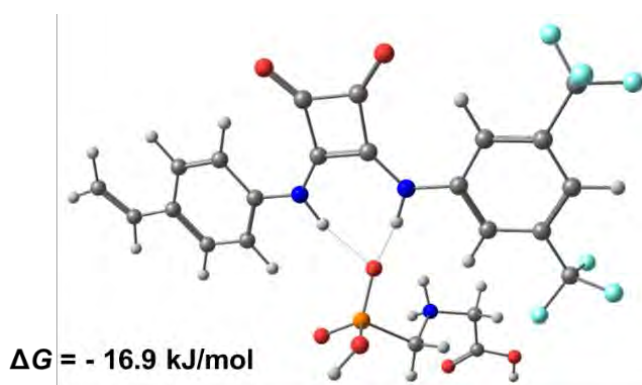
Scheme 3.4-7. The DFT-optimized structure of the complex of GLY with the SQ6 monomer.

On this ground, different monomers were chosen for testing in the subsequent laboratory experiments.

3.4.2   Preparing MIP NPs for chemosensor fabrication

Four formulations of MIP NPs were prepared, as described in Section 2.2.2.2 above.

UV-triggered polymerization in an organic solvent solution usually involves the application of MAA for MIP preparation. Therefore, prevailingly methacrylate-based monomers were used for the present MIP NPs synthesis. Moreover, these monomers mainly bear either carboxyl groups, as ITA and MAA, or amine groups, as AAm and AU, providing hydrogen bonds with GLY functional groups. Furthermore, in a polar aprotic solvent solution used for polymerization, deprotonated, negatively charged carboxyl groups and protonated, positively charged amine groups of chosen functional monomers might electrostatically interact with a protonated amine group, and a deprotonated phosphonic group of the GLY zwitterion. The selected squaramide-based

186

monomer provides superior hydrogen-bond donor ability and acidity.[352, 414-415] Finally, a ferrocene derivative was applied for polymerization, serving as the internal redox probe generating an electrochemical signal.

3.4.3 Characterizing the synthesized MIP NPs

The MIP NPs prepared were characterized by DLS, UV-vis spectroscopy, XPS, and SEM. Moreover, the MIP NPs-1 and MIP NPs-2 were imaged with TEM.

3.4.3.1 *DLS analysis of MIP NPs*

The size of MIP NPs was determined using DLS. The DLS measurements revealed an average particle size of MIP NPs-1, MIP NPs-2, MIP NPs-3, and MIP NPs-4, equal to 211 (±12), 413 (±28), 218 (±1), and 253 (±20) nm, respectively. The PdI values of MIP NPs-1, MIP NPs-3, and MIP NPs-4 were acceptably low, suggesting uniform distributions of prepared MIP NPs' hydrodynamic diameters, while PdI value above 0.4 for MIP NPs-2 might imply a broad size distribution of NPs synthesized.[416] Values obtained from the DLS analysis are summarized in Table 3.4-1.

Table 3.4-1. The size of synthesized MIP NPs after dialysis and their polydispersity index (PdI) determined by *Z*-average.

MIP NPs sample No.	MIP NPs size (±st.dev.), nm	Polydispersity index (PdI±st.dev.)
1	211 ± 12	0.31 ± 0.02
2	413 ± 28	0.49 ± 0.04
3	218 ± 1	0.29 ± 0.02
4	254 ± 20	0.34 ± 0.02

3.4.3.2 *SEM imaging of MIP NPs*

The size and morphology of all MIP NPs samples were determined by SEM imaging.

Samples' SEM images revealed quite regular, spherical MIP NPs drop-cast on the bare surface of the Au-glass slide electrodes (Figure 3.4-1). The nanoparticles' average size assessed by SEM for MIP NPs-1, MIP NPs-2, MIP NPs-3, and MIP NPs-4 was 139 (±4), 181 (± 7), 202 (±23), and 282 (±13) nm, respectively (Figures 3.4-2 to 3.4.5). MIP NPs sizes determined by DLS and assessed by SEM differ because the former

technique measures the hydrodynamic particle diameter. Hence, solvation effects will likely increase the particles' apparent size for the former.[417] Moreover, aggregates of particles might be formed in the solution.[418] Furthermore, polystyrene cuvettes used in DLS measurements might be slightly dissolved by ethanol resulting in Z-average sizes of nanoparticles bigger than those obtained from the SEM analysis.
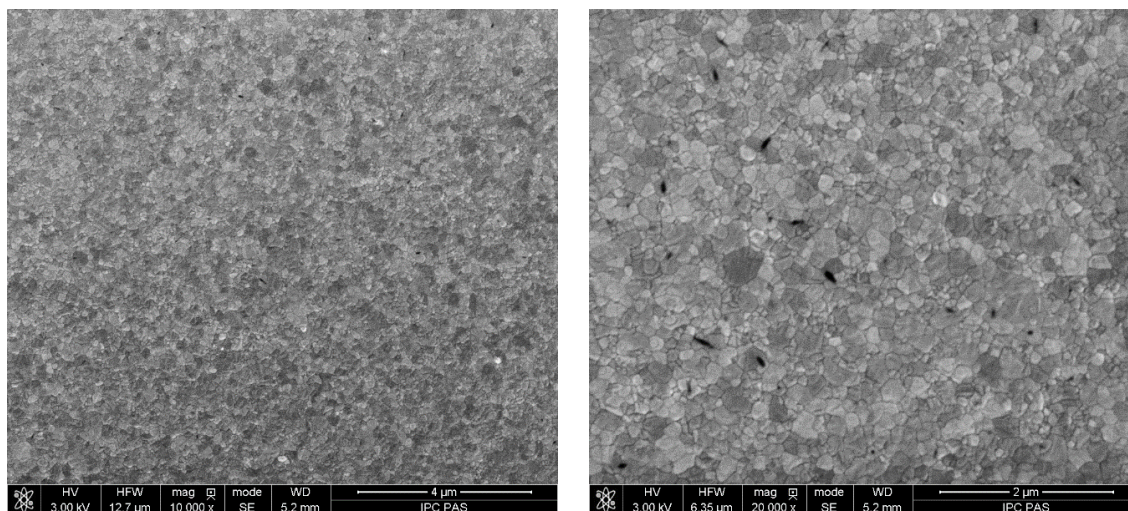
Figure 3.4-1. SEM images of the bare surface of the Au-layered glass slide electrode at different magnifications.
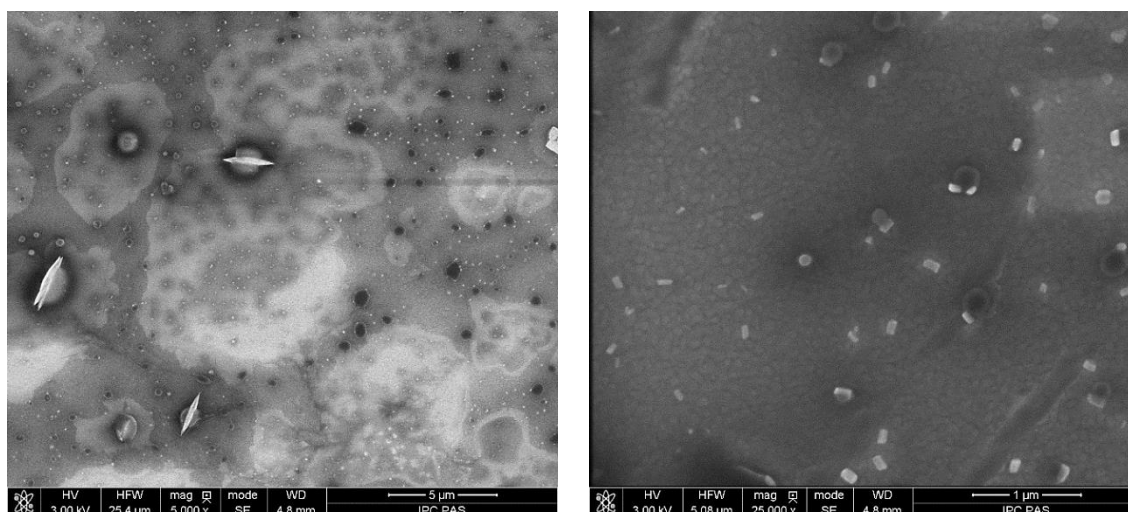
Figure 3.4-2. SEM images of MIP NPs-1, drop-cast on the Au-layered glass slide electrode, at different magnifications.
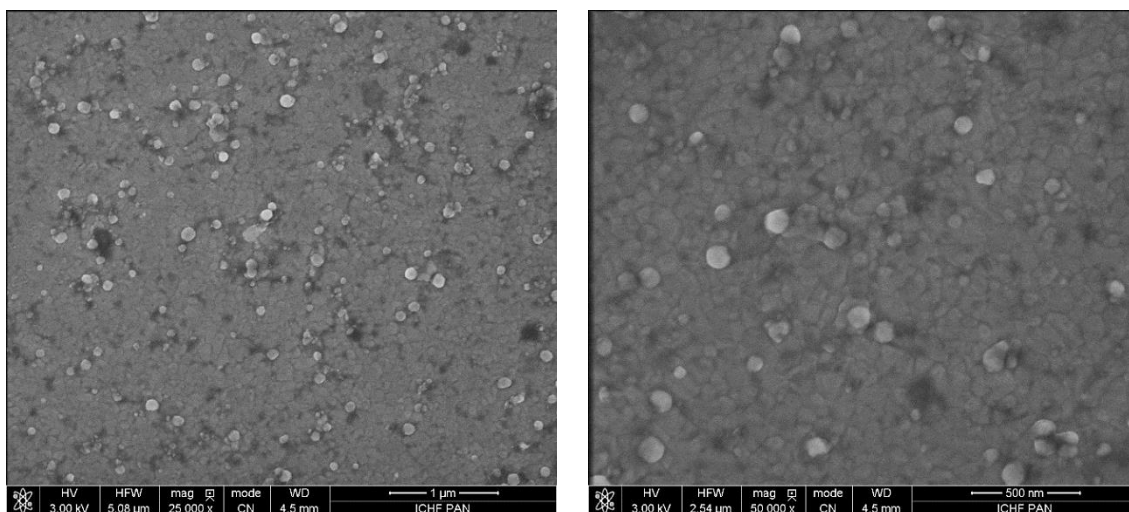
Figure 3.4-3. SEM images of MIP NPs-2, drop-cast on the Au-layered glass slide electrode, at different magnifications.
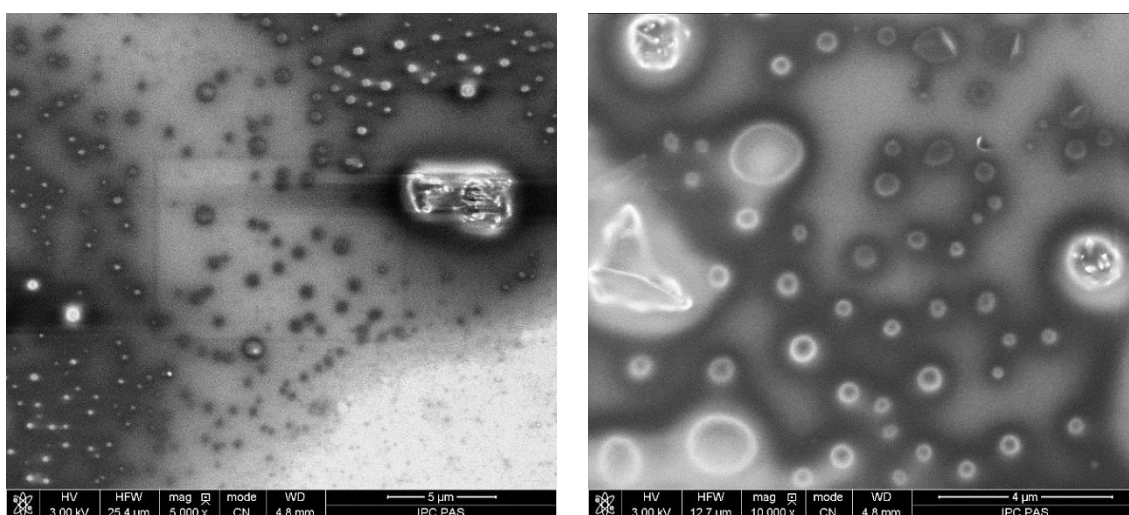
Figure 3.4-4. SEM images of MIP NPs-3, drop-cast on the Au-layered glass slide electrode, at different magnifications.
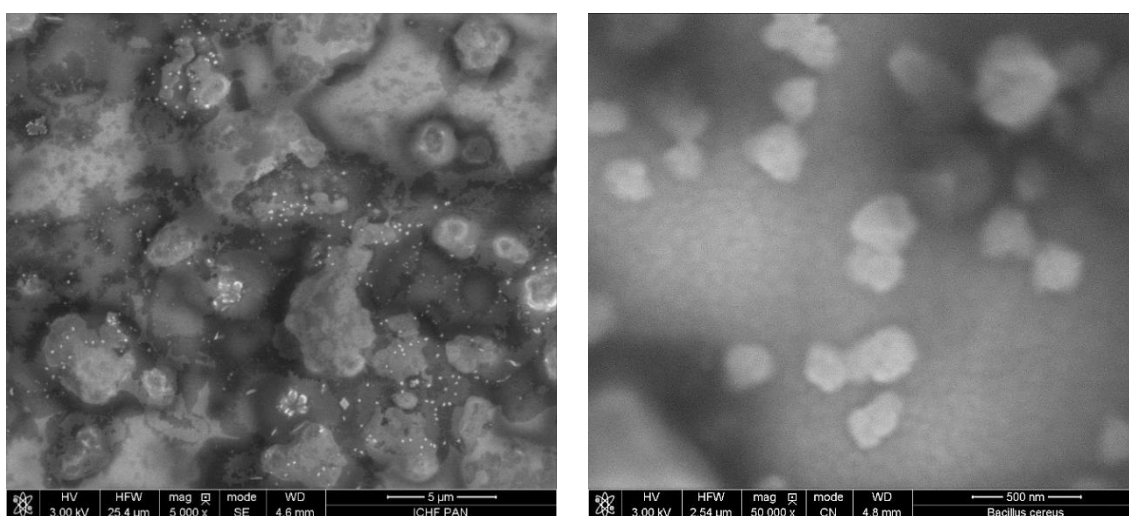
Figure 3.4-5. SEM images of MIP NPs-4, drop-cast on the Au-glass slide electrode, at different magnifications.
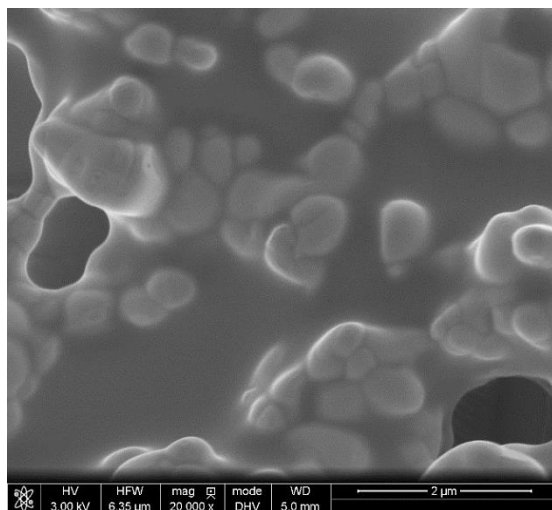
Figure 3.4-6. SEM image of the bare surface of the screen-printed Pt electrode (SPPtE).
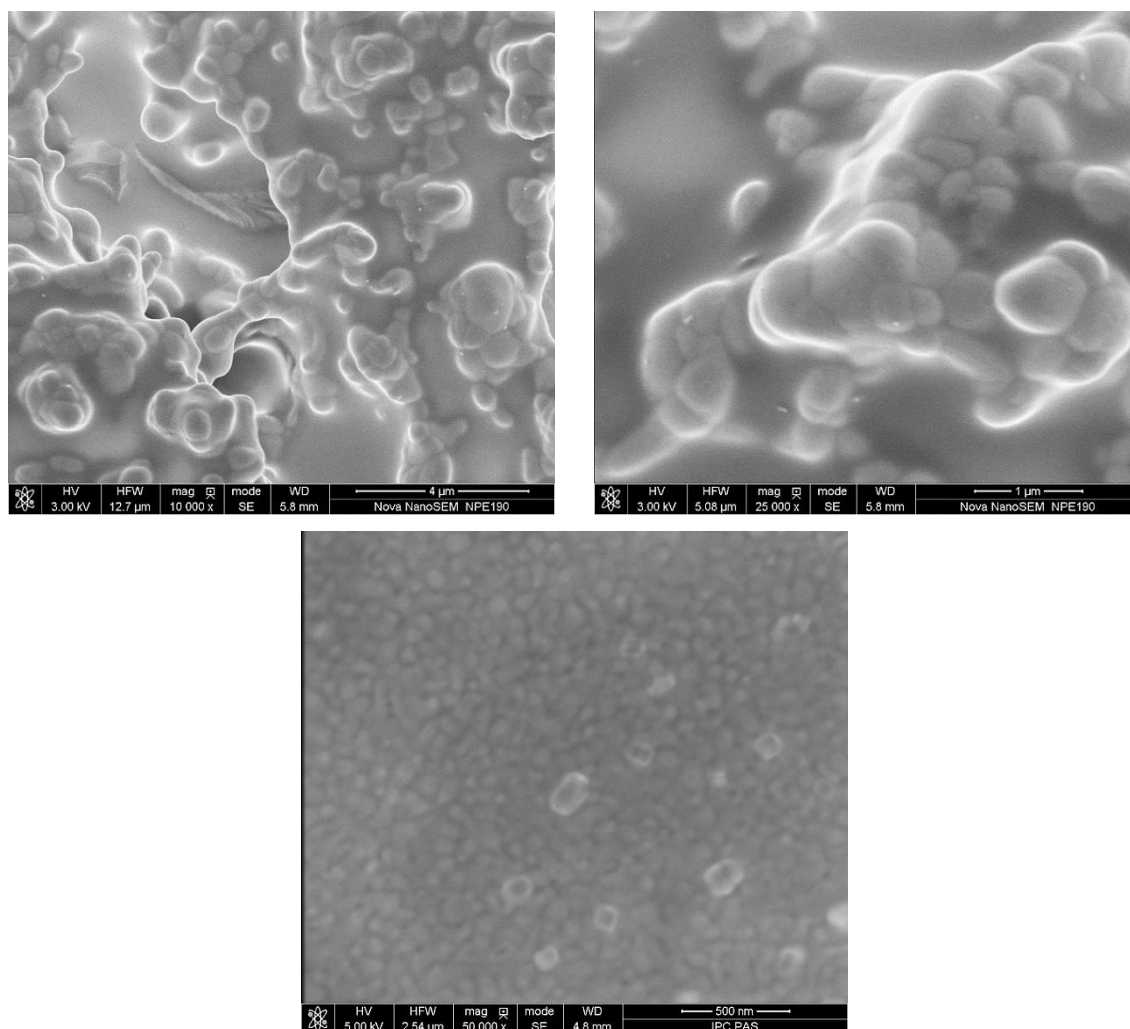
Figure 3.4-7. SEM images of MIP NPs-1, immobilized on the surface of the screen-printed Pt electrode (SPPtE), at different magnifications.
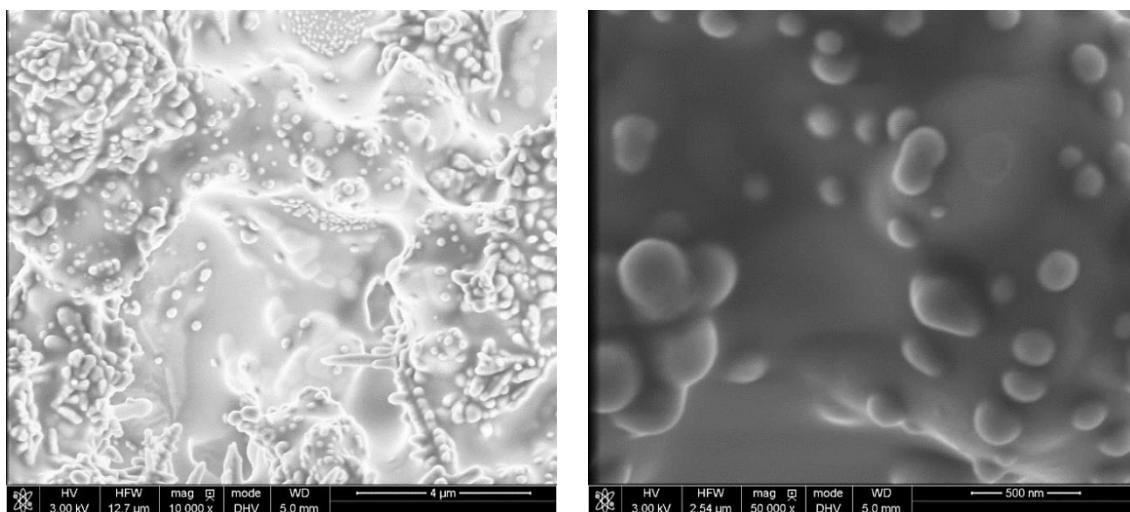
Figure 3.4-8. SEM images of MIP NPs-2, immobilized on the screen-printed Pt electrode (SPPtE), at different magnifications.
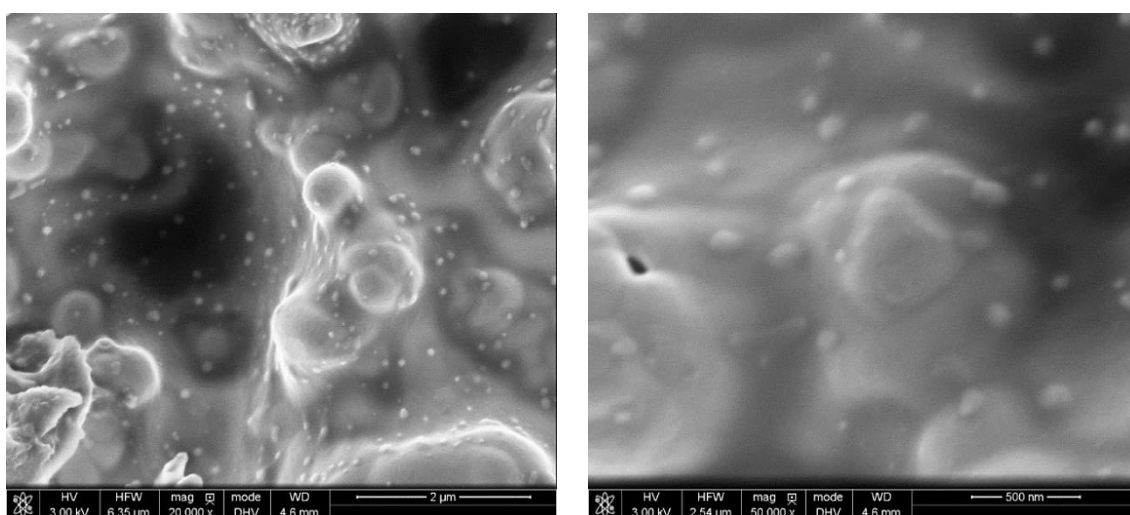
Figure 3.4-9. SEM images of MIP NPs-3, immobilized on the screen-printed platinum electrode (SPPtE), at different magnifications.
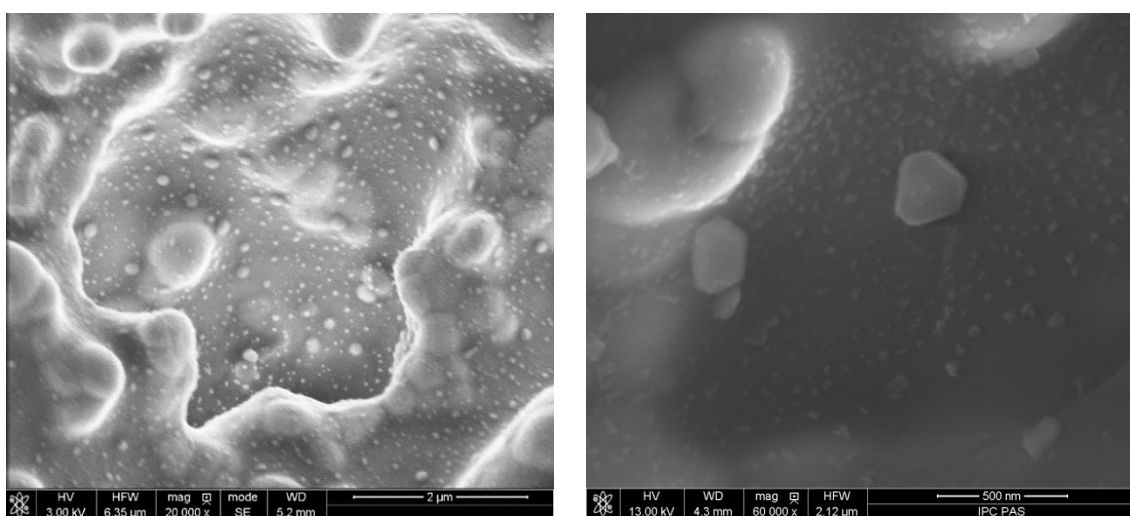
Figure 3.4-10. SEM images of MIP NPs-4, immobilized on the screen-printed platinum electrode (SPPtE), at different magnifications.

191

Moreover, SPPtEs modified with MIP NPs were SEM images to verify MIP NPs' immobilization on the electrode surface. SEM analysis revealed the presence of MIP NPs on the surface of electrodes (Figures 3.4-7 to 3.4-10), whereas these NPs were absent on the surface of the bare SPPtE (Figure 3.4-6). SEM images of SPPtE coated with MIP NPs-1 showed a disadvantageously low quantity of immobilized MIP (Figure 3.4-7). Nevertheless, the EDX spectroscopy analysis confirmed that the Fe atom presence originated from the component of the pre-polymerization complex mixtures, the ferrocene derivative, on the surface of SPPtEs (Tables 3.4-10 to 3.4.13).

3.4.3.3 *XPS and EDX spectroscopy analysis of MIP NPs*

XPS was used to determine the surface elemental composition of the synthesized MIP NPs. That way, the successful formation of MIP NPs was confirmed. The XPS determined iron atom surface concentrations of MIP NPs were negligibly low (Tables 3.4-2 to 3.4-5). Hence, the MIP NPs were also investigated with EDX spectroscopy (Tables 3.4-6 to 3.4-9). The EDX spectroscopy analysis showed that the Fe L line was more pronounced for MIP NPs-1, -2, and -4, and the calculated iron concentrations in MIP NPs were higher than in the case of XPS analysis. That is, they varied from 1.58 to 5.43 atomic %. Apparently, ferrocenium moieties were hidden inside MIP NPs, so their surface concentration might be lower than that in the MIP NPs bulk.

Table 3.4-2. The XPS-determined surface elemental composition of MIP NPs-1.

Element	Concentration, atomic %
Na	5.40
F	0.84
O	18.87
N	1.17
C	59.99
S	1.40
Au	12.32

192

Table 3.4-3. The XPS-determined surface elemental composition of MIP NPs-2.

Element	Concentration, atomic %
Na	7.93
O	25.06
N	0.85
C	57.26
S	1.42
P	0.47
Si	2.89
Au	4.12

Table 3.4-4. The XPS-determined surface elemental composition of MIP NPs-3.

Element	Concentration, atomic %
O	5.70
N	2.13
C	90.93
S	1.23

Table 3.4-5. The XPS-determined surface elemental composition of MIP NPs-4.

Element	Concentration, atomic %
Na	0.55
O	7.73
N	0.85
C	86.63
S	0.74
Si	3.24
Au	0.27

Table 3.4-6. The (EDX spectroscopy)-determined composition of MIP NPs-1 drop-cast on the Au substrate.

Element	Concentration, atomic %
Na	1.12
Fe	3.37
O	13.57
N	8.56
C	56.31
Au	17.07

Table 3.4-7. The (EDX spectroscopy)-determined composition of MIP NPs-2 drop-cast on the Au substrate.

Element	Concentration, atomic %
Na	2.89
Fe	3.19
O	20.99
N	7.32
C	47.12
Cl	0.64
S	2.06
Au	15.80

Table 3.4-8. The (EDX spectroscopy)-determined composition of MIP NPs-3 drop-cast on the Au substrate.

Element	Concentration, atomic %
Na	0.69
Fe	1.58
O	8.19
N	3.36
C	78.91
Au	5.73
S	1.54

Table 3.4-9. The (EDX spectroscopy)-determined composition of MIP NPs-4 drop-cast on the Au substrate.

Element	Concentration, atomic %
Na	0.30
Fe	5.43
O	8.99
N	9.29
C	52.16
S	2.92
Au	20.91

Moreover, the EDX spectroscopy analysis of electrodes functionalized with MIP NPs was performed to confirm the presence of the MIP NPs immobilized on the surface of SPPtEs (Tables 3.4-10 to 3.4-13). The Fe presence originates from the ferrocene derivative, ranging from 0.61 to 3.04 atomic %. Even though the iron concentration on the surface of SPPtEs modified with MIP NPs was lower than that of MIP NPs just drop-cast on the Au substrates, iron was detectable in all cases.

Table 3.4-10. The (EDX spectroscopy)-determined composition of MIP NPs-1 immobilized on the SPPtE surface.

Element	Concentration, atomic %
C	24.20
N	9.44
O	45.29
Fe	2.36
Al	4.13
Si	2.46
Pt	9.78
Pb	2.34

195

Table 3.4-11. The (EDX spectroscopy)-determined composition of MIP NPs-2 immobilized on the SPPtE surface.

Element	Concentration, atomic %
C	39.65
N	3.18
O	31.54
Fe	0.61
Na	18.10
Al	1.13
Si	1.16
Pt	3.96
Pb	0.67

Table 3.4-12. The (EDX spectroscopy)-determined composition of MIP NPs-3 immobilized on the SPPtE surface.

Element	Concentration, atomic %
C	47.23
N	8.00
O	28.73
Fe	1.40
Na	3.91
Al	1.51
Si	1.70
Pt	6.74
Pb	0.79

Table 3.4-13. The (EDX spectroscopy)-determined composition of MIP NPs-4 immobilized on the SPPtE surface.

Element	Concentration, atomic %
C	24.84
N	6.70
O	43.25
Fe	3.04
Na	0.29
Al	6.28
Si	0.97
Pt	12.53
Pb	2.09

3.4.3.4   IR spectroscopy analysis of MIP NPs

Successful preparation of GLY-MIP NPs was also confirmed by PM-IRRAS measurements (Figure 3.4-11). Notably, three well-pronounced partially overlapped bands at 2956, 2927, and 2854 cm^{-1} originating from alkanes' C–H bond stretching were present in the spectra. Moreover, bands at 1727 cm^{-1} and those broad between 1200 and 1000 cm^{-1} may represent stretching vibrations of ester –C=O and –C–O– groups in all four types of MIP NPs synthesized. Furthermore, the broadening of the second band can be assigned to the –C–N– bond, whose vibrations are manifested with bands at similar wavenumbers. Likewise, bands at 1465 and 1457 cm^{-1} may be attributed to the bending vibrations of the –CH$_2$– group.
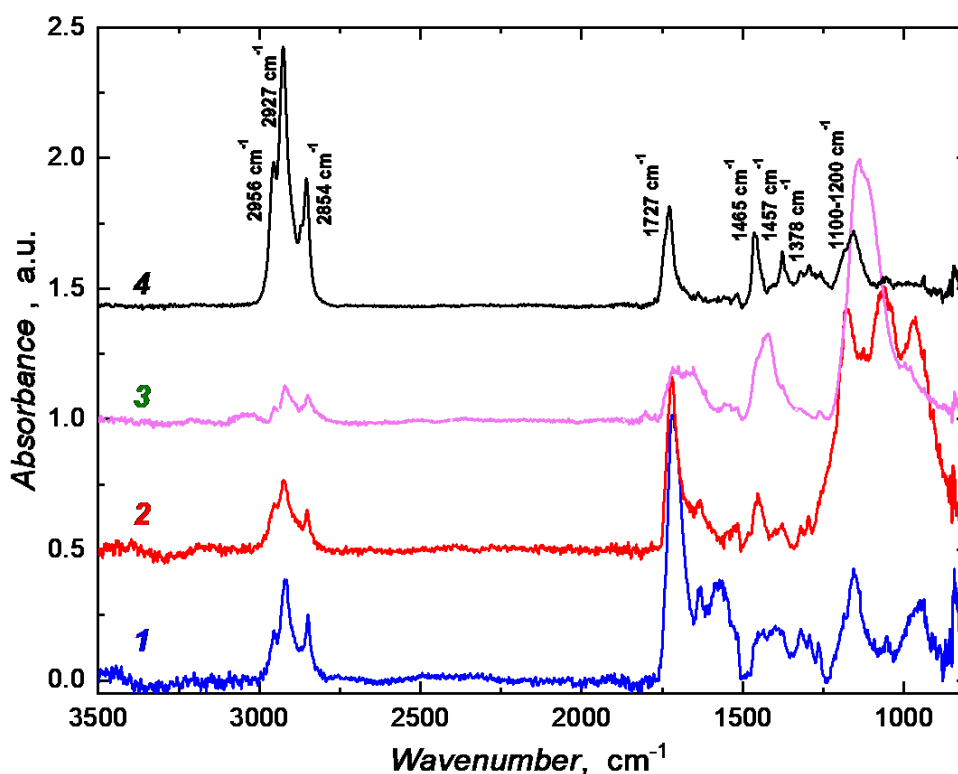
Figure 3.4-11. The PM-IRRAS spectra of (spectrum *1*) MIP NPs-1, (spectrum *2*) MIP NPs-2, (spectrum *3*) MIP NPs-3, and (spectrum *4*) MIP NPs-4.

3.4.4   Electrochemical characterizing of MIP NPs chemosensors

DPV and EIS measurements were performed to characterize the MIP NPs-based chemosensors electrochemically. The EIS results comply with the DPV results. First, measurements were carried out at bare SPPtEs in blank 10 mM PBS (pH = 7.4). In this case, there was no DPV peak (curve *1* in Figure 3.4-12a), and the Nyquist plot showed

an almost straight line, typical for a diffusion-limited process (curve *1* in Figure 3.4-12b). No significant changes in the DPV voltammogram and the EIS Nyquist plot were observed after silanization of the SPPtE as no redox process occurred at the electrode (curves *2* in Figures 3.4-12a and 3.4-12b). These results may suggest that the SPPtE was coated with silane. Electrode surface modification with MIP NPs-1 resulted in the appearance of the ferrocene DPV peak at ~0.20 V vs. Ag quasi-reference electrode (curves *3* in Figure 3.4-12a). Simultaneously, the semi-circle diameter in the respective Nyquist plot decreased (curves *3* in Figure 3.4-12b). Immobilizing electroactive MIP NPs bearing ferrocene moieties on the electrode surface led to occurring DPV currents and decreasing the R_{ct} at the SPPtE recorded in the (redox probe)-free PBS solution. After immersing the modified SPPtE in 10 nM GLY in PBS (pH = 7.4), the DPV peak increased, whereas the R_{ct} of the MIP NPs chemosensor decreased (curves *4* in Figures 3.4-14a and 3.4-14b).
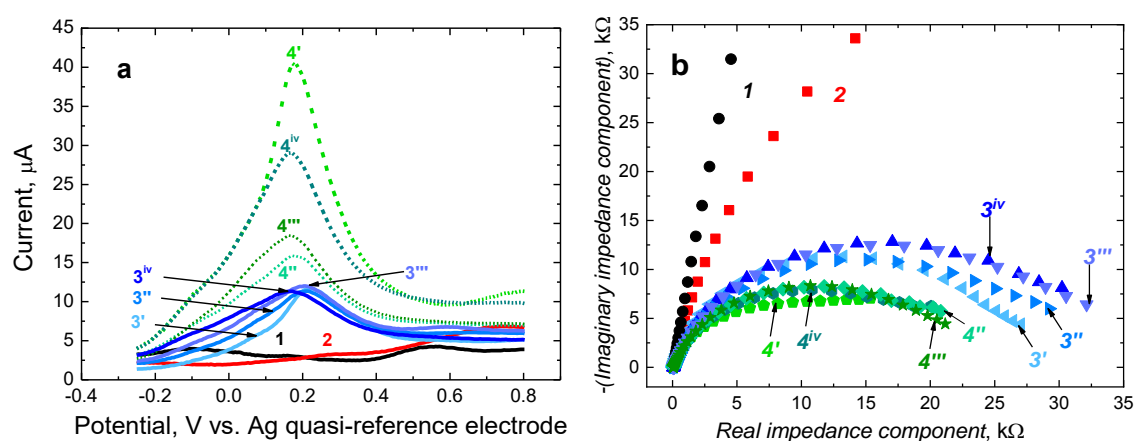
Figure 3.4-12. (a) The DPV and (b) EIS Nyquist curves for SPPtEs in blank PBS (pH = 7.4) for the (curve *1*) bare, (curve *2*) silanized, then modified with (curve *3'*) MIP NPs-1, (curve *3''*) MIP NPs-2, (curve *3'''*) MIP NPs-3, (curve *3^{iv}*) MIP NPs-4 coated electrodes in blank PBS (pH = 7.4), and then for the electrodes coated with (curve *4'*) MIP NPs-1, (curve *4''*) MIP NPs-2, (curve *4'''*) MIP NPs-3, (curve *4^{iv}*) MIP NPs-4 immersed in 10 nM glyphosate in PBS (pH = 7.4).

Presumably, GLY binding sites interaction with recognizing sites of MIP NPs causes conformational changes in the polymer structure,[419] thus influencing the density of ferrocene moieties present in MIP NPs. Therefore, GLY binding to MIP NPs causes DPV and EIS signal changes, confirming the MIP NPs' chemosensor applicability for GLY sensing.

198

3.4.5 Optimizing electrode modification conditions

Two chemosensors based on MIP NPs-1 prepared using either APTES or AAPS were analyzed by comparing their DPV peaks for GLY of different concentrations in 10 mM PBS, pH = 7.4 (Figure 3.4-13).
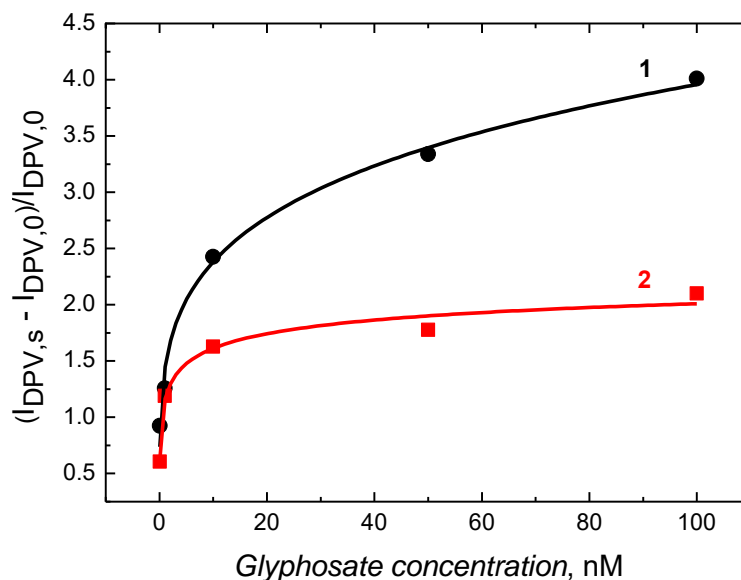
Figure 3.4-13. Normalized DPV peak currents vs. glyphosate concentration in 10 mM PBS (pH = 7.4) for the (MIP NPs-1)-containing chemosensor prepared using either (curve *1*) AAPS or (curve *2*) APTES for SPPtE modification.

Applying AAPS for electrode modification led to a superior chemosensor response to GLY. Therefore, this silane was selected for subsequent electrode silanizations.

3.4.6 Analytical performance of MIP NPs chemosensors

The analytical performance of the (MIP NPs)-containing chemosensors for GLY determination was examined with DPV. For all chemosensors, the DPV peaks, present at ~0.20 V vs. Ag quasi-reference electrode in blank 10 mM PBS (pH = 7.4), originated from the electro-oxidation of the internal redox probe. After GLY addition to the test solution, the peak increased (Panels a in Figures 3.4-14 to 3.4-18). The Langmuir-Freundlich isotherm well described the DPV peak dependence on the GLY concentration for electrodes functionalized with MIP NPs for GLY in the concentration range of 0.05 to 100 nM (Panels b in Figures 3.4-14 to 3.4-17). The DPV-determined isotherm parameters for all four chemosensors are summarized in Tables 3.4.14 to 3.4.17. Moreover, semi-logarithmic calibration curves were constructed

(Figures c 3.4-14 to 3.4-17). Furthermore, a linear calibration plot was built in a low concentration range of 25 to 500 pM for the chemosensor with MIP NPs-4 (Figure 3.4-18b). The chemosensors' selectivity was determined by analyzing their responses to compounds bearing the same functional groups as GLY, i.e., adenosine triphosphate (ATP), L-leucine, and clopyralid, which is also an herbicide like a GLY. Thus, the selectivity was calculated by dividing the slope of the calibration plot for the (MIP NPs)-coated electrode for GLY by the slopes of the calibration plots, independently, for each above interference.

The MIP NPs-1 chemosensor selectivity to ATP and L-leucine was high. However, it was lower to clopyralid, a compound with the –COOH group like GLY (Figure 3.4-14b). The response of the electrode modified with MIP NPs-1 obeyed the semi-logarithmic calibration equation of $(I_{\mathrm{DPV,0}} - I_{\mathrm{DPV,s}})/I_{\mathrm{DPV,0}} = 1.3\,(\pm 0.1) +$ $1.19\,(\pm 0.07 \times 10^{-2})\log[c_{\mathrm{GLY}}, \mathrm{nM}]$ with the correlation coefficient, $R^2 = 0.985$ and LOD $= 5.0$ pM at $S/N = 3$. The selectivity to ATP, L-leucine, and clopyralid was 2.69, 3.50, and 2.02, respectively (Figure 3.4-14c). Unfortunately, the (MIP NPs-2)- and (MIP NPs-3)-containing chemosensors were not selective to the above interferences in DPV determinations (Figures 3.4-15b and 3.4-16b). The response of the electrode functionalized with MIP NPs-2 obeyed the semi-logarithmic calibration equation of $(I_{\mathrm{DPV,0}} - I_{\mathrm{DPV,s}})/I_{\mathrm{DPV,0}} = 0.47\,(\pm 0.04) + 0.14\,(\pm 0.02)\log[c_{\mathrm{GLY}}, \mathrm{nM}]$ with the correlation coefficient $R^2 = 0.8979$. For GLY, LOD was 37 pM at $S/N = 3$. The selectivity to ATP, L-leucine, and clopyralid was 0.79, 0.80, and -2.65, respectively (Figure 3.4-15c). The response of the electrode modified with MIP NPs-3 conformed to the semi-logarithmic calibration equation of $(I_{\mathrm{DPV,0}} - I_{\mathrm{DPV,s}})/I_{\mathrm{DPV,0}} =$ $0.65\,(\pm 0.02) + 0.21\,(\pm 0.01)\log[c_{\mathrm{GLY}}, \mathrm{nM}]$ with the correlation coefficient $R^2 = 0.989$ and LOD $= 22$ pM at $S/N = 3$. The selectivity to ATP, L-leucine, and clopyralid was 1.11, 0.78, and 0.96, respectively (Figure 3.4-16c). Furthermore, the (MIP NPs-4)-based chemosensor was selective to GLY and discriminative to clopyralid, ATP, and L-leucine interferences (Figure 3.4-17b). The DPV response of the electrode modified with MIP NPs-4 followed the semi-logarithmic calibration equation of $(I_{\mathrm{DPV,0}} - I_{\mathrm{DPV,s}})/I_{\mathrm{DPV,0}} = 0.95\,(\pm 0.02) + 0.53\,(\pm 0.02)\log[c_{\mathrm{GLY}}, \mathrm{nM}]$ with the correlation coefficient, $R^2 = 0.996$. For GLY, the LOD was 13 pM at $S/N = 3$. The selectivity to ATP, L-leucine, and clopyralid was 2.93, 3.67, and 2.23, respectively (Figure 3.4-17c). DPV measurements demonstrated that the (MIP NPs-1)- and (MIP

NPs-4)-containing chemosensors responded to the GLY analyte selectively. Presumably, interactions with GLY of functional monomers chosen for constructing these chemosensors were the strongest, thus forming molecular cavities of high affinity to GLY molecules. For instance, ITA proposed as the functional monomer for the MIP NPs-1 containing chemosensor bears two carboxyl groups, which might interact through hydrogen bonds[420] with the amine group of GLY. Furthermore, negatively charged ITA carboxyl groups could electrostatically interact with the positively charged amino group of the GLY zwitterion in an aprotic polar solvent, DMF, used for polymerization. The SQ6 monomer applied as the functional monomer for the MIP NPs-4 containing chemosensor belongs to the squaramide class of compounds, being four-membered ring systems derived from squaric acid.[415] They consist of a conformationally rigid cyclobutene ring with two carbonyl hydrogen-bond acceptors and two N-H hydrogen-bond donors.[421] Therefore, substrates bearing squaramide moiety interact via strong hydrogen bonds with compounds bearing different functional groups, including carbonyl, nitro, and imino functionalities.[422] Then, the SQ6 squaramide-based vinyl monomer might serve as a functional building block in co-polymerizations with many co-monomers and cross-linking monomers,[352] and as a strong Brønsted acid capable of forming hydrogen bonds with either the carboxyl, amine, or phosphonic group of GLY. Moreover, AAm and 2-hydroxyethyl methacrylate, along with the squaramide-based monomer for (MIP NPs-4)-containing chemosensor preparation, can strongly associate with GLY through hydrogen bonding.[423-424] Hydrogen bonds can be formed between the amine group of AAm or hydroxyl group of 2-hydroxyethyl methacrylate and the carboxyl or phosphonic group of GLY. Furthermore, in a polar aprotic solvent, positively charged AAm may electrostatically interact with the GLY zwitterion's negatively charged phosphonic group.[424] Additionally, the SQ6 monomer can strongly interact via its squaramide center with the phosphate moiety of GLY.

The (MIP NPs-1)- and (MIP NPs-4)-containing chemosensors were chosen for further investigations because their DPV responses to the GLY analyte were the highest. The repeatability of the chemosensors was examined by measuring six times the ferrocene moiety DPV peaks for 50 nM GLY at a single SPPtE under the same conditions, resulting in the relative standard deviation (RSD) of 2.5% and 4.1% for the (MIP NPs-1)- and (MIP NPs-4)-containing chemosensor, respectively. Furthermore, the reproducibility was examined by comparing the DPV responses of six chemosensors

to 50 nM GLY under identical conditions. For the (MIP NPs-1)- and (MIP NPs-4)-containing chemosensors, the RSD was 8.1% and 4.9%, respectively.

Moreover, since (MIP NPs-4)-containing chemosensor selectivity was higher than that containing MIP NPs-1, the former was selected to prepare the calibration plot in the pseudo-linear initial part of the Langmuir-Freundlich isotherm. The DPV peak recorded at the SPPtE coated with MIP NPs-4 linearly increased with the increase of the GLY analyte concentration in the range of 25 pM to 500 pM (Figure 3.4.18a), obeying the semi-logarithmic regression equation of $(I_{DPV,0} - I_{DPV,s})/I_{DPV,0} = 0.95\,(\pm 0.02) + 0.53\,(\pm 0.02)\,\log[c_{GLY}, nM]$ with the correlation coefficient, $R^2 = 0.981$ (Figure 3.4.18b). The LOD was 18.2 pM at $S/N = 3$. The selectivity coefficients for ATP, L-leucine, and clopyralid were 2.31, 4.54, and 2.72, respectively.
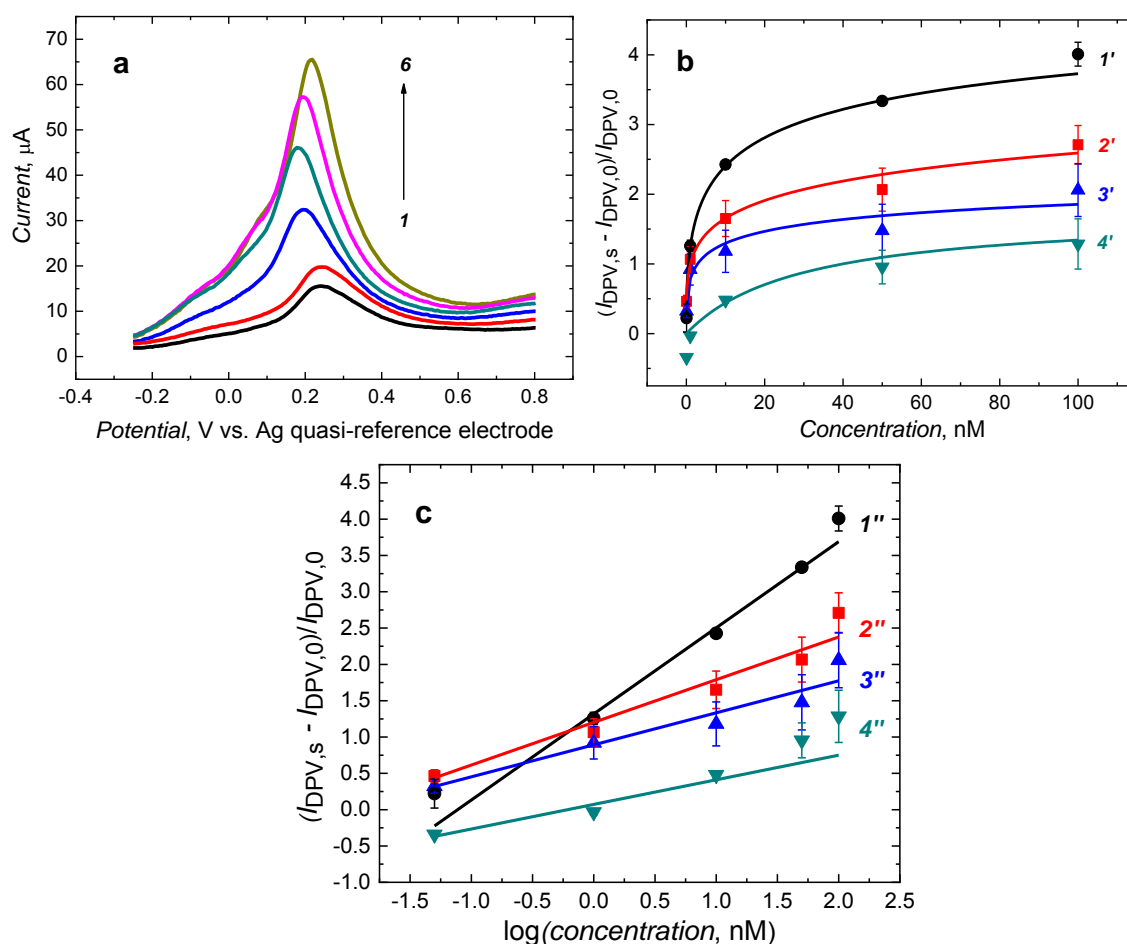
Figure 3.4-14. (a) The DPV curves for the screen-printed platinum electrode (SPPtE) coated with MIP NPs-1 in (curve *1*) 10 mM PBS (pH = 7.4), and the glyphosate (GLY) presence at the concentration of (curve *2*) 0.05, (curve *3*) 1 (curve *4*) 10, (curve *5*) 50, and (curve *6*) 100 nM. (b) The DPV peak dependence on concentration for (curve *1′*) GLY, (curve *2′*) clopyralid, (curve *3′*) ATP, and (curve *4′*) L-leucine. (c) Calibration plots for the (MIP NPs-1)-containing DPV chemosensor for (curve *1′*) GLY, (curve *2″*) clopyralid, (curve *3″*) ATP, and (curve *4″*) L-leucine.

202

Table 3.4-14. The DPV determined parameters of Langmuir-Freundlich isotherms for the (MIP NPs-1)-containing chemosensor.

Compound	ΔI_{max}	K_S, nM^{-1}	n'
Glyphosate	6 ± 2	0.28 ± 0.09	0.4 ± 0.1
ATP	3 ± 2	0.4 ± 0.5	0.3 ± 0.2
L-Leucine	2 ± 4	0.03 ± 0.1	-
Clopyralid	8 ± 10	0.2 ± 0.2	0.27 ± 0.08

ΔI_{max} – maximal relative change in the DPV peak current.
K_S – the concentration of the compound at equilibrium/equilibrium constant for heterogeneous solid.
n' – the homogeneity factor.
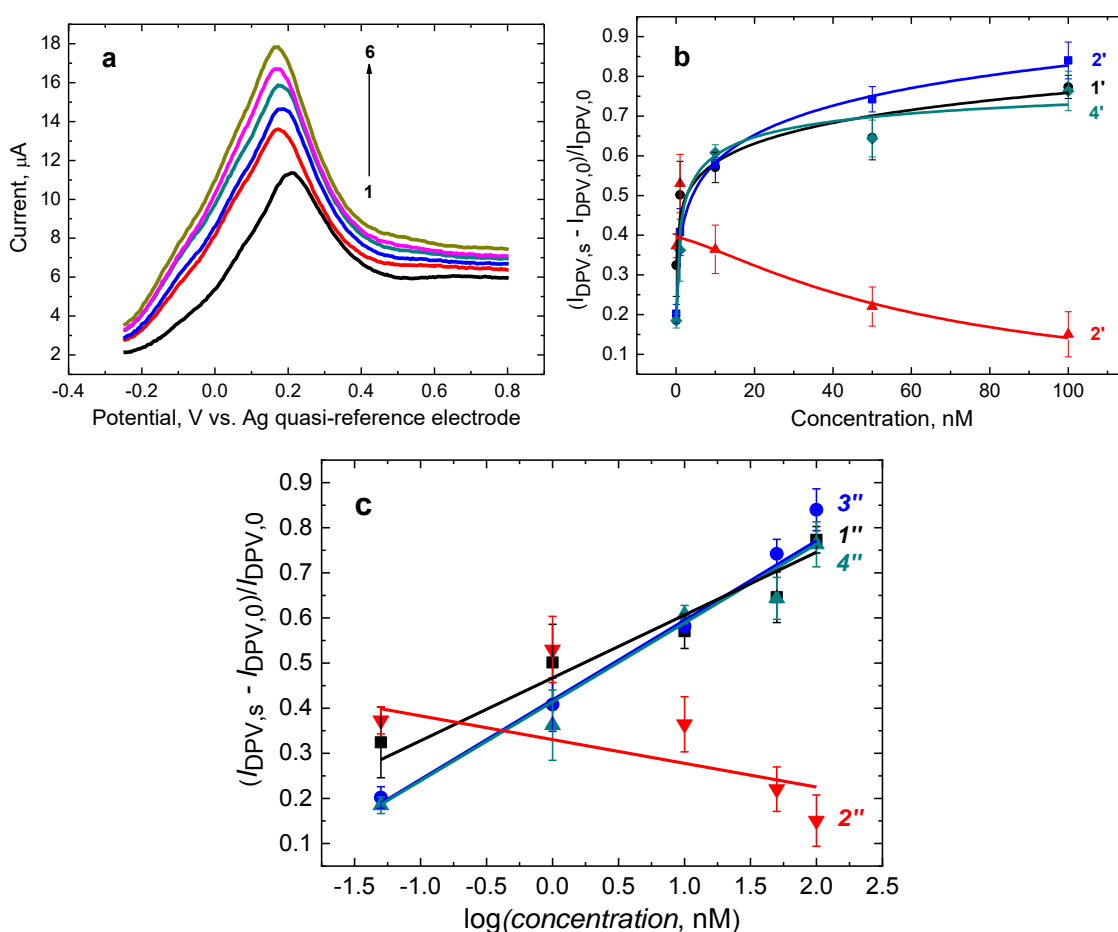
Figure 3.4-15. (a) The DPV curves for the screen-printed platinum electrode (SPPtE) coated with MIP NPs-2 in (curve *1*) 10 mM PBS (pH = 7.4) and in the glyphosate (GLY) presence at the concentration of (curve *2*) 0.05, (curve *3*) 1 (curve *4*) 10, (curve *5*) 50, and (curve *6*) 100 nM. (b) The DPV peak currents for (curve *1′*) GLY, (curve *2′*) clopyralid, (curve *3′*) ATP, and (curve *4′*) L-leucine of different concentrations. (c) Calibration plots for the (MIP NPs-2)-containing DPV chemosensor for (curve *1″*) GLY, (curve *2″*) clopyralid, (curve *3″*) ATP, and (curve *4″*) L-leucine.

Table 3.4-15. The DPV determined parameters of Langmuir-Freundlich isotherms for the (MIP NPs-2)-based chemosensor.

Compound	ΔI_{max}	K_S, nM^{-1}	n'
Glyphosate	44 ± 4085	0.01 ± 1	0.1 ± 0.2
ATP	1.8 ± 0.4	0.26 ± 0.08	0.25 ± 0.02
L-Leucine	0.8 ± 0.1	1 ± 0.4	0.41 ± 0.09
Clopyralid	0.40 ± 0.04	223 ± 1109	-1 ± 1

ΔI_{max} – maximal relative change in the DPV peak current.

K_S – the concentration of the compound at equilibrium/equilibrium constant for heterogeneous solid.

n' – the homogeneity factor.
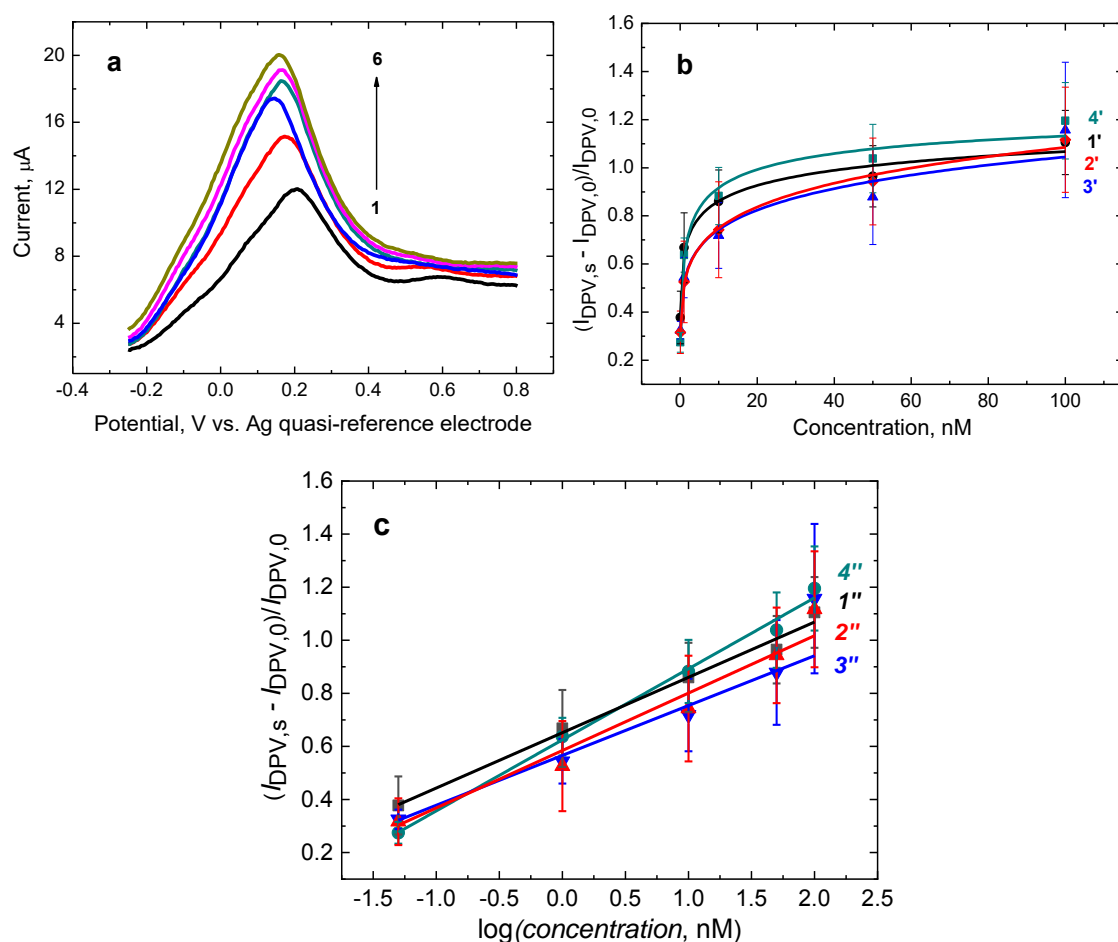
Figure 3.4-16. (a) The DPV curves for the screen-printed platinum electrode (SPPtE) coated with MIP NPs-3 in (curve *1*) 10 mM PBS (pH = 7.4), then after the addition of glyphosate (GLY) to reach the concentration of (curve *2*) 0.05, (curve *3*) 1 (curve *4*) 10, (curve *5*) 50, and (curve *6*) 100 nM. (b) The DPV peak dependence on concentration for (curve *1'*) GLY, (curve *2'*) clopyralid, (curve *3'*) ATP, and (curve *4'*) L-leucine. (c) The (MIP NPs-3)-containing DPV chemosensor calibration plots for (curve *1''*) GLY, (curve *2''*) clopyralid, (curve *3''*) ATP, and (curve *4''*) L-leucine.

Table 3.4-16. The DPV-determined parameters of Langmuir-Freundlich isotherms for the MIP NPs-3 containing chemosensor.

Compound	ΔI_{max}	K_S, nM^{-1}	n'
Glyphosate	1.5 ± 0.5	0.7 ± 0.5	0.25 ± 0.08
ATP	10 ± 69	0.06 ± 0.4	0.16 ± 0.07
L-Leucine	1.3 ± 0.2	0.9 ± 0.2	0.40 ± 0.06
Clopyralid	61 ± 1426	0.009 ± 0.2	0.16 ± 0.04

ΔI_{max} – maximal relative change in the DPV peak current

K_S – the concentration of the compound at equilibrium/equilibrium constant for heterogeneous solid

n' – the homogeneity factor.
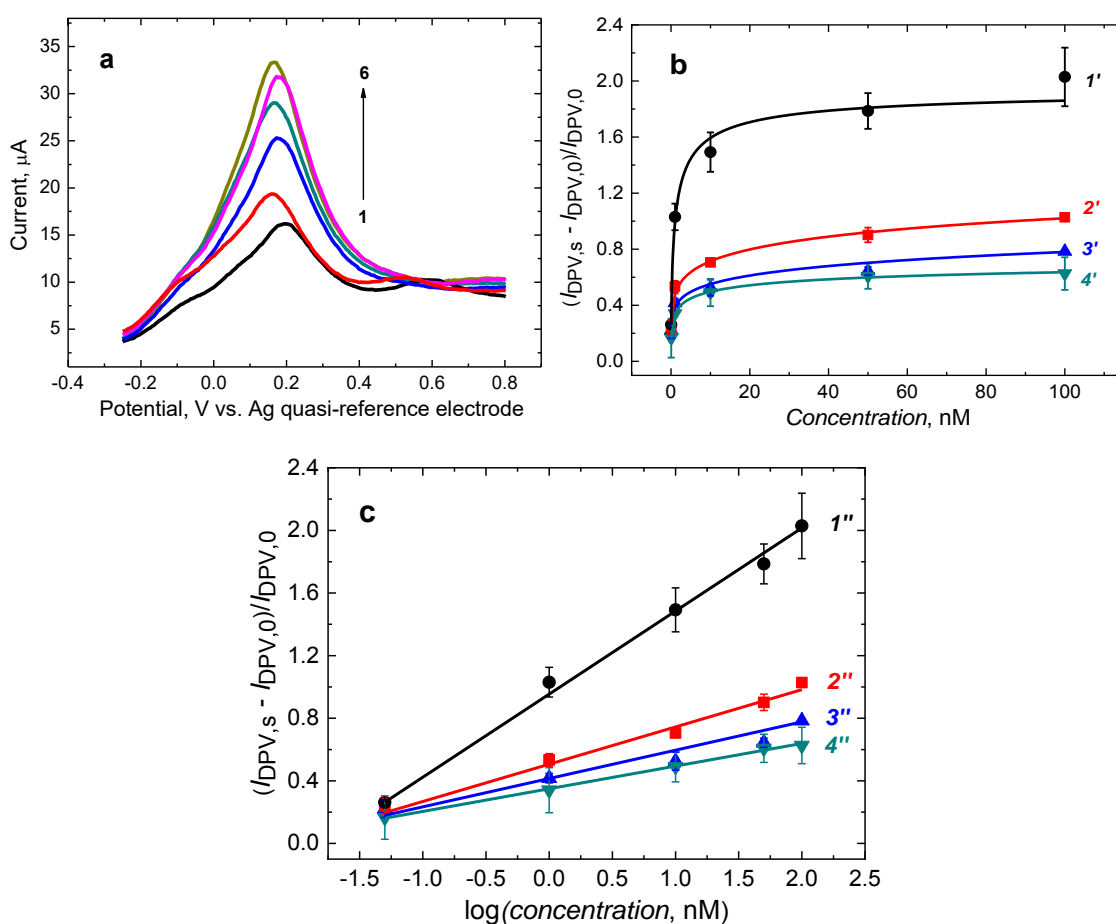
Figure 3.4-17. (a) The DPV curves for the screen-printed platinum electrode coated with MIP NPs-4 in (curve *1*) 10 mM PBS (pH = 7.4) and in the presence of glyphosate (GLY) at the concentration of (curve *2*) 0.05, (curve *3*) 1 (curve *4*) 10, (*5*) 50, and (curve *6*) 100 nM. (b) DPV peak dependence on concentration for (curve *1′*) GLY, (curve *2′*) clopyralid, (curve *3′*) ATP, and (curve *4′*) L-leucine. (c) The (MIP NPs-4)-containing DPV chemosensor calibration plots for (curve *1″*) GLY, (curve *2″*) clopyralid, (curve *3″*) ATP, and (curve *4″*) L-leucine.

Table 3.4-17. The DPV-determined parameters of Langmuir-Freundlich isotherms for the (MIP NPs-4)-containing chemosensor.

Compound	ΔI_{max}	K_S, nM^{-1}	n'
Glyphosate	2.0 ± 0.1	1.0 ± 0.3	0.63 ± 0.07
ATP	20 ± 900	0.02 ± 0.9	0.2 ± 0.2
L-Leucine	0.84 ± 0.08	0.7 ± 0.1	0.34 ± 0.04
Clopyralid	4 ± 6	0.2 ± 0.3	0.20 ± 0.08

ΔI_{max} – maximal relative change in the DPV peak current
K_S – the concentration of the compound at equilibrium/equilibrium constant for heterogeneous solid
n' – the homogeneity factor.
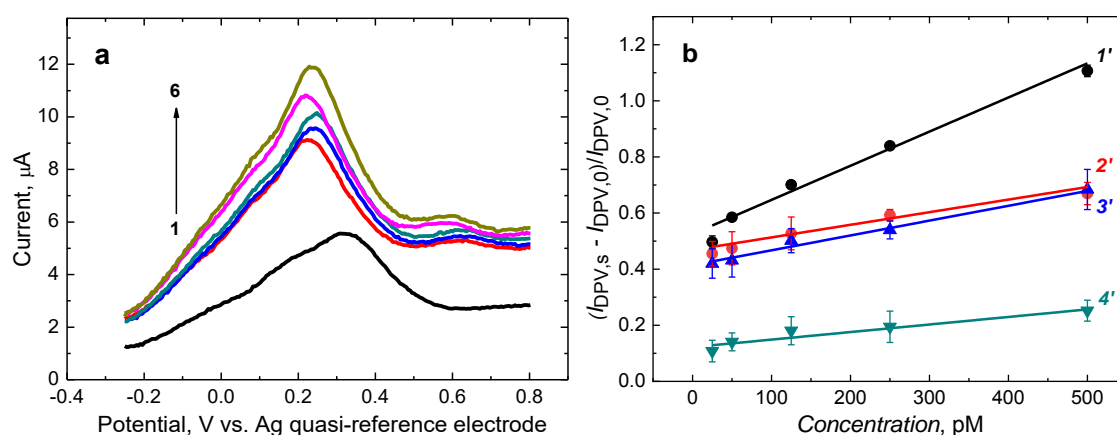
Figure 3.4-18. (a) The DPV curves for the screen-printed platinum electrode (SPPtE) coated with MIP NPs-4 in (curve *1*) 10 mM PBS (pH = 7.4) and in the presence of glyphosate (GLY) at the concentration of (curve *2*) 25, (curve *3*) 50 (curve *4*) 125, (curve *5*) 250, and (curve *6*) 500 pM. (b) The DPV calibration curves for the (MIP NPs-4)-containing chemosensor for (curve *1'*) GLY, (curve *2'*) clopyralid, (curve *3'*) ATP, and (curve 4') L-leucine.

The analytical parameters of all chemosensors devised are summarized in Table 3.4-18.

Table 3.4-18. Comparison of analytical parameters of chemosensors fabricated.

Chemosensor No.	Linear regression calibration curve	LOD, pM	Selectivity to			Linear dynamic concentration range, nM
			ATP	L-leucine	clopyralid	
MIP NPs-1	$(I_{DPV,0} - I_{DPV,s})/I_{DPV,0} =$ $1.32(\pm1.14\times10^{-1}) +$ $1.19(\pm7.29\times10^{-2})$ $\log[c_{GLY}, nM]$	5	2.69	3.50	2.02	
MIP NPs-2	$(I_{DPV,0} - I_{DPV,s})/I_{DPV,0} =$ $0.47(\pm3.77\times10^{-2}) +$ $0.14(\pm2.32\times10^{-2})$ $\log[c_{GLY}, nM]$	37	0.79	0.80	−0.73	
MIP NPs-3	$(I_{DPV,0} - I_{DPV,s})/I_{DPV,0} =$ $0.65(\pm1.57\times10^{-2}) +$ $0.21(\pm1.12\times10^{-2})$ $\log[c_{GLY}, nM]$	22	1.11	0.78	0.96	$1 - 100$
MIP NPs-4	$(I_{DPV,0} - I_{DPV,s})/I_{DPV,0} =$ $0.95(\pm2.13\times10^{-2}) +$ $0.53(\pm1.65\times10^{-2})$ $\log[c_{GLY}, nM]$	13	2.93	3.67	2.23	
MIP NPs-4	$(I_{DPV,0} - I_{DPV,s})/I_{DPV,0} =$ $0.53(\pm7.39\times10^{-3}) +$ $1.22\times10^{-3}(\pm4.13\times10^{-5})$ $c_{Gly}, [pM]$	18.2	2.31	4.54	2.72	$0.025 - 0.5$

3.4.7 Glyphosate determination in real river water samples

The (MIP NPs-1)- and (MIP NPs-4)-containing chemosensors were applied for DPV determination of GLY in river water samples in the concentration range of 0.05 nM to 100 nM, as adopted previously (Figures 3.4-19a and 3.4-20a) to verify if the detectability of the chemosensors fabricated was sufficient for real sample analysis. The samples were prepared as described in Section 2.2.2.7, then spiked with GLY. The results are compiled in Tables 3.4-19 and 3.4-21. In the GLY analyte concentration range of 0.05 nM to 100 nM, the recovery of GLY ranged from 53% to 127% and from 91% to 124% for GLY determination with the (MIP NPs-1)- and (MIP NPs-4)-containing chemosensor, respectively. The GLY concentration determined in river water samples, particularly using the (MIP NPs-4)-containing chemosensor, well complied with those determined using PBS. Moreover, all tested chemosensors

207

appeared independent of the matrix effect (panels b and c in Figures 3.4-19 to 3.4-20). Advantageously, the satisfying GLY determination in river water samples signifies that the (MIP NPs-1)- and (MIP NPs-4)-containing chemosensors can effectively monitor this herbicide in natural water samples.
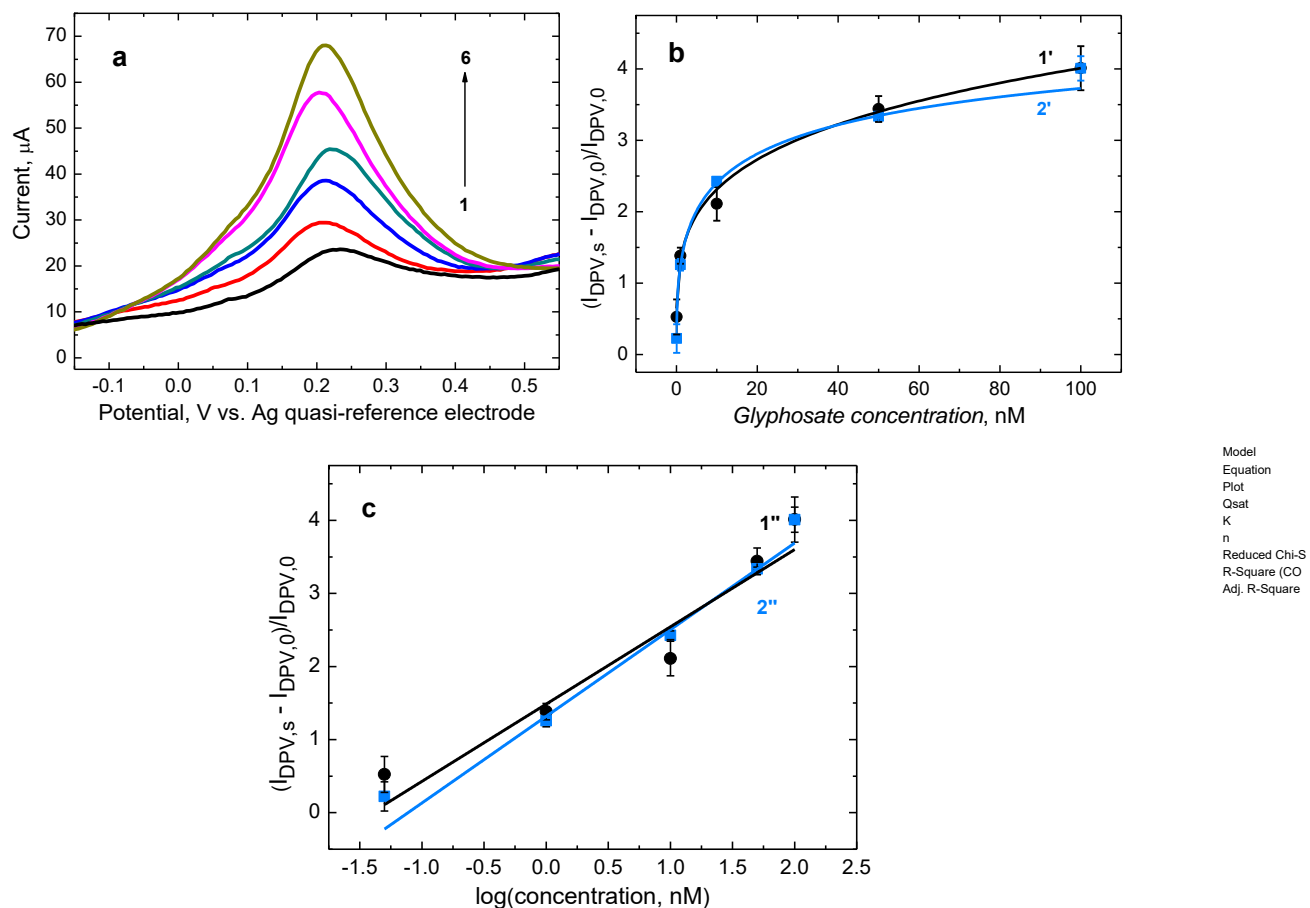
Figure 3.4-19. (a) The DPV curves for the screen-printed platinum electrode (SPPtE) modified with MIP NPs-1 in (curve *1*) river water samples, and these samples containing glyphosate (GLY) at the concentration of (curve *2*) 0.05, (curve *3*) 1, (curve *4*) 10, (curve *5*) 50, and (curve *6*) 100 nM. (b) Comparison of the (MIP NPs-1)-containing DPV chemosensor response to GLY in (curve *1′*) river water sample and (curve *2′*) 10 mM PBS (pH = 7.4). (c) Comparison of calibration plots for the (MIP NPs-1)-containing DPV chemosensor for GLY in (curve *1″*) a river water sample and (curve *2″*) 10 mM PBS (pH = 7.4).

208

Table 3.4-19. DPV determination of glyphosate (GLY) in river water samples with the (MIP NPs-1)-containing chemosensor in the GLY concentration range of 0.05 nM to 100 nM.

Sample No.	Known concentration, nM	Relative current change	Calculated concentration, nM	Recovery, %
1	0.05	0.525	0.027	53
2	1	1.383	1.064	106
3	10	2.110	6.085	61
4	50	3.439	57.36	115
5	100	4.012	127.1	127
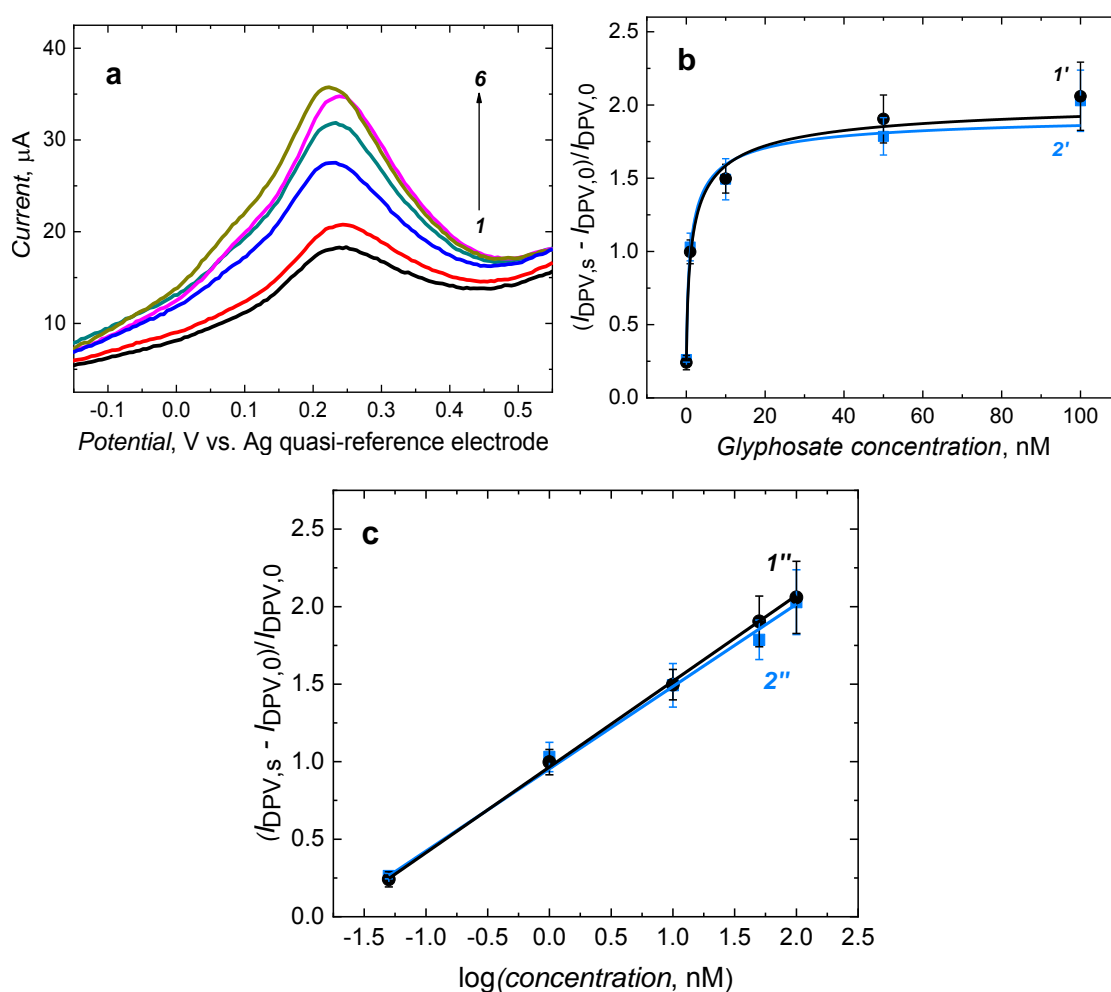
Figure 3.4-20. (a) The DPV curves for the screen-printed platinum electrode (SPPtE) modified with MIP NPs-4 in (curve *1*) river water samples and with glyphosate (GLY) present in these samples at the concentration of (curve *2*) 0.05, (curve *3*) 1 (curve *4*) 10, (curve *5*) 50, and (curve *6*) 100 nM. (b) Comparison of the (MIP NPs-4)-containing DPV chemosensor response to GLY in (curve *1'*) river water sample and (curve *2'*) 10 mM PBS (pH = 7.4). (c) Comparison of calibration plots for the (MIP NPs-4)-containing DPV chemosensor for GLY in (curve *1''*) a river water sample and (curve *2''*) 10 mM PBS (pH = 7.4).

Table 3.4-20. DPV determination of glyphosate (GLY) in river water samples with the (MIP NPs-4)-containing chemosensor in the GLY concentration range of 0.05 nM to 100 nM.

Sample No.	Known concentration, nM	Relative current change	Calculated concentration, nM	Recovery, %
1	0.05	0.241	0.045	91
2	1	0.997	1.206	121
3	10	1.497	10.54	105
4	50	1.905	61.79	124
5	100	2.060	121.0	121

Chapter 4

4.   Conclusions

The electrochemical sensors with recognition units of MIP films were devised, fabricated, and examined for selective determination of chosen food and dietary supplement' toxins, vis., Pro-NO and SYN.   The most stable pre-polymerization complexes of (functional monomer)-template were computationally selected and used for potentiodynamic electropolymerization to form thin films on the surface of electrodes.   DPV, XPS, and PM-IRRAS measurements confirmed the imprinting of Pro-NO and SYN in MIPs, then their subsequent removal.   After template extracting from the MIP, chemosensors were used to determine Pro-NO and SYN analytes. The chemosensor for Pro-NO fabricated that way revealed a low DPV and EIS-determined LOD equal to 80.9 and 36.9 nM, respectively, with appreciable sensitivity of 0.094 μA μM^{-1} and 8.651 Ω μM^{-1}, respectively, and a reasonably broad linear dynamic concentration range of 9.1 to 43.9 μM Pro-NO.   The PM at EQCM under FIA conditions determined Pro-NO in the concentration range of 0.125 to 2.0 mM with a LOD of 10 μM.   Moreover, a high *IF* exceeding 20 implies that MIP cavities of high affinity to Pro-NO molecules were formed.   The chemosensor for SYN was also characterized by a low LOD of 12.2 nM in DPV determination, achieving appreciable sensitivity of 3.21×10^{-4} nM^{-1} in a satisfying linear dynamic concentration range of 0.1 to 0.99 μM SYN.   Similarly, in the EIS determination, this chemosensor reached a LOD of 5.69 nM SYN, exhibiting high sensitivity of 0.47 Ω nM^{-1} in the linear dynamic concentration range of 0.1 to 0.99 μM SYN.   Moreover, the results have demonstrated that the chemosensors were selective to interferences, including urea, adrenalin, glucose, and creatinine.   The Pro-NO analyte was successfully determined in real meat samples, demonstrating that the developed procedure using these chemosensors is promising for sensing toxins in complex food matrices.

The present Ph.D. thesis also details the mechanism of the so-called "gate effect" accounting for the operation of chemosensors constructed from conductive MIP films. A functionalized polythiophene film imprinted with SYN was applied as the model sensing system.   Importantly, the DPV peak decrease at the SYN-MIP film-coated electrode for the $K_4[Fe(CN)_6]/K_3[Fe(CN)_6]$ and $Ru(NH_3)_6Cl_3$ redox probes after the

211

addition of SYN did not originate from MIP film swelling or shrinking. Instead, this decrease originated from changes in the inherent electrochemical properties of the MIP film, namely, its conductivity. UV-vis spectroscopy results indicated that the conductivity decrease with the increase of the SYN concentration presumably originated from the decrease of radical cation (polaron) mobility in this semiconductive MIP film.

The above investigation enabled the devising of a redox self-reporting MIP chemosensor with the covalently immobilized ferrocene redox probe for label-free electrochemical sensing of the SYN model analyte. A ferrocene-derivatized polythiophene monomer was designed, synthesized, and then used for MIP film deposition on the electrode surface to immobilize the Fc redox probe in the MIP matrix covalently. These electrodes were used for the electrochemical determination of SYN without the external redox probe in the test solutions. Since the thickness and morphology of the prepared MIP film were significant parameters in terms of sensor performance, the electropolymerization conditions were optimized. Moreover, it was necessary to copolymerize the (sulfonyl acid moiety)-containing monomer for proper chemosensor operation. Under these conditions, even 40% of the ferrocene moieties contributed to the self-reporting MIP film chemosensor response. Significantly, this sensor's analytical parameters determined by DPV, including sensitivity $(3.99 \times 10^{-2} \, nM^{-1})$ and LOD (0.57 nM SYN), favorably compared to those of the previously described traditional chemosensor using an external redox probe with the sensitivity and LOD equaling $3.21 \times 10^{-4} \, nM^{-1}$ and 12.2 nM SYN, respectively. Successful determination of SYN in real dietary supplement samples confirmed the analytical usefulness of the chemosensor with the self-reporting MIP film.

Furthermore, four chemosensors containing electroactive MIP NPs with the covalently immobilized ferrocene derivative were fabricated and examined for the DPV determination of GLY. MIP NPs with ferrocene moieties acted as both the recognition unit and the internal redox probe. The performance of the MIP NPs sensor prepared in the presence of Ally and SQ6 functional monomers was superior to other chemosensors based on MIP NPs. Apparently, interactions of Ally and SQ6 functional monomers with GLY were the strongest, allowing them to form well-defined molecular cavities and thus achieve low LOD equaling 13 pM GLY. Moreover, GLY was determined in river water samples, proving that the fabricated sensor applies to real samples' analysis.

212

References

1.   Hulanicki, A.; Glab, S.; Ingman, F., Chemical sensors: definitions and classification. *Pure Appl. Chem.* **1991,** *63*, 1247-1250.

2.   Leibl, N.; Haupt, K.; Gonzato, C.; Duma, L., Molecularly Imprinted Polymers for Chemical Sensing: A Tutorial Review. *Chemosensors* **2021,** *9*, 123.

3.   Thevenot, D. R.; Toth, K.; Durst, R. A.; Wilson, G. S., Electrochemical biosensors: Recommended definitions and classification - (Technical Report). *Pure Appl. Chem.* **1999,** *71* (12), 2333-2348.

4.   Turner, A. P. F., Biosensors: sense and sensibility. *Chem. Soc. Rev.* **2013,** *42*, 3184-3196.

5.   Naresh, V.; Lee, N., A Review on Biosensors and Recent Development of Nanostructured Materials-Enabled Biosensors. *Sensors* **2021,** *21*, 1109.

6.   Vigneshvar, S.; Sudhakumari, C. C.; Senthilkumaran, B.; Prakash, H., Recent Advances in Biosensor Technology for Potential Applications – An Overview. *Front. Bioeng. Biotechnol.* **2016,** *4*, 11.

7.   Bhalla, N.; Jolly, P.; Formisano, N.; Estrela, P., Introduction to biosensors. *Essays Biochem.* **2016,** *60*, 1-8.

8.   Ansari, S.; Masoum, S., Molecularly imprinted polymers for capturing and sensing proteins: Current progress and future implications. *Trends Anal. Chem.* **2019,** *114*, 29-47.

9.   Yarman, A.; Kurbanoglu, S.; Zebger, I.; Scheller, F. W., Simple and robust: The claims of protein sensing by molecularly imprinted polymers. *Sens. Actuators B Chem.* **2021,** *330*.

10.   Cieplak, M.; Węgłowski, R.; Iskierko, Z.; Węgłowska, D.; Sharma, P. S.; Noworyta, K. R.; D'Souza, F.; Kutner, W., Protein Determination with Molecularly Imprinted Polymer Recognition Combined with Birefringence Liquid Crystal Detection. *Sensors* **2020,** *20*, 4692.

11.   Idil, N.; Mattiasson, B., Imprinting of Microorganisms for Biosensor Applications. *Sensors* **2017,** *17*, 708.

12.   Amorim, M. S.; Sales, M. G. F.; Frasco, M. F., Recent advances in virus imprinted polymers. *Biosens. Bioelectron. X* **2022,** *10*, 100131.

13.   Jamalipour Soufi, G.; Iravani, S.; Varma, R. S., Molecularly imprinted polymers for the detection of viruses: challenges and opportunities. *Analyst* **2021,** *146*, 3087-3100.

14.   Yarman, A.; Kurbanoglu, S.; Scheller, F. W., Present state of MIP-based sensors for SARS-CoV-2. In *Sensing Tools and Techniques for COVID-19*, 2022; pp 3-25.

15.   Sukjee, W.; Thitithanyanont, A.; Manopwisedjaroen, S.; Seetaha, S.; Thepparit, C.; Sangma, C., Virus MIP-composites for SARS-CoV-2 detection in the aquatic environment. *Mater. Lett.* **2022,** *315*, 131973.

16.   Amouzadeh Tabrizi, M.; Fernández-Blázquez, J. P.; Medina, D. M.; Acedo, P., An ultrasensitive molecularly imprinted polymer-based electrochemical sensor for the determination of SARS-CoV-2-RBD by using macroporous gold screen-printed electrode. *Biosens. Bioelectron.* **2022,** *196*, 113729.

213

17.   Wang, R.; Wang, L.; Yan, J.; Luan, D.; Tao, s.; Wu, J.; Bian, X., Rapid, sensitive and label-free detection of pathogenic bacteria using a bacteria-imprinted conducting polymer film-based electrochemical sensor. *Talanta* **2021,** *226*, 122135.

18.   Sharma, R.; Lakshmi, G. B. V. S.; Kumar, A.; Solanki, P., Polypyrrole Based Molecularly Imprinted Polymer Platform for Klebsiella pneumonia Detection. *ECS Sensors Plus* **2022,** *1*, 010603.

19.   Morales, M. A.; Halpern, J. M., Guide to Selecting a Biorecognition Element for Biosensors. *Bioconjugate Chem.* **2018,** *29*, 3231-3239.

20.   Sharma, P. S.; Iskierko, Z.; Pietrzyk-Le, A.; D'Souza, F.; Kutner, W., Bioinspired intelligent molecularly imprinted polymers for chemosensing: A mini review. *Electrochem. Commun.* **2015,** *50*, 81-87.

21.   BelBruno, J. J., Molecularly Imprinted Polymers. *Chem. Rev.* **2018,** *119*, 94-119.

22.   Ansari, S.; Masoum, S., Recent advances and future trends on molecularly imprinted polymer-based fluorescence sensors with luminescent carbon dots. *Talanta* **2021,** *223*, 121411.

23.   Svitkova, V.; Palchetti, I., Functional polymers in photoelectrochemical biosensing. *Bioelectrochemistry* **2020,** *136*, 107590.

24.   Dong, X.; Zhang, C.; Du, X.; Zhang, Z., Recent Advances of Nanomaterials-Based Molecularly Imprinted Electrochemical Sensors. *Nanomaterials* **2022,** *12*, 1913.

25.   Yang, Y.; Yan, W.; Guo, C.; Zhang, J.; Yu, L.; Zhang, G.; Wang, X.; Fang, G.; Sun, D., Magnetic molecularly imprinted electrochemical sensors: A review. *Anal. Chim. Acta* **2020,** *1106*, 1-21.

26.   Lahcen, A. A.; Surya, S. G.; Beduk, T.; Vijjapu, M. T.; Lamaoui, A.; Durmus, C.; Timur, S.; Shekhah, O.; Mani, V.; Amine, A.; Eddaoudi, M.; Salama, K. N., Metal–Organic Frameworks Meet Molecularly Imprinted Polymers: Insights and Prospects for Sensor Applications. *ACS Appl. Mater. Interfaces* **2022,** *14*, 49399–49424.

27.   Ramanavicius, S.; Samukaite-Bubniene, U.; Ratautaite, V.; Bechelany, M.; Ramanavicius, A., Electrochemical molecularly imprinted polymer based sensors for pharmaceutical and biomedical applications (review). *J. Pharm. Biomed. Anal.* **2022,** *215*, 114739.

28.   Ramanavičius, S.; Morkvėnaitė-Vilkončienė, I.; Samukaitė-Bubnienė, U.; Ratautaitė, V.; Plikusienė, I.; Viter, R.; Ramanavičius, A., Electrochemically Deposited Molecularly Imprinted Polymer-Based Sensors. *Sensors* **2022,** *22*, 1282.

29.   Lowdon, J. W.; Diliën, H.; Singla, P.; Peeters, M.; Cleij, T. J.; van Grinsven, B.; Eersels, K., MIPs for commercial application in low-cost sensors and assays – An overview of the current status quo. *Sens. Actuators B Chem.* **2020,** *325*, 128973.

30.   Ashley, J.; Shahbazi, M.-A.; Kant, K.; Chidambara, V. A.; Wolff, A.; Bang, D. D.; Sun, Y., Molecularly imprinted polymers for sample preparation and biosensing in food analysis: Progress and perspectives. *Biosens. Bioelectron.* **2017,** *91*, 606-615.

31.   Wackerlig, J.; Schirhagl, R., Applications of Molecularly Imprinted Polymer Nanoparticles and Their Advances toward Industrial Use: A Review. *Anal. Chem.* **2015,** *88*, 250-261.

32.   Cao, Y.; Feng, T.; Xu, J.; Xue, C., Recent advances of molecularly imprinted polymer-based sensors in the detection of food safety hazard factors. *Biosens. Bioelectron.* **2019,** *141*, 111447.

33.   Pan, Y.; Liu, X.; Liu, J.; Wang, J.; Liu, J.; Gao, Y.; Ma, N., Chemiluminescence sensors based on molecularly imprinted polymers for the determination of organophosphorus in milk. *J. Dairy Sci.* **2022,** *105*, 3019-3031.

34.   El-Akaad, S.; Mohamed, M. A.; Abdelwahab, N. S.; Abdelaleem, E. A.; De Saeger, S.; Beloglazova, N., Capacitive sensor based on molecularly imprinted polymers for detection of the insecticide imidacloprid in water. *Sci. Rep.* **2020,** *10*, 14479.

35.   Aaryashree; Takeda, Y.; Kanai, M.; Hatano, A.; Yoshimi, Y.; Kida, M., A "Single-Use" Ceramic-Based Electrochemical Sensor Chip Using Molecularly Imprinted Carbon Paste Electrode. *Sensors* **2020,** *20*.

36.   Liu, Y.; Wei, M.; Hu, Y.; Zhu, L.; Du, J., An electrochemical sensor based on a molecularly imprinted polymer for determination of anticancer drug Mitoxantrone. *Sens. Actuators B Chem.* **2018,** *255*, 544-551.

37.   Diouf, A.; Bouchikhi, B.; El Bari, N., A nonenzymatic electrochemical glucose sensor based on molecularly imprinted polymer and its application in measuring saliva glucose. *Mater. Sci. Eng. C* **2019,** *98*, 1196-1209.

38.   Caldara, M.; Lowdon, J. W.; Rogosic, R.; Arreguin-Campos, R.; Jimenez-Monroy, K. L.; Heidt, B.; Tschulik, K.; Cleij, T. J.; Diliën, H.; Eersels, K.; van Grinsven, B., Thermal Detection of Glucose in Urine Using a Molecularly Imprinted Polymer as a Recognition Element. *ACS Sens.* **2021,** *6*, 4515-4525.

39.   Liang, R.; Chen, L.; Qin, W., Potentiometric detection of chemical vapors using molecularly imprinted polymers as receptors. *Sci. Rep.* **2015,** *5*, 12462.

40.   Chen, L.; Wang, X.; Lu, W.; Wu, X.; Li, J., Molecular imprinting: perspectives and applications. *Chem. Soc. Rev.* **2016,** *45*, 2137-2211.

41.   Uzun, L.; Turner, A. P. F., Molecularly-imprinted polymer sensors: realising their potential. *Biosens. Bioelectron.* **2016,** *76*, 131-144.

42.   Mazzotta, E.; Di Giulio, T.; Malitesta, C., Electrochemical sensing of macromolecules based on molecularly imprinted polymers: challenges, successful strategies, and opportunities. *Anal. Bioanal. Chem.* **2022,** *414*, pages 5165–5200.

43.   Slomkowski, S.; Alemán, J. V.; Gilbert, R. G.; Hess, M.; Horie, K.; Jones, R. G.; Kubisa, P.; Meisel, I.; Mormann, W.; Penczek, S.; Stepto, R. F. T., Terminology of polymers and polymerization processes in dispersed systems (IUPAC Recommendations 2011). *Pure Appl. Chem.* **2011,** *83*, 2229-2259.

44.   Olcer, Y. A.; Demirkurt, M.; Demir, M. M.; Eroglu, A. E., Development of molecularly imprinted polymers (MIPs) as a solid phase extraction (SPE) sorbent for the determination of ibuprofen in water. *RSC Adv.* **2017,** *7*, 31441-31447.

45.   Hasanah, A. N.; Dwi Utari, T. N.; Pratiwi, R., Synthesis of Atenolol-Imprinted Polymers with Methyl Methacrylate as Functional Monomer in Propanol Using Bulk and Precipitation Polymerization Method. *J. Anal. Methods Chem.* **2019,** *2019*, 9853620.

46.   Pardeshi, S.; Singh, S. K., Precipitation polymerization: a versatile tool for preparing molecularly imprinted polymer beads for chromatography applications. *RSC Adv.* **2016,** *6*, 23525-23536.

47.   Xia, Q.; Yun, Y.; Li, Q.; Huang, Z.; Liang, Z., Preparation and characterization of monodisperse molecularly imprinted polymer microspheres by precipitation polymerization for kaempferol. *Des. Monomers. Polym.* **2017,** *20*, 201-209.

48.   Dai, C.-m.; Zhou, X.-f.; Zhang, Y.-l.; Liu, S.-g.; Zhang, J., Synthesis by precipitation polymerization of molecularly imprinted polymer for the selective extraction of diclofenac from water samples. *J. Hazard. Mater.* **2011,** *198*, 175-181.

49.   Lovell, P. A.; Schork, F. J., Fundamentals of Emulsion Polymerization. *Biomacromolecules* **2020,** *21*, 4396-4441.

50.   Zhao, G.; Liu, J.; Liu, M.; Han, X.; Peng, Y.; Tian, X.; Liu, J.; Zhang, S., Synthesis of Molecularly Imprinted Polymer via Emulsion Polymerization for Application in Solanesol Separation. *Appl. Sci.* **2020,** *10*, 2868.

51.   Yang, J.; Li, Y.; Wang, J.; Sun, X.; Cao, R.; Sun, H.; Huang, C.; Chen, J., Molecularly imprinted polymer microspheres prepared by Pickering emulsion polymerization for selective solid-phase extraction of eight bisphenols from human urine samples. *Anal. Chim. Acta* **2015,** *872*, 35-45.

52.   Sun, Y.; Zhang, Y.; Ju, Z.; Niu, L.; Gong, Z.; Xu, Z., Molecularly imprinted polymers fabricated by Pickering emulsion polymerization for the selective adsorption and separation of quercetin from Spina Gleditsiae. *New J. Chem.* **2019,** *43*, 14747-14755.

53.   Zhu, F.; Li, L.; Xing, J., Selective adsorption behavior of Cd(II) ion imprinted polymers synthesized by microwave-assisted inverse emulsion polymerization: Adsorption performance and mechanism. *J. Hazard. Mater.* **2017,** *321*, 103-110.

54.   Mayes, A. G.; Mosbach, K., Molecularly Imprinted Polymer Beads: Suspension Polymerization Using a Liquid Perfluorocarbon as the Dispersing Phase. *Anal. Chem.* **1996,** *68*, 3769-3774.

55.   Öter, Ç.; Zorer, Ö. S., Molecularly imprinted polymer synthesis and selective solid phase extraction applications for the detection of ziram, a dithiocarbamate fungicide. *Chem. Eng. J. Adv.* **2021,** *7*, 100118.

56.   Liu, X.; Wu, F.; Au, C.; Tao, Q.; Pi, M.; Zhang, W., Synthesis of molecularly imprinted polymer by suspension polymerization for selective extraction of p-hydroxybenzoic acid from water. *J. Appl. Polym. Sci.* **2019,** *136*, 46984.

57.   Song, L.; He, J.; Chen, N.; Huang, Z., Combined biocompatible medium with molecularly imprinted polymers for determination of aflatoxins B1 in real sample. *J. Sep. Sci.* **2019,** *42*, 3679-3687.

58.   Alizadeh, T.; Ganjali, M. R.; Rafiei, F.; Akhoundian, M., Synthesis of nano-sized timolol-imprinted polymer via ultrasonication assisted suspension polymerization in silicon oil and its use for the fabrication of timolol voltammetric sensor. *Mater. Sci. Eng. C* **2017,** *77*, 300-307.

59.   Dong, C.; Shi, H.; Han, Y.; Yang, Y.; Wang, R.; Men, J., Molecularly imprinted polymers by the surface imprinting technique. *Eur. Polym. J.* **2021,** *145*, 110231.

60.   Kalecki, J.; Iskierko, Z.; Cieplak, M.; Sharma, P. S., Oriented Immobilization of Protein Templates: A New Trend in Surface Imprinting. *ACS Sens.* **2020,** *5*, 3710-3720.

61.   Cui, F.; Zhou, Z.; Zhou, H. S., Molecularly Imprinted Polymers and Surface Imprinted Polymers Based Electrochemical Biosensor for Infectious Diseases. *Sensors* **2020,** *20*, 996.

62.   Yilmaz, E.; Haupt, K.; Mosbach, K., The Use of Immobilized Templates—A New Approach in Molecular Imprinting. *Angew. Chem. Int. Ed.* **2000,** *39*, 2115-2118.

63.   Pasquardini, L.; Bossi, A. M., Molecularly imprinted polymers by epitope imprinting: a journey from molecular interactions to the available bioinformatics resources to scout for epitope templates. *Anal. Bioanal. Chem.* **2021,** *413*, 6101-6115.

64.   Khumsap, T.; Corpuz, A.; Nguyen, L. T., Epitope-imprinted polymers: applications in protein recognition and separation. *RSC Adv.* **2021,** *11*, 11403-11414.

65.   Yang, K.; Li, S.; Liu, L.; Chen, Y.; Zhou, W.; Pei, J.; Liang, Z.; Zhang, L.; Zhang, Y., Epitope Imprinting Technology: Progress, Applications, and Perspectives toward Artificial Antibodies. *Adv. Mater.* **2019,** *31*, 1902048.

66.   Xing, R.; Ma, Y.; Wang, Y.; Wen, Y.; Liu, Z., Specific recognition of proteins and peptides via controllable oriented surface imprinting of boronate affinity-anchored epitopes. *Chem. Sci.* **2019,** *10*, 1831-1835.

67.   Yang, F.; Lin, S.; Dong, X., An artificial receptor synthesized by surface-confined imprinting for the recognition of acetylation on histone H4 K16. *Chem. Commun.* **2015,** *51*, 7673-7676.

68.   Li, S.; Yang, K.; Zhao, B.; Li, X.; Liu, L.; Chen, Y.; Zhang, L.; Zhang, Y., Epitope imprinting enhanced IMAC (EI-IMAC) for highly selective purification of His-tagged protein. *J. Mater. Chem. B* **2016,** *4*, 1960-1967.

69.   Tang, A.-n.; Duan, L.; Liu, M.; Dong, X., An epitope imprinted polymer with affinity for kininogen fragments prepared by metal coordination interaction for cancer biomarker analysis. *J. Mater. Chem. B* **2016,** *4*, 7464-7471.

70.   Moein, M. M.; Abdel-Rehim, A.; Abdel-Rehim, M., Recent Applications of Molecularly Imprinted Sol-Gel Methodology in Sample Preparation. *Molecules (Basel, Switzerland)* **2019,** *24*, 2889.

71.   Kajihara, K., Recent advances in sol–gel synthesis of monolithic silica and silica-based glasses. *J. Asian Ceram. Soc.* **2013,** *1*, 121-133.

72.   Kalogiouri, N. P.; Tsalbouris, A.; Kabir, A.; Furton, K. G.; Samanidou, V. F., Synthesis and application of molecularly imprinted polymers using sol–gel matrix imprinting technology for the efficient solid-phase extraction of BPA from water. *Microchem. J.* **2020,** *157*, 104965.

73.   Sharma, P. S.; Pietrzyk-Le, A.; D'Souza, F.; Kutner, W., Electrochemically synthesized polymers in molecular imprinting for chemical sensing. *Anal. Bioanal. Chem.* **2012,** *402*, 3177-3204.

74.   Crapnell, R. D.; Dempsey-Hibbert, N. C.; Peeters, M.; Tridente, A.; Banks, C. E., Molecularly imprinted polymer based electrochemical biosensors: Overcoming the challenges of detecting vital biomarkers and speeding up diagnosis. *Talanta Open* **2020,** *2*, 100018.

75.   Moreira Gonçalves, L., Electropolymerized molecularly imprinted polymers: perceptions based on recent literature for soon-to-be world-class scientists. *Curr. Opin. Electrochem.* **2021,** *25*, 100640.

76.   Fomo, G.; Waryo, T.; Feleni, U.; Baker, P.; Iwuoha, E., Electrochemical Polymerization. In *Functional Polymers*, Jafar Mazumder, M. A.; Sheardown, H.; Al-Ahmed, A., Eds. Springer International Publishing: Cham, 2019; pp 1-28.

77.   Mustafa, Y. L.; Keirouz, A.; Leese, H. S., Molecularly imprinted polymers in diagnostics: accessing analytes in biofluids. *J. Mater. Chem. B* **2022,** *10*, 7418-7449.

78.   Sajini, T.; Mathew, B., A brief overview of molecularly imprinted polymers: Highlighting computational design, nano and photo-responsive imprinting. *Talanta Open* **2021,** *4*, 100072.

79.   Turiel, E.; Martín-Esteban, A., Molecularly imprinted polymers for sample preparation: A review. *Anal. Chim. Acta* **2010,** *668*, 87-99.

80.   Gornik, T.; Shinde, S.; Lamovsek, L.; Koblar, M.; Heath, E.; Sellergren, B.; Kosjek, T., Molecularly Imprinted Polymers for the Removal of Antide-Pressants from Contaminated Wastewater. *Polymers* **2020,** *13*, 120.

81.   Sadia, M.; Ahmad, I.; Ali, F.; Zahoor, M.; Ullah, R.; Khan, F.; Ali, E.; Sohail, A., Selective Removal of the Emerging Dye Basic Blue 3 via Molecularly Imprinting Technique. *Molecules (Basel, Switzerland)* **2022,** *27*, 3276.

82.   Fu, Y.; Pessagno, F.; Manesiotis, P.; Borrull, F.; Fontanals, N.; Maria Marcé, R., Preparation and evaluation of molecularly imprinted polymers as selective SPE sorbents for the determination of cathinones in river water. *Microchem. J.* **2022,** *175*, 107100.

83.   Ansell, R. J., Molecularly imprinted polymers for the enantioseparation of chiral drugs. *Adv. Drug Deliv. Rev.* **2005,** *57*, 1809-1835.

84.   Zhou, W.-H.; Guo, X.-C.; Zhao, H.-Q.; Wu, S.-X.; Yang, H.-H.; Wang, X.-R., Molecularly imprinted polymer for selective extraction of domoic acid from seafood coupled with high-performance liquid chromatographic determination. *Talanta* **2011,** *84*, 777-782.

85.   Azizi, A.; Bottaro, C. S., A critical review of molecularly imprinted polymers for the analysis of organic pollutants in environmental water samples. *J. Chromatogr. A* **2020,** *1614*, 460603.

86.   Bagheri, A. R.; Aramesh, N.; Khan, A. A.; Gul, I.; Ghotekar, S.; Bilal, M., Molecularly imprinted polymers-based adsorption and photocatalytic approaches for mitigation of environmentally-hazardous pollutants ─ A review. *J. Environ. Chem. Eng.* **2021,** *9*, 104879.

87.   Aravind, A.; Mathew, B., Electrochemical sensor based on nanostructured ion imprinted polymer for the sensing and extraction of Cr(III) ions from industrial wastewater. *Polym. Int.* **2018,** *67*, 1595-1604.

88.   Aravind, A.; Mathew, B., Tailoring of nanostructured material as an electrochemical sensor and sorbent for toxic Cd(II) ions from various real samples. *J. Anal. Sci. Technol.* **2018,** *9*, 22.

89.   Kusumkar, V. V.; Galamboš, M.; Viglašová, E.; Daňo, M.; Šmelková, J., Ion-Imprinted Polymers: Synthesis, Characterization, and Adsorption of Radionuclides. *Materials* **2021,** *14*, 1083.

90.   Zare, E. N.; Fallah, Z.; Le, V. T.; Doan, V.-D.; Mudhoo, A.; Joo, S.-W.; Vasseghian, Y.; Tajbakhsh, M.; Moradi, O.; Sillanpää, M.; Varma, R. S., Remediation of pharmaceuticals from contaminated water by molecularly imprinted polymers: a review. *Environ. Chem. Lett.* **2022,** *20*, 2629-2664.

91.   Moein, M. M., Advancements of chiral molecularly imprinted polymers in separation and sensor fields: A review of the last decade. *Talanta* **2021,** *224*, 121794.

92.   Yang, S.; Wang, Y.; Jiang, Y.; Li, S.; Liu, W., Molecularly Imprinted Polymers for the Identification and Separation of Chiral Drugs and Biomolecules. *Polymers* **2016,** *8*, 216.

93.   Mizutani, N.; Yang, D.-H.; Selyanchyn, R.; Korposh, S.; Lee, S.-W.; Kunitake, T., Remarkable enantioselectivity of molecularly imprinted TiO2 nano-thin films. *Anal. Chim. Acta* **2011,** *694*, 142-150.

94.   Ramström, O.; Ye, L.; Gustavsson, P. E., Chiral recognition by molecularly imprinted polymers in aqueous media. *Chromatographia* **1998,** *48*, 197-202.

95.   He, S.; Zhang, L.; Bai, S.; Yang, H.; Cui, Z.; Zhang, X.; Li, Y., Advances of molecularly imprinted polymers (MIP) and the application in drug delivery. *Eur. Polym. J.* **2021,** *143*, 110179.

96.   Zaidi, S. A., Molecular imprinting: A useful approach for drug delivery. *Mater. Sci. Energy Technol.* **2020,** *3*, 72-77.

97.   Tarannum, N.; Hendrickson, O. D.; Khatoon, S.; Zherdev, A. V.; Dzantiev, B. B., Molecularly imprinted polymers as receptors for assays of antibiotics. *Crit. Rev. Anal. Chem.* **2020,** *50*, 291-310.

98.   Chen, C.; Luo, J.; Li, C.; Ma, M.; Yu, W.; Shen, J.; Wang, Z., Molecularly Imprinted Polymer as an Antibody Substitution in Pseudo-immunoassays for Chemical Contaminants in Food and Environmental Samples. *J. Agric. Food Chem.* **2018,** *66*, 2561-2571.

99.   Parisi, O. I.; Ruffo, M.; Scrivano, L.; Malivindi, R.; Vassallo, A.; Puoci, F., Smart Bandage Based on Molecularly Imprinted Polymers (MIPs) for Diclofenac Controlled Release. *Pharmaceuticals* **2018,** *11*, 92.

100.   Mohebali, A.; Abdouss, M.; Mazinani, S.; Zahedi, P., Synthesis and characterization of poly(methacrylic acid)-based molecularly imprinted polymer nanoparticles for controlled release of trinitroglycerin. *Polym. Adv. Technol.* **2016,** *27*, 1164-1171.

101.   Hashemi-Moghaddam, H.; Zavareh, S.; Karimpour, S.; Madanchi, H., Evaluation of molecularly imprinted polymer based on HER2 epitope for targeted drug delivery in ovarian cancer mouse model. *React. Funct. Polym.* **2017,** *121*, 82-90.

102.   Hemmati, K.; Masoumi, A.; Ghaemy, M., Tragacanth gum-based nanogel as a superparamagnetic molecularly imprinted polymer for quercetin recognition and controlled release. *Carbohydr. Polym.* **2016,** *136*, 630-640.

103.   Sharma, P. S.; Wojnarowicz, A.; Kutner, W.; D'Souza, F., 9 - Molecularly Imprinted Polymers as Synthetic Catalysts. In *Molecularly Imprinted Catalysts*, Li, S.; Cao, S.; Piletsky, S. A.; Turner, A. P. F., Eds. Elsevier: Amsterdam, 2016; pp 183-210.

104.   Mirata, F.; Resmini, M., Molecularly Imprinted Polymers for Catalysis and Synthesis. In *Molecularly Imprinted Polymers in Biotechnology*, Mattiasson, B.; Ye, L., Eds. Springer International Publishing: Cham, 2015; pp 107-129.

105.   Wulff, G., Enzyme-like Catalysis by Molecularly Imprinted Polymers. *Chem. Rev.* **2002,** *102*, 1-28.

106.   Mathew, D.; Thomas, B.; Devaky, K. S., Design, synthesis and characterization of enzyme-analogue-built polymer catalysts as artificial hydrolases. *Artif. Cells Nanomed. Biotechnol.* **2019,** *47*, 1149-1172.

107.   Wulff, G.; Sarhan, A.; Zabrocki, K., Enzyme-analogue built polymers and their use for the resolution of racemates. *Tetrahedron Lett.* **1973,** *14*, 4329-4332.

108.   Cliver, D. O.; Riemann, H. P., *Foodborne diseases*. 2nd Ed.; Academic Press: London, 2002.

109.   Wu, M.; Deng, H.; Fan, Y.; Hu, Y.; Guo, Y.; Xie, L., Rapid Colorimetric Detection of Cartap Residues by AgNP Sensor with Magnetic Molecularly Imprinted Microspheres as Recognition Elements. *Molecules (Basel, Switzerland)* **2018,** *23*, 1443.

110.   Feng, S.; Hu, Y.; Ma, L.; Lu, X., Development of molecularly imprinted polymers-surface-enhanced Raman spectroscopy/colorimetric dual sensor for determination of chlorpyrifos in apple juice. *Sens. Actuators B Chem.* **2017,** *241*, 750-757.

111.   Ye, T.; Yin, W.; Zhu, N.; Yuan, M.; Cao, H.; Yu, J.; Gou, Z.; Wang, X.; Zhu, H.; Reyihanguli, A.; Xu, F., Colorimetric detection of pyrethroid metabolite by using surface molecularly imprinted polymer. *Sens. Actuators B Chem.* **2018,** *254*, 417-423.

112.   Greene, N. T.; Shimizu, K. D., Colorimetric Molecularly Imprinted Polymer Sensor Array using Dye Displacement. *J. Am. Chem. Soc.* **2005,** *127*, 5695-5700.

113.   Lamaoui, A.; Karrat, A.; Amine, A., Molecularly imprinted polymer integrated into paper-based analytical device for smartphone-based detection: Application for sulfamethoxazole. *Sens. Actuators B Chem.* **2022,** *368*, 132122.

114.   Liu, G.; Huang, X.; Li, L.; Xu, X.; Zhang, Y.; Lv, J.; Xu, D., Recent Advances and Perspectives of Molecularly Imprinted Polymer-Based Fluorescent Sensors in Food and Environment Analysis. *Nanomaterials* **2019,** *9*, 1030.

115.   Yang, Q.; Li, J.; Wang, X.; Peng, H.; Xiong, H.; Chen, L., Strategies of molecular imprinting-based fluorescence sensors for chemical and biological analysis. *Biosens. Bioelectron.* **2018,** *112*, 54-71.

116.   Sun, C.; Su, R.; Bie, J.; Sun, H.; Qiao, S.; Ma, X.; Sun, R.; Zhang, T., Label-free fluorescent sensor based on aptamer and thiazole orange for the detection of tetracycline. *Dyes and Pigments* **2018,** *149*, 867-875.

117.   Du, X.-w.; Zhang, Y.-x.; She, Y.-x.; Liu, G.-y.; Zhao, F.-n.; Wang, J.; Wang, S.-s.; Jin, F.; Shao, H.; Jin, M.-j.; Zheng, L.-f., Fluorescent competitive assay for melamine using dummy molecularly imprinted polymers as antibody mimics. *J. Integr. Agric.* **2016,** *15*, 1166-1177.

118.   Cheubong, C.; Takano, E.; Kitayama, Y.; Sunayama, H.; Minamoto, K.; Takeuchi, R.; Furutani, S.; Takeuchi, T., Molecularly imprinted polymer nanogel-based fluorescence sensing of pork contamination in halal meat extracts. *Biosens. Bioelectron.* **2021,** *172*, 112775.

119.   Mattsson, L.; Xu, J.; Preininger, C.; Tse Sum Bui, B.; Haupt, K., Competitive fluorescent pseudo-immunoassay exploiting molecularly imprinted polymers for the detection of biogenic amines in fish matrix. *Talanta* **2018,** *181*, 190-196.

120.   René, W.; Lenoble, V.; Chioukh, M.; Branger, C., A turn-on fluorescent ion-imprinted polymer for selective and reliable optosensing of lead in real water samples. *Sens. Actuators B Chem.* **2020,** *319*, 128252.

121.   Ng, S. M.; Narayanaswamy, R., Fluorescence sensor using a molecularly imprinted polymer as a recognition receptor for the detection of aluminium ions in aqueous media. *Anal. Bioanal. Chem.* **2006,** *386*, 1235-1244.

122.   Nsibande, S. A.; Forbes, P. B. C., Development of a quantum dot molecularly imprinted polymer sensor for fluorescence detection of atrazine. *Luminescence* **2019,** *34*, 480-488.

123. Kimani, M.; Pérez-Padilla, V.; Valderrey, V.; Gawlitza, K.; Rurack, K., Red-Emitting Polymerizable Guanidinium Dyes as Fluorescent Probes in Molecularly Imprinted Polymers for Glyphosate Detection. *Chemosensors* **2022,** *10*, 99.

124. Carrasco, S.; Canalejas-Tejero, V.; Navarro-Villoslada, F.; Barrios, C. A.; Moreno-Bondi, M. C., Cross-linkable linear copolymer with double functionality: resist for electron beam nanolithography and molecular imprinting. *J. Mater. Chem. C* **2014,** *2*, 1400.

125. Urraca, J. L.; Barrios, C. A.; Canalejas-Tejero, V.; Orellana, G.; Moreno-Bondi, M. C., Molecular recognition with nanostructures fabricated by photopolymerization within metallic subwavelength apertures. *Nanoscale* **2014,** *6*, 8656-8663.

126. Ton, X.-A.; Acha, V.; Haupt, K.; Tse Sum Bui, B., Direct fluorimetric sensing of UV-excited analytes in biological and environmental samples using molecularly imprinted polymer nanoparticles and fluorescence polarization. *Biosens. Bioelectron.* **2012,** *36*, 22-28.

127. Wu, C.; Cheng, R.; Wang, J.; Wang, Y.; Jing, X.; Chen, R.; Sun, L.; Yan, Y., Fluorescent molecularly imprinted nanoparticles for selective and rapid detection of ciprofloxacin in aquaculture water. *J. Sep. Sci.* **2018,** *41*, 3782-3790.

128. Liang, C.; Wang, H.; He, K.; Chen, C.; Chen, X.; Gong, H.; Cai, C., A virus-MIPs fluorescent sensor based on FRET for highly sensitive detection of JEV. *Talanta* **2016,** *160*, 360-366.

129. Feng, W.; Liang, C.; Gong, H.; Cai, C., Sensitive detection of Japanese encephalitis virus by surface molecularly imprinted technique based on fluorescent method. *New J. Chem.* **2018,** *42*, 3503-3508.

130. Ensafi, A. A.; Zakery, M.; Rezaei, B., An optical sensor with specific binding sites for the detection of thioridazine hydrochloride based on ZnO-QDs coated with molecularly imprinted polymer. *Spectrochim. Acta A Mol. Biomol.* **2019,** *206*, 460-465.

131. Zhang, C.; Cui, H.; Cai, J.; Duan, Y.; Liu, Y., Development of Fluorescence Sensing Material Based on CdSe/ZnS Quantum Dots and Molecularly Imprinted Polymer for the Detection of Carbaryl in Rice and Chinese Cabbage. *J. Agric. Food Chem.* **2015,** *63*, 4966-4972.

132. Jia, M.; Zhang, Z.; Li, J.; Shao, H.; Chen, L.; Yang, X., A molecular imprinting fluorescence sensor based on quantum dots and a mesoporous structure for selective and sensitive detection of 2,4-dichlorophenoxyacetic acid. *Sens. Actuators B Chem.* **2017,** *252*, 934-943.

133. Zhao, Y.; Ma, Y.; Li, H.; Wang, L., Composite QDs@MIP Nanospheres for Specific Recognition and Direct Fluorescent Quantification of Pesticides in Aqueous Media. *Anal. Chem.* **2011,** *84*, 386-395.

134. Jiao, Z.; Li, J.; Mo, L.; Liang, J.; Fan, H., A molecularly imprinted chitosan doped with carbon quantum dots for fluorometric determination of perfluorooctane sulfonate. *Microchim. Acta* **2018,** *185*, 473.

135. Hassanzadeh, J.; Moghadam, B. R.; Sobhani-Nasab, A.; Ahmadi, F.; Rahimi-Nasrabadi, M., Specific fluorometric assay for direct determination of amikacin by molecularly imprinting polymer on high fluorescent g-C3N4 quantum dots. *Spectrochim. Acta A Mol. Biomol.* **2019,** *214*, 451-458.

136.   Zhou, T.; Halder, A.; Sun, Y., Fluorescent Nanosensor Based on Molecularly Imprinted Polymers Coated on Graphene Quantum Dots for Fast Detection of Antibiotics. *Biosensors* **2018,** *8*, 82.

137.   Beyazit, S.; Ambrosini, S.; Marchyk, N.; Palo, E.; Kale, V.; Soukka, T.; Tse Sum Bui, B.; Haupt, K., Versatile Synthetic Strategy for Coating Upconverting Nanoparticles with Polymer Shells through Localized Photopolymerization by Using the Particles as Internal Light Sources. *Angew. Chem. Int. Ed.* **2014,** *53*, 8919-8923.

138.   Guo, T.; Deng, Q.; Fang, G.; Ma, L.; Wang, S., Fluorescence sensor based on molecularly imprinted polymers and core–shell upconversion nanoparticles@metal–organic frameworks for detection of bovine serum albumin. *Spectrochim. Acta A Mol. Biomol.* **2022,** *279*, 121460.

139.   Wu, X.; Zhang, Z.; Li, J.; You, H.; Li, Y.; Chen, L., Molecularly imprinted polymers-coated gold nanoclusters for fluorescent detection of bisphenol A. *Sens. Actuators B Chem.* **2015,** *211*, 507-514.

140.   Deng, C.; Zhong, Y.; He, Y.; Ge, Y.; Song, G., Selective determination of trace bisphenol a using molecularly imprinted silica nanoparticles containing quenchable fluorescent silver nanoclusters. *Microchim. Acta* **2015,** *183*, 431-439.

141.   Kim, D.; Lee, B., Fluorescence detection of bisphenol A in aqueous solution using magnetite core-shell material with gold nanoclusters prepared by molecular imprinting technique. *Korean J. Chem. Eng.* **2019,** *36*, 1509-1517.

142.   Anirban, S.; Dutta, A., Structural and ionic transport mechanism of rare earth doped cerium oxide nanomaterials: Effect of ionic radius of dopant cations. *Solid State Ion.* **2017,** *309*, 137-145.

143.   Zheng, X.; Pan, J.; Gao, L.; Wei, X.; Dai, J.; Shi, W.; Yan, Y., Silica nanoparticles doped with a europium(III) complex and coated with an ion imprinted polymer for rapid determination of copper(II). *Microchim. Acta* **2015,** *182*, 753-761.

144.   Tang, Y.; Gao, Z.; Wang, S.; Gao, X.; Gao, J.; Ma, Y.; Liu, X.; Li, J., Upconversion particles coated with molecularly imprinted polymers as fluorescence probe for detection of clenbuterol. *Biosens. Bioelectron.* **2015,** *71*, 44-50.

145.   Tang, Y.; Liu, H.; Gao, J.; Liu, X.; Gao, X.; Lu, X.; Fang, G.; Wang, J.; Li, J., Upconversion particle@Fe3O4@molecularly imprinted polymer with controllable shell thickness as high-performance fluorescent probe for sensing quinolones. *Talanta* **2018,** *181*, 95-103.

146.   Pesavento, M.; Zeni, L.; De Maria, L.; Alberti, G.; Cennamo, N., SPR-Optical Fiber-Molecularly Imprinted Polymer Sensor for the Detection of Furfural in Wine. *Biosensors* **2021,** *11*, 72.

147.   Xu, X.-Y.; Tian, X.-G.; Cai, L.-G.; Xu, Z.-L.; Lei, H.-T.; Wang, H.; Sun, Y.-M., Molecularly imprinted polymer based surface plasmon resonance sensors for detection of Sudan dyes. *Anal. Methods* **2014,** *6*, 3751-3757.

148.   Cakir, O.; Bakhshpour, M.; Yilmaz, F.; Baysal, Z., Novel QCM and SPR sensors based on molecular imprinting for highly sensitive and selective detection of 2,4-dichlorophenoxyacetic acid in apple samples. *Mater. Sci. Eng. C* **2019,** *102*, 483-491.

149.   Jiang, S.; Peng, Y.; Ning, B.; Bai, J.; Liu, Y.; Zhang, N.; Gao, Z., Surface plasmon resonance sensor based on molecularly imprinted polymer film for detection of histamine. *Sens. Actuators B Chem.* **2015,** *221*, 15-21.

150. Nguyen, H.; Park, J.; Kang, S.; Kim, M., Surface Plasmon Resonance: A Versatile Technique for Biosensor Applications. *Sensors* **2015,** *15*, 10481-10510.

151. Ayerdurai, V.; Lach, P.; Lis-Cieplak, A.; Cieplak, M.; Kutner, W.; Sharma, P. S., An advantageous application of molecularly imprinted polymers in food processing and quality control. *Crit. Rev. Food Sci. Nutr.* **2022**, xxx-xxx.

152. Akgönüllü, S.; Yavuz, H.; Denizli, A., Development of Gold Nanoparticles Decorated Molecularly Imprinted–Based Plasmonic Sensor for the Detection of Aflatoxin M1 in Milk Samples. *Chemosensors* **2021,** *9*, 363.

153. Yao, T.; Gu, X.; Li, T.; Li, J.; Li, J.; Zhao, Z.; Wang, J.; Qin, Y.; She, Y., Enhancement of surface plasmon resonance signals using a MIP/GNPs/rGO nano-hybrid film for the rapid detection of ractopamine. *Biosens. Bioelectron.* **2016,** *75*, 96-100.

154. Altintas, Z., Surface plasmon resonance based sensor for the detection of glycopeptide antibiotics in milk using rationally designed nanoMIPs. *Sci. Rep.* **2018,** *8*, 11222.

155. Yao, G. H.; Liang, R. P.; Huang, C. F.; Wang, Y.; Qiu, J. D., Surface plasmon resonance sensor based on magnetic molecularly imprinted polymers amplification for pesticide recognition. *Anal. Chem.* **2013,** *85*, 11944-11951.

156. Kara, M.; Uzun, L.; Kolayli, S.; Denizli, A., Combining molecular imprinted nanoparticles with surface plasmon resonance nanosensor for chloramphenicol detection in honey. *J. Appl. Polym. Sci.* **2013,** *129*, 2273-2279.

157. Çimen, D.; Bereli, N.; Denizli, A., Patulin Imprinted Nanoparticles Decorated Surface Plasmon Resonance Chips for Patulin Detection. *Photonic Sensors* **2022,** *12*, 117-129.

158. Li, W.; Zheng, Y.; Zhang, T.; Wu, S.; Zhang, J.; Fang, J., A Surface Plasmon Resonance-Based Optical Fiber Probe Fabricated with Electropolymerized Molecular Imprinting Film for Melamine Detection. *Sensors* **2018,** *18*, 828.

159. Cennamo, N.; D'Agostino, G.; Porto, G.; Biasiolo, A.; Perri, C.; Arcadio, F.; Zeni, L., A Molecularly Imprinted Polymer on a Plasmonic Plastic Optical Fiber to Detect Perfluorinated Compounds in Water. *Sensors* **2018,** *18*, 1836.

160. Li, H.; Jiang, J.; Wang, Z.; Wang, X.; Liu, X.; Yan, Y.; Li, C., A high performance and highly-controllable core-shell imprinted sensor based on the surface-enhanced Raman scattering for detection of R6G in water. *J. Colloid Interface Sci.* **2017,** *501*, 86-93.

161. Fang, G.; Fan, C.; Liu, H.; Pan, M.; Zhu, H.; Wang, S., A novel molecularly imprinted polymer on CdSe/ZnS quantum dots for highly selective optosensing of mycotoxin zearalenone in cereal samples. *RSC Adv.* **2014,** *4*, 2764-2771.

162. Zhang, Y.; Huang, Y.; Kang, Y.; Miao, J.; Lai, K., Selective recognition and determination of malachite green in fish muscles via surface-enhanced Raman scattering coupled with molecularly imprinted polymers. *Food Control* **2021,** *130*, 108367.

163. Ma, J.; Yan, M.; Feng, G.; Ying, Y.; Chen, G.; Shao, Y.; She, Y.; Wang, M.; Sun, J.; Zheng, L.; Wang, J.; Abd El-Aty, A. M., An overview on molecular imprinted polymers combined with surface-enhanced Raman spectroscopy chemical sensors toward analytical applications. *Talanta* **2021,** *225*, 122031.

164.   Guo, X.; Li, J.; Arabi, M.; Wang, X.; Wang, Y.; Chen, L., Molecular-Imprinting-Based Surface-Enhanced Raman Scattering Sensors. *ACS Sens.* **2020,** *5*, 601-619.

165.   Zhao, B.; Feng, S.; Hu, Y.; Wang, S.; Lu, X., Rapid determination of atrazine in apple juice using molecularly imprinted polymers coupled with gold nanoparticles-colorimetric/SERS dual chemosensor. *Food Chem.* **2019,** *276*, 366-375.

166.   Hua, M. Z.; Feng, S.; Wang, S.; Lu, X., Rapid detection and quantification of 2,4-dichlorophenoxyacetic acid in milk using molecularly imprinted polymers–surface-enhanced Raman spectroscopy. *Food Chem.* **2018,** *258*, 254-259.

167.   Gao, F.; Hu, Y.; Chen, D.; Li-Chan, E. C. Y.; Grant, E.; Lu, X., Determination of Sudan I in paprika powder by molecularly imprinted polymers–thin layer chromatography–surface enhanced Raman spectroscopic biosensor. *Talanta* **2015,** *143*, 344-352.

168.   Wang, J.; Li, J.; Zeng, C.; Qu, Q.; Wang, M.; Qi, W.; Su, R.; He, Z., Sandwich-Like Sensor for the Highly Specific and Reproducible Detection of Rhodamine 6G on a Surface-Enhanced Raman Scattering Platform. *ACS Appl. Mater. Interfaces.* **2020,** *12*, 4699-4706.

169.   Hu, Y.; Lu, X., Rapid Detection of Melamine in Tap Water and Milk Using Conjugated "One-Step" Molecularly Imprinted Polymers-Surface Enhanced Raman Spectroscopic Sensor. *J. Food Sci.* **2016,** *81*, N1272-N1280.

170.   Piletsky, S. A.; Piletska, E. V.; Bossi, A.; Karim, K.; Lowe, P.; Turner, A. P. F., Substitution of antibodies and receptors with molecularly imprinted polymers in enzyme-linked and fluorescent assays. *Biosens. Bioelectron.* **2001,** *16*, 701-707.

171.   Xu, Z. X.; Gao, H. J.; Zhang, L. M.; Chen, X. Q.; Qiao, X. G., The Biomimetic Immunoassay Based on Molecularly Imprinted Polymer: A Comprehensive Review of Recent Progress and Future Prospects. *J. Food Sci.* **2011,** *76*, R69-R75.

172.   Munawar, H.; Smolinska-Kempisty, K.; Cruz, A. G.; Canfarotta, F.; Piletska, E.; Karim, K.; Piletsky, S. A., Molecularly imprinted polymer nanoparticle-based assay (MINA): application for fumonisin B1 determination. *Analyst* **2018,** *143*, 3481-3488.

173.   Zhao, X.; He, Y.; Wang, Y.; Wang, S.; Wang, J., Hollow molecularly imprinted polymer based quartz crystal microbalance sensor for rapid detection of methimazole in food samples. *Food Chem.* **2020,** *309*, 125787.

174.   Pan, M.; Gu, Y.; Zhang, M.; Wang, J.; Yun, Y.; Wang, S., Reproducible Molecularly Imprinted QCM Sensor for Accurate, Stable, and Sensitive Detection of Enrofloxacin Residue in Animal-Derived Foods. *Food Anal. Methods* **2018,** *11*, 495-503.

175.   Pietrzyk, A.; Kutner, W.; Chitta, R.; Zandler, M. E.; D'Souza, F.; Sannicolò, F.; Mussini, P. R., Melamine Acoustic Chemosensor Based on Molecularly Imprinted Polymer Film. *Anal. Chem.* **2009,** *81*, 10061-10070.

176.   Liu, J.; Cai, X.; Liu, J.; Liang, D.; Chen, K.; Tang, S.; Xu, B., Study on the Preparation of Estrone Molecularly Imprinted Polymers and Their Application in a Quartz Crystal Microbalance Sensor via a Computer-Assisted Design. *Int. J. Mol. Sci.* **2022,** *23*, 5758.

177.   Lin, X. H.; Aik, S. X. L.; Angkasa, J.; Le, Q.; Chooi, K. S.; Li, S. F. Y., Selective and sensitive sensors based on molecularly imprinted poly(vinylidene

fluoride) for determination of pesticides and chemical threat agent simulants. *Sens. Actuators B Chem.* **2018,** *258*, 228-237.

178.   Fang, G.; Yang, Y.; Zhu, H.; Qi, Y.; Liu, J.; Liu, H.; Wang, S., Development and application of molecularly imprinted quartz crystal microbalance sensor for rapid detection of metolcarb in foods. *Sens. Actuators B Chem.* **2017,** *251*, 720-728.

179.   Ballantine Jr, D.; White, R. M.; Martin, S. J.; Ricco, A. J.; Zellers, E.; Frye, G.; Wohltjen, H., *Acoustic wave sensors: theory, design and physico-chemical applications*. Elsevier: 1996.

180.   Ayankojo, A. G.; Reut, J.; Nguyen, V. B. C.; Boroznjak, R.; Syritski, V., Advances in Detection of Antibiotic Pollutants in Aqueous Media Using Molecular Imprinting Technique— A Review. *Biosensors* **2022,** *12*, 441.

181.   Mazouz, Z.; Rahali, S.; Fourati, N.; Zerrouki, C.; Aloui, N.; Seydou, M.; Yaakoubi, N.; Chehimi, M. M.; Othmane, A.; Kalfat, R., Highly Selective Polypyrrole MIP-Based Gravimetric and Electrochemical Sensors for Picomolar Detection of Glyphosate. *Sensors* **2017,** *17*, 2586.

182.   Ayankojo, A. G.; Tretjakov, A.; Reut, J.; Boroznjak, R.; Öpik, A.; Rappich, J.; Furchner, A.; Hinrichs, K.; Syritski, V., Molecularly Imprinted Polymer Integrated with a Surface Acoustic Wave Technique for Detection of Sulfamethizole. *Anal. Chem.* **2016,** *88*, 1476-1484.

183.   Iskierko, Z.; Noworyta, K.; Sharma, P. S., Molecular recognition by synthetic receptors: Application in field-effect transistor based chemosensing. *Biosens. Bioelectron.* **2018,** *109*, 50-62.

184.   Iskierko, Z.; Sharma, P. S.; Noworyta, K. R.; Borowicz, P.; Cieplak, M.; Kutner, W.; Bossi, A. M., Selective PQQPFPQQ Gluten Epitope Chemical Sensor with a Molecularly Imprinted Polymer Recognition Unit and an Extended-Gate Field-Effect Transistor Transduction Unit. *Anal. Chem.* **2019,** *91*, 4537-4543.

185.   Iskierko, Z.; Sharma, P. S.; Prochowicz, D.; Fronc, K.; D'Souza, F.; Toczydłowska, D.; Stefaniak, F.; Noworyta, K., Molecularly Imprinted Polymer (MIP) Film with Improved Surface Area Developed by Using Metal–Organic Framework (MOF) for Sensitive Lipocalin (NGAL) Determination. *ACS Appl. Mater. Interfaces* **2016,** *8*, 19860-19865.

186.   van Grinsven, B.; Eersels, K.; Peeters, M.; Losada-Pérez, P.; Vandenryt, T.; Cleij, T. J.; Wagner, P., The Heat-Transfer Method: A Versatile Low-Cost, Label-Free, Fast, and User-Friendly Readout Platform for Biosensor Applications. *ACS Appl. Mater. Interfaces* **2014,** *6*, 13309-13318.

187.   van Grinsven, B.; Betlem, K.; Cleij, T. J.; Banks, C. E.; Peeters, M., Evaluating the potential of thermal read-out techniques combined with molecularly imprinted polymers for the sensing of low-weight organic molecules. *J. Mol. Recognit.* **2017,** *30*, e2563.

188.   Athikomrattanakul, U.; Gajovic-Eichelmann, N.; Scheller, F. W., Thermometric Sensing of Nitrofurantoin by Noncovalently Imprinted Polymers Containing Two Complementary Functional Monomers. *Anal. Chem.* **2011,** *83*, 7704-7711.

189.   Cornelis, P.; Givanoudi, S.; Yongabi, D.; Iken, H.; Duwé, S.; Deschaume, O.; Robbens, J.; Dedecker, P.; Bartic, C.; Wübbenhorst, M.; Schöning, M. J.; Heyndrickx, M.; Wagner, P., Sensitive and specific detection of E. coli using biomimetic receptors in combination with a modified heat-transfer method. *Biosens. Bioelectron.* **2019,** *136*, 97-105.

225

190.   Arreguin-Campos, R.; Frigoli, M.; Caldara, M.; Crapnell, R. D.; Ferrari, A. G.-M.; Banks, C. E.; Cleij, T. J.; Diliën, H.; Eersels, K.; van Grinsven, B., Functionalized screen-printed electrodes for the thermal detection of Escherichia coli in dairy products. *Food Chem.* **2023,** *404*, 134653.

191.   Elfadil, D.; Lamaoui, A.; Pelle, F. D.; Compagnone, D., Molecularly Imprinted Polymers Combined with Electrochemical Sensors for Food Contaminants Analysis. *Molecules (Basel, Switzerland)* **2021,** *26*, 4607.

192.   Hassan, A. H. A.; Sappia, L.; Moura, S. L.; Ali, F. H. M.; Moselhy, W. A.; Sotomayor, M. d. P. T.; Pividori, M. I., Biomimetic magnetic sensor for electrochemical determination of scombrotoxin in fish. *Talanta* **2019,** *194*, 997-1004.

193.   Akhoundian, M.; Rüter, A.; Shinde, S., Ultratrace Detection of Histamine Using a Molecularly-Imprinted Polymer-Based Voltammetric Sensor. *Sensors* **2017,** *17*, 645.

194.   Li, Y.; Liu, Y.; Yang, Y.; Yu, F.; Liu, J.; Song, H.; Liu, J.; Tang, H.; Ye, B.-C.; Sun, Z., Novel Electrochemical Sensing Platform Based on a Molecularly Imprinted Polymer Decorated 3D Nanoporous Nickel Skeleton for Ultrasensitive and Selective Determination of Metronidazole. *ACS Appl. Mater. Interfaces* **2015,** *7*, 15474-15480.

195.   Deng, P.; Xu, Z.; Kuang, Y., Electrochemical determination of bisphenol A in plastic bottled drinking water and canned beverages using a molecularly imprinted chitosan–graphene composite film modified electrode. *Food Chem.* **2014,** *157*, 490-497.

196.   Qin, C.; Guo, W.; Liu, Y.; Liu, Z.; Qiu, J.; Peng, J., A Novel Electrochemical Sensor Based on Graphene Oxide Decorated with Silver Nanoparticles–Molecular Imprinted Polymers for Determination of Sunset Yellow in Soft Drinks. *Food Anal. Methods* **2017,** *10*, 2293-2301.

197.   Motaharian, A.; Motaharian, F.; Abnous, K.; Hosseini, M. R. M.; Hassanzadeh-Khayyat, M., Molecularly imprinted polymer nanoparticles-based electrochemical sensor for determination of diazinon pesticide in well water and apple fruit samples. *Anal. Bioanal. Chem.* **2016,** *408*, 6769-6779.

198.   Li, N.; Xie, D.; Zhao, H.; Yu, C.; Li, Z.; Li, F.; Cao, Q., A novel molecularly imprinted electrode modified with carbon nanohorn and polydopamine for highly sensitive determination of erythrocin in food. *Microchem. J.* **2022,** *181*, 107728.

199.   Zhang, M.; Zhao, H. T.; Xie, T. J.; Yang, X.; Dong, A. J.; Zhang, H.; Wang, J.; Wang, Z. Y., Molecularly imprinted polymer on graphene surface for selective and sensitive electrochemical sensing imidacloprid. *Sens. Actuators B Chem.* **2017,** *252*, 991-1002.

200.   Yang, L.; Zhao, F.; Zeng, B., Electrochemical determination of eugenol using a three-dimensional molecularly imprinted poly (p-aminothiophenol-co-p-aminobenzoic acids) film modified electrode. *Electrochim. Acta* **2016,** *210*, 293-300.

201.   Do, M. H.; Florea, A.; Farre, C.; Bonhomme, A.; Bessueille, F.; Vocanson, F.; Tran-Thi, N.-T.; Jaffrezic-Renault, N., Molecularly imprinted polymer-based electrochemical sensor for the sensitive detection of glyphosate herbicide. *Int. J. Environ. Anal. Chem.* **2015,** *95*, 1489-1501.

202.   Bougrini, M.; Florea, A.; Cristea, C.; Sandulescu, R.; Vocanson, F.; Errachid, A.; Bouchikhi, B.; El Bari, N.; Jaffrezic-Renault, N., Development of a novel sensitive molecularly imprinted polymer sensor based on electropolymerization of a microporous-metal-organic framework for tetracycline detection in honey. *Food Chem.* **2016,** *59*, 424-429.

203. Liu, B.; Tang, D.; Zhang, B.; Que, X.; Yang, H.; Chen, G., Au(III)-promoted magnetic molecularly imprinted polymer nanospheres for electrochemical determination of streptomycin residues in food. *Biosens. Bioelectron.* **2013,** *41*, 551-556.

204. Alizadeh, T.; Ganjali, M. R.; Zare, M.; Norouzi, P., Selective determination of chloramphenicol at trace level in milk samples by the electrode modified with molecularly imprinted polymer. *Food Chem.* **2012,** *130*, 1108-1114.

205. Hassan, A. H. A.; Moura, S. L.; Ali, F. H. M.; Moselhy, W. A.; Taboada Sotomayor, M. d. P.; Pividori, M. I., Electrochemical sensing of methyl parathion on magnetic molecularly imprinted polymer. *Biosens. Bioelectron.* **2018,** *118*, 181-187.

206. Wei, X.; Xu, X.; Qi, W.; Wu, Y.; Wang, L., Molecularly imprinted polymer/graphene oxide modified glassy carbon electrode for selective detection of sulfanilamide. *Prog. Nat. Sci.* **2017,** *27*, 374-379.

207. Yang, Y.; Fang, G.; Wang, X.; Pan, M.; Qian, H.; Liu, H.; Wang, S., Sensitive and selective electrochemical determination of quinoxaline-2-carboxylic acid based on bilayer of novel poly(pyrrole) functional composite using one-step electro-polymerization and molecularly imprinted poly(o-phenylenediamine). *Anal. Chim. Acta* **2014,** *806*, 136-143.

208. Yang, G.; Zhao, F., Molecularly imprinted polymer grown on multiwalled carbon nanotube surface for the sensitive electrochemical determination of amoxicillin. *Electrochim. Acta* **2015,** *174*, 33-40.

209. Wei, S.; Liu, Y.; Hua, T.; Liu, L.; Wang, H., Molecularly imprinted electrochemical sensor for the determination of ampicillin based on a gold nanoparticle and multiwalled carbon nanotube-coated pt electrode. *J. Appl. Polym. Sci.* **2014,** *131*, 40613.

210. Surya, S. G.; Khatoon, S.; Ait Lahcen, A.; Nguyen, A. T. H.; Dzantiev, B. B.; Tarannum, N.; Salama, K. N., A chitosan gold nanoparticles molecularly imprinted polymer based ciprofloxacin sensor. *RSC Adv.* **2020,** *10*, 12823-12832.

211. Jafari, S.; Dehghani, M.; Nasirizadeh, N.; Baghersad, M. H.; Azimzadeh, M., Label-free electrochemical detection of Cloxacillin antibiotic in milk samples based on molecularly imprinted polymer and graphene oxide-gold nanocomposite. *Measurement* **2019,** *145*, 22-29.

212. Song, B.; Zhou, Y.; Jin, H.; Jing, T.; Zhou, T.; Hao, Q.; Zhou, Y.; Mei, S.; Lee, Y.-I., Selective and sensitive determination of erythromycin in honey and dairy products by molecularly imprinted polymers based electrochemical sensor. *Microchem. J.* **2014,** *116*, 183-190.

213. Chen, D.; Deng, J.; Liang, J.; Xie, J.; Hu, C.; Huang, K., A core–shell molecularly imprinted polymer grafted onto a magnetic glassy carbon electrode as a selective sensor for the determination of metronidazole. *Sens. Actuators B Chem.* **2013,** *183*, 594-600.

214. Feier, B.; Blidar, A.; Pusta, A.; Carciuc, P.; Cristea, C., Electrochemical Sensor Based on Molecularly Imprinted Polymer for the Detection of Cefalexin. *Biosensors* **2019,** *9*, 31.

215. Pacheco, J. G.; Castro, M.; Machado, S.; Barroso, M. F.; Nouws, H. P. A.; Delerue-Matos, C., Molecularly imprinted electrochemical sensor for ochratoxin A detection in food samples. *Sens. Actuators B Chem.* **2015,** *215*, 107-112.

216.   Gao, X.; Cao, W.; Chen, M.; Xiong, H.; Zhang, X.; Wang, S., A High Sensitivity Electrochemical Sensor Based on Fe3+-Ion Molecularly Imprinted Film for the Detection of T-2 Toxin. *Electroanalysis* **2014,** *26*, 2739-2746.

217.   Munawar, H.; Garcia-Cruz, A.; Majewska, M.; Karim, K.; Kutner, W.; Piletsky, S. A., Electrochemical determination of fumonisin B1 using a chemosensor with a recognition unit comprising molecularly imprinted polymer nanoparticles. *Sens. Actuators B Chem.* **2020,** *321*, 128552.

218.   Singh, A. K.; Lakshmi, G. B. V. S.; Fernandes, M.; Sarkar, T.; Gulati, P.; Singh, R. P.; Solanki, P. R., A simple detection platform based on molecularly imprinted polymer for AFB1 and FuB1 mycotoxins. *Microchem. J.* **2021,** *171*, 106730.

219.   Wu, W.; Yang, L.; Zhao, F.; Zeng, B., A vanillin electrochemical sensor based on molecularly imprinted poly(1-vinyl-3-octylimidazole hexafluoride phosphorus) −multi-walled carbon nanotubes@polydopamine–carboxyl single-walled carbon nanotubes composite. *Sens. Actuators B Chem.* **2017,** *239*, 481-487.

220.   Shi, X.; Lu, J.; Yin, H.; Qiao, X.; Xu, Z., A Biomimetic Sensor with Signal Enhancement of Ferriferrous Oxide-Reduced Graphene Oxide Nanocomposites for Ultratrace Levels Quantification of Methamidophos or Omethoate in Vegetables. *Food Anal. Methods* **2017,** *10*, 910-920.

221.   Li, S.; Li, J.; Luo, J.; Xu, Z.; Ma, X., A microfluidic chip containing a molecularly imprinted polymer and a DNA aptamer for voltammetric determination of carbofuran. *Microchim. Acta* **2018,** *185*, 295.

222.   Wang, H.; Yao, S.; Liu, Y.; Wei, S.; Su, J.; Hu, G., Molecularly imprinted electrochemical sensor based on Au nanoparticles in carboxylated multi-walled carbon nanotubes for sensitive determination of olaquindox in food and feedstuffs. *Biosens. Bioelectron.* **2017,** *87*, 417-421.

223.   Qi, P.; Wang, J.; Wang, Z.; Wang, X.; Wang, X.; Xu, X.; Xu, H.; Di, S.; Zhang, H.; Wang, Q.; Wang, X., Construction of a probe-immobilized molecularly imprinted electrochemical sensor with dual signal amplification of thiol graphene and gold nanoparticles for selective detection of tebuconazole in vegetable and fruit samples. *Electrochim. Acta* **2018,** *274*, 406-414.

224.   Yang, G.; Zhao, F., Electrochemical sensor for dimetridazole based on novel gold nanoparticles@molecularly imprinted polymer. *Sens. Actuators B Chem.* **2015,** *220*, 1017-1022.

225.   Xu, G.; Chi, Y.; Li, L.; Liu, S.; Kan, X., Imprinted propyl gallate electrochemical sensor based on graphene/single walled carbon nanotubes/sol–gel film. *Food Chem.* **2015,** *177*, 37-42.

226.   dos Santos Moretti, E.; de Oliveira, F. M.; Scheel, G. L.; DalÍAntônia, L. H.; Borsato, D.; Kubota, L. T.; Segatelli, M. G.; Tarley, C. R. T., Synthesis of Surface Molecularly Imprinted Poly(methacrylic acid-hemin) on Carbon Nanotubes for the Voltammetric Simultaneous Determination of Antioxidants from Lipid Matrices and Biodiesel. *Electrochim. Acta* **2016,** *212*, 322-332.

227.   Li, J.; Wang, X.; Duan, H.; Wang, Y.; Bu, Y.; Luo, C., Based on magnetic graphene oxide highly sensitive and selective imprinted sensor for determination of sunset yellow. *Talanta* **2016,** *147*, 169-176.

228.   Somnet, K.; Soravech, P.; Karuwan, C.; Tuantranont, A.; Amatatongchai, M., A compact N-nitrosodiphenylamine imprinted sensor based on a Pd nanoparticles-MIP

microsphere modified screen-printed graphene electrode. *J. Electroanal. Chem.* **2022,** *914*, 116302.

229.   Lach, P.; Sharma, P. S.; Golebiewska, K.; Cieplak, M.; D'Souza, F.; Kutner, W., Molecularly Imprinted Polymer Chemosensor for Selective Determination of an N-Nitroso-l-proline Food Toxin. *Chem. Eur. J.* **2017,** *23*, 1942-1949.

230.   Dadkhah, S.; Ziaei, E.; Mehdinia, A.; Baradaran Kayyal, T.; Jabbari, A., A glassy carbon electrode modified with amino-functionalized graphene oxide and molecularly imprinted polymer for electrochemical sensing of bisphenol A. *Microchim. Acta* **2016,** *183*, 1933-1941.

231.   Karthika, P.; Shanmuganathan, S.; Viswanathan, S.; Delerue-Matos, C., Molecularly imprinted polymer-based electrochemical sensor for the determination of endocrine disruptor bisphenol-A in bovine milk. *Food Chem.* **2021,** *363*, 130287.

232.   Sharma, P. S.; Garcia-Cruz, A.; Cieplak, M.; Noworyta, K. R.; Kutner, W., 'Gate effect' in molecularly imprinted polymers: the current state of understanding. *Curr. Opin. Electrochem.* **2019,** *16*, 50-56.

233.   Wang, J., Electrochemical detection for microscale analytical systems: a review. *Talanta* **2002,** *56*, 223-231.

234.   Rojas, D.; Della Pelle, F.; Del Carlo, M.; Fratini, E.; Escarpa, A.; Compagnone, D., Nanohybrid carbon black-molybdenum disulfide transducers for preconcentration-free voltammetric detection of the olive oil o-diphenols hydroxytyrosol and oleuropein. *Microchim. Acta* **2019,** *186*, 363.

235.   Turco, A.; Corvaglia, S.; Mazzotta, E.; Pompa, P. P.; Malitesta, C., Preparation and characterization of molecularly imprinted mussel inspired film as antifouling and selective layer for electrochemical detection of sulfamethoxazole. *Sens. Actuators B Chem.* **2018,** *255*, 3374-3383.

236.   Amatatongchai, M.; Sroysee, W.; Jarujamrus, P.; Nacapricha, D.; Lieberzeit, P. A., Selective amperometric flow-injection analysis of carbofuran using a molecularly-imprinted polymer and gold-coated-magnetite modified carbon nanotube-paste electrode. *Talanta* **2018,** *179*, 700-709.

237.   Lian, W.; Liu, S.; Yu, J.; Xing, X.; Li, J.; Cui, M.; Huang, J., Electrochemical sensor based on gold nanoparticles fabricated molecularly imprinted polymer film at chitosan–platinum nanoparticles/graphene–gold nanoparticles double nanocomposites modified electrode for detection of erythromycin. *Biosens. Bioelectron.* **2012,** *38*, 163-169.

238.   Cui, M.; Liu, S.; Lian, W.; Li, J.; Xu, W.; Huang, J., A molecularly-imprinted electrochemical sensor based on a graphene–Prussian blue composite-modified glassy carbon electrode for the detection of butylated hydroxyanisole in foodstuffs. *Analyst* **2013,** *138*, 5949-5955.

239.   Lian, W.; Liu, S.; Yu, J.; Li, J.; Cui, M.; Xu, W.; Huang, J., Electrochemical sensor using neomycin-imprinted film as recognition element based on chitosan-silver nanoparticles/graphene-multiwalled carbon nanotubes composites modified electrode. *Biosens. Bioelectron.* **2013,** *44*, 70-76.

240.   Zdrachek, E.; Bakker, E., Potentiometric Sensing. *Anal. Chem.* **2019,** *91*, 2-26.

241.   Bobacka, J.; Ivaska, A.; Lewenstam, A., Potentiometric Ion Sensors. *Chem. Rev.* **2008,** *108*, 329-351.

242.   Liang, R.; Zhang, R.; Qin, W., Potentiometric sensor based on molecularly imprinted polymer for determination of melamine in milk. *Sens. Actuators B Chem.* **2009,** *141*, 544-550.

243.   Kupis-Rozmysłowicz, J.; Wagner, M.; Bobacka, J.; Lewenstam, A.; Migdalski, J., Biomimetic membranes based on molecularly imprinted conducting polymers as a sensing element for determination of taurine. *Electrochim. Acta* **2016,** *188*, 537-544.

244.   Branger, C.; Meouche, W.; Margaillan, A., Recent advances on ion-imprinted polymers. *React. Funct. Polym.* **2013,** *73*, 859-875.

245.   Shirzadmehr, A.; Afkhami, A.; Madrakian, T., A new nano-composite potentiometric sensor containing an Hg2+-ion imprinted polymer for the trace determination of mercury ions in different matrices. *J. Mol. Liq.* **2015,** *204*, 227-235.

246.   Abdel-Ghany, M. F.; Hussein, L. A.; El Azab, N. F., Novel potentiometric sensors for the determination of the dinotefuran insecticide residue levels in cucumber and soil samples. *Talanta* **2017,** *164*, 518-528.

247.   D'Agostino, G.; Alberti, G.; Biesuz, R.; Pesavento, M., Potentiometric sensor for atrazine based on a molecular imprinted membrane. *Biosens. Bioelectron.* **2006,** *22*, 145-152.

248.   Alberti, G.; Zanoni, C.; Spina, S.; Magnaghi, L. R.; Biesuz, R., MIP-Based Screen-Printed Potentiometric Cell for Atrazine Sensing. *Chemosensors* **2022,** *10*, 339.

249.   Abdalla, N. S.; Amr, A. E.-G. E.; El-Tantawy, A. S. M.; Al-Omar, M. A.; Kamel, A. H.; Khalifa, N. M., Tailor-Made Specific Recognition of Cyromazine Pesticide Integrated in a Potentiometric Strip Cell for Environmental and Food Analysis. *Polymers* **2019,** *11*, 1526.

250.   Anirudhan, T. S.; Alexander, S., Design and fabrication of molecularly imprinted polymer-based potentiometric sensor from the surface modified multiwalled carbon nanotube for the determination of lindane (γ-hexachlorocyclohexane), an organochlorine pesticide. *Biosens. Bioelectron.* **2015,** *64*, 586-593.

251.   Liang, R.-N.; Song, D.-A.; Zhang, R.-M.; Qin, W., Potentiometric Sensing of Neutral Species Based on a Uniform-Sized Molecularly Imprinted Polymer as a Receptor. *Angew. Chem. Int. Ed.* **2010,** *49*, 2556-2559.

252.   Jaishankar, M.; Tseten, T.; Anbalagan, N.; Mathew, B. B.; Beeregowda, K. N., Toxicity, mechanism and health effects of some heavy metals. *Interdisciplinary toxicology* **2014,** *7*, 60-72.

253.   Fu, J.; Chen, L.; Li, J.; Zhang, Z., Current status and challenges of ion imprinting. *J. Mater. Chem. A* **2015,** *3*, 13598-13627.

254.   Wang, J.; Liang, R.; Qin, W., Molecularly imprinted polymer-based potentiometric sensors. *Trends Anal. Chem.* **2020,** *130*, 115980.

255.   Liang, R.; Wang, Q.; Qin, W., Highly sensitive potentiometric sensor for detection of mercury in Cl−-rich samples. *Sens. Actuators B Chem.* **2015,** *208*, 267-272.

256.   Moro, G.; Cristofori, D.; Bottari, F.; Cattaruzza, E.; De Wael, K.; Moretto, L. M., Redesigning an Electrochemical MIP Sensor for PFOS: Practicalities and Pitfalls. *Sensors* **2019,** *19*, 4433.

257.   Shamsipur, M.; Moradi, N.; Pashabadi, A., Coupled electrochemical-chemical procedure used in construction of molecularly imprinted polymer-based electrode: a highly sensitive impedimetric melamine sensor. *J. Solid State Electrochem.* **2018,** *22*, 169-180.

258.   Lach, P.; Cieplak, M.; Majewska, M.; Noworyta, K. R.; Sharma, P. S.; Kutner, W., "Gate Effect" in p-Synephrine Electrochemical Sensing with a Molecularly Imprinted Polymer and Redox Probes. *Anal. Chem.* **2019,** *91*, 7546-7553.

259.   Kutner, W.; Garcia-Cruz, A.; Lach, P.; Sharma, P. S.; Pieta, P.; Golebiewska, K. K.; Cieplak, M.; Noworyta, K. R.; Schulz, E.; D'Souza, F., Conducting Molecularly Imprinted Polymer (MIP) Chemical Sensors for Toxic N-Nitrosamines Selective Determination in Heat Processed Food of Animal Origin. *ECS Meeting Abstracts* **2017,** *MA2017-01*, 1919-1919.

260.   Ayerdurai, V.; Cieplak, M.; Noworyta, K. R.; Gajda, M.; Ziminska, A.; Sosnowska, M.; Piechowska, J.; Borowicz, P.; Lisowski, W.; Shao, S.; D'Souza, F.; Kutner, W., Electrochemical sensor for selective tyramine determination, amplified by a molecularly imprinted polymer film. *Bioelectrochemistry* **2021,** *138*, 107695.

261.   Motia, S.; Bouchikhi, B.; El Bari, N., An electrochemical molecularly imprinted sensor based on chitosan capped with gold nanoparticles and its application for highly sensitive butylated hydroxyanisole analysis in foodstuff products. *Talanta* **2021,** *223*, 121689.

262.   Radi, A. E.; Oreba, R.; Elshafey, R., Molecularly Imprinted Electrochemical Sensor for the Detection of Organophosphorus Pesticide Profenofos. *Electroanalysis* **2021,** *33*, 1945-1951.

263.   Apodaca, D. C.; Pernites, R. B.; Ponnapati, R.; Del Mundo, F. R.; Advincula, R. C., Electropolymerized Molecularly Imprinted Polymer Film: EIS Sensing of Bisphenol A. *Macromol.* **2011,** *44*, 6669-6682.

264.   Bolat, G.; Yaman, Y. T.; Abaci, S., Molecularly imprinted electrochemical impedance sensor for sensitive dibutyl phthalate (DBP) determination. *Sens. Actuators B Chem.* **2019,** *299*, 127000.

265.   Nagabooshanam, S.; Roy, S.; Deshmukh, S.; Wadhwa, S.; Sulania, I.; Mathur, A.; Krishnamurthy, S.; Bharadwaj, L. M.; Roy, S. S., Microfluidic Affinity Sensor Based on a Molecularly Imprinted Polymer for Ultrasensitive Detection of Chlorpyrifos. *ACS Omega* **2020,** *5*, 31765-31773.

266.   Piletsky, S. A.; Piletskaya, E. V.; Yano, K.; Kugimiya, A.; Elgersma, A. V.; Levi, R.; Kahlow, U.; Takeuchi, T.; Karube, I.; Panasyuk, T. I.; El'skaya, A. V., A Biomimetic Receptor System for Sialic Acid Based on Molecular Imprinting. *Anal. Lett.* **1996,** *29*, 157-170.

267.   Yoshimi, Y.; Ohdaira, R.; Iiyama, C.; Sakai, K., "Gate effect" of thin layer of molecularly-imprinted poly(methacrylic acid-co-ethyleneglycol dimethacrylate). *Sens. Actuators B Chem.* **2001,** *73*, 49-53.

268.   Yoshimi, Y.; Sato, K.; Ohshima, M.; Piletska, E., Application of the 'gate effect' of a molecularly imprinted polymer grafted on an electrode for the real-time sensing of heparin in blood. *Analyst* **2013,** *138*, 5121-5128.

269.   Yoshimi, Y.; Narimatsu, A.; Nakayama, K.; Sekine, S.; Hattori, K.; Sakai, K., Development of an enzyme-free glucose sensor using the gate effect of a molecularly imprinted polymer. *J. Artif. Organs* **2009,** *12*, 264.

270.   Herrera-Chacón, A.; Cetó, X.; del Valle, M., Molecularly imprinted polymers - towards electrochemical sensors and electronic tongues. *Anal. Bioanal. Chem.* **2021,** *413*, 6117-6140.

271. Yarman, A.; Scheller, F. W., How Reliable Is the Electrochemical Readout of MIP Sensors? *Sensors* **2020,** *20*, 2677.

272. Ahmad, O. S.; Bedwell, T. S.; Esen, C.; Garcia-Cruz, A.; Piletsky, S. A., Molecularly Imprinted Polymers in Electrochemical and Optical Sensors. *Trends Biotechnol.* **2019,** *37*, 294-309.

273. Zidarič, T.; Finšgar, M.; Maver, U.; Maver, T., Artificial Biomimetic Electrochemical Assemblies. *Biosensors* **2022,** *12*, 44.

274. Cardoso, A. R.; Marques, A. C.; Santos, L.; Carvalho, A. F.; Costa, F. M.; Martins, R.; Sales, M. G. F.; Fortunato, E., Molecularly-imprinted chloramphenicol sensor with laser-induced graphene electrodes. *Biosens. Bioelectron.* **2019,** *124-125*, 167-175.

275. Zamora-Gálvez, A.; Ait-Lahcen, A.; Mercante, L. A.; Morales-Narváez, E.; Amine, A.; Merkoçi, A., Molecularly Imprinted Polymer-Decorated Magnetite Nanoparticles for Selective Sulfonamide Detection. *Anal. Chem.* **2016,** *88*, 3578-3584.

276. Pacheco, J. G.; Rebelo, P.; Freitas, M.; Nouws, H. P. A.; Delerue-Matos, C., Breast cancer biomarker (HER2-ECD) detection using a molecularly imprinted electrochemical sensor. *Sens. Actuators B Chem.* **2018,** *273*, 1008-1014.

277. Waffo, A. F. T.; Yesildag, C.; Caserta, G.; Katz, S.; Zebger, I.; Lensen, M. C.; Wollenberger, U.; Scheller, F. W.; Altintas, Z., Fully electrochemical MIP sensor for artemisinin. *Sens. Actuators B Chem.* **2018,** *275*, 163-173.

278. Jyoti; Gonzato, C.; Żołek, T.; Maciejewska, D.; Kutner, A.; Merlier, F.; Haupt, K.; Sharma, P. S.; Noworyta, K. R.; Kutner, W., Molecularly imprinted polymer nanoparticles-based electrochemical chemosensors for selective determination of cilostazol and its pharmacologically active primary metabolite in human plasma. *Biosens. Bioelectron.* **2021,** *193*, 113542.

279. Raziq, A.; Kidakova, A.; Boroznjak, R.; Reut, J.; Öpik, A.; Syritski, V., Development of a portable MIP-based electrochemical sensor for detection of SARS-CoV-2 antigen. *Biosens. Bioelectron.* **2021,** *178*, 113029.

280. Jolly, P.; Tamboli, V.; Harniman, R. L.; Estrela, P.; Allender, C. J.; Bowen, J. L., Aptamer–MIP hybrid receptor for highly sensitive electrochemical detection of prostate specific antigen. *Biosens. Bioelectron.* **2016,** *75*, 188-195.

281. Moreira, F. T. C.; Dutra, R. A. F.; Noronha, J. P. C.; Fernandes, J. C. S.; Sales, M. G. F., Novel biosensing device for point-of-care applications with plastic antibodies grown on Au-screen printed electrodes. *Sens. Actuators B Chem.* **2013,** *182*, 733-740.

282. Moreira, F. T. C.; Sharma, S.; Dutra, R. A. F.; Noronha, J. P. C.; Cass, A. E. G.; Sales, M. G. F., Protein-responsive polymers for point-of-care detection of cardiac biomarker. *Sens. Actuators B Chem.* **2014,** *196*, 123-132.

283. Moreira, F. T. C.; Dutra, R. A. F.; Noronha, J. P. C.; Sales, M. G. F., Electrochemical biosensor based on biomimetic material for myoglobin detection. *Electrochim. Acta* **2013,** *107*, 481-487.

284. Karimian, N.; Vagin, M.; Zavar, M. H. A.; Chamsaz, M.; Turner, A. P. F.; Tiwari, A., An ultrasensitive molecularly-imprinted human cardiac troponin sensor. *Biosens. Bioelectron.* **2013,** *50*, 492-498.

285. Kamon, Y.; Matsuura, R.; Kitayama, Y.; Ooya, T.; Takeuchi, T., Precisely controlled molecular imprinting of glutathione-s-transferase by orientated template

immobilization using specific interaction with an anchored ligand on a gold substrate. *Polym. Chem.* **2014,** *5*, 4764-4771.

286.   Dechtrirat, D.; Gajovic-Eichelmann, N.; Bier, F. F.; Scheller, F. W., Hybrid Material for Protein Sensing Based on Electrosynthesized MIP on a Mannose Terminated Self-Assembled Monolayer. *Adv. Funct. Mater.* **2014,** *24*, 2233-2239.

287.   Tretjakov, A.; Syritski, V.; Reut, J.; Boroznjak, R.; Öpik, A., Molecularly imprinted polymer film interfaced with Surface Acoustic Wave technology as a sensing platform for label-free protein detection. *Anal. Chim. Acta* **2016,** *902*, 182-188.

288.   Peng, L.; Yarman, A.; Jetzschmann, K. J.; Jeoung, J.-H.; Schad, D.; Dobbek, H.; Wollenberger, U.; Scheller, F. W., Molecularly Imprinted Electropolymer for a Hexameric Heme Protein with Direct Electron Transfer and Peroxide Electrocatalysis. *Sensors* **2016,** *16*, 272.

289.   Stojanovic, Z.; Erdőssy, J.; Keltai, K.; Scheller, F. W.; Gyurcsányi, R. E., Electrosynthesized molecularly imprinted polyscopoletin nanofilms for human serum albumin detection. *Anal. Chim. Acta* **2017,** *977*, 1-9.

290.   Karimian, N.; Turner, A. P. F.; Tiwari, A., Electrochemical evaluation of troponin T imprinted polymer receptor. *Biosens. Bioelectron.* **2014,** *59*, 160-165.

291.   Ozcelikay, G.; Kurbanoglu, S.; Zhang, X.; Kosak Soz, C.; Wollenberger, U.; Ozkan, S. A.; Yarman, A.; Scheller, F. W., Electrochemical MIP Sensor for Butyrylcholinesterase. *Polymers* **2019,** *11*, 1970.

292.   Buffon, E.; Stradiotto, N. R., Electrochemical sensor based on molecularly imprinted poly(ortho-phenylenediamine) for determination of hexahydrofarnesol in aviation biokerosene. *Sens. Actuators B Chem.* **2019,** *287*, 371-379.

293.   Abo-Elmagd, I. F.; Mahmoud, A. M.; Al-Ghobashy, M. A.; Nebsen, M.; El Sayed, N. S.; Nofal, S.; Soror, S. H.; Todd, R.; Elgebaly, S. A., Impedimetric Sensors for Cyclocreatine Phosphate Determination in Plasma Based on Electropolymerized Poly(o-phenylenediamine) Molecularly Imprinted Polymers. *ACS Omega* **2021,** *6*, 31282-31291.

294.   Pedroso, M. M.; Foguel, M. V.; Silva, D. H. S.; Sotomayor, M. d. P. T.; Yamanaka, H., Electrochemical sensor for dodecyl gallate determination based on electropolymerized molecularly imprinted polymer. *Sens. Actuators B Chem.* **2017,** *253*, 180-186.

295.   Dai, Y.-Q.; Zhou, D.-M.; Shiu, K.-K., Permeability and permselectivity of polyphenylenediamine films synthesized at a palladium disk electrode. *Electrochim. Acta* **2006,** *52*, 297-303.

296.   Randviir, E. P.; Banks, C. E., Electrochemical impedance spectroscopy: an overview of bioanalytical applications. *Anal. Methods* **2013,** *5*, 1098-1115.

297.   Zamfir, L.-G.; Puiu, M.; Bala, C., Advances in Electrochemical Impedance Spectroscopy Detection of Endocrine Disruptors. *Sensors* **2020,** *20*, 6443.

298.   Uygun, Z. O.; Ertuğrul Uygun, H. D., A short footnote: Circuit design for faradaic impedimetric sensors and biosensors. *Sens. Actuators B Chem.* **2014,** *202*, 448-453.

299.   Pacheco, J. G.; Silva, M. S. V.; Freitas, M.; Nouws, H. P. A.; Delerue-Matos, C., Molecularly imprinted electrochemical sensor for the point-of-care detection of a breast cancer biomarker (CA 15-3). *Sens. Actuators B Chem.* **2018,** *256*, 905-912.

300.   Bu, L.; Chen, X.; Song, Q.; Jiang, D.; Shan, X.; Wang, W.; Chen, Z., Supersensitive detection of chloramphenicol with an EIS method based on molecularly imprinted polypyrrole at UiO-66 and CDs modified electrode. *Microchem. J.* **2022,** *179*, 107459.

301.   Peeters, M.; Troost, F. J.; van Grinsven, B.; Horemans, F.; Alenus, J.; Murib, M. S.; Keszthelyi, D.; Ethirajan, A.; Thoelen, R.; Cleij, T. J.; Wagner, P., MIP-based biomimetic sensor for the electronic detection of serotonin in human blood plasma. *Sens. Actuators B Chem.* **2012,** *171-172*, 602-610.

302.   Prusty, A. K.; Bhand, S., A capacitive sensor for 2,4-D determination in water based on 2,4-D imprinted polypyrrole coated pencil electrode. *Mater. Res. Express.* **2017,** *4*, 035306.

303.   Sharma, P. S.; Iskierko, Z.; Noworyta, K.; Cieplak, M.; Borowicz, P.; Lisowski, W.; D'Souza, F.; Kutner, W., Synthesis and application of a "plastic antibody" in electrochemical microfluidic platform for oxytocin determination. *Biosens. Bioelectron.* **2018,** *100*, 251-258.

304.   Gong, J. L.; Gong, F. C.; Kuang, Y.; Zeng, G. M.; Shen, G. L.; Yu, R. Q., Capacitive chemical sensor for fenvalerate assay based on electropolymerized molecularly imprinted polymer as the sensitive layer. *Anal. Bioanal. Chem.* **2004,** *379*, 302-307.

305.   Ratautaite, V.; Janssens, S. D.; Haenen, K.; Nesládek, M.; Ramanaviciene, A.; Baleviciute, I.; Ramanavicius, A., Molecularly Imprinted Polypyrrole Based Impedimentric Sensor for Theophylline Determination. *Electrochim. Acta* **2014,** *130*, 361-367.

306.   Otero, T. F., Structural and Conformational Chemistry from Electrochemical Molecular Machines. Replicating Biological Functions. A Review. *Chem. Rec.* **2018,** *18*, 788-806.

307.   Heinze, J.; Frontana-Uribe, B. A.; Ludwigs, S., Electrochemistry of Conducting Polymers—Persistent Models and New Concepts. *Chem. Rev.* **2010,** *110*, 4724-4771.

308.   Trotta, F.; Biasizzo, M.; Caldera, F., Molecularly Imprinted Membranes. *Membranes* **2012,** *2*, 440-477.

309.   Cho, I.-H.; Lee, J.; Kim, J.; Kang, M.-s.; Paik, J.; Ku, S.; Cho, H.-M.; Irudayaraj, J.; Kim, D.-H., Current Technologies of Electrochemical Immunosensors: Perspective on Signal Amplification. *Sensors* **2018,** *18*, 207.

310.   Bakker, E.; Qin, Y., Electrochemical Sensors. *Anal. Chem.* **2006,** *78*, 3965-3984.

311.   Liu, G.; Lin, Y., Nanomaterial labels in electrochemical immunosensors and immunoassays. *Talanta* **2007,** *74*, 308-317.

312.   Lim, S. A.; Ahmed, M. U., Electrochemical immunosensors and their recent nanomaterial-based signal amplification strategies: a review. *RSC Adv.* **2016,** *6*, 24995-25014.

313.   Sanaullah, A. F. M.; Jeong, B.; Akter, R.; Han, O. H.; Rahman, M. A., Nanoparticles Supported-Methylene Blue Labels and Multiwall Carbon Nanotubes-Based Highly Sensitive Electrochemical Immunosensor. *Bull. Korean Chem. Soc.* **2014,** *35*, 2193-2196.

314.   Ding, Y.; Li, D.; Li, B.; Zhao, K.; Du, W.; Zheng, J.; Yang, M., A water-dispersible, ferrocene-tagged peptide nanowire for amplified electrochemical immunosensing. *Biosens. Bioelectron.* **2013,** *48*, 281-286.

315. Lim, S. A.; Yoshikawa, H.; Tamiya, E.; Yasin, H. M.; Ahmed, M. U., A highly sensitive gold nanoparticle bioprobe based electrochemical immunosensor using screen printed graphene biochip. *RSC Adv.* **2014,** *4*, 58460-58466.

316. Xiong, P.; Gan, N.; Cao, Y.; Hu, F.; Li, T.; Zheng, L., An Ultrasensitive Electrochemical Immunosensor for Alpha-Fetoprotein Using an Envision Complex-Antibody Copolymer as a Sensitive Label. *Materials* **2012,** *5*, 2757-2772.

317. Lai, G.; Cheng, H.; Xin, D.; Zhang, H.; Yu, A., Amplified inhibition of the electrochemical signal of ferrocene by enzyme-functionalized graphene oxide nanoprobe for ultrasensitive immunoassay. *Anal. Chim. Acta* **2016,** *902*, 189-195.

318. Akanda, M. R.; Ju, H., A Tyrosinase-Responsive Nonenzymatic Redox Cycling for Amplified Electrochemical Immunosensing of Protein. *Anal. Chem.* **2016,** *88*, 9856-9861.

319. Lakhin, A. V.; Tarantul, V. Z.; Gening, L. V., Aptamers: problems, solutions and prospects. *Acta Naturae* **2013,** *5*, 34-43.

320. Samuel, V. R.; Rao, K. J., A review on label free biosensors. *Biosens. Bioelectron. X* **2022,** *11*, 100216.

321. Li, Z.; Mohamed, M. A.; Vinu Mohan, A. M.; Zhu, Z.; Sharma, V.; Mishra, G. K.; Mishra, R. K., Application of Electrochemical Aptasensors toward Clinical Diagnostics, Food, and Environmental Monitoring: Review. *Sensors* **2019,** *19*, 5435.

322. Subjakova, V.; Oravczova, V.; Tatarko, M.; Hianik, T., Advances in electrochemical aptasensors and immunosensors for detection of bacterial pathogens in food. *Electrochim. Acta* **2021,** *389*, 138724.

323. Ikebukuro, K.; Kiyohara, C.; Sode, K., Novel electrochemical sensor system for protein using the aptamers in sandwich manner. *Biosens. Bioelectron.* **2005,** *20*, 2168-2172.

324. Polsky, R.; Gill, R.; Kaganovsky, L.; Willner, I., Nucleic Acid-Functionalized Pt Nanoparticles: Catalytic Labels for the Amplified Electrochemical Detection of Biomolecules. *Anal. Chem.* **2006,** *78*, 2268-2271.

325. He, P.; Shen, L.; Cao, Y.; Li, D., Ultrasensitive Electrochemical Detection of Proteins by Amplification of Aptamer−Nanoparticle Bio Bar Codes. *Anal. Chem.* **2007,** *79*, 8024-8029.

326. Zhou, L.; Ou, L.-J.; Chu, X.; Shen, G.-L.; Yu, R.-Q., Aptamer-Based Rolling Circle Amplification: A Platform for Electrochemical Detection of Protein. *Anal. Chem.* **2007,** *79*, 7492-7500.

327. Song, S.; Wang, L.; Li, J.; Fan, C.; Zhao, J., Aptamer-based biosensors. *Trends Anal. Chem.* **2008,** *27*, 108-117.

328. Xie, S.; Ye, J.; Yuan, Y.; Chai, Y.; Yuan, R., A multifunctional hemin@metal–organic framework and its application to construct an electrochemical aptasensor for thrombin detection. *Nanoscale* **2015,** *7*, 18232-18238.

329. Zhang, Y.; Xia, J.; Zhang, F.; Wang, Z.; Liu, Q., Ultrasensitive label-free homogeneous electrochemical aptasensor based on sandwich structure for thrombin detection. *Sens. Actuators B Chem.* **2018,** *267*, 412-418.

330. Ding, J.; Qin, W., Recent advances in potentiometric biosensors. *Trends Anal. Chem.* **2020,** *124*, 115803.

331.   Ding, J.; Chen, Y.; Wang, X.; Qin, W., Label-Free and Substrate-Free Potentiometric Aptasensing Using Polycation-Sensitive Membrane Electrodes. *Anal. Chem.* **2012,** *84*, 2055-2061.

332.   Ding, J.; Lei, J.; Ma, X.; Gong, J.; Qin, W., Potentiometric Aptasensing of Listeria monocytogenes Using Protamine as an Indicator. *Anal. Chem.* **2014,** *86*, 9412-9416.

333.   Tang, W.; Yu, J.; Wang, Z.; Jeerapan, I.; Yin, L.; Zhang, F.; He, P., Label-free potentiometric aptasensing platform for the detection of Pb2+ based on guanine quadruplex structure. *Anal. Chim. Acta* **2019,** *1078*, 53-59.

334.   Leva-Bueno, J.; Peyman, S. A.; Millner, P. A., A review on impedimetric immunosensors for pathogen and biomarker detection. *Med. Microbiol. Immunol.* **2020,** *209*, 343-362.

335.   Sheikhzadeh, E.; Chamsaz, M.; Turner, A. P. F.; Jager, E. W. H.; Beni, V., Label-free impedimetric biosensor for Salmonella Typhimurium detection based on poly [pyrrole-co-3-carboxyl-pyrrole] copolymer supported aptamer. *Biosens. Bioelectron.* **2016,** *80*, 194-200.

336.   Brosel-Oliu, S.; Ferreira, R.; Uria, N.; Abramova, N.; Gargallo, R.; Muñoz-Pascual, F.-X.; Bratov, A., Novel impedimetric aptasensor for label-free detection of Escherichia coli O157:H7. *Sens. Actuators B Chem.* **2018,** *255*, 2988-2995.

337.   Tertis, M.; Leva, P. I.; Bogdan, D.; Suciu, M.; Graur, F.; Cristea, C., Impedimetric aptasensor for the label-free and selective detection of Interleukin-6 for colorectal cancer screening. *Biosens. Bioelectron.* **2019,** *137*, 123-132.

338.   Muniandy, S.; Dinshaw, I. J.; Teh, S. J.; Lai, C. W.; Ibrahim, F.; Thong, K. L.; Leo, B. F., Graphene-based label-free electrochemical aptasensor for rapid and sensitive detection of foodborne pathogen. *Anal. Bioanal. Chem.* **2017,** *409*, 6893-6905.

339.   Mazaafrianto, D. N.; Ishida, A.; Maeki, M.; Tani, H.; Tokeshi, M., Label-Free Electrochemical Sensor for Ochratoxin A Using a Microfabricated Electrode with Immobilized Aptamer. *ACS Omega* **2018,** *3*, 16823-16830.

340.   Ge, C.; Yuan, R.; Yi, L.; Yang, J.; Zhang, H.; Li, L.; Nian, W.; Yi, G., Target-induced aptamer displacement on gold nanoparticles and rolling circle amplification for ultrasensitive live Salmonella typhimurium electrochemical biosensing. *J. Electroanal. Chem.* **2018,** *826*, 174-180.

341.   Udomsap, D.; Branger, C.; Culioli, G.; Dollet, P.; Brisset, H., A versatile electrochemical sensing receptor based on a molecularly imprinted polymer. *Chem. Commun.* **2014,** *50*, 7488-7491.

342.   Udomsap, D.; Brisset, H.; Culioli, G.; Dollet, P.; Laatikainen, K.; Siren, H.; Branger, C., Electrochemical molecularly imprinted polymers as material for pollutant detection. *Mater. Today Commun.* **2018,** *17*, 458-465.

343.   Ekomo, V. M.; Branger, C.; Bikanga, R.; Florea, A.-M.; Istamboulie, G.; Calas-Blanchard, C.; Noguer, T.; Sarbu, A.; Brisset, H., Detection of Bisphenol A in aqueous medium by screen-printed carbon electrodes incorporating electrochemical molecularly imprinted polymers. *Biosens. Bioelectron.* **2018,** *112*, 156-161.

344.   Mazzotta, E.; Turco, A.; Chianella, I.; Guerreiro, A.; Piletsky, S. A.; Malitesta, C., Solid-phase synthesis of electroactive nanoparticles of molecularly imprinted polymers. A novel platform for indirect electrochemical sensing applications. *Sens. Actuators B Chem.* **2016,** *229*, 174-180.

345.   Garcia-Cruz, A.; Ahmad, O. S.; Alanazi, K.; Piletska, E.; Piletsky, S. A., Generic sensor platform based on electro-responsive molecularly imprinted polymer nanoparticles (e-NanoMIPs). *Microsyst. Nanoeng.* **2020,** *6*, 83.

346.   Muzyka, K.; Karim, K.; Guerreiro, A.; Poma, A.; Piletsky, S., Optimisation of the synthesis of vancomycin-selective molecularly imprinted polymer nanoparticles using automatic photoreactor. *Nanoscale Res. Lett.* **2014,** *9*, 154.

347.   Haq, I.; Alanazi, K.; Czulak, J.; Di Masi, S.; Piletska, E.; Mujahid, A.; Hussain, T.; Piletsky, S. A.; Garcia-Cruz, A., Determination of sitagliptin in human plasma using a smart electrochemical sensor based on electroactive molecularly imprinted nanoparticles. *Nanoscale Adv.* **2021,** *3*, 4276-4285.

348.   Garcia Cruz, A.; Haq, I.; Cowen, T.; Di Masi, S.; Trivedi, S.; Alanazi, K.; Piletska, E.; Mujahid, A.; Piletsky, S. A., Design and fabrication of a smart sensor using in silico epitope mapping and electro-responsive imprinted polymer nanoparticles for determination of insulin levels in human plasma. *Biosens. Bioelectron.* **2020,** *169*, 112536.

349.   Alanazi, K.; Garcia Cruz, A.; Di Masi, S.; Voorhaar, A.; Ahmad, O. S.; Cowen, T.; Piletska, E.; Langford, N.; Coats, T. J.; Sims, M. R.; Piletsky, S. A., Disposable paracetamol sensor based on electroactive molecularly imprinted polymer nanoparticles for plasma monitoring. *Sens. Actuators B Chem.* **2021,** *329*, 129128.

350.   Tang, H.; Chen, J.; Zeng, Y.; Li, Z.; Huang, H.; Li, L., An electrochemical sensor for 1-naphthylamine based on a novel composite of cyclodextrin-graphene and molecularly imprinted poly(vinylferrocene). *Anal. Methods* **2016,** *8*, 1681-1689.

351.   Rebocho, S.; Cordas, C. M.; Viveiros, R.; Casimiro, T., Development of a ferrocenyl-based MIP in supercritical carbon dioxide: Towards an electrochemical sensor for bisphenol A. *J. Supercrit. Fluids* **2018,** *135*, 98-104.

352.   Manesiotis, P.; Riley, A.; Bollen, B., Polymerisable squaramide receptors for anion binding and sensing. *J. Mat. Chem. C* **2014,** *2*, 8990-8995.

353.   Thordarson, P., Determining association constants from titration experiments in supramolecular chemistry. *Chem. Soc. Rev.* **2011,** *40*, 1305-1323.

354.   Koh, W.; Kutner, W.; Jones, M. T.; Kadish, K. M., An improved holder for the electrochemical quartz crystal microbalance and its cyclic voltammetry characteristics. *Electroanal.* **1993,** *5*, 209-214.

355.   Kochman, A.; Krupka, A.; Grissbach, J.; Kutner, W.; Gniewińska, B.; Nafalski, L., Design and Performance of a New Thin-Layer Radial-Flow Holder for a Quartz Crystal Resonator of an Electrochemical Quartz Crystal Microbalance. *Electroanal.* **2006,** *18*, 2168-2173.

356.   Cowen, T.; Karim, K.; Piletsky, S., Computational approaches in the design of synthetic receptors – A review. *Anal. Chim. Acta* **2016,** *936*, 62-74.

357.   Leach, A. R., *Molecular modelling: principles and applications.* 2nd ed.; Prentice Hall: Harlow, England ; New York, 2001.

358.   Canfarotta, F.; Poma, A.; Guerreiro, A.; Piletsky, S., Solid-phase synthesis of molecularly imprinted nanoparticles. *Nat. Protoc.* **2016,** *11*, 443-455.

359.   Guerreiro, A. R.; Chianella, I.; Piletska, E.; Whitcombe, M. J.; Piletsky, S. A., Selection of imprinted nanoparticles by affinity chromatography. *Biosens. Bioelectron.* **2009,** *24*, 2740-2743.

360.   Otsu, T., Iniferter concept and living radical polymerization. *J. Polym. Sci.* **2000,** *38*, 2121-2136.

361.   Kannurpatti, A. R.; Lu, S.; Bunker, G. M.; Bowman, C. N., Kinetic and Mechanistic Studies of Iniferter Photopolymerizations. *Macromol.* **1996,** *29*, 7310-7315.

362.   Compton, R. G.; Banks, C. E., *Understanding Voltammetry*. 2nd Ed.; Imperial College Press: London, 2010.

363.   Zoski, C. G., *Handbook of Electrochemistry*. 1st Ed.; Elsevier: Amsterdam, 2007.

364.   Bard, A. J.; Faulkner, L. R., *Electrochemical methods: Fundamentals and Applications*. 2nd Ed.; John Wiley & Sons: New York, 2000.

365.   Unwin, P. R., Instrumentation and electroanalytical chemistry. In *Encyclopedia of Electrochemistry*; Bard, A. J.; Stratmann, M., Ed.; Wiley-VCH: Weinheim, 2003.

366.   Wang, S.; Zhang, J.; Gharbi, O.; Vivier, V.; Gao, M.; Orazem, M. E., Electrochemical impedance spectroscopy. *Nat. Rev. Methods Primers* **2021,** *1*, 41.

367.   Magar, H. S.; Hassan, R. Y. A.; Mulchandani, A., Electrochemical Impedance Spectroscopy (EIS): Principles, Construction, and Biosensing Applications. *Sensors* **2021,** *21*, 6578.

368.   Buck, R. P.; Lindner, E.; Kutner, W.; Inzelt, G., Piezoelectric chemical sensors - (IUPAC Technical Report). *Pure Appl. Chem.* **2004,** *76*, 1139-1160.

369.   Sauerbrey, G., Verwendung Von Schwingquarzen Zur Wagung Dunner Schichten Und Zur Mikrowagung. *Z Phys* **1959,** *155*, 206-222.

370.   Ispas, A.; Bund, A., Electrochemical Quartz Crystal Microbalance. In *Encyclopedia of Applied Electrochemistry*, 2014; pp 554-568.

371.   Bruckenstein, S.; Shay, M., Experimental aspects of use of the quartz crystal microbalance in solution. *Electrochim. Acta* **1985,** *30*, 1295-1300.

372.   Kanazawa, K. K.; Gordon, J. G., Frequency of a quartz microbalance in contact with liquid. *Anal. Chem.* **2002,** *57*, 1770-1771.

373.   Buttry, D. A.; Ward, M. D., Measurement of interfacial processes at electrode surfaces with the electrochemical quartz crystal microbalance. *Chem. Rev.* **1992,** *92*, 1355-1379.

374.   Davies, J.; Davies, J. S., *Surface analytical techniques for probing biomaterial processes*. CRC Press: Boca Raton, Fl. ; London, 1996.

375.   Schasfoort, R. B. M., *Handbook of Surface Plasmon Resonance*. 2017.

376.   Otto, A., Excitation of nonradiative surface plasma waves in silver by the method of frustrated total reflection. *Z. Phys. A-Hadrons Nucl.* **1968,** *216*, 398-410.

377.   Kretschmann, E.; Raether, H., Notizen: Radiative Decay of Non-Radiative Surface Plasmons Excited by Light. *Z. Naturforsch., A* **1968,** *23*, 2135-2136.

378.   Šípová, H.; Homola, J., Surface plasmon resonance sensing of nucleic acids: A review. *Anal. Chim. Acta* **2013,** *773*, 9-23.

379.   De Caro, C. A.; Haller, C., UV/VIS Spectrophotometry - Fundamentals and Applications. Mettler-Toledo Publication No. ME-30256131: 2015.

380.   Golden, W., A method for measuring infrared reflection?Absorption spectra of molecules adsorbed on low-area surfaces at monolayer and submonolayer concentrations. *J. Catal.* **1981,** *71*, 395-404.

381.   Golden, W. G.; Kunimatsu, K.; Seki, H., Application of polarization-modulated Fourier transform infrared reflection-absorption spectroscopy to the study of carbon monoxide adsorption and oxidation of a smooth platinum electrode. *J. Phys. Chem.* **1984,** *88*, 1275-1277.

382.   Buffeteau, T.; Desbat, B.; Turlet, J. M., Polarization Modulation Ft-Ir Spectroscopy of Surfaces and Ultra-Thin Films: Experimental Procedure and Quantitative Analysis. *Appl Spectrosc* **1991,** *45*, 380-389.

383.   Hertz, H., Ueber sehr schnelle electrische Schwingungen. *Ann. Phys. Chem.* **1887,** *267*, 421-448.

384.   Einstein, A., Zur Elektrodynamik bewegter Körper. *Ann. Phys.* **1905,** *322*, 891-921.

385.   Haasch, R. T., X-Ray Photoelectron Spectroscopy (XPS) and Auger Electron Spectroscopy (AES). In *Practical Materials Characterization*, 2014; pp 93-132.

386.   Stevie, F. A.; Donley, C. L., Introduction to x-ray photoelectron spectroscopy. *J. Vac. Sci. Technol. A: Vac. Surf.* **2020,** *38*, 063204.

387.   Guo, D.; Xie, G.; Luo, J., Mechanical properties of nanoparticles: basics and applications. *J. Phys. D: Appl. Phys.* **2014,** *47*, 013001.

388.   Howland, R.; Benatar, L., *A Practical Guide to Scanning Probe Microscopy*. Park Scientific Instruments: 1996.

389.   Zavala, G., Atomic force microscopy, a tool for characterization, synthesis and chemical processes. *Colloid Polym. Sci.* **2007,** *286*, 85-95.

390.   Inkson, B. J., Scanning electron microscopy (SEM) and transmission electron microscopy (TEM) for materials characterization. In *Materials Characterization Using Nondestructive Evaluation (NDE) Methods*, 2016; pp 17-43.

391.   Stetefeld, J.; McKenna, S. A.; Patel, T. R., Dynamic light scattering: a practical guide and applications in biomedical sciences. *Biophys. Rev.* **2016,** *8*, 409-427.

392.   Johannsmann, D., Studies of Viscoelasticity with the QCM. In *Piezoelectric Sensors*, Janshoff, A.; Steinem, C., Eds. Springer Berlin Heidelberg: Berlin, Heidelberg, 2007; pp 49-109.

393.   Johannsmann, D., Viscoelastic, mechanical, and dielectric measurements on complex samples with the quartz crystal microbalance. *Phys. Chem. Chem. Phys.* **2008,** *10*, 4516-4534.

394.   Thompson, M.; Kipling, A. L.; Duncan-Hewitt, W. C.; Rajaković, L. V.; Čavić-Vlasak, B. A., Thickness-shear-mode acoustic wave sensors in the liquid phase. A review. *Analyst* **1991,** *116*, 881-890.

395.   Socrates, G., *Infrared and Raman characteristic group frequencies*. 3rd ed.; Wiley: New York, 2001.

396.   Gök, A.; Omastová, M.; Yavuz, A. G., Synthesis and characterization of polythiophenes prepared in the presence of surfactants. *Synth. Met.* **2007,** *157*, 23-29.

397.   Urbanski, T. In *Ultraviolet and Infrared Spectra of Some Nitrosamines*, 2012.

398.   Iskierko, Z.; Sharma, P. S.; Bartold, K.; Pietrzyk-Le, A.; Noworyta, K.; Kutner, W., Molecularly imprinted polymers for separating and sensing of macromolecular compounds and microorganisms. *Biotechnol. Adv.* **2016,** *34*, 30-46.

399.   Yoshimi, Y.; Yoshiizumi, R.; Arai, R.; Nakano, I.; Sekine, S., Chiral-Discriminative Gate Effect in Self-Supporting Phenylalanine-Imprinted Poly(Methacrylic Acid-*co*-2-Vinylpyridine-*co*-Triethyleneglycol Dimethacrylate) Membrane. *J. Chem. Eng. Jpn.* **2009,** *42*, 600-606.

400.   Li, Y.; Liu, J.; Zhang, Y.; Gu, M.; Wang, D.; Dang, Y.-y.; Ye, B.-C.; Li, Y., A robust electrochemical sensing platform using carbon paste electrode modified with molecularly imprinted microsphere and its application on methyl parathion detection. *Biosens. Bioelectron.* **2018,** *106*, 71-77.

401.   Liu, Y.; Liu, J.; Liu, J.; Gan, W.; Ye, B.-c.; Li, Y., Highly sensitive and selective voltammetric determination of dopamine using a gold electrode modified with a molecularly imprinted polymeric film immobilized on flaked hollow nickel nanospheres. *Microchim. Acta* **2017,** *184*, 1285-1294.

402.   Pietrzyk, A.; Suriyanarayanan, S.; Kutner, W.; Chitta, R.; D'Souza, F., Selective Histamine Piezoelectric Chemosensor Using a Recognition Film of the Molecularly Imprinted Polymer of Bis(bithiophene) Derivatives. *Anal. Chem.* **2009,** *81*, 2633-2643.

403.   Karthick, T.; Balachandran, V.; Perumal, S., Spectroscopic investigations, molecular interactions, and molecular docking studies on the potential inhibitor "thiophene-2-carboxylic acid". *Spectrochim. Acta A* **2015,** *141*, 104-112.

404.   Łępicka, K.; Majewska, M.; Nowakowski, R.; Kutner, W.; Pieta, P., High electrochemical stability of meso-Ni-salen based conducting polymer manifested by potential-driven reversible changes in viscoelastic and nanomechanical properties. *Electrochim. Acta* **2019,** *297*, 94-100.

405.   Enengl, C.; Enengl, S.; Pluczyk, S.; Havlicek, M.; Lapkowski, M.; Neugebauer, H.; Ehrenfreund, E., Doping-Induced Absorption Bands in P3HT: Polarons and Bipolarons. *ChemPhysChem* **2016,** *17*, 3836-3844.

406.   Choi, Y.; Tepavcevic, S.; Xu, Z.; Hanley, L., Optical and Chemical Properties of Polythiophene Films Produced via Surface Polymerization by Ion-Assisted Deposition. *Chem. Mater.* **2004,** *16*, 1924-1931.

407.   Grebner, D.; Helbig, M.; Rentsch, S., Size-Dependent Properties of Oligothiophenes by Picosecond Time-Resolved Spectroscopy. *J. Phys. Chem.* **1995,** *99*, 16991-16998.

408.   Criado, C.; Galán-Montenegro, P.; Velásquez, P.; Ramos-Barrado, J. R., Diffusion with general boundary conditions in electrochemical systems. *J. Electroanal. Chem.* **2000,** *488*, 59-63.

409.   Bisquert, J., Theory of the Impedance of Electron Diffusion and Recombination in a Thin Layer. *J. Phys. Chem. B* **2002,** *106*, 325-333.

410.   Huang, J., Diffusion impedance of electroactive materials, electrolytic solutions and porous electrodes: Warburg impedance and beyond. *Electrochim. Acta* **2018,** *281*, 170-188.

411.   Bisquert, J.; Garcia-Belmonte, G.; Fabregat-Santiago, F.; Bueno, P. R., Theoretical models for ac impedance of finite diffusion layers exhibiting low frequency dispersion. *J. Electroanal. Chem.* **1999**, 152-163.

412.   Valincius, G.; Mickevicius, M.; Penkauskas, T.; Jankunec, M., Electrochemical Impedance Spectroscopy of Tethered Bilayer Membranes: An Effect of Heterogeneous Distribution of Defects in Membranes. *Electrochim. Acta* **2016,** *222*, 904-913.

413.   Galus, Z., *Fundamentals of Electrochemical Analysis*. Polish Scientific Publishers PWN: Warsaw, 1994.

414.   Rostami, A.; Colin, A.; Li, X. Y.; Chudzinski, M. G.; Lough, A. J.; Taylor, M. S., N,N′-Diarylsquaramides: General, High-Yielding Synthesis and Applications in Colorimetric Anion Sensing. *J. Org. Chem.* **2010,** *75*, 3983-3992.

415.   Ian Storer, R.; Aciro, C.; Jones, L. H., Squaramides: physical properties, synthesis and applications. *Chem. Soc. Rev.* **2011,** *40*, 2330-2346.

416.   Bhattacharjee, S., DLS and zeta potential – What they are and what they are not? *J. Control. Release* **2016,** *235*, 337-351.

417.   Teulon, J.-M.; Godon, C.; Chantalat, L.; Moriscot, C.; Cambedouzou, J.; Odorico, M.; Ravaux, J.; Podor, R.; Gerdil, A.; Habert, A.; Herlin-Boime, N.; Chen, S.-W. W.; Pellequer, J.-L., On the Operational Aspects of Measuring Nanoparticle Sizes. *Nanomaterials* **2018,** *9*, 18.

418.   Zhang, W., Nanoparticle Aggregation: Principles and Modeling. In *Nanomaterial: Impacts on Cell Biology and Medicine*, Capco, D. G.; Chen, Y., Eds. Springer Netherlands: Dordrecht, 2014; pp 19-43.

419.   Piletsky, S. A.; Piletskaya, E. V.; Elgersma, A. V.; Yano, K.; Karube, I.; Parhometz, Y. P.; El'skaya, A. V., Atrazine sensing by molecularly imprinted membranes. *Biosens. Bioelectron.* **1995,** *10*, 959-964.

420.   Nogami, H.; Nakahori, Y.; Murashima, T.; Matsui, J., Nicotine-Selective Polymeric Adsorbent Obtained by Molecular Imprinting with Excess Use of Itaconic Acid. *Chromatography* **2017,** *38*, 15-21.

421.   Marchetti, L. A.; Kumawat, L. K.; Mao, N.; Stephens, J. C.; Elmes, R. B. P., The Versatility of Squaramides: From Supramolecular Chemistry to Chemical Biology. *Chem* **2019,** *5*, 1398-1485.

422.   Chauhan, P.; Mahajan, S.; Kaya, U.; Hack, D.; Enders, D., Bifunctional Amine-Squaramides: Powerful Hydrogen-Bonding Organocatalysts for Asymmetric Domino/Cascade Reactions. *Adv. Synth. Catal.* **2015,** *357*, 253-281.

423.   Morita, S., Hydrogen-bonds structure in poly(2-hydroxyethyl methacrylate) studied by temperature-dependent infrared spectroscopy. *Front Chem* **2014,** *2*, 10-10.

424.   Mercante, L. A.; Pavinatto, A.; Iwaki, L. E. O.; Scagion, V. P.; Zucolotto, V.; Oliveira, O. N.; Mattoso, L. H. C.; Correa, D. S., Electrospun Polyamide 6/Poly(allylamine hydrochloride) Nanofibers Functionalized with Carbon Nanotubes for Electrochemical Detection of Dopamine. *ACS Appl. Mater. Interfaces* **2015,** *7*, 4784-4790.

Institute of Physical Chemistry
Polish Academy of Science

Kasprzaka 44/52
01-224 Warsaw, Poland